Development of Sintered Lamellar Soft Magnetic Composites (SL-SMC)

Patrick Lemieux

Degree of Doctor of Philosophy

Department of Mining and Materials Engineering, Faculty of Engineering

McGill University

Montreal, Quebec, Canada

April 14, 2013

A thesis submitted to McGill University in partial fulfillment of the requirements of the degree of Doctor of Philosophy

DEDICATION

This document is dedicated to all young people of Quebec, to tell them to never to stop dreaming and to keep focussed on the long term targets of their dreams. Never compromise the long term goals for short term objectives. It is never too late to accomplish what you were supposed or wanted to do (e.g. a PhD at 45!). I would like also to dedicate this work to God, who put me on this track, allowed me to pursue this work to completion.

ACKNOWLEDGMENTS

I would like, first of all, to thank and acknowledge the important contribution of Dr. Roderick Guthrie, and Dr Mihaiela Isac, and all the MMPC team and organisation, who provided me support, an important knowledge base and all the equipment that has been needed for this important research program. It is important to mention that Prof Guthrie and Dr. Isac worked hard to secure important financing from NSERC and FQRNT that allowed the research work to progress above our hope.

I would also like to acknowledge Dr Kinnor Chattopadhyay, of the MMPC, for guidance with the FLUENT mathematical modelling work, and Jacques Bergeron and Maxime Gagné, who helped me with all the technical aspects of the experiments at the McGill Metals Processing Centre's Process Metallurgy Laboratories.

I would also like also to acknowledge the Industrial Material Institute of CNRC and the powder shaping group, particularly Yannig Thomas, Patrick England, Fabrice Bernier, Shirley Mercier, Mario Laplume, Sylvain Pelletier and Eric Baril.

Similarly, I would like to acknowledge the LEEPCI group of the Electrical Eng. Department at Laval University, Prof. Maxime Dubois and M. Jude Delma and all the research team at Quebec Metal Powders Ltd.,

particularly Sylvain St-Laurent, Claude Gélinas and Chantal Labrecque, for their help in supplying different products and measurement apparatus from time to time.

Finally I would like to acknowledge my business partners in this adventure of IMFINE Corp., Paul Caron, Bernard Larouche and Jean Bédard.

I am very grateful to my wife and children, who have supported and encouraged me all the way along this long process. Also, to my parents, who always trusted in my ideas and gave me the confidence I need in life.

TABLE OF CONTENTS

LIST OF TABLES

LIST OF FIGURES

ABSTRACT

Research carried out over the last ten years has shown that Soft Magnetic Composite (SMC) materials are potentially good candidates to replace laminated steel sheets in electric motors. Indeed, their increased isotropy, combined with a near net shape forming technology, will allow motor designers more flexibility for the efficient design of electric motors. Literature already reports many new designs with higher power to weight, or power to volume, ratios of motors, while simultaneously decreasing their assembling costs. However, SMC materials that are currently available in the marketplace do not have sufficiently good mechanical and magnetic properties to fully benefit from the design advantages brought about by the SMC approach. They are based on irregular shaped water atomized iron particles, an intricate and expensive process.

By combining three different technologies; a) the direct casting of iron ribbons, b) thin coating (Sol-Gel/ PVD) and c) powder metallurgy, it should be possible to produce a low cost magnetic material with superior mechanical and magnetic properties. This new composite material is referred to as a Sintered Lamellar Soft Magnetic Composite (SL-SMC).

All the technological barriers in the SL-SMC process have been addressed during the course of this doctoral study. In the first part of this thesis, the mathematical modeling of a new direct casting technology adapted to the base ribbon required for the SL-SMC is first reported and the results discussed. A few casting experiments were performed in order to validate the model of this new casting approach and the results compared to similar experiments reported in the literature. The most important parameters were determined. The second part of the thesis focusses on the development of an economic coating technology to insulate individual particles of the SL-SMC composite. The third part of the thesis concerns the development of a viable mass production, net shaping technology, based on standard powder metallurgy compaction techniques.

Finally, SL-SMC behaviour, mechanical and magnetic properties as a function of the numerous processing conditions tested with different base alloys and additives are presented, and compared to the best SMC's and Standard Lamination solutions presently available in the marketplace. The thesis is completed by a modelling experiment and some calculations of the potential improvements of different kinds of motors by using SL-SMC's. Avenues for further optimization are considered and presented.

SOMMAIRE

La recherche des dernières années a démontré que les Composites Magnétiques Doux (Soft Magnetic Composites, SMC) pouvaient être de bons candidats pour remplacer les empilements de tôles magnétiques dans les moteurs électriques. En effet, leur isotropie accrue combinée au procédé de mise en forme aux cotes qu'est la métallurgie des poudres permet une plus grande flexibilité aux designers de moteurs. La litérature rapporte à cet effet déjà plusieurs nouveaux design de moteurs avec de meilleurs ratio puissance/poids ou puissance /volume à des couts d'assemblages plus bas. Par contre les SMC présentement sur le marche ne possèdent pas des propriétés mécaniques et magnétiques suffisantes pour tirer pleinement profit des avantages reliés aux nouveaux designs apparus grâce au SMC. Ils sont fabriqués à base de poudre de fer de forme irrégulières atomises à l'eau, un procédé complexe et onéreux.

En combinant trois technologies; a) la coulée directe de rubans ferromagnétiques, b) les revêtements par couches minces (PVD ou Sol-Gel) et c) la métallurgie des poudres, il doit être possible de produire à bas coût un matériau composite avec des propriétés mécaniques et

magnétiques améliorées. Ce matériau est nommé Sintered Lamellar-Soft Magnetic Composite (SL-SMC).

Cette étude doctorale adresse toutes les barrières technologiques rencontrées dans le développement de la technologie SL-SMC. En conséquence, cette thèse comprend quatre grandes divisions en plus de se terminer par un exercice de modélisation de quelques design typiques de moteurs à haute performance pour estimer les améliorations potentielles que peut apporter la technologie SL-SMC avec les propriétés obtenus comparés aux SMC typiques et aux empilements de tôles conventionnels. La première section présente et discute les résultats d'un exercice de modélisation mathématique du nouveau procédé de coulée direct adapté aux besoins en ruban du procédé SL-SMC. Quelques expériences de coulée furent effectuées pour valider le modèle et l'approche préconisé et les résultats sont comparés aux approches les plus similaires trouvés dans la littérature. La deuxième partie concerne le développement d'un procédé économique de revêtement en couche mince pour l'isolation des particules du composite. La troisième relate le développement d'un procédé de masse viable de mise en forme aux cotes basé sur les techniques de mise en forme en métallurgie des poudres.

Finalement, la dernière partie, qui précédent l'exercice d'estimation des performances dans différents moteurs, identifie les paramètres les plus influant sur le comportement des SL-SMC, leur tenue mécanique et leurs propriétés magnétiques. Elle présente ces propriétés en fonction des différentes conditions de procédés testés avec différents alliages de bases et les compare aux meilleurs SMC et tôles laminés du marché. La thèse est conclue par la présentation de différentes avenus pour poursuivre l'amélioration de ce nouveau type de composite magnétique.

NOMENCLATURE

k, Kinetic energy of turbulence per unit mass, m^2/s^2

ε, Rate of energy dissipation per unit mass, m^2/s^3

G_k, Rate of production of k, $kg/m\text{-}s^3$

C_1, C_2, C_μ, σ_ε, σ_k , are Empirical Constants in the k-ε model of turbulence.

$\vec{v}$, Fluid Velocity, m s^{-1}

$\overrightarrow{v_p}$, is the solid velocity due to the pulling of solidified material out of the domain (also referred to as the pull velocity)

S, source or sink term in the momentum equation (m/s), the energy equation (j/s), the turbulence kinetic energy equation (m^2/s), and the rate of energy dissipation equation (m^2/s^4).

β, the liquid volume fraction,

α, a small number (0.001) to prevent division by zero,

$A_{mush,}$ the mushy zone constant, Empirical

h, enthalpy variation of the material from its reference temperature, j

ΔH, latent heat, j

L, latent heat of the material, j

h_{ref} reference enthalpy, j

T, temperature of the fluid, K

$T_{solidus}$, solidus temperature of the alloy, K

$T_{liquidus}$, liquidus temperature of the alloy, K

T_{ref} , reference temperature, K

C_p , specific heat at constant pressure, j/kg.K

$\emptyset$, a variable of interest

μ, Molecular or dynamic viscosity of the fluid, kg m^{-1} s^{-1}

ρ, Density, kg m^{-3}

$\nu = \mu/\rho$, kinematic viscosity of the fluid, m^2/s,

ν_t, turbulent kinematic viscosity of the fluid, m^2/s

ν_{eff}, effective kinematic viscosity of the fluid, $\nu_{eff} = \nu + \nu_t$, m^2/s,

SL-SMC, Sintered Lamellar-Soft Magnetic Composites.

μ_r, magnetic permeability of a material relative to air,

ρ_e, electrical resistivity of a material (Ω-m)

f, frequency of the applied magnetic field in Hz (s^{-1})

P_h, Hysteresis or DC magnetic losses in a material (W/m^3)

P_e, Eddy Current or dynamic electric energetic losses in a material (W/m^3)

B_m , Maximum Induction reached (T)

β a geometric coefficient expressed by: 6/[1-(0.633w/h) tanh(1.58h/w)] for a rectangle of height h and width w.

Chapter 1 INTRODUCTION

This doctoral project, entitled “Development of Sintered Lamellar Soft Magnetic Composites”, concerns the development of a new process intended for mass production of integral power (>1HP) rotating electrical machines. The hybrid automotive powertrain market is particularly targeted by this research work. Adopting powder metallurgy techniques, the new soft magnetic composite presented in this thesis has the potential to be conveniently contoured so as to reduce the total weight of copper windings placed around the armatures of electric motors and alternators destined for use in future electric cars, trucks and buses. Potential copper weight savings of ~ 40% have been proposed just for that reason alone [1].

This new product could greatly facilitate the commercial penetration of hybrid and electric cars, truck and buses, into the marketplace. This transformation will be helped through a combination of lower cost motors/alternators, with enhanced performance of electric powertrains through weight and volume reductions, and associated increases in efficiency. As such, this doctoral project answers calls for efforts to develop Sustainable Energy Systems. Furthermore, the carbon footprint of

the whole process is significantly lower than the standard electrical steel lamination stampings and stacking of armatures. Indeed, laminated steel products involve many rolling passes and reheating cycles that are not needed in producing the present composite. Lamination stacking processes require one to cut the rolled steel sheets to the exact geometry of a specific rotating machine, prior to stacking them. This inevitably generates an important amount of scrap (recuts). Similar to any net shape process like powder metallurgy, the proposed new Sintered Lamellar Soft Magnetic Composite (SL-SMC) process does not involve any scrap generation. Moreover, the process presented here is a lot simpler and less energy demanding than the present steel powder production process. The latter is produced by water atomisation of a falling stream of liquid steel and is currently used to produce the (non-lamellar) Soft Magnetic Composites presently on the market.

Research carried out over the last ten years has shown that Soft Magnetic Composite (SMC) materials are good candidates for replacing laminated steel sheets in electric motors. Their increased isotropy, combined with a near net shape forming technology, allow motor designers more flexibility to improve a machine’s efficiency and costs. Laminate-based motor designs have design limitations due to their

stacked geometry. This is particularly true for high efficiency motors needed for hybrid power trains used in the transportation sector. New designs are possible with SMC technology [1,2] and have the potential to greatly improve power to weight or power to volume ratios of electric motors by decreasing their assembly costs. Unfortunately, SMC materials presently available in the marketplace are based on irregularly shaped, water atomized, iron particles [3]. This is a relatively intricate, and expensive, powder production process. These types of SMC materials do not have sufficiently good mechanical and magnetic properties to fully benefit from the design advantages brought about by the SMC technology [4]. For that reason, motor designers have limited their trials to incorporate SMC into permanent magnet motors only. In fact, the low magnetic permeability values of SMC compacts are less detrimental to the overall performance of such motors due to the large air gap in those types of machines. Even with their low performance, SMC components can give a reduction in the weight and volume of the motors largely in relation to the copper windings and the design advantages of powder metallurgy that give them an important advantage over conventional armatures [4, 5, 6].

On the other hand, with their high permeability values, the Sintered Lamellar Soft Magnetic Composite (SL-SMC) process, presented in this

work, is capable of supplying composites that give only a minor decrease in electrical performance compared to lamination stacking in a conventional 2 D design motor with or without permanent magnets, employing thin air gaps such as those encountered in induction machines. These designs were developed for the lamination stacking technology about 100 years ago. If designs are reviewed as was done for the permanent magnet motors using SMC's that was recently launched into the market, so as to take full advantage of the 3D advantage given by composites, SL-SMC could produce motors with, or without, permanent magnets, with never before reached levels of performance and power densities. SL-SMC's could become very important in the future, given the current shortage of rare earth elements, and their availability for the production of rare earth magnets.

However, as starting materials to produce SL-SMC composites, conventionally rolled sheet steel are extremely expensive, even more than conventional laminates, since the soft magnetic steel sheets needed for these lamellar composites must be rolled to a smaller thickness than the material normally used for producing electric machines. At the thinnest thickness used by conventional high efficiency motors, i.e. 125 μm, rolling costs account for more than 90% of the selling price. Consequently,

conventional processing of slabs to sheets, then to thin ribbons, and finally to flat chopped lamellae, naturally leads to even higher costs, and higher energy consumption (by neglecting the savings due to the elimination of punched lamination recuts). Figure 1 shows the process flow charts for the production of the new soft magnetic composites in this thesis. Figure 2 (a few pages later) provides a schematic of the soft magnetic lamellar composite structure being attempted, and shows why the flat rectangular lamellae need to be thinner than equivalent motor laminations.

On the other hand, contrary to the lamination stacking technology, the final stacking factor, or the final electromagnetic material density in the SL-SMC parts, do not depend on the surface finish of the base material, nor on its uniformity of thickness. The pressing operation and any subsequent standard densification process used in the powder metallurgy technology (e.g. double pressing-double sintering, hot pressing, sizing, hot forging) comes to eliminate inter-particle voids and defects. It opens the door to develop an economic direct casting process that will directly provide the thickness and quality required for the base ribbons used for the SL-SMC process.

For that reason, the present doctoral study includes the development of a new, tilted, casting/melt dragging process

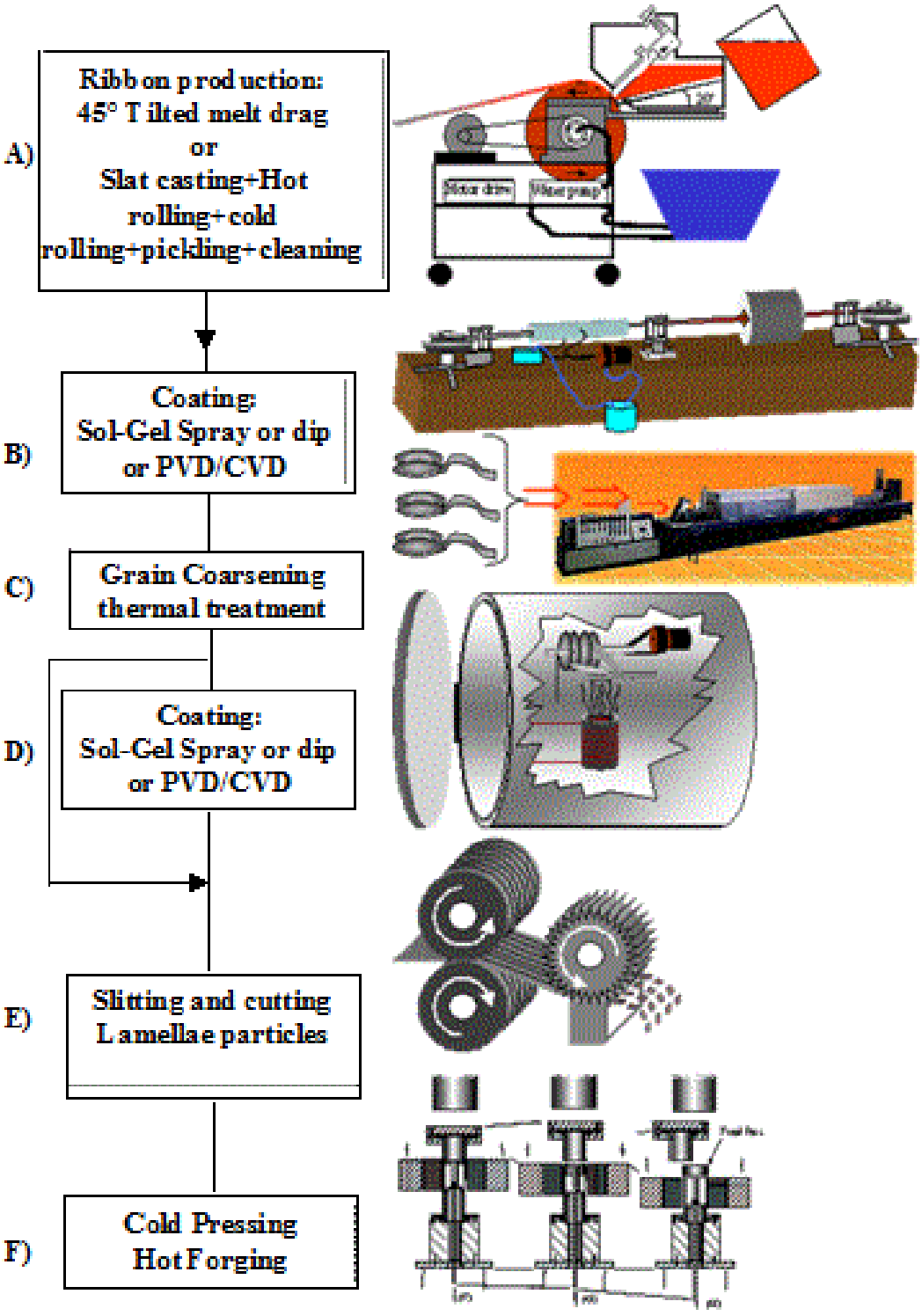

Figure 1: Illustrated Process flow chart for the production of the new Sintered Lamellar Soft Magnetic Composites [7]

that was designed, mathematically modeled and validated with a few experiments. This work then proves the feasibility of supplying ribbons, at a very low cost, and of a sufficient quality, by a direct casting technology for the production of Sintered Lamellar-Soft Magnetic Composites (SL-SMC). The SL-SMC process can potentially be provided with very thin strips of cast steel ribbon, using a copper wheel or a single belt casting machine. The current casting concept presented is not pressurised so it can be done continuously, not in a confined system (vacuum) because pouring is done by the bottom of the tundish like any major industrial continuous casting process, allowing the use of a protective gas or a slag layer on its top to prevent oxidation of the metal, the complete emptying of the tundish, and a short liquid metal residence time in the tundish. It also allows for a precise strip thickness adjustment through the use of a gate. CFD modelling calculations were performed to find the optimum casting parameters for the various alloys needed, and to help in the understanding of this new casting approach. A limited number of casting experiments were done during the PhD study in order to test the model's validity, but not to produce high fusion point ferromagnetic ribbons at the base of the

SL-SMC process. This will now come later, after this thesis, at the Post-Doctoral Fellow level.

In developing this new class of SMC, one needs to first understand the problems facing the use of iron-based materials in electric motors. When an actuator is used at a higher frequency than a few cycles per second, overheating rapidly appears in those magnetic parts, which is generated at distances shorter than the mean magnetic depth of penetration into the material. This value, commonly termed “the skin depth” of a magnetic material in an AC magnetic field, can be described by the following equation:

$$\delta(cm) = \frac{5030}{\sqrt{\left(\mu_r \cdot f / \rho_e\right)}} \qquad \textbf{(1)}$$

Where,

μ_r is the magnetic permeability of the material relative to air,

ρ_e is its electrical resistivity (Ω.cm) and

f is the frequency of the applied magnetic field in Hz (s^{-1}).

This limitation is due to the formation of eddy currents in the part. In addition to causing overheating and energetic losses, Eddy Currents work to oppose an electric field applied to the part, thereby limiting the magnitude of the induced field in the part.

As can be seen in the equation, as the electrical resistivity increases, then the penetrating depth of the magnetic field in the part increases, leading to a more efficient use of the material. A decrease of the permeability of the material will give the same result but will also limit the strength of the induction and torque that could be generated by this part at a certain applied field, following the Maxwell's equation ($B=\mu H$).

The only way to increase the penetration of the magnetic field and thus the efficiency of the device at a certain frequency without affecting its magnetic induction is to increase the electrical resistivity of the magnetic material. Obviously if the material has an isotropic behaviour or insulation, like for spheres or irregular water atomized powders, in an application where the magnetic field has a preferential direction, many demagnetizing gaps will be present in the main field direction. This will decrease the magnetic permeability, increase the coercive field and thus the hysteresis losses of the material [8, 9]. We must then conclude that the material should not be fully isotropic in order to minimize non-magnetic material presence in the main direction of the field, acting like a demagnetizing field like any air gap in a magnetic circuit. Efforts should then be made to use insulated lamellar particles oriented mainly in the main direction of the magnetic field and, preferably sintered on their edges (see Figure 2). If

their edges are sintered, electrical insulation will decrease because each contact zone between adjacent particles will represent potentially a zone of double thickness none insulated material in the normal direction to the field. In order to limit Eddy currents as well as in standard lamination stacking, particles must then have thickness a few times lower than comparative lamination used for the same application.

It becomes an interesting field of research to determine the level of mechanical strength that could be achieved in such a composite without losing too much electrical insulation. Another question is how much can the coercive field and permeability benefit from this new approach, tolerating distributed metal contacts between lamellar insulated particles?

In the Figure 2 (bottom right), The A zones are sintered to improve DC magnetic properties (increased permeability, decreased coercive field or hysteresis losses), while the B regions have only one layer of insulating coating, so as to act as a diffusion gate. Insulation layers are designed to remain efficient along all longitudinal planar surfaces of the lamellar particles, particularly when they are of double thickness.

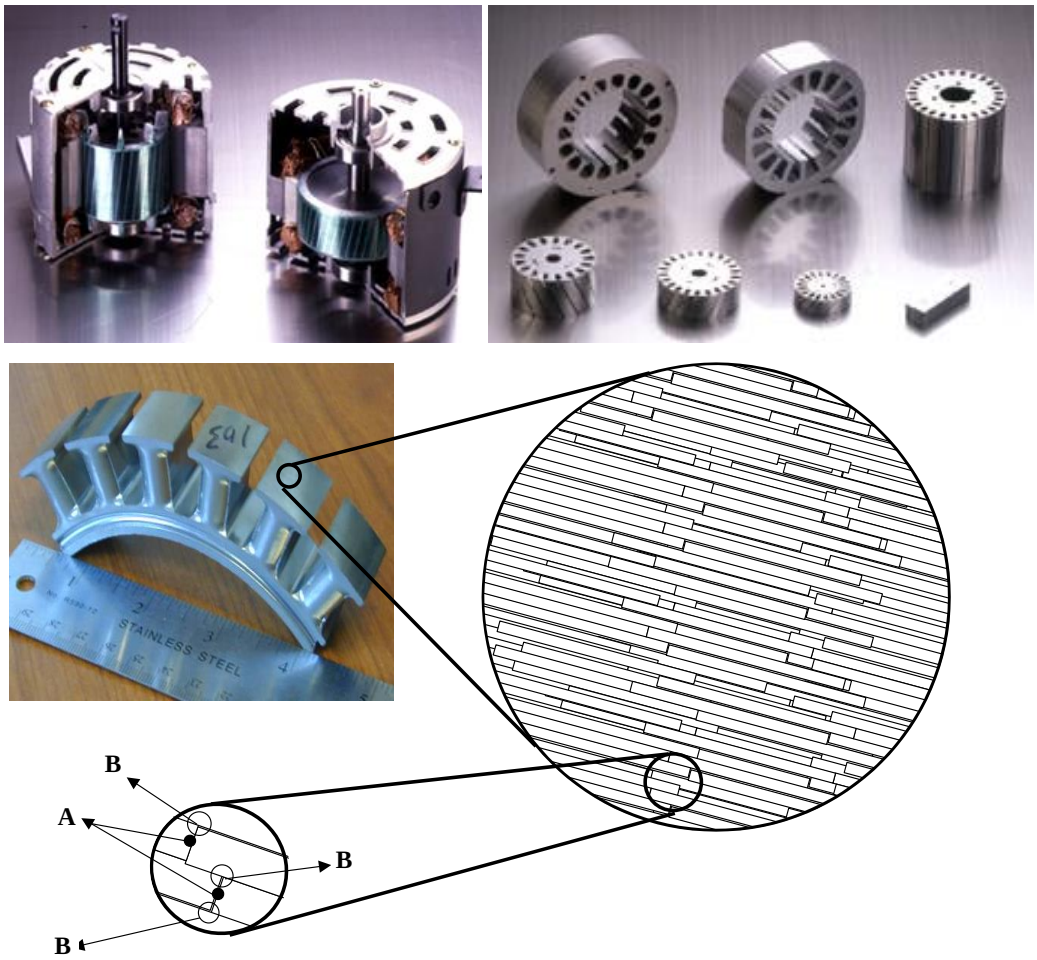

Figure 2: Cut-outs of two electric motors (top left), and seven armatures (top right). The armatures comprise a number of conventionally stacked laminated sheets of steel. Bottom left is a new design of armature fabricated via powder metallurgy (SMC). Bottom right is the proposed solution to the construction of a new SMC, showing the typical "microstructure" of a sintered soft magnetic lamellar composite, composed of particles coated with insulating layers on their main faces, but not at their edges.

However, even if electrical insulation is not perfectly maintained in zones B (say only one layer is present at edges in contact with adjacent planar surfaces), the probability that an insulation defect would be in line with another one on the next layer of particles, is low. Thus, the equivalent of perfectly insulated lamellae for suppressing Eddy Currents would then be approximately equal to two thicknesses of particles. Conservatively, the rectangular lamellar sheets (or particles), should therefore be thinner than the half the thickness of conventional laminations, and used at frequencies that preclude unacceptably high Eddy Current losses.

Due to the high stacking factor (ratio of the volume of electromagnetic material on the total volume of the stack of lamination or part) required by high efficiency electric machines, the conventional armature process do not use ribbons produced by near net shape casting process such as high speed twin roll casting, horizontal belt casting, planar flow casting, or melt dragging. These new processes do not generally produce the quality and uniformity of thin sheet thickness required [10]. However, the proposed soft magnetic lamellar composite process involves a powder metallurgy pressing step that is capable of accommodating small variations in ribbon thickness to nevertheless give

very high density armature parts, particularly if an economic repressing (sizing) or powder forging process is used [11].

With the development of thin coating technologies during the last 20 years, the use of the sol-gel process, and/or CVD-PVD technologies is now possible to obtain uniform, thin refractory coatings, at a low cost. As mentioned, in this work, all the aspects of the process that could represent a technological barrier for its implementation were reviewed and the best parameters were identified. For that reason, in addition to a direct casting technology development, complete development work was done on the thin layer coating process, including the use of a PVD technique (magnetron sputtering) and a specially developed inexpensive Sol-Gel technique. The part shaping process was also investigated since the lamellar powder produced must be used eventually in standard powder pressing production presses even if lamellar powders have very poor flow compared to irregular water atomised powders normally used in such mass production process. A special feeding system was developed and tested with positive results, with the collaboration of the Industrial Material Institute of the National Research Council of Canada.

Finally, after presenting the best mechanical and magnetic properties obtained with this new family of composite based on different alloys, theoretical calculations and mathematical modeling of the performance of different rotating electrical machine topologies are presented, using the properties obtained with the new composite, in order to give an example of the kind of improvements that can be obtained using the present composite material.

This thesis intends to prove that this technology has the potential to replace laminations in all continuous duty applications, with improved energy efficiency (up to 5%), with lower weight and volume (up to 50%), and with lower production costs and a lower carbon footprint. SL-SMC composites have the potential to meet the demanding requirements of power train components for cars, buses and trucks [7].

Chapter 2 LITERATURE REVIEW

2.1. DIRECT CASTING OF RIBBONS

The SL-SMC process requires very thin ribbons or strip, either manufactured conventionally [12], or directly cast, using melt drag, melt spinning, or planar flow casting techniques, either on one, or between two, circular wheels, or on a horizontal single belt, or double belt, caster [13, 14, 15, 16]. Industrial production is now possible using horizontal single belt casters (HSBC) for different materials in the range of 20 to 100 mm thickness [17,18,19], but this is still far too high for SL-SMC material. Mathematical modelling of those processes to produce strips greater than 20 mm thick is now thoroughly studied for process optimization.

On the other hand, very thin ribbons in the range of 10 to 30 μm have been cast by melt spinning or by planar flow casting operations, for close to 50 years. These rapid solidification processes achieve rapidly solidified properties, producing amorphous or nano-crystalline material structures [20, 21, 22]. Those processes are optimized for targeted thicknesses giving very high cooling rates, but those thicknesses are too low for SL-SMC's, limiting the grain size in the final particles, and thus giving greater hysteresis losses and worsened DC magnetic properties (HC, μ and B_{max}).

Those metal casting processes are set vertically above the wheel, and are operated at high pressure, so as to match the speed of the ejected liquid stream to the speed of the substrate passing under it. They are, consequently, batch processes. One drawback to these processes is that the thin slotted quartz nozzle used, rapidly suffers from erosion due to the high speed of the ejected metal. In addition, if one would like to use this kind of process to cast standard crystalline alloys rather than amorphous alloys, it will greatly complicate the set up. In fact, boron and other glass formers (ex. Silicon, Phosphorus) are added to the base alloy composition to increase their glass forming ability by importanttly increasing the time the molten metal stays in the supercooled state. It has the effect of significantly decreasing the liquidus temperature of the glassy alloys containing them. Thus, amorphous alloys usually processed by melt spinning and planar flow casting have measurably lower fusion temperatures than standard crystalline ferromagnetic alloys. It is the reason why the set up developed up to now for planar flow casting integrates quartz components, the operating temperature being under the softening temperature of the quartz. With standard crystalline alloys used for ferromagnetic parts, creep problems from a quartz nozzle would occur rapidly which will be dramatic

for the set up and operation, the nozzle being just above the wheel at a very short distance from it (very small gap).

Another complication of the melt spinning process is that the constant and very precise high pressure required to match the speed of the wheel with ejected metal must be maintained all the time, complicating or making impossible the refill of the tundish for continuous production.

On the other hand, one advantage of melt spinning or planar flow casting versus horizontal high speed melt dragging or extraction, that can also produce thin ribbons, is that the metal is fed from the bottom of the tundish or nozzle, like for any conventional continuous casting process, allowing the possibility to use a top layer of slag or a stagnant protective gas atmosphere in the tundish and in the ladle during casting operations, so as to protect the metal from oxidation during continuous operation.

However, due to its required high and constant pressure, planar flow casting operations can hardly take advantage of this configuration to be continuous, but any melt dragging operation from an horizontal bath of metal can absolutely not use slag or a stagnant protective gas layer on the top of their fusion bath. In fact, the slag would be cast/solidified first rather than metal or the protective gas layer will be significantly affected by ejected solidified metal, compromising its oxidation protection. Horizontal

Melt drag or extraction is thus necessarily done in a confined chamber, in vacuum or a controlled atmosphere.

Thus, very few experiments and set ups have been proposed and developed to specifically target a range of thicknesses varying between 100 and 200 µm [23, 24, 25, 26, 27, 28, 29], particularly for high fusion point alloys. Furthermore, no direct casting industrial production exists for this range of thicknesses, and no mathematical modelling efforts have been conducted up until now. The reason for this is that the only markets existing for this thickness range of material up to present requires a perfect surface finish that can be obtained only through an extensive rolling operation (electric motor laminations, finishing sheets for OEM, etc...). In addition to providing a very high level of planarity and uniform thickness required for magnetic lamination stacking, etc., rolling operations break the remaining inclusions in metals, making them less susceptible to initiate fractures in structural applications. For that reason, one prefers that any structural application stay with a rolling process rather than considering a direct casting process.

Thus, SL-SMC’s create a new and essentially unique market that can be fulfilled conveniently by low quality ribbons in term of planarity, thickness uniformity, inclusions, and minimum widths. As explained earlier, ribbons

are eventually cut into small rectangular particles and consolidated in a net shape process using a high pressure, uniaxial compaction press, to reach close to full density, even with a starter ribbon of imperfect surface planarity.

2.2. SOFT MAGNETIC MATERIALS AND COMPOSITES

Soft magnets are usually used in electric motors operating with alternating currents. For maximum efficiency, it is essential to minimize the energy losses associated with the changing electric field. These energy losses, or core losses, as they are sometimes called, result in the conversion of electric energy to thermal energy. The losses are usually expressed in terms of watts/kg (W/kg) for a given magnetic flux density (in Tesla) at a given frequency (in Hertz).

There are two principal mechanisms by which energy or core losses occur. These are 1) hysteresis losses and 2) eddy current losses. Soft magnetic materials have to have a small hysteresis loop (a small coercive field H_c and a high magnetic permeability, μ_r) and a high flux density (B) at saturation. As well explained in the literature [30, 31, 32, 33, 34, 35], hysteresis losses are due to the energy dissipated by the nucleation of magnetic domains, and movement of magnetic domain walls (Bloch walls), and are proportional to the frequency of the AC current. They are also

influenced by the chemical composition and the structure of the material and are proportional, in a non linear manner, to the maximum induction developed in the part.

Eddy currents, by contrast, are induced when a magnetic field is exposed to an alternating magnetic field. These currents, which travel normal to the direction of the magnetic flux, lead to an energy loss through Joule (resistance) heating in the magnetic part. Eddy current losses are expected to vary with the square of the frequency, and inversely with the material's resistivity. The relative importance of the eddy current losses thus depends on the electrical resistivity of the material and the frequency of the field. They are also proportional to the square of the induction level developed in the part, or the intensity of the applied field [36].

In the literature, soft magnetic parts for alternative current of low and medium frequency applications (between 50 Hz and 50 000 Hz) have been produced, basically using two different technologies, each having its advantages and limitations.

2.2.1. Lamination stacking

The first method, widely used since the end of the 19th century, consists of punching and stacking rolled steel sheets or laminations [12]. This well-

known process involves material losses, since scrap material (re-cuts) is generated from notches, center and edges of the laminations, when stamping. This material loss can be very costly for some specific alloys and high performance designs. The process also requires a default-free roll of material whose dimensions are greater than the dimensions of the part to be produced. The laminations have the final geometry, or a subdivision of the final geometry, of the parts and can be coated with an organic and/or inorganic insulating material.

Every imperfection on the laminations such as burred edges, uneven thickness, poor planarity, uneven coating thickness, decreases the stacking factor or ferromagnetic density of the final part and thus its maximum induction. Also, the mass production of uni-shaped, uni-sized, laminations prevents designs of armatures with rounded edges, to efficiently accommodate copper wire winding. Due to the planar nature of the laminations, their use limits the design of devices to a 2 dimensional distribution of the magnetic field. Indeed, the field is limited to travel only in the plane of the laminations.

The cost of the laminations is related to their thickness. To limit energy losses generated by eddy currents, as the magnetic field frequency of the application increases, the thickness of the laminations must be decreased,

as expressed in the skin depth penetration of a magnetic field in the part (see equation 1 page 10), or by the classical energy losses equation developed by Maxwell, described in both Bozorth [35] and Betotti [36] for eddy current losses (Pe) :

$$Pe = [(\pi\ d\ Bm\ f)^2] / \beta\rho_e \qquad (2)$$

Where

P_e (W/m^3) = Eddy Current or dynamic energy losses in a material;

d (m)= Ribbon, lamination or part thickness or particle diameter;

B_m (T)= Maximum Induction reached;

f (Hz)= excitation frequency

ρ_e (Ohm/m)= $1/\sigma$ = Alloy or composite equivalent electrical resistivity (intrinsic and extrinsic).

β= a geometric coefficient expressed by $6/[1-(0.633w/h)\ \tanh(1.58h/w)]$ for a rectangle of height, h and width, w.

This thickness limitation increases the rolling cost of the material and decreases the stacking factor of the final part due to imperfect surface finish of the laminations and burrs and the relative importance of the insulating coating. Laminations are thus well suited but limited to low frequency applications, up to 1 KHz.

2.2.2. Soft Magnetic parts or composites with irregular particles.

The second process for the production of soft magnetic parts for alternating current applications, well-known since the beginning of the 20th century, is a variant of the mass production powder metallurgy process where the particles used are close to non-electrically conducting or electrically insulated from each other by a coating [37, 38, 39, 40, 41, 42, 43, 44, 45, 46, 47, 48, 49]. One kind of particles for very high frequencies (KHz to MHz) are oxides. They are commonly named “ferrites” and are spinel of iron oxides (Fe2O3-MnO-NiO-ZnO) for instance. They have limited maximum induction and are very fragile (it is ceramics). Their usage is limited to chokes, inductors, antennas, high frequency field concentrators and transformers. To reach higher maximum induction, for AC applications, when the material is not made from an oxide of metal, the powder particles are not sintered to prevent the formation of electrical contacts between the powder particles. It, thereby reduces eddy current losses. Parts fabricated using this process are commonly referred to as “powdered cores”, “dust cores” or more recently, “soft magnetic composites, or SMC’s”. Obviously, this process has the advantage of eliminating material loss.

SMC’s are isotropic and thus offer the possibility of designing components which allow for the magnetic fields to move in three

dimensions. SMC's also allow for the production of rounded edges using conventional powder metallurgy pressing techniques. As mentioned above, those rounded edges help winding the electric conductors. Due to the higher curvature radius of the rounded edges, the electrical conductors require less insulation. Furthermore, a reduction in the length of the conductors due to the rounded edges of the soft magnetic part is a great advantage, since it allows the amount of copper used to be minimized, as well as the copper loss (loss due to Joule effect eating, related to the electrical resistivity of the electrical conductor carrying the current in the electromagnetic device) [4].

With rounded edges, the overall dimensions of the electrical component can be reduced, since electrical winding can be partially inlaid within the volume normally occupied by the soft magnetic part. In addition, due to the increased isotropy of the material as compared to laminations, and the gain of freedom of the pressing process, new designs that increase the total yield, and decrease the volume or the weight of the armature for the same power output of an electric machine is possible, since a better distribution or movement of the magnetic field in three dimensional space is possible [2, 4, 5, 6].

Another advantage of the powder metallurgy process route is the elimination of the clamping means that are needed to secure laminations together in the final part. With laminations, clamping is sometimes replaced by a welding of the edges of laminations. Using the latter approach, eddy currents are considerably increased, and the total yield of the device, or its frequency range of application, is decreased.

To date, one reason preventing the use of powder metallurgy to produce high efficiency and high mechanical resistance soft magnetic composites,(SMC's) for electrical rotating machines has been the impossibility of forming strong metallic bonds between particles while concurrently maintaining electrical insulation to limit eddy currents. If particles are spherical or irregular in shape, it is impossible. As soon as metallic bonds are formed between powders, isotropic electrical insulation decreases. On the other hand, if insulators completely surround each particle, demagnetizing fields due to the presence of insulator interfaces between particles are present in all directions, harming magnetic performance in the main direction of the magnetic field [9]. This explains why no SMC component has yet demonstrated the capacity to have a relative magnetic permeability above 1000.

In addition, the distributed air gap in SMC materials due to the total encapsulation of each particle not only significantly decreases the magnetic permeability, but also increases the coercive field and thus the hysteresis losses. It limits their usage compared to steel laminations. Additionally, to prevent the destruction of the insulation or coating, SMC's are very hard to fully anneal or to achieve complete recrystallisation with grain coarsening. The temperatures reported for annealing SMC without losing insulation are about 600°C in a non-reducing atmosphere, using a partially or totally inorganic coating [30, 50, 51, 52, 53, 54, 55]. Although the annealing temperature commonly used with SMC's is not sufficient to completely remove residual strain in the particles nor to cause recrystallisation or grain growth, a substantial improvement in the hysteresis losses can be observed, when a stress relief treatment at only 300 to 600°C is applied.

Ultimately, for all soft magnetic composites comprising irregular or spherical particles developed so far for AC applications, even if residual strain would have been removed and grain growth would have been possible at temperatures used for the annealing cycle of finished parts, the metallic grain dimensions are still limited to the size of the particles. The small grain sizes involved obviously will always limit the possibility of increasing the permeability, decreasing the coercive field or simply, the

hysteresis losses in the material. Indeed, the smaller the metallic grains are, the higher is the number of grain boundaries, and the more energy is required for moving the magnetic domain walls and increasing the induction of the material in one direction. Therefore, the resulting total energy losses (or core losses) of SMC parts at low frequency (below 400Hz) is greater than the total energy losses obtained with laminations. The low permeability values also require more copper wire to achieve the same induction or torque in the electromagnetic device. An optimized three dimensional design of the part with rounded winding edges made with SMC's with irregular or spherical particles can partially or completely compensate for these higher hysteresis losses and low permeability values encountered with SMC material at low frequency.

It must nevertheless be mentioned that important attempts have been made to develop better performing inorganic coatings and processes for soft magnetic composites that would allow for a full annealing of compacts and even recrystallisation, without losing too much electrical insulation between particles [56, 57]. These documents teach a heat treatment at around 1000°C to consolidate particles by the diffusion or interaction of the insulating material surrounding each particle. In all these cases, however, the goal is to produce a soft magnetic composite with discontinuous,

separated, soft magnetic particles, joined by a continuous electrical insulating medium. Accordingly, even with those efforts, the DC magnetic properties (coercive field, maximum induction and permeability) and thus hysteresis losses of the composites produced are far inferior to those of the main wrought soft magnetic constitutive material, particularly if this material is processed in the form of a thin sheet, as motor laminations. As mentioned, the electrical current, or the number of turns of copper wire required to reach the same force, power or torque in a device using this kind of material, as compared to the use of lamination stacking, will always remain higher. Properties of those composites are well suited for high frequency applications. If power frequencies are targeted [58], the design of the component must compensate for the lower permeability and higher hysteresis losses of the material [2, 5, 6].

2.2.3. Lamellar particle SMC's (not sintered)

Finally, some researchers who have discovered the benefit of using lamellar particles for making soft magnetic components, have developed coatings able to sustain stress relief temperatures, that is to say temperatures which are high enough to remove the major part of the remaining stress in the parts [59, 60, 61, 62, 63]. Once again, however, magnetic properties and energetic losses in an AC magnetic field at

frequencies under 400Hz are not those reached with good electrical laminations used commercially, since metallic diffusion between soft magnetic particles has to be avoided so as to keep a high electrical resistivity in the composite.

2.2.4. Research groups on SMC

As explained earlier, the replacement of steel sheet laminates with net shape soft magnetic composites on new, better adapted, machine designs and the potential improvement or cost decrease on rotating electrical machinery, has seen renewed interest and become an important topic for research over the last 20 years, with recent development of insulated “non oxide” metal particles having high induction with good electrical resistivity.

Research efforts have been primarily conducted by the largest powder metal producers since their powders are readily available and of low cost. They have collaborated with machine designers, mainly electrical engineering researchers, in order to adapt electric machines and try to compensate for the poor magnetic properties of their composites. Dr Allen Jack’s team at Newcastle University, U.K., which collaborated with Hoganas, Sweden, and Dr Philip Viarouge’s team at Laval University, which worked in collaboration with Quebec Metal Powders Ltd., are the two most important groups of people that have worked on new 3 D machine designs

optimised for the use of metal powder composites [2,3,4,5,6,64]. The team of metallurgists of the powder metal producing companies have also worked in collaboration with some external research centers in order to optimise the magnetic properties of their composites, and particularly their levels of insulation [1,34,42,44,46,47,48,49,54,55, 71]. Recently, as mass production applications start to be considered, design efforts are tending to extend to many more universities and research centers, such as the Department of Electrical Power Engineering Ghent University, Belgium, or SATIE UMR CNRS, France, or the Faculty of Eng. of the University of Technology, Sydney, Australia, or the School of Electrical Eng., Southeast Univ., Jiangsu, China, etc.... [65, 66, 67, 68].

However, as previously mentioned, the magnetic and mechanical properties of these composites will always be limited, because of the total encapsulation of the individual metal particles with insulating films. Whenever those films are present, being composed of organic [69] or ceramic/oxide material [70, 71], the mechanical properties of such parts will always remain low , while the parts behaviour under deformation or stress, is also expected to remain fragile.

2.2.5. Amorphous or nano-crystalline powders SMC

In addition to the consolidation of insulated low cost irregular water atomized iron or steel particles, another approach has been studied by academic researchers. It is based on the consolidation of amorphous or nano-crystalline particles, due to their very low hysteresis losses [72]. This approach stems from the exceptionally good magnetic properties of ribbons obtained via rapid cooling technologies such as the net shape direct casting of ribbons to produce amorphous or nano-crystalline materials. The problem with base amorphous and microcrystalline materials is that they cannot be consolidated with metallic joints without losing their desirable magnetic properties if heated to temperatures above their re-crystallization points. These temperatures are very low (often less than 300°C, maximum ~700°C [20,73]). Consequently, these ribbons can only be consolidated at low temperatures using organic or oxide bonding technologies. As a result, the final products are brittle and of low mechanical strength.

Furthermore, it is very difficult to produce parts with rounded shapes at high density with such brittle, non- deformable materials. The density of such composites are thus limited [74, 75]. They already possess limited saturation induction due to their base composition, while the density

limitation of formed parts additionally limits their reachable maximum induction or magnetisation.

A recent development is to consolidate the powders by applying a high, pulsed, current, thereby producing sparks between particles. The method is termed “Spark-Plasma Sintering” . Better densities can be achieved without losing the amorphous or nano-crystalline structure [76]. However, this compacting procedure is long (~ 10 minutes per part), rendering it unsuitable for mass production, particularly in the highly competitive transportation sector. The magnetic properties of these materials can also be compromised during service as a result of thermal aging, while their brittleness makes them unsuitable for use in the transportation sector.

2.2.6. Fully sintered soft magnetic materials

Finally, also reported in the literature, and not to be confused with soft magnetic composites of high electrical resistivity values to limit eddy currents, are the fully sintered, non-coated particles. These powder components are currently used to make parts for DC magnetic applications (a few cycles per minute to a few per second maximum). These soft magnetic parts should not be named composites. They show properties similar to their wrought machined counterparts with the same alloy. The powder metallurgy technique is used in this case only to decrease the

shaping cost of the part. These net-shape pressed and sintered parts have low resistivity and are generally not used in AC applications (maximum a few cycles per second intermittently). In the literature, when sintering treatments (metal to metal) or metallic diffusion are involved, parts produced are limited to DC magnetic applications, where eddy currents are not a concern (see ref 30, 77 for instance), or for non-magnetic applications such as structural parts [78].

2.2.7. Coating processes and Importance of the electric resistance for lamellae SMC

With lamellar particles that are coated on their planar faces but not on their edges, it should be possible to form metallic bonds only on their edges. This will avoid the demagnetizing fields present in all other soft magnetic composites, while keeping the insulation needed to curb eddy currents. This will be true, provided the insulating coatings are able to resist sintering conditions. Powder metallurgy parts require a thermal diffusion treatment at approximately 80% of the fusion temperature of the base material to form strong metallic joints between particles. These metallic joints can be generated by conventional sintering treatments following cold pressing [78] or by a hot pressing or forging process.

Conventional stamped lamination stacking in the industry commonly uses a magnesium methylate coating to insulate laminations between each layer of ferromagnetic material. This coating can resist a maximum of ~850°C without important degradation [63,79]. However, this temperature is not sufficient for sintering or forging powders of iron or steel. The advanced solutions reported before in the previous section regarding SMC particles insulation that could resist to 1000°C allowing for a complete annealing treatment after consolidation is not sufficient either to allow sintering or forging of lamellae powders without losing their electrical insulation. Better insulating layers must therefore be developed to take advantage of using partially insulated lamellar particles.

The Sol-Gel and the PVD-CVD technology route needs to be considered, so as to be able to produce highly refractive coatings such as alumina, silica, titanium dioxide, magnesia, zirconia, or mixtures of the same. Much literature is available to develop and use both of these technologies, and just one of those would represent a long literature revue by itself. As such, they will not be presented here, since this is not the main target of the research project and they are now considered to be well known technologies. They were extensively studied and developed at the end of 80’s and the 90’s. We will only mention that for the Sol-Gel route,

(with the exception of the spin coating technology which produces high centrifugal accelerations allowing for uniform and thin layers to form quickly), this process normally involves a very slow coating technique (dip coating), where the samples are retrieved from the Sol at speeds of a few mm per second [80]. This low speed is needed to allow time for the surface tension forces acting at the surface of the Sol bath to keep the thickness of the liquid layer, deposited on the surface of the substrate leaving the bath, very low [81].Too rapid a substrate retrieval speed leads to a thicker coating that tends to crack and peel off the substrate when it dries. The cracking/peeling effect occurs when the thickness of the coating is sufficient to confer more mechanical strength in the coating than that available at the coating-substrate interface to retain it as a coherent film during the drying cycle where the coating densifies and shrinks. If the coating is thin enough, the shrinking and densification will create a coating thinning effect. Otherwise, the densification produces a longitudinal shrinking and associated stress with a net translation movement at the interface, or a rupture of this interface.

The use of plasticisers in the Sol will enhance its elasticity during the drying, shrinking and densification phase. Plasticisers can also help in strengthening the film’s adhesion force to the substrate [82]. As such, its

use can allow for the formation of thicker coatings, and/or, higher retrieval speeds. This avenue will be exploited. Even though this is not the main goal of the PhD study, the development of an accelerated Sol Gel route for maintaining coating adhesion, film density, and process efficiency, is definitely a critical point in the overall success of the research program.

Regarding the production of magnetron sputtering coatings using RF or DC pulsed sources under a reactive atmosphere, the literature is also abundant [83, 84, 85, 86, 87, 88, 89, 90, 91]. The RF source (13 MHz) process results in very low deposition rates. It is consequently very difficult to scale up to commercial applications. Reactive processing with a DC source is very unstable because alumina will not only form on the substrate but also on the aluminium target, which will then cease being pulverized with the initial settings of the control parameters (voltage, current, partial pressure of oxygen). As such, it is a process exhibiting hysteresis behaviour, that is very unstable and is difficult to control.

The best way to achieve a good deposition rate using a stable PVD process, is to use a pulsed mode DC deposition, using a medium frequency range (10-200 KHz**).** The process needs to be maintained in the transition mode between an oxidized and a non-oxidized target, so as to maximize the deposition rate. The fully oxidized, or poisoned, target mode must be

avoided to obtain a deposition rate typical of that of a pure material like aluminium, rather than alumina, which is a lot more difficult to pulverize, because it is insulating. In fact, this insulation behavior greatly limits the effect of the polarization voltage or the electrical field to accelerate the impacting ions. In order to avoid the poisoned mode, the ion etching rate, or sputtering rate, of the target, must be higher than its oxidation rate.

More information on the coating thickness required to obtain a good insulation, and the techniques used, will be presented in Chapter 3 section 3.3 and Chapter 4, section 4.5.1.

Chapter 3 THEORY FOR EACH PART OF THE PROCESS STUDIED

3.1. DIRECT CASTING OF THE RIBBONS AND COMPUTER FLUID DYNAMIC OF THE MODEL STUDIED

As explained in the introduction, the most economic way to produce lamellar particles, which is at the base of the currently proposed composite process, is to start from a coated ribbon, and to then chop it up into little pieces. It consequently involves using strip, either manufactured conventionally, or directly cast, using melt dragging, melt spinning, or planar flow casting, on a circular wheel or on a horizontal single belt caster. Industrial production is now possible using a horizontal single belt caster (HSBC) for different materials in the range of 20 to 100 mm. On the other hand, very thin ribbons in the range of 10 to 30 μm are cast by melt spinning or by planar flow casting operations, so as to achieve rapidly solidified properties, producing amorphous or nano-crystalline material structures. The latter are relatively expensive batch processes. As mentioned in Chapter 2, very few experiments and set-ups have been developed to target a range of thicknesses varying between 100 and 200 μm [23, 29]. This range of thicknesses is needed to produce a good Sintered Lamellar-Soft Magnetic Composite (SL-SMC). In fact, as explained

and demonstrated [92, 93], the thickness of the base strip material needed for the fabrication of a sintered lamellar soft magnetic composite, must be a few times thinner than the optimum laminations of electrical steels used for the same application. Indeed, according to the depth of penetration equation of a magnetic field into a ferromagnetic material, the best commercial laminations are produced by standard rolling processes at a thickness around 350 μm for 60 Hz magnetic field applications or even at a thickness of 125 μm for applications running at frequencies up to 400 Hz (~20 000 RPM). The cost of the required rolling operations becomes very high for such materials.

In the case of SL-SMC, contrary to what is needed for standard lamination stacking, the base ribbon does not need to have a high quality of flatness, or thickness variation, or width, or even surface quality, while surface oxidation is not a problem. In fact, in the SL-SMC process, the ribbon will be processed later, in the same way as with other metallurgical powders. It will therefore be consolidated at a very high pressure to achieve high ferromagnetic density in the parts to be manufactured, and will be sintered under reducing atmospheres to reduce carbon and oxygen levels. This SL-SMC process opens the door to using a cheap direct casting process, provided the casting process can deliver the targeted thicknesses

at operating speeds that can be easily industrialized. Therefore, it is different to the very high speeds associated with typical amorphous ferrous casting operations (~20 m/s). In addition, as mentioned, those processes normally use alloys with lower melting temperature ranges (silicon and boron amorphizing agents that reduce the melting temperatures) vs the standard ferromagnetic materials at the base of the SL-SMC composition. This allows METGLAS operations to use quartz nozzles and components without important creep or erosion problems. But even with that simplification, they have costs of production around ten times higher than what is reached in standard steel production, owing to the complexity of producing products at such high speeds. Indeed, as explained in the literature review, it requires a very precise and constant pressure to be applied to the exiting stream of metal. This limits the operation to a batch type process, under controlled atmosphere. Standard horizontal melt drag or extraction processes also require a protective atmosphere that can only be reached in a closed chamber, or in a vacuum system, increasing the cost of such an operation.

In the present project, a process was therefore developed, keeping all these, and other practical considerations, in mind. In order to verify its feasibility theoretically, mathematical modelling was conducted. This

section of the theory presents the equations behind the model, involving liquid metal flow in different regimes (with turbulence at some points), energy transfer and solidification phenomenon. In all, six partial differential equations must be solved at the same time to find solutions for the model proposed.

3.2. CFD MATHEMATICAL MODELING

The popular standard k-ε model of Launder and Spalding [94] was used in this work. In the k-ε model, k represents the kinetic energy of turbulence per unit mass (m^2/s^2), while ε, represents the rate of dissipation of turbulence energy(m^2/s^3). Thus, for this moving boundary problem, involving alloy solidification, the model requires simultaneous solution of six partial differential equations. The continuity equation is standard. However, the momentum, energy, turbulent kinetic energy and turbulent energy dissipation, equations, have to be modified, in order to take into account the presence of solid material that is solidifying in the contact zone with the cooling moving boundary and at the outlet of the tundish. The energy equation must take into account the latent heat as it evolves as a function of the liquid fraction solidified. All the other equations can be expressed so as to allow for the presence of the solidifying zone, by using an additional source term.

It is assumed, for practical purposes, that the solidifying liquid metal is porous. For this, the enthalpy-porosity technique is used, which treats the mushy region (the partially solidified region) as being equivalent to a porous medium, allowing liquid metal to flow within the porosity. The porosity in each cell is set equal to the liquid fraction in that cell. In fully solidified regions, the porosity is equal to zero. This extinguishes velocities in these regions or, in our case, makes the velocity equal to the wheel's velocity. In the momentum equation, the sink term, S, needed to take into account the reduced porosity or liquid fraction in the mushy or partially solidified zone, takes the following form:

$$S = \frac{(1-\beta)^2}{(\beta^3+\alpha)} \, A_{mush} \left(\vec{v} - \overrightarrow{v_p}\right) \quad (3)$$

where; β is the liquid volume fraction, and α is a small number (0.001) to prevent division by zero, A_{mush} is the mushy zone constant, and $\overrightarrow{v_p}$ is the solid velocity due to the pulling of solidified material out of the domain (also referred to as the pull velocity) [95]. This pull velocity is included in Equation 3 to account for the movement of the solidified material as it is continuously withdrawn from the domain. The presence of this term in the equation allows newly solidified material to move at the pull velocity, i.e. at the casting wheel's speed of rotation.

This non-linear expression was first developed empirically by Kozeny (1927) and later modified to the form presented in Equation 3, by Carman (1937, 1956). It is thus known as a part of the Von Carmen- Kozeny equation [96]. It was derived from Darcy's law, which is an empirical expression derived to describe the flow of water through beds of sand, and has been very widely adopted in hydrogeology and for fluid flows through packed beds. Darcy's law, which finally appears to be more than an empirical equation can also be derived from a simplification of the Navier-Stokes equation for stationary, creeping, incompressible flow where $\frac{d}{dt}(\rho u_i) \approx 0$. It simply states that the flow is proportional to the pressure drop and inversely proportional to the fluid viscosity.

The variant in Equation 3 with the original Carman-Kozeny equation is that the porosity of the bed was simply replaced by the liquid fraction of the mushy zone. Voller, Brent and Prakash [97, 98] first proposed to bring this approach in the CFD modelling of mushy phase change problems. Fluent software selected this approach to match what is observed in liquid/solid mixtures, where for a β value close to one, when no solid exists in the model, this sink term tends to disappear from the momentum equation (no effect). The same is true when there is no difference between the liquid velocity and the pull velocity (wheel speed). However, when β decreases

(metal is solidifying), the sink term can become very high and dominant, as long as there is a difference between the liquid velocity and the pull velocity, requiring the momentum equation to include Darcy's law. The next graph shows the value of the sink term as a function of the liquid fraction. It can be seen that the influence of the sink term changes drastically once the solid-liquid ratio reaches about 70% solid. Before that, it has a weak influence, but over it, its influence grows very quickly.

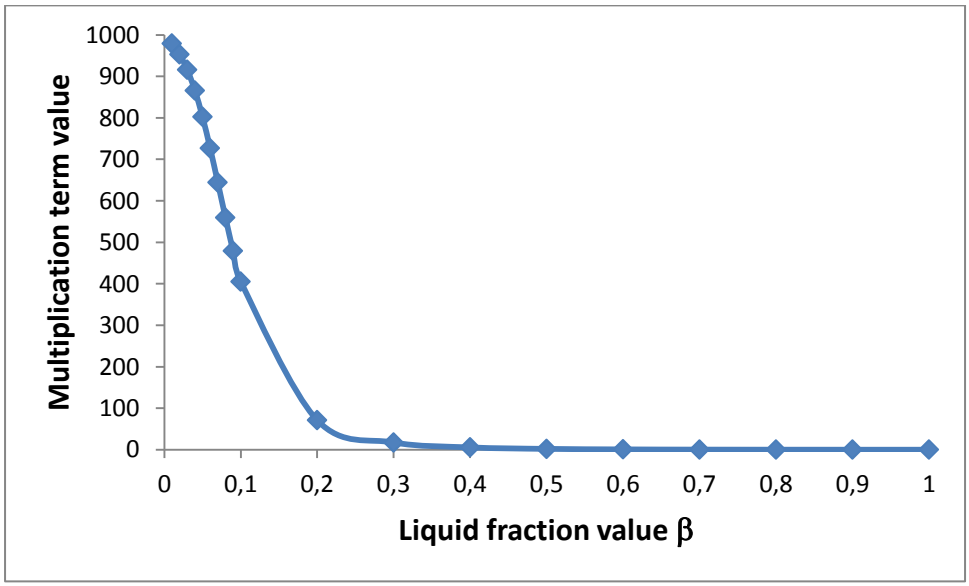

Figure 3: Graph of the influence of the mushy zone constant multiplication term of the Equation 3, as a function of the liquid fraction of the mixture

The mushy zone constant, A_{mush}, also adjusts the amplitude of the damping; the higher this value, the steeper is the transition of the velocity of the material to zero (or to the pull velocity), as it solidifies. Very large values may cause the solution to oscillate. Since the non-linear multiplication term

developed is not adjustable in the Fluent model, the access to the mushy zone constant is the way offered to the user to play on the influence of the sink term as a function of the liquid fraction variation. A recommended value for ease of convergence and realistic results is 100 000. Based on the experience of the Fluent team, it is not recommended to adjust that value unless one has good reason to expect that the liquid/solid mixture behavior is very different from what was modelled, observed and validated in all past applications studied by the Fluent development team. It was not modified for the present calculations.

For the Energy equation, as explained above, the enthalpy of the material is computed as the sum of the sensible enthalpy, h, and a portion of the latent heat of the material (L), named ΔH, which takes into account the solid fraction formed at each time step:

$$\Delta H = \beta L \tag{4}$$

β is again the liquid fraction of the volume. Then, the latent heat content can vary between zero (for a solid) and L (for a liquid).

The liquid fraction, β can be defined as

$$\beta = 0 \text{ if } T < T_{\text{solidus}}$$

$$\beta = 1 \text{ if } T > T_{\text{liquidus}}$$

$$\boldsymbol{\beta} = \frac{\boldsymbol{T - T_{solidus}}}{\boldsymbol{T_{liquidus} - T_{solidus}}} \quad \text{if } \boldsymbol{T_{solidus}} < T < \boldsymbol{T_{liquidus}} \tag{5}$$

Thus, the enthalpy of the material is

$$\mathrm{H} = \mathrm{h} + \Delta\mathrm{H} \tag{6}$$

where

$$h = h_{cop} + \int_{T_{cop}}^{T} C_p dT \tag{7}$$

and $\mathrm{h_{cop}}$ = the enthalpy of the cast material at the temperature of the copper wheel substrate, taken as the reference enthalpy.

$\mathrm{T_{cop}}$ = temperature of the copper wheel substrate

$\mathrm{C_p}$ = specific heat of the cast material (Tin, AA6111 or Fe-3%Si) at constant pressure.

For solidification/melting problems, the energy equation can be written as

$$\frac{d}{dt}(\rho H) + \nabla \cdot (\rho \vec{v} H) = \nabla \cdot (k \nabla T) + S \tag{8}$$

where H = enthalpy (see Equation 6)

ρ = density

$\vec{\mathrm{v}}$ = fluid velocity

k = thermal conductivity

S = source term, to account for any source of heat or of cooling added to the system.

The solution for temperature is essentially iterations between the energy equation (Equation 8) and the liquid fraction equation (Equation 5).

Then, for the next iteration (to decrease the residuals in every partial differential equation), the liquid fraction is updated in the source term of the continuity and momentum equations as described in Equations 3 and 9 below, and this procedure is repeated throughout all the volume elements within the calculation zone, until convergence is achieved.

Finally, the sink terms added to all of the turbulence equations in the mushy and solidified zones to account for the presence of solid matter are very similar to the momentum sink term (Equation 3 and Figure 3 for its behavior):

$$S = \frac{(1-\beta)^2}{\beta^3+\alpha} A_{mush}\ \emptyset \tag{9}$$

where $\emptyset$ represents the turbulence quantity being solved, namely k and ε in this particular case, using the Launder and Spalding k-ε model. The mushy zone constant, A_{mush} , is the same as the one used in Equation 3.

Expanding In more detail, in the Launder and Spalding model, the following equations must be solved:

$$\frac{Dk}{Dt} = \frac{\nu_t}{\sigma_k}\nabla^2 \mathrm{k} + \mathrm{G_k} - \varepsilon + S \tag{10}$$

$$\boldsymbol{\frac{D\varepsilon}{Dt} = \frac{\nu_t}{\sigma_\varepsilon}\nabla^2\varepsilon + \frac{\varepsilon}{\mathrm{k}}(\mathbf{C_1 G_k} - \mathbf{C_2}\varepsilon) + S} \tag{11}$$

Here G_k is the rate of production of k and is given by the following equation:

$$G_k = \nu_t\left[\frac{\partial u_i}{\partial x_j} + \frac{\partial u_j}{\partial x_i}\right]\frac{\partial u_i}{\partial x_j} \quad (12)$$

The turbulent and effective kinematic viscosity is calculated by the following equations:

$$\nu_t = \frac{C_\mu \rho k^2}{\varepsilon} \quad (13)$$

$$\nu_{eff} = \nu + \nu_t \quad (14)$$

The recommended values of the constants adopted in this study were C_1= 1.44, C_2= 1.92, C_μ= 0.09, σ_k = 1 and σ_ε=1.3, as proposed by Launder and Spalding.

In the model, the commercial software used also includes micro-segregation/species transport formulae and equations capability. This capability was not used in the present study, because the very high cooling rate and speed involved with the solidification process developed here renders species transport effects negligible. In addition, the scope of the required precision from the CFD modelling experiments in this thesis was limited to the determination of a good relation between the solidified thickness and the wheel speed, and validation of the feasibility of this casting method to reach the targeted thickness range (under 200 μm). The metallographic and microscopic study of the ribbons produced was absolutely not an objective of the present study. Any metal grains and crystalline structure in the cast ribbons are, in fact, completely modified

after the casting process, since many thermal treatments are involved in the subsequent use of the ribbons for the SL-SMC process. These are required to remove the compaction stress in the particles, and to sinter the “SL-SMC” lamellar particles together. These heat treatments have the effect of completely homogenizing the concentration of the elements within the ribbons, given the long diffusion times at elevated temperatures. Those considerations thus allowed a simplification where no species diffusion is considered in the solid and liquid phases and fixed values are used for the liquidus and solidus temperatures of the alloys studied, for all calculations.

However, since this capability is now available, and could be used eventually to refine the model developed and obtain a better correlation between physical experiments and the predictions of the mathematical model for the lowest speed of the casting wheel studied, it is interesting to describe how the model can take into account the micro-segregation phenomena occurring during solidification. Thus, it changes the solidification temperature at the solidification boundary. It gives a more precise prediction of the solidification boundary position and thus of the effective flow of material in the mushy and adjacent liquid regions. Liquid recirculation phenomena in the tundish that could cool down the interior of

the tundish and clog the system are better estimated with this micro-segregation calculation.

As explained earlier, during the solidification and melting of an alloy, a freeze/melt or mushy zone exists between the solidus and liquidus temperatures. When the liquid solidifies, solutes diffuse from the solid phase into the liquid phase. This effect can be quantified by defining the partition coefficient of solute i, denoted by K_i, which is the ratio of the mass fraction in the solid to that in the liquid at the interface. ANSYS FLUENT computes the solidus and liquidus temperatures in the alloy as,

$$T_{solidus} = T_{melt} + \sum_{solutes} m_i Y_i / K_i \tag{15}$$

$$T_{liquidus} = T_{melt} + \sum_{solutes} m_i Y_i \tag{16}$$

where T_{melt} is the melting temperature of the pure solvent, K_i is the partition coefficient of solute i, Y_i is the mass fraction of solute i, and m_i is the slope of the liquidus surface, with respect to Y_i. It is assumed that the last species material of the mixture is the solvent and that the other species are the solutes. The liquidus slope of species i, m_i, is calculated from the Eutectic temperature and the Eutectic mass fraction as,

$$m_i = \frac{T_{Eut} - T_{melt}}{Y_{i,\,Eut}} \tag{17}$$

According to Ansys Fluent, updating the liquid fraction via Equation 5 can cause numerical errors and convergence difficulties with an alloy. Instead, the liquid fraction, for the transient mode can be updated from,

$$\beta^{n+1} = \beta^{n} - \lambda \frac{a_p (T - T^*)\Delta t}{\rho V L - a_p \Delta t L \frac{\partial T^*}{\partial \beta}} \tag{18}$$

where the superscript n indicates the iteration number, λ is a relaxation factor with a default value of 0.9, a_p is the cell matrix coefficient, Δt is the time-step, ρ is the current density, V is the cell volume, T is the current cell temperature and T^* is the interface temperature.

Two models are available in Fluent for species segregation at the micro-scale. They are for equilibrium solidification (Lever rule) and non-equilibrium solidification (Scheil). The Lever rule assumes equilibrium solidification, which in turn, implies an infinite diffusion coefficient of the solute species within the solid (Lever). For rapid solidification processes, which are far from the thermodynamic equilibrium, the Scheil rule is more appropriate, in that it assumes zero diffusion in the solid. In fact, even the diffusion in the liquid can be neglected with acceptable results for such processes, as this study will show.

However, for more precision, the Scheil rule evaluates $T*$ as,

$$T^* = T_{melt} - (T_{melt} - T_{liquidus})\beta^{(P-1)} \quad (19)$$

Where

$$P = \frac{T_{melt} - T_{liquidus}}{T_{melt} - T_{solidus}} \quad (20)$$

Then, the liquid ($Y_{i,liq}$) and solid ($Y_{i,sol}$) mass fractions are related to each other by the partition coefficient K_i:

$$Y_{i,sol} = K_i Y_{i,liq} \quad (21)$$

Fluent solves for $Y_{i,liq}$ as the dependent variable by using:

$$\frac{\partial}{\partial t}(\rho Y_{i,liq}) + \nabla \cdot (\rho[\beta \vec{v}_{liq} Y_{i,liq} + (1-\beta)\vec{v}_p Y_{i,sol}]) = R_i +$$

$$\nabla \cdot (\rho \beta D_{i,m,liq} \nabla Y_{i,liq}) - K_i Y_{i,liq} \frac{\partial}{\partial t}(\rho(1-\beta)) + \frac{\partial}{\partial t}(\rho(1-\beta)Y_{i,liq}) \quad (22)$$

where $D_{i,m,liq}$ is the species diffusion coefficient in the liquid, R_i is the reaction rate, which is nil in the case of a basic alloy solidification process where only a phase change occurs without any chemical reaction, $\vec{v}_{liq}$ is the velocity of the liquid and $\vec{v}_p$ is the solid (pull) velocity. $\vec{v}_p$ is also the copper wheel speed in the present problem, since it is a melt drag topology, with assumed non-slip conditions.

Different approaches are offered in Fluent to compute the pull velocity of a continuous casting experiment, or it can simply be set constant, as was

done in the present study. The liquid velocity can be found from the average velocity (as determined by the flow equation) as

$$\vec{v}_{liqu} = \frac{(\vec{v} - \vec{v}_p(1-\beta))}{\beta} \tag{23}$$

It is important to note that it is the relative velocity between the molten liquid and the solid that is used in the momentum sink term (Equation 3) rather than the absolute velocity of the liquid.

3.3. THIN COATING ELECTRICAL INSULATION

The SL-SMC process should lead to a minimum of non-magnetic material content in the final composite so as to keep the saturation induction of the material as high as possible. This requires that the insulator layer to be as thin as possible. The insulator material between the particles should also be stable at temperatures commonly used to sinter metallic particles, i.e. at 80% of their absolute melting temperature (up to 1300°C for common ferromagnetic materials). This limits the choice to a few very stable metal oxides, or/and their mixes or alloys of them (e.g. SiO_2, TiO_2, Al_2O_3, ZrO_2). Three possibilities exist to uniformly coat such refractive dielectric materials as a very thin layer on the metal substrate: 1) Chemical Vapour Deposition processes (CVD), 2) Physical Vapour Deposition

processes (PVD) and 3) Sol-Gel techniques. The CVD processes were discounted due to the highly toxic and often explosive gases needed to generate the coatings. The two other processes were applied to metallic ribbons for validation purposes, but eventually only the Sol-Gel Technology was retained as the preferred method for placing a refractive layer for mass production. Nonetheless, PVD will still be considered for eventual industrialisation, if the use of an aluminium underlayer, under the Sol-Gel coating, proves to be beneficial for adhesion and helps in the stability of the alumina layer (flexibility, ductility, deformability, cracks, and self-repairing effects).

Regarding the insulation thickness, common high efficiency and high performance motors have stacking factors above 95%. This tells us that the insulator layer must be as thin as a maximum of 5% by volume of the composite. Small rectangular particles, with a maximum thickness of 150μm, if insulated on both flat sides of the particles, provide two intermediate layers when being stacked. Therefore, the thickness of one layer must not be more than 2.5% of the particle's thickness. That is, 3.75 μm. However, we know that the compacted parts will not be fully dense, and in the best cases, except for the powder forging process, will have a few percentage points of porosity remaining. It must therefore be an

objective of this research to keep the insulator thickness under 1% of the volume of the composite, if possible (~1.5 μm), in order to surpass the 95% theoretical ferromagnetic density. This, as noted, is the best value for the stacking factor for conventional lamination stacking technology.

We can wonder to what extent high sintering temperatures during the final thermal treatment of the parts will affect the resistivity of the thin alumina insulating layers.

In order to test this concern, some simple calculations can be done. The diffusion coefficient of iron in the alumina layer at around 1000°C is in the order of 10^{-16} cm^2/s [99]. A good approximation in mass transport phenomena that is very useful to have an idea of the importance of diffusion occurring and affecting powders and compacts can be expressed as the “diffusion distance” , x. It is the distance where the concentration approaches to zero, from an origin maintained at a constant concentration. It consists of the two first term of the Taylor series of the complementary error function (*erfc)* contained in the solution of the Fick’s second law of diffusion for a one dimensional situation. This distance can be expressed by:

$$x \approx \sqrt{D.t} \tag{24}$$

where D is the diffusion coefficient of an atom in the lattice and t is time.

The distance where the concentration reaches half of the original one (C = $C_o/2$) is equal to 0.45 of the previous one.

The Arrhenius equation is used to calculate the diffusion coefficient:

$$D = D_0 \exp(\frac{-Q}{RT}) \quad (25)$$

where

D_0 is the maximum diffusion coefficient (at infinite temperature),

Q is the activation energy for diffusion in dimensions of energy per unit mass of material,

R is the constant of gas (energy and temperature per unit mass) and

T is the absolute temperature (K).

This equation tells us that around 1000°C, for every increase of 100°C, the diffusion coefficient is increased by approximately 3 times, taking Q ~ 150 kJ/mole (35 kcals/mole) [100]. At 1175°C, it is close to ten times higher than at 1000°C, giving an affected zone of 0.1μm with pure iron, for one hour of treatment. For three hours, the known optimal treatment for the FeNi alloy, it is roughly 0.2 μm that is affected, and this starts to be important. For the Fe-3%Si alloy, some treatments in the powder metallurgy industry can be done at up to 1350°C for 10 minutes. Following the same rule, we can say that the diffusion coefficient at that temperature is roughly five times higher than at 1200°C, giving 0.5 μm affected in one hour, or 2.5

times less in 10 minutes. If we take into account the heating and cooling time above 1000 °C to reach 1350°C at 5°C/min, we can evaluate the affected zone as approximately 0.35µm. This is far from negligible. However, for sintering conditions up to 1250°C for less than 30 minutes, we can consider that an insulator with a thickness above 1 µm will be resistant to the diffusion of the base metal of the ribbon.

3.4. MAGNETISM

Without reviewing all the magnetism theory, we will, in this section, review the most important terms and their definitions and relations. We will limit our review to the terms used to characterize soft ferromagnetic materials. We will also briefly demonstrate the equations describing the magnetic field in a ring, the ring being the easiest way to test magnetic properties of materials produced by the powder metallurgy technique.

3.5. TERMS DEFINITION

3.5.1. Magnetic field

To have a magnetic field, we must have a perturbation of the electromagnetic field of a space. The simplest perturbation of an electromagnetic field is made by a magnetic dipole. This dipole has one pole from which magnetic field lines leave and one pole where they enter.

Those lines are also named force lines or field lines. A dipole can be a simple magnet (hard magnet) with its north and south natural poles, or it can be made by an electric conductor winding (loop or spiral) where an electric current flows.

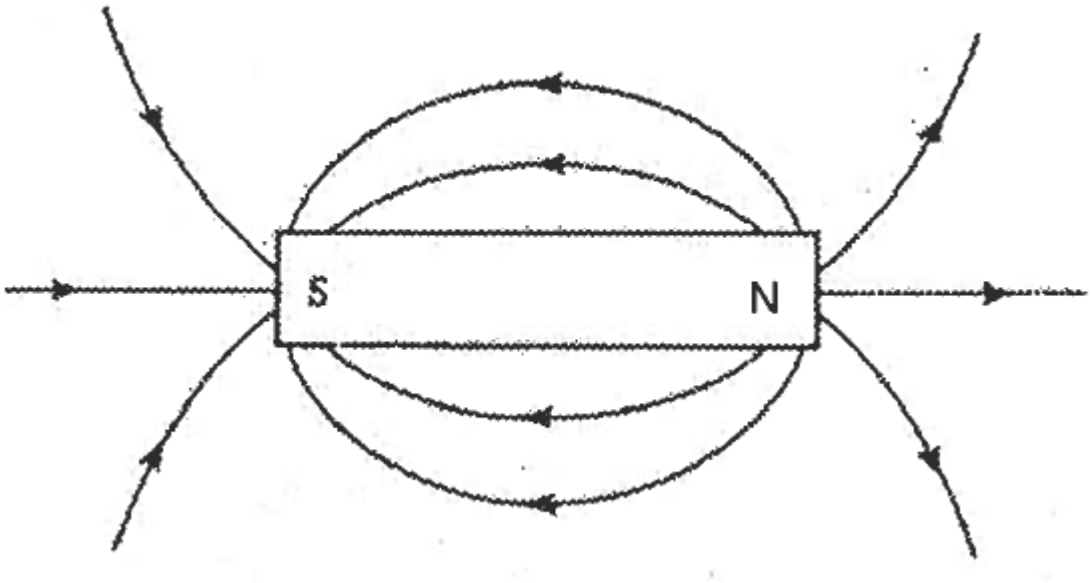

Figure 4: Force lines around a natural magnet.

By definition, field lines leave by the North Pole and come toward the South Pole. To understand from where comes the definition of the direction of the field lines, we must go back to the magnetism theory demonstrated by moving charges. We will only say here that force lines are all closing on themselves in the magnet to form loops. The space where those force lines travel is named the magnetic field.

3.5.2. Magnetic flux (ϕ)

The magnetic flux across a given surface is the total of the field lines crossing this surface. The flux depends on the angle of the surface and the direction of the field lines crossing it. If the surface is normal to the field lines, the magnetic flux is at its maximum. The International System (S.I.) unit of the magnetic flux is the Weber (1 Wb = 108 field lines).

3.5.3. Magnetic flux density or magnetic induction (B)

The number of the field lines (or flux) crossing a given surface, divided by the projection of this surface in the plane normal to the field lines direction crossing it gives the magnetic flux density or magnetic induction. The S.I. unit of the magnetic induction is the Tesla (1T= 1Wb/m2). The CGS equivalent unit is Gauss and one Tesla gives 10 000 Gauss.

3.5.4. Magnetic field intensity (H)

To define the magnetic field intensity or commonly the « applied field value», it is easier to study the magnetic field produced by moving charges, thus the field produced by a current flowing in a wire.

A flowing current in a wire produces a circular magnetic field around it in a plane normal to its axis. Outside this wire, everywhere in the space surrounding it, the magnetic field intensity (H) at a radius distance “r” from the wire axe, is equal to:

$$\mathbf{H} = \frac{\mathbf{2i}}{\mathbf{4\pi r}} \quad (26)$$

Where

H: Magnetic field intensity, A/m;

I: Electric current in the wire, A;

r: Distance from the center of the wire axis, m.

The I.S. unit of the field intensity is then the Ampere per meter. The corresponding CGS unit was the Oersted (1 Oe= 1000/4π A/m= 79.6 A/m).

For a magnet, field lines are moving from the North to the South, but for a current flowing in a wire from left to right (or negative charges, electrons moving from right to left), the field lines are turning clockwise when looking in the direction of the current, see Figure 5.

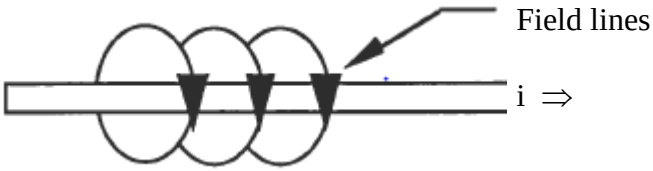

Figure 5: Field line directions around an electric wire bringing an electric current (right hand rule).

3.5.5. Magnetisation (M) and permeability (μ)

In the vacuum, a general law links the field intensity (H) to the Induction (B).

$$B = \mu_o H \quad (27)$$

Where μ_o is the magnetic permeability of vacuum, a constant equal to:

$\mu_o = 4 \pi \times 10^{-7}$ T.m/A.

For all other media other than the vacuum, the magnetic Induction of a point in the space is the sum of the induction produced by the applied field in vacuum plus the induction produced by any magnetised material placed in space and affected by that field. This last component is called the Magnetisation (M, A/m).

$$B = \mu o\, H + \mu o\, M \qquad (28)$$

The magnetic field in a medium other than vacuum is also commonly expressed that way :

$$B = \mu_o\, \mu r\, H \quad \text{or} \quad B = \mu\, H \quad \text{and} \qquad (29)$$

$$\mu_r = \mu / \mu_o \qquad (30)$$

where

μ (T m/A) is the magnetic permeability of the material exposed to the field and

μ_r is the relative permeability of this material compared to the magnetic permeability of vacuum.

We thus commonly characterize a ferromagnetic material by two characteristic relative permeability values, the initial (μ_i) and the maximum (μ_{max}) relative permeability. The following graph shows both values taken

from the initial magnetisation curve of a material. The two values correspond to the initial slope of the magnetisation curve and the highest slope formed by the origin point and the point where a straight line will be tangent to the curve.

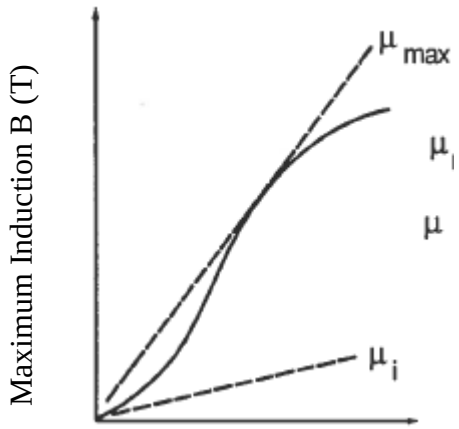

μ_{max}= maximum relative permeability.

μ_i= Initial relative permeability

Figure 6: Initial magnetisation curve (B-H curve) of a material

3.5.6. Equations for the magnetic field produced in a wound ring

We can express the magnetic field produced anywhere in the loop of a coil of wire winded around a very long bar compared to its diameter (L>>a) where a current flows by:

$$B = \mu_o \mu_r NI/L \qquad (31)$$

Where N is the number of loops of wire forming the coil

I is the current in the wire (A) and

L is the length of the coil or the bar.

If we close the bar on itself to form a ring, this equation becomes, by replacing the length of the coil by the average circumference of the ring

$$B = \frac{\mu o \, \mu r \, NI}{2\pi \, R} \tag{32}$$

where

R is the average diameter of the ring as shown on the next figure.

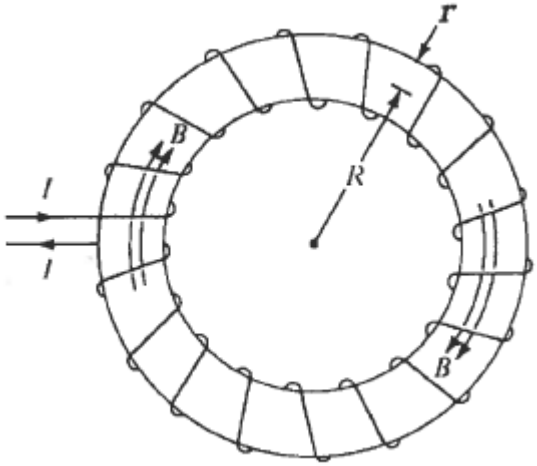

Figure 7: Magnetic field produced in a wound ring.

Thus, to produce a magnetic field of a known intensity in a ring, we only need to know the current and the number of wire loops around its circumference, and as the intensity of the field is the same everywhere in the loop area, the diameter of the loop (r) in the Figure 7 has no influence on the applied field intensity (H). However, as the magnetic field intensity decreases with the square of the distance to this field, a pick up coil winded around the ring to measure the field produced in it must be as close as possible to its surface. This second coil should then be winded first, directly

on the ring surface and be surrounded by the primary coil producing the field. The distance of this second coil to the surface is really important and must be minimised.

3.5.7. Ferromagnetism

Five different type of magnetism are present in materials, and are produced by the electrons of the atoms of that material. They are named paramagnetism, diamagnetism, ferromagnetism, antiferromagnetism and ferrimagnetism. The paramagnetism and diamagnetism in a material are of weak intensity and disappear as soon as the external applied field is removed. However, the ferromagnetism, antiferromagnetism and ferrimagnetism are stronger and can be maintained in the absence of an external field. The ferrimagnetism is produced mainly by ceramic materials or metal oxides commonly named « ferrites » and can reach induction values close to one Tesla. Those materials often with spinel ceramic structures have very high electrical resistivity and are, accordingly preferred for very high frequencies applications where their limited maximum induction is not critical (antennas, chokes, inductors). The two last categories, ferromagnetism and antiferromagnetism, are seen in metallic materials and are due to the electron 3d of the metal atoms. The ferromagnetism produces very strong magnetic fields that can be very easy

(soft magnetic) or difficult (hard magnetic) to vary in intensity. The most important ones are iron (Fe), cobalt (Co) and Nickel (Ni). The gadolinium (Gd) is also ferromagnetic under 16°C but it is very rarely used in the industry. The ferromagnetic properties of the transition elements of the periodic table are due to the alignment of the spins of the unmatched electrons of the internal layers of the crystalline lattice. In non-ferromagnetic materials, electronic layers of each atom are filled with pair of electrons with opposed spins, and there is thus no resulting dipolar magnetic moment. In compounds, the valence electrons are paired with the one of neighbouring atoms to form chemical bonds and there are thus no significant resulting magnetic moments from them.

Table 1: Magnetic moment of the neutral atoms of the 3d family of the transition elements.

Number of unpaired electrons	Atom	Number of electrons	3d orbital electronic configuration	4 s electrons
3	V	23		2
5	Cr	24		1
5	Mn	25		2
4	Fe	26		2
3	Co	27	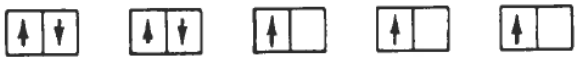	2
2	Ni	28	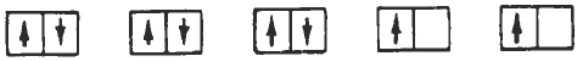	2
0	Cu	29		1

In iron, cobalt and nickel, the 3d sub-layers non paired electrons are responsible for the ferromagnetism. Iron has 4 of those unpaired electrons, cobalt has 3 and nickel has two (see the Table 1).

A phenomenon named “spontaneous magnetisation” aligns in a parallel direction the spins of the unpaired 3D electrons of adjacent atoms of solid iron, cobalt and nickel at room temperature. This parallel alignment of atomic magnetic dipoles is produced only in microscopic area named “magnetic domains” [101]. If those domains are randomly oriented, there is no net resulting magnetisation in a sample or part. The parallel alignment or spontaneous magnetisation of the dipole in Iron, Cobalt or Nickel is due to the creation of positive exchange energy between adjacent atoms. For this exchange energy balance to be positive when parallel alignment of dipole occurs, the ratio of the inter-atomic space on the 3d layer orbital diameter must be comprised between 1.4 and 2.7. (see the Figure 8). As we can see, Iron in its ferritic (body centered cubic) structure, Cobalt, Nickel and one rare earth element named Gadolinium are ferromagnetic, and Manganese, Chromium and austenitic (face centered cubic) structured iron are rather antiferromagnetic. The rare earth ferromagnetism however disappears at a very low temperature (~20°C) and it is due to its unpaired 5 d orbital electron.

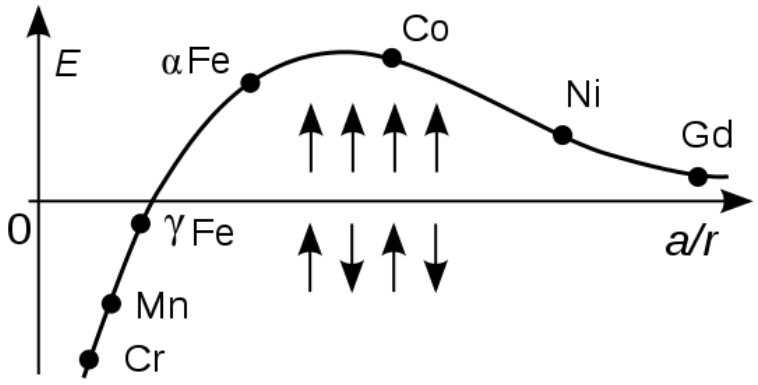

Figure 8: Bethe-Slater curve, showing the exchange energy between adjacent atoms as a function of ratio of the inter-atomic distance to the orbital radius of the 3d electron layer of different materials, and its correlation with the type of magnetism observed (ferromagnetic above zero, and antiferromagnetic when negative) [102].

3.6. FERROMAGNETIC DOMAINS

Under the Curie temperature, known point where thermal agitation starts to be sufficient to destroy the needed order for ferromagnetism to occur, when an external magnetic field is applied to a ferromagnetic part showing no resulting moment before this magnetisation is done, magnetic domains which have initially a parallel direction to the applied field grows above the domains having initially a less favorable orientation of their moments. This growth is operated by a movement of the domain walls as described in the following figure and the total induction (B) or magnetisation (M) increase rapidly with the applied magnetic field intensity (H). After the growth of the domain stage is finished, if the applied field is increased considerably, the magnetic domains start to rotate to better align in the applied field. This

rotation is a lot more energy demanding than the growth or wall movements of the domains. It explains why the domain growth and wall movement occurs first and why the magnetisation curve slope tends to decrease suddenly after a certain applied field value.

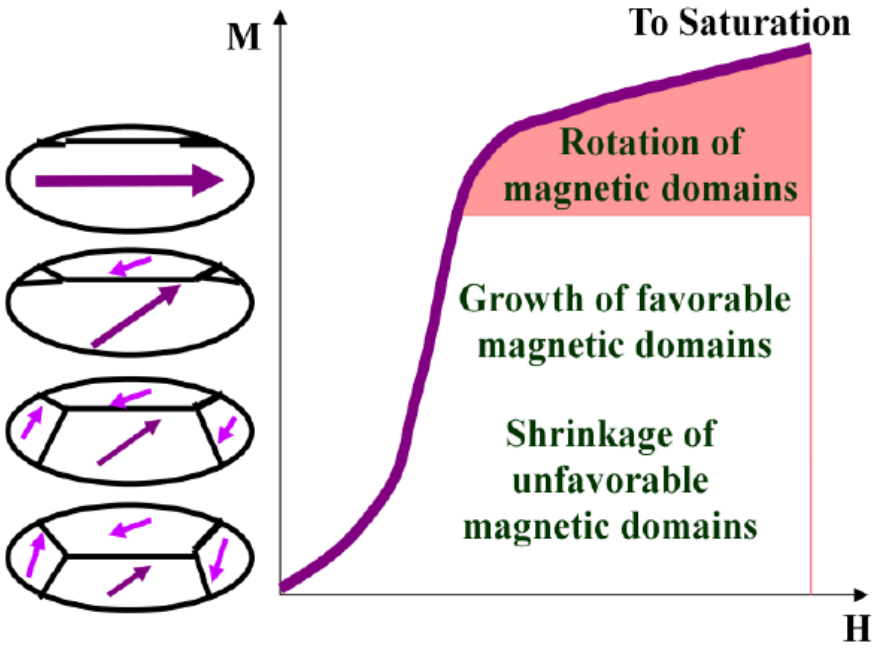

Figure 9: Magnetization curve for a ferromagnetic material associated (on the left) with different state of magnetic domains from random orientation to favorable and unfavorable orientation growth and shrink through wall movements and finally to the rotation of the moments within remaining domains [102]

3.7. ENERGY INVOLVED IN THE STRUCTURE EQUILIBRIUM OF THE FERROMAGNETIC DOMAINS

The equilibrium structure of the ferromagnetic domains in a ferromagnetic part is set to minimize the total of the different type of

potential energy involved. The total energy is the sum of the following contributions:

1-the exchange energy;

2- the magneto-static energy;

3- the magneto-crystalline anisotropy energy;

4-the domain wall energy and

5- the magneto-strictive energy.

Here is a brief description of each of them.

3.7.1. The exchange energy

The potential energy in a part is minimized when all the atom magnetic dipoles are aligned in the same direction, forming a sole domain in the part. The exchange energy between each atom is then minimized.

3.7.2. The magneto-static energy

The magneto-static energy is the potential energy developed by a ferromagnetic material to generate a field surrounding hitself. If the part minimizes its exchange energy by aligning all its dipole and forming only one domain, an important energy is required to form a magnetic field that buckle up around hit on the air or in vacuum. Equilibrium of those two first energies is reached with a good configuration of domains in the part, minimizing the flux outside of the part and the number of domains or its

exchange energy. The magneto-static potential energy per unit of volume is at the maximum for a part having only one domain, and is minimized when all the field lines can buckle up inside the material by crossing through many differently oriented domains, rather than having to go outside of him. The Figure 10 illustrates this situation.

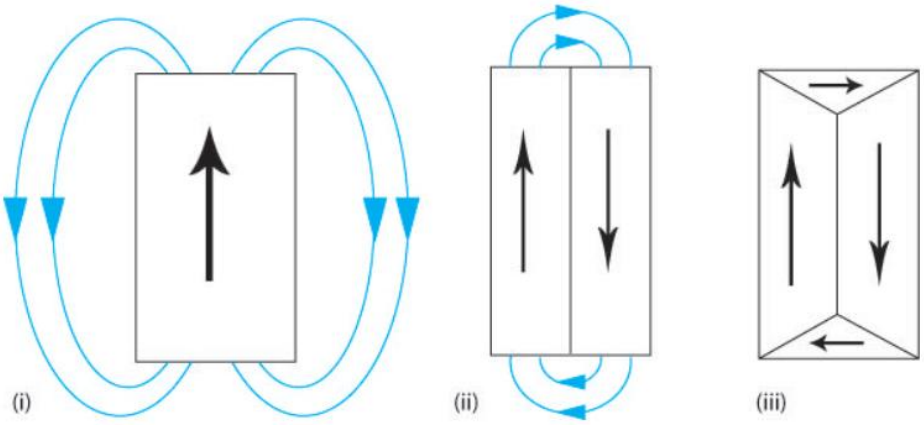

Figure 10: Pictures showing how smaller domains lead to lower magneto-static energy by decreasing external magnetic fields, (i)=high energy, (ii)=lower energy, and (iii)= no magneto-static energy.

3.7.3. Magneto-crystalline anisotropy energy

To explain this form of energy, we must explain the effect of the crystalline orientation on the magnetisation of a material. The magnetisation produced by field lines in a mono-crystal varies as a function of the crystal orientation relative to those field lines. For pure iron with its body centered cubic structure, the easy axis of magnetisation is <100> and its hard direction is <111>. The following figure shows how the

magnetisation curve varies for different crystal orientations. For a polycrystalline material like iron or Nickel, the different grains in the metal will reach their saturation magnetisation at different applied fields due to their different orientation. The ones parallel to the applied field will reach their saturation at a weak applied field and the other ones will have to rotate, requiring a higher amount of energy, in a strong applied field to reach their saturation. The work done to rotate all magnetic domains due to their anisotropy is named the magneto-crystalline anisotropy energy. A material having a lattice structure showing a larger number of easy axes of magnetisation will have a lower magneto-crystalline anisotropy energy when it is in a polycrystalline form.

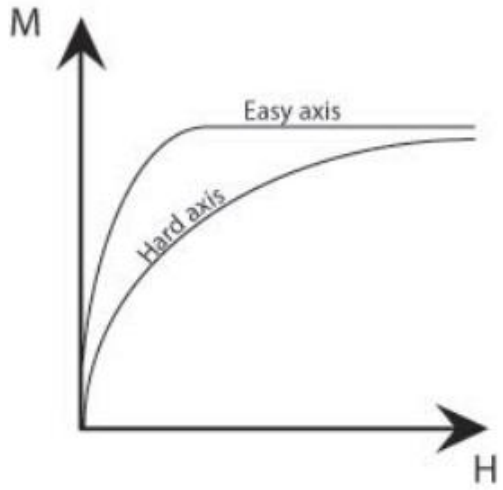

Figure 11: Magnetisation curves of different crystal orientations in a lattice.

Also, an alloy where the base lattice structure shows less symmetry due to the presence of substitution or insertion atoms will have a lower

magneto-crystalline anisotropy energy when in a polycrystalline form. Amorphous materials have no magneto-crystalline anisotropy energy, which is the main reason why they have so low hysteresis losses.

3.7.4. Domain wall energy

A domain wall is a limit between two adjacent domains where the magnetic orientation is different. It is similar to a grain boundary where the two adjacent grains have different crystalline orientation. However, grain boundaries can have very abrupt orientation changes, on the order of three atomic distances. In contrast, magnetic domain orientation changes will occur very gradually on a large distance on the order of 300 atom layers.

The following figure illustrates a domain wall where the dipole orientation varies from 180°, form one domain to the other. It shows also how the equilibrium thickness of a domain wall is done. This equilibrium involves two energies, the exchange energy and the magneto-crystalline anisotropy energy. When there is less difference between the orientations of neighboring dipole, the exchange force between those dipoles is minimised and the associated energy is low. Exchange forces thus tend to widen the domain walls. However, the larger is the domain wall, the higher is the number of dipoles oriented in a direction not parallel to the easy direction of magnetisation of the lattice. This situation tends to increase the

magneto-crystalline anisotropy energy. The equilibrium is made when the total of both energies is minimised.

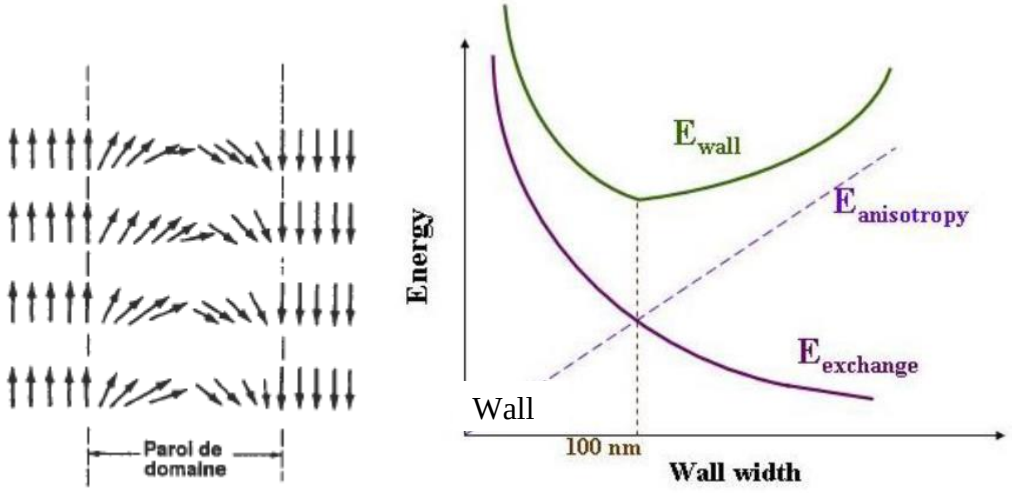

Figure 12: Schematic illustration of the dipole arrangement in a wall between two magnetic domains (left) and graph of the energy of a domain wall as a function of its thickness showing the two contributing energy curves (exchange energy and magnetocrystalline anisotropy energy). Equilibrium is reached at 100 nm [35].

3.7.5. Magneto-strictive energy

When a ferromagnetic material is magnetised, its dimensions change slightly. This reversible elastic deformation is magnetically induced and is named magneto-striction. It is in the order of 10^{-6} magnitude. The associated energy coming from this mechanical stress is named magneto-strictive energy. It is positive in a weak applied field but turns negative in a higher field for pure Iron. It is characteristic of a given material and depends

on the electronic structure of its atoms, their bending strength and the geometry of its basic lattice. The following figure shows the magneto-striction curves for Iron, Cobalt and Nickel.

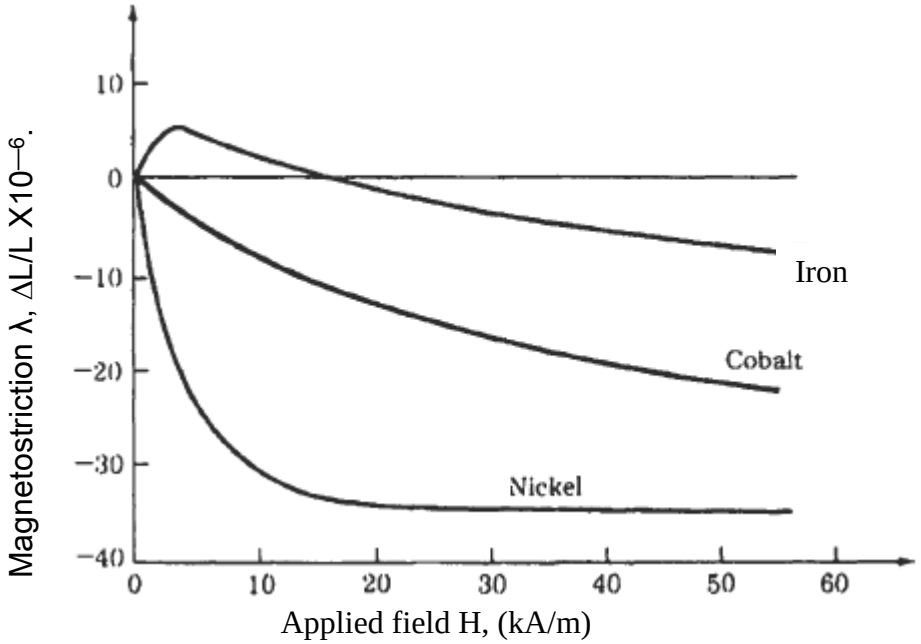

Figure 13: Mangeto-striction of Iron, Cobalt and Nickel as a function of the applied magnetic field [35].

It can happen that very large magnetic domains in a part would minimize the domain wall energy (less walls) and exchange energy, as well as the magneto-static energy with a good arrangement, but as the domain size increases, magneto-strictive energy increases under an applied field, due to more cumulative internal mechanical stress. Indeed, the larger are the domains; the longer are the areas where the stress accumulates at domain boundaries. The equilibrium is thus achieved with smaller domains,

giving lower magneto-strictive energy but higher total domain wall volume and associated energy.

3.8. MAGNETISATION AND DEMAGNETISATION OF A FERROMAGNETIC MATERIAL

The following figure shows a typical magnetisation curve or B vs H curve of a ferromagnetic material where the different steps of its magnetisation and demagnetisation can be identified.

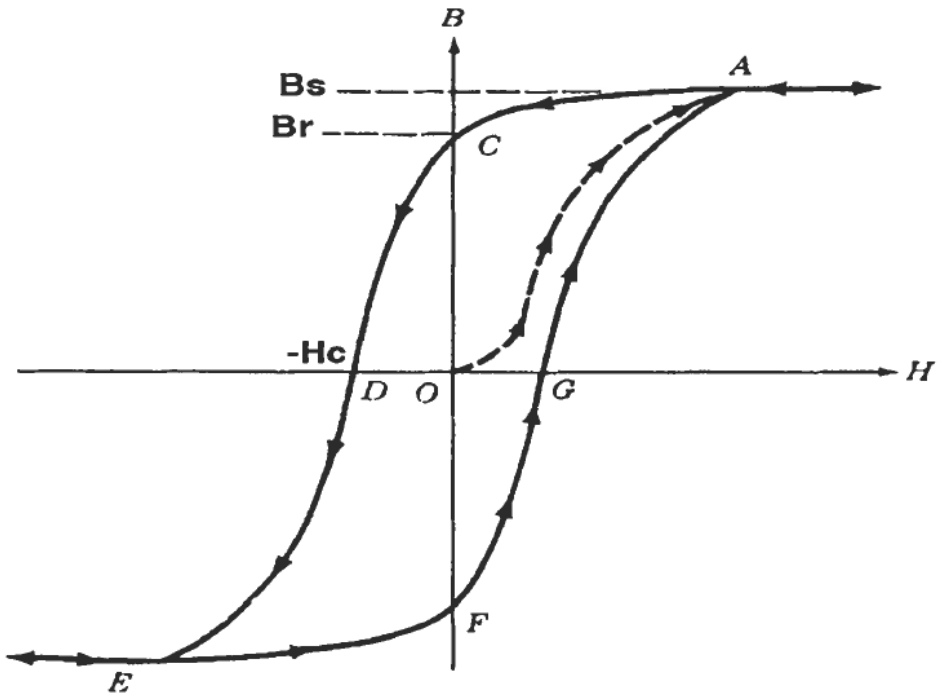

Figure 14: Induction (B) as a function of the applied magnetic field (H) for a ferromagnetic material showing its complete hysteresis cycle.

The curve from O to A is named initial magnetisation obtained from a totally demagnetised material. The curve from A to C, D, E, F, G, and back

to A is the complete magnetisation demagnetisation curve from one saturated direction to the other. In theory, the saturation can be obtained, but practically, since this value is asymptotic, one measures the maximum induction (B_{max}) at certain applied field (from 10 000 to 50 000 A/m) rather than the saturation induction (B_s) which would require too strong an applied field and costly equipment. From the saturation, or at a very high value of the induction, if the applied field is decreased to zero, the remaining induction will be named the remnant Induction (B_r), which correspond to the point C on the curve. If the field is reversed and increased until the induction is brought back to zero, the needed field value is named the coercive field (H_c) and is indicated as point D on the curve. The saturation can then be obtained in the reverse direction and the remnant induction (B_r) and the coercive field (H_c) will be measured exactly at the same value (negative rather than positive) at point F and G on the curve. If this curve is traced completely another time during an alternatiing cycle, the area in the center the curve, HxB, gives an energy, corresponding to the value of the total hysteresis losses per cycle.

3.9. SOFT MAGNETIC MATERIAL

Soft magnetic materials, also called electromagnets or soft magnets, are relatively easy to magnetise and demagnetise compared to hard magnetic

materials. Hard magnets are also called permanent magnets or just “magnets”. Hard and soft refers to their ease of magnetisation but also, for crystalline materials, to their hardness in general. It thus excludes amorphous or nano-crystalline materials, which can be soft magnets but have a rather high hardness. Spinel ferrites are also commonly termed “soft ferrites” but are also very hard even if they exhibit soft magnetic properties. They are mainly composed of metal oxides and they are not ferromagnetic materials but rather ferrimagnetic materials.

The following figure provides a comparison between soft and hard magnetic hysteresis curves. It can be seen that for a soft magnetic material, the area under the curve must be minimised and the height of this curve and its slopes must be as high as possible.

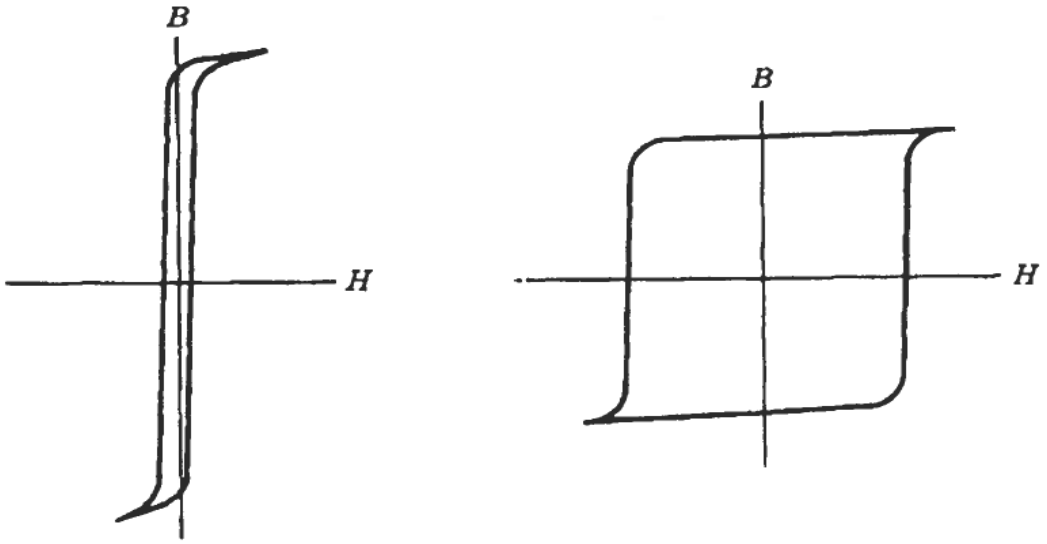

Figure 15: Typical hysteresis curve of a soft (left) and hard (right) magnetic material.

3.10. HYSTERESIS LOSSES

Hysteresis losses are due to the energy required to move the magnetic domain walls, and after to turn the domain moment in the direction of the applied field at every cycle of magnetisation in one direction and in reverse one or in a rotating field. The hysteresis losses increase linearly with the frequency of the applied field. It increases with a power exponent between 1.5 and 2.5 of the value of the maximum induction (B_{max}) reached in the part at every cycle according to this empirical equation, as stated by the classical model of losses [35, 36]:

$$P_h = K_h \times f \times B^n \quad (33)$$

Where

P_h is the hysteresis losses (watts/m^3),

K_h and n are constants specific to a given material,

f is the frequency of the applied field,

B is the maximum induction reached during the hysteresis cycle (T).

A proposed refinement of the model by Chen and Pillay [103] states that n, the exponent of B_{max}, should be replaced by a factor that is also dependent on the maximum induction reached by itself, giving that equation:

$$P_h = K_h \times f \times B^{(a+bB)} \quad (34)$$

3.11. EDDY CURRENT LOSSES

Any variable magnetic field caused by an alternative electric current applied to a winding around “a” in a magnetised material will create electric field gradients in the part. These will then create secondary electric currents in the part. These secondary electric currents are called “eddy currents”. They cause energy losses in the magnetic material, by heating it due to its electrical resistivity when crossed by those electric currents. All ways to increase electrical resistivity of the material will contribute to a decrease in those eddy currents and help to lower those losses. The eddy current losses (Pe) are also dependent on the frequency of the applied field and its intensity. It follows the equation (classical losses model) [35, 36],

$$P_e=K_e f^2 B^2 \qquad (35)$$

Where

P_e is the eddy current losses (watts/m^3),

K_e is a constant, which depend on the lamination material, thickness, conductivity, as well as other material specific factors.

f is the frequency of the applied field,

B is the maximum induction reached during the hysteresis cycles (T).

Another term is often added to the hysteresis losses and eddy current losses empirical equation, in order to better fit the curve of losses as a function of the frequency and the maximum induction, and is called the

abnormal (P_a) or excess losses. It is a function of the frequency and the maximum induction reached, both to a power of 1.5. We will not study or describe it in this present work since it is not required and it is not the purpose of this work to study specifically the nature of the losses in the material under development. We will nevertheless write the complete and most accurate version of the empirical total energy losses equation:

$$P_{tot} = P_h + P_e + P_a = K_h \times f \times B^n + K_e f^2 B^2 + K_a f^{1.5} B^{1.5} \quad (36)$$

Chapter 4 EXPERIMENTAL PROCEDURE FOR EACH PART OF THE PROCESS STUDIED

4.1. INTRODUCTION

The following figure presents the complete process developed to produce the new SL-SMC.

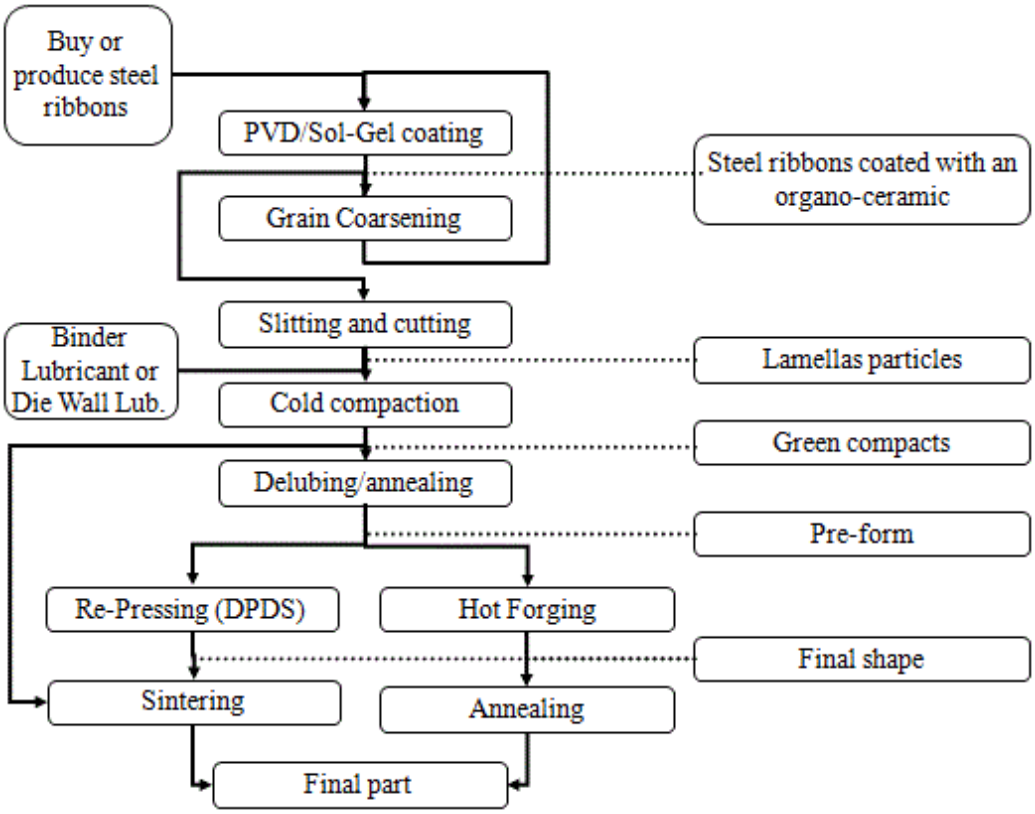

Figure 16: Process flow chart for the production of the new Sintered Lamellar Soft Magnetic Composites

This chapter will present all the experimental procedures developed and the reasons behind their choice, in order to be able to prove the feasibility of this new concept and material, and to test the properties of the final product. They will be presented in their logical order of use, as presented in

Figure 16, with the casting procedure first, then comes its CFD modelling procedure and parameters, followed by the coating procedure, the cutting procedure and finally the shaping procedure. Magnetic and mechanical testing procedures will conclude this chapter. The next chapter with the results and their analysis will also follow this logical order.

4.2. RIBBON CASTING PROCEDURE

Figure 17 and Figure 18 presented below, show the basic set-up developed to cast ferromagnetic ribbons in the range of thickness,100-200 μm.

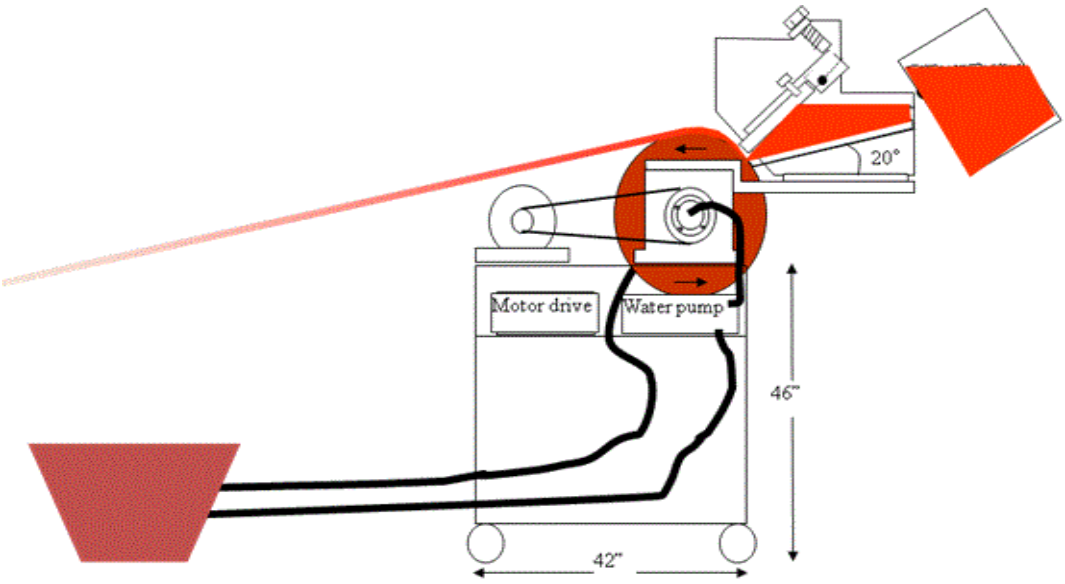

Figure 17: Schematic of the 45° Tilted Casting tundish developed at the McGill Metal Processing Center.

A 30 cm diameter copper wheel with a 6 mm thick outer water-cooled wall, containing a lot of inner water channels, was used, combined with a

2.5 cm wide slotted (casting channel) tundish. The tundish was fitted with an adjustable opening gate, which allows one to adjust the solidification contact length and the outlet opening.

The tundish constructed has 5 cm thick alumina cast refractory walls, acting as an insulating structure for the melt. It can be pre-heated to 1700°C, using a manually inserted $MoSi_2$ electric element into the casting slot. This electric element had to be removed prior to the casting operation. Three other elements were inserted in the refractory walls on either side, and under, the tundish walls. Those elements can be replaced by regular Nichrome 80/20 elements when casting low melting point alloys like tin. All moving parts (i.e. the adjustable gate) are made with a 5 mm layer of replaceable quartz plates, which come into contact with the liquid alloy to be cast. These quartz plates are installed on top of an under-layer of 1 cm thick, machined alumina bisque.

The overall tundish dimensions are: 40 cm long, 10 cm wide, and 25 cm high. The pouring cavity dimensions are: 38 cm long, 2.5 cm wide, 13 cm high (metallo-static column or pressure) from the casting wheel slit to the entering of the metal, but the top gate cuts this volume into a triangle as seen in Figure 17, while the bottom of the tundish cavity is installed at an angle of 20° from the horizon.

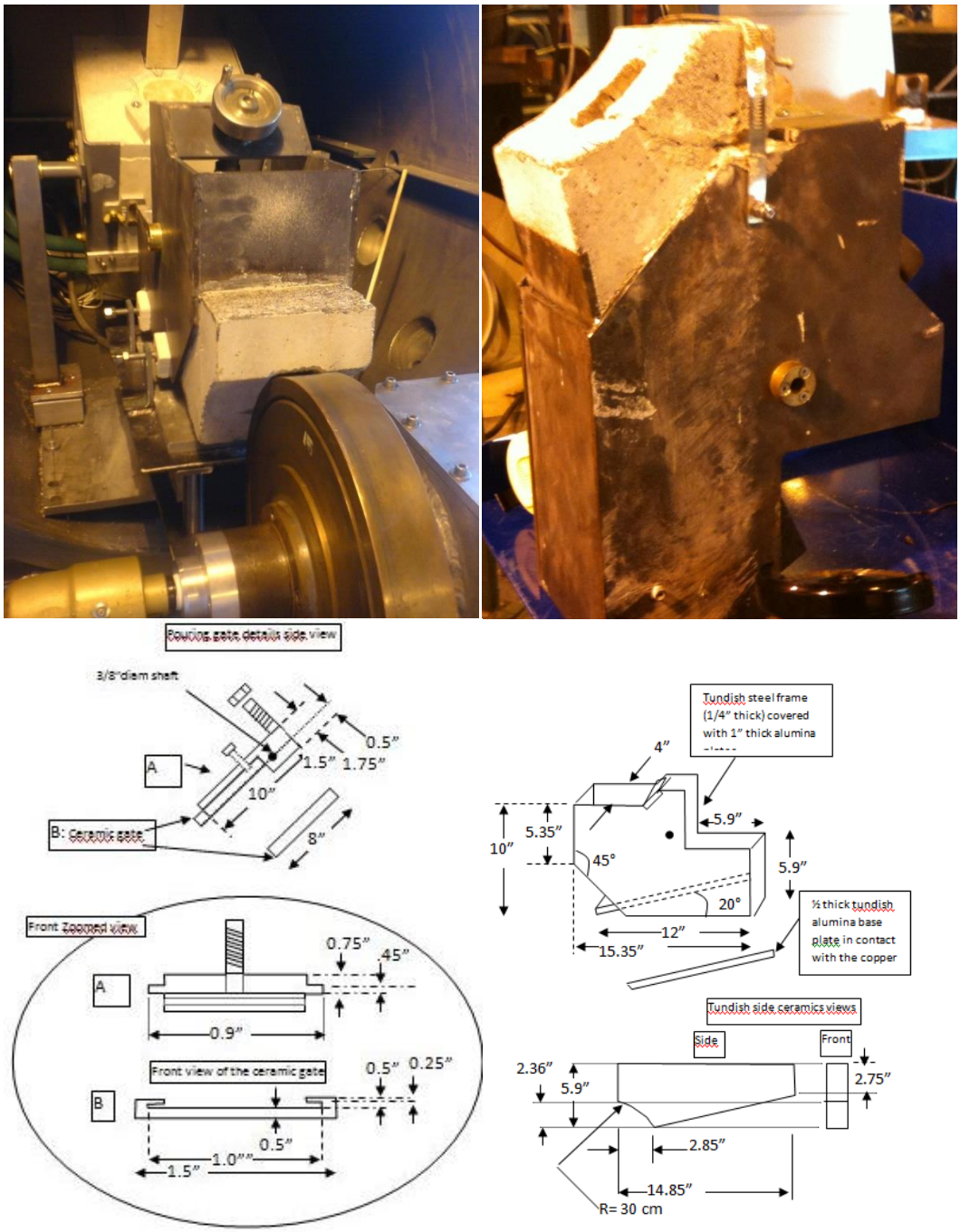

Figure 18: 45° tilted melt drag set up developed to validate the casting feasibility of high temperature 100-200 μm thick crystalline ferromagnetic ribbon at a speed under 2.5 m/s.

Different tundish nozzles or tips were tried all along of the experimentations. We started directly with the tip formed by the cast refractory walls that were improved by machining with a diamond cutting wheel. The porosity of the refractory walls caused metal to leak all around the tip. A high temperature, ceramic glue, was used to repair surface cracks and porosities in the tundish, in order to try to improve the situation (Ceramabond 503 from AREMCO). Then, the walls and floor of the tundish were machined so as to be able to fix a machined nozzle made of pure alumina bisque. This improvement corrected the leaking problems. For experiments at lower temperatures (with molten tin), the alumina bisque nozzle was replaced by a boron nitride coated steel nozzle. This last one was preheated with inserted “glow plugs” of diesel engines.

The other research teams that have worked on a similar casting configuration to the present approach, in 2007, as discussed in the literature review, did not use a gate to fix the ribbon thickness [23]. Their strip thicknesses were thus a function of the wheel speed and the level of the liquid metal. This is not the case with our fixed gate metering nozzle. It causes a problem for the correlation study with the mathematical model that will be developed. The ribbon thickness does not depend on the copper wheel speed. Only the solidified portion of the thickness should vary with

the wheel speed at the exit. The amount of recirculation of liquid within the "tundish" should also vary with the speed.

On the reverse side of validating the casting process by producing a good ribbon, validating the mathematical model developed (CFD model), appears very difficult. It is very difficult to directly validate the model quantitatively, since there are no practical ways to measure the solidified thickness, or the liquid fraction, at the outlet to the tundish, as a function of the casting wheel speed. The final thickness of the ribbon produced is fixed by the gate opening. The ribbon thickness produced is thus not a measure that can be correlated with the modeled results. Clogging problems related to the minimum casting speed could be used, but this is more of a qualitative (yes /no) test, that would doubtless be highly time consuming. The value of the minimum casting speed at which the clogging problems occur in practise, also depends strongly on other non-modeled parameters, such as inclusions, oxide scale formation, 3D flow effects (particularly those related to the wall heat exchange), and non-slip conditions (that impose zero velocity on the side walls). A measurement of the casting speed, where rubbing of the solidified metal strip against the gate starts to improve the top surface finish of the ribbon ejected, can be used. In fact, the rubbing effect of the gate is only visible on the top surface of the ribbon, when the

solid fraction of the top surface at the outlet is sufficiently high to maintain the history of a given rubbing geometry. Accordingly, the speed range where the accumulation of liquid above the gate stops, or decreases, can be used as an indicator of the important decrease in the liquid fraction reached at the outlet. Those strategies will be used to correlate casting experimentation with the CFD model.

Three different metal compositions have been investigated. The first one was Fe-3%Si, which will be used eventually as a base ferromagnetic ribbon. The second one was AA6111 aluminium alloy (Mg 0.74 wt.%, Fe 0.23 wt.%, Si 0.63 wt.%, Cu 0.74 wt.%, Mn 0.20 wt.%). This alloy has a wide freezing range (i.e. a large difference between the liquidus and solidus temperatures.) Accordingly, it has a large mushy zone. Finally, pure tin was investigated, since it has similar thermal behavior to Fe-3%Si at comparable superheat values, but at a much lower melting point temperature. In fact, pure tin has a similar viscosity and surface tension as Fe-3%Si, and has only a very small mushy zone. This is related only to the latent heat dissipated during solidification. The use of tin allows one to experiment at much lower temperatures, giving safe experimental conditions and minimizing any effects of heat losses through the refractory.

Tin also has a very low tendency to oxidize, and does not form an oxide scale, unlike molten aluminium.

As seen, this process involves a direct casting approach using the melt drag effect. This effect renders this process able to potentially operate at a speed range under 1 meter per second, which is at a range accessible with the first industrial HSBC machine that was delivered to Salzgitter, from SMS. In fact, by tilting the tundish or the delivery system of an HSBC downwards, it would be possible to produce a ribbon that is partially solidified at the exit, in the range of 0.2 mm thick, at a convenient operating speed under 1 m/s, without clogging problems, according to the CFD simulation that will be presented in this thesis.

As explained earlier, after an optional single rolling pass to improve top surface finish and ribbon thickness uniformity, those ribbons should be suitable to serve as the base material for a new process to manufacture Sintered Lamellar-Soft Magnetic Composites (SL-SMC's).

4.3. CFD MODELLING PROCEDURE AND SELECTED PARAMETERS FOR THE CASTING PROCESS

The following steps were involved in the mathematical modeling;

1) Drawing of the tundish cavity (calculation domain) using basic CAD tools. Due to the simplicity of the tundish geometry and the 2D model used, the drawing software associated with the Fluent ANSYS software (Gambit) was sufficient to conveniently draw the tundish, the gate and the copper wheel (moving boundary). The dimensions of the model of the tundish are exactly the same as the tundish developed. The tundish cavity and its meshing are shown in Figure 19.
2) Discretization of the whole domain into tiny cells (commonly termed “meshing”), with 1640 cells in total, ranging between 1.2 $x10^{-5}$ m^2 and 3.2 $x10^{-2}$ m^2, with 10 cell layers in the outlet. This was the smallest and the most sensitive, or precise area, within the domain. There, they are 20 μm wide, increasing linearly at a rate of 10% per cell, from the outlet to the inlet.
3) Exporting the mesh to an appropriate CFD package (Ansys Fluent).
4) Setting up of material properties and boundary conditions (described below).

5) Setting up of solution parameters (described below).

6) Iterative solution of the discretized equations, until convergence was reached for every cell in the computational zone.

7) Post processing and graphical representation.

The following figure shows the meshing strategy developed, with its overall position relative to the copper wheel.

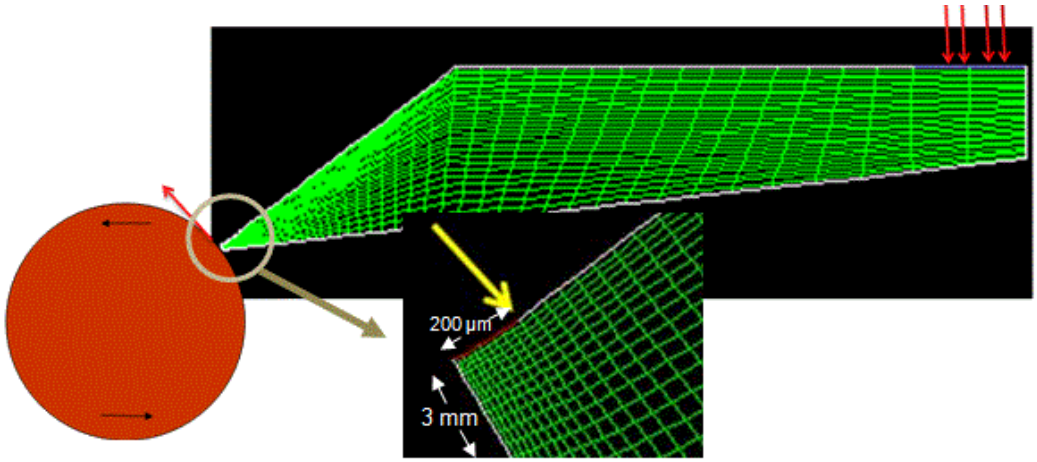

Figure 19: Meshing of the tundish with its inlet and outlet (200 µm opening shown by the arrow with a 3 mm contact length between the liquid metal and the copper wheel, with a minimum of 10 cells for the outlet, plus a 10% linear increase in the cell size from the outlet to the inlet, 1640 cells)

The mathematical model predicting the behavior of the two phases, solid and liquid, flowing from the inlet to the outlet, was based on the following assumptions:

- The fluid in the tundish (different metal properties) is an incompressible Newtonian fluid.
- The different property values between the liquidus and solidus temperature, during solidification, vary linearly as a function of the temperature (Thermal conductivity, heat capacity and density).They were interpolated “piece wise linear” in the model, (see the 4 points used in the Table 2).
- Species transport phenomena (micro-segregation) were neglected since the liquid fraction was updated, using Equation 5 (steady state) or 18 (transient mode) (see section 3.2), directly with a fixed liquidus and solidus temperature. The high speed of the solidification process and the required precision limited to only the solidified thickness as a function of the wheel speed, allow such simplifications.
- Thermal dissipation at the wall boundaries (refractories of the tundish) were neglected in this base model (adiabatic).
- Fixed heat flow at the moving boundary, i.e. the copper wheel was assumed to be a 6 mm thick pure copper wall, water cooled at 350 K (77^{o}C) in its center, with a surface resistance nil, surface roughness height set at zero, roughness constant set at 0.5, heat conductivity of pure copper at 350 K (401 W/m.K), non-slip condition. Those

simplifications were applied because any increase of the surface resistance has the same effect as an increase of the copper wheel wall thickness or a decrease of the thermal conductivity of the substrate (pure copper here so it is fixed), or an increase of the water temperature, i.e. a decrease of the heat flow and thus a lower solidified thickness at a given time and position in a given condition. It does not change the basic phenomenon and the behavior of the model. Trials were nevertheless done with different water temperature values and different thermal contact resistance and results are discussed at the end of the section 5.1.1. Regarding surface roughness, it influence only the boundary layer formed, and since the turbulence is very low, the flow being close to laminar, it was neglected. Trials were done at different values close to the real roughness value (Ra~0.5 μm) and it has no effect on the results.

- Boundary condition at the Inlet was set to “Velocity Inlet” and the value of the velocity was fixed, normal to the boundary, with an absolute magnitude value to counterbalance the flow at the outlet (mass balance). The flow at the outlet was calculated considering that the metal at the outlet is fully solidified and exit at the speed of the wheel surface. The turbulence specification method at the inlet

was set to “Intensity and Viscosity Ratio”. The intensity was set to 2% and the viscosity ratio was set to 10. The temperature at the Inlet was constant and adjusted to a superheat value of 50, 100 or 150 K.

- Boundary condition at the Outlet was set to “Pressure Outlet” with a constant relative pressure value set at zero. The Backflow Direction Specification Method used was “Normal to boundary” and its turbulence specification method was also set to “Intensity and Viscosity ratio” with 5% for the Backflow Turbulent Intensity, and 10 for the Backflow Turbulent Intensity ratio.
- For Fe-3%Si, solidus1773 K, liquidus1793 K, see the following table
- Re outlet= ~500... Transition to turbulent flow
- Standard k-ε model of Launder and Spalding [94]
- Solidification including Computed Pull (or wheel) Velocities
- Pressure-Velocity Coupling: SIMPLE
- Discretization: First Order Upwind for the momentum, k, ε, and energy equation and PRESTO! for the pressure (continuity) equation.

Under Relaxation Factors adjusted to:

- Pressure: 0.3
- Density, Energy, Body Forces & Turbulent viscosity :1
- Momentum: 0.7

- Turbulent Kinetic Energy: 0.8
- Turbulent Dissipation Rate:0.8
- Liquid Fraction update: 0.9
- Energy : 1

The following table provides data on the physical properties used for densities, viscosities, specific heats, solidus and liquidus temperatures, used in the model for the different materials investigated.

Table 2: Values of density, viscosity, specific heat, heat capacity, thermal conductivity, and solidus and liquidus temperatures, used in the model for the different materials and alloys investigated.

		Fe-3%Si		AA6111		Sn	
		Temp. (K)		Temp. (K)		Temp. (K)	
Viscosity (Kg/m-s)		1793	0.005	923	0.0018	506	0.0178
Latent Heat (J/Kg)		---	266800	---	390000	---	60657
Thermal conductivity		300	30	300	250	300	66
(W/Km)	Liquidus	1773	30	858	250	504	66
	Solidus	1793	25	923	200	506	32
		2000	25	1000	200	1000	32
Cp		300	449	300	1090	300	227
(J/kg-K)	Liquidus	1773	449	858	1090	504	267
	Solidus	1793	825	923	2000	506	267
		2000	825	200	2000	1000	250
Densité		300	7650	300	2700	300	7365
(Kg/m^3)	Liquidus	1773	7650	858	2700	504	7365
	Solidus	1793	7035	923	2370	506	6990
		2000	6850	1100	2320	1000	6990

Some modeling was also done for a transient mode, starting from a solution converged without the energy equation (only the balance of mass in-and-out of the tundish and the momentum equation, no heat flux through the copper wheel). Once that has been done, the energy equation was introduced at time zero, and the formation of the solidified layer and the movement of the solidification front, was monitored, or predicted. The final result, after a sufficient period of time, should correspond to the same result as those obtained in the steady state mode.

4.4. ROLLED RIBBONS PURCHASED

In this research project, in order to be able to test the coating, cutting, and shaping processes and to test the mechanical and magnetic properties of the composite, while the development of the casting process was ongoing, many rolled ribbons of different alloys were purchased. They were all bought as 5 cm width (or 2 inches) ribbons, and were at the minimum thickness available from the worldwide steel industry. A table of the purchased ribbons and their compositions are given below.

Table 3: List of purchased ribbons for the project

Name	Thickness (μm)	Composition
Pure Iron, ARMCO, Induction Iron Inc.	75	Fe, 0.3% Mn.
Arnon 5, Arnold Eng.	125	Fe-3%Si
Fe-3%Si Tissenkrupt	125	Fe-3%Si+0.5% Al
Supra 50 SP, APERAM/IMPHY	50	Fe-48.5%Ni
AK 502 APERAM/IMPHY	50	Fe-49%Co-2V

4.5. COATING PROCESSES; EXPERIMENTAL SET UP

4.5.1. PVD trials

The PVD technique used was a magnetron sputtering process. This was used only at the start of the project, in order to estimate the potential and limitations of the sintered lamellar soft magnetic composite technology, or SL-SMC's. This process is too slow to be competitively mass productive for the automotive industry.

Consequently, as soon as the concept was proven, efforts were next directed toward the use of an economical Sol-Gel method, involving one of the cheapest precursors. In fact, aluminium iso-propoxide is now abundant, because it can be produced easily by recuperating the dross from the aluminium can recycle process [104].

The following figure illustrates how the PVD set up was performed. For the PVD experimentations, coating thickness calibration was performed by simultaneously depositing a layer on a small ribbon part and on a glass. One part of the glass was covered with a tape. After removing the tape, the thickness of the coating on the glass at the edge formed by the transition from the uncovered to the covered area was measured with a profilometer (DEKTAK). The corresponding covered ribbon sample was ion etched at Laval University using Secondary Ion Mass Spectrometry (SIMS), while

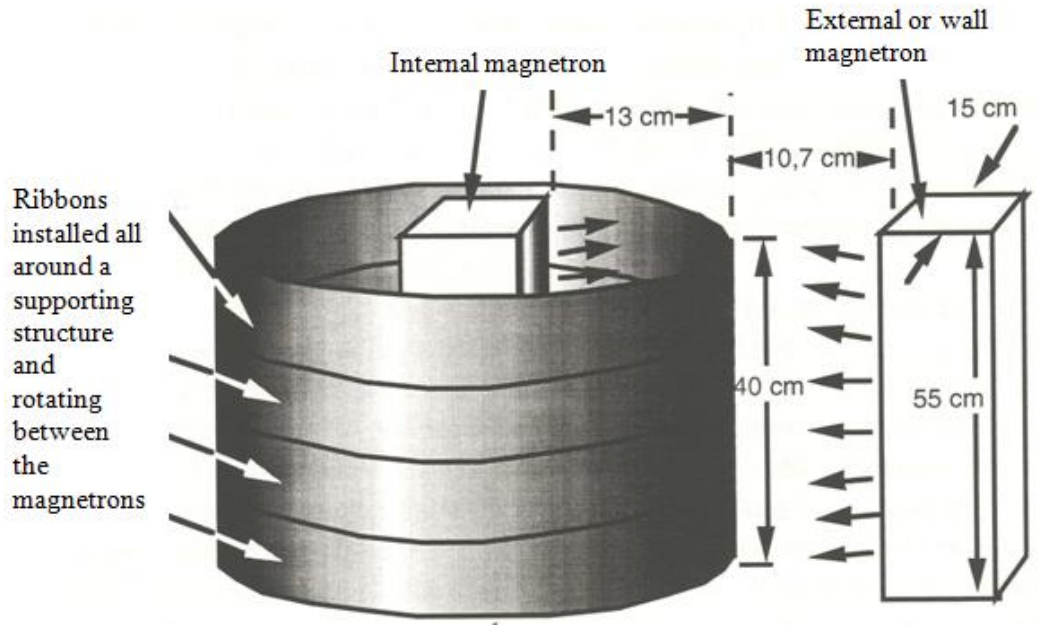

Figure 20: PVD coating set up in the vacuum chamber of a SICN coating system (now commercialized by the HEF Group) using a DC pulsed power supply.

analysing the etched atoms with a mass spectrometer. An etching calibration curve was carried out between the glass profilometer measurement and the disappearance of the aluminium peak on the spectrometer reading. The calibration curve was subsequently used to directly determine the deposited thickness of aluminium or alumina on the ribbons. The thickness of the layer deposited was adjusted to the desired value, based on the analysis of the first deposition experiment. The following figures shows one of the DEKTAK profilometer measurements on a glass and the equivalent SIMS analysis on an aluminium covered FeNi foil.

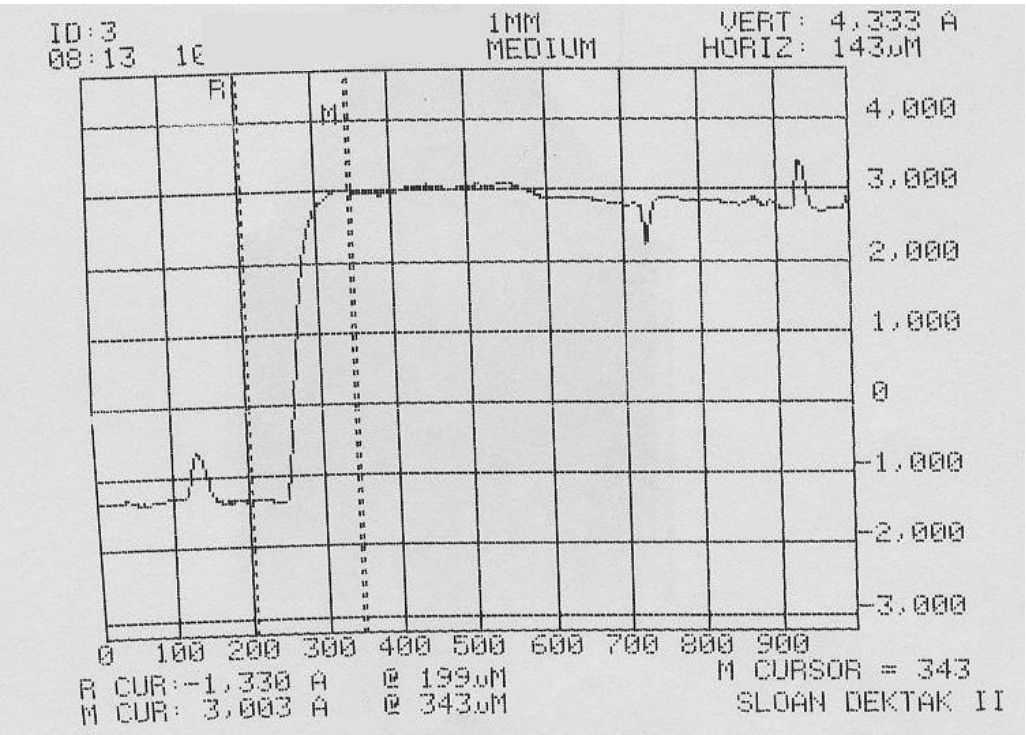

Figure 21: Dektak profilometer measurement results (thermal paper print) of a 0.4 µm thick aluminium layer on a glass slide.

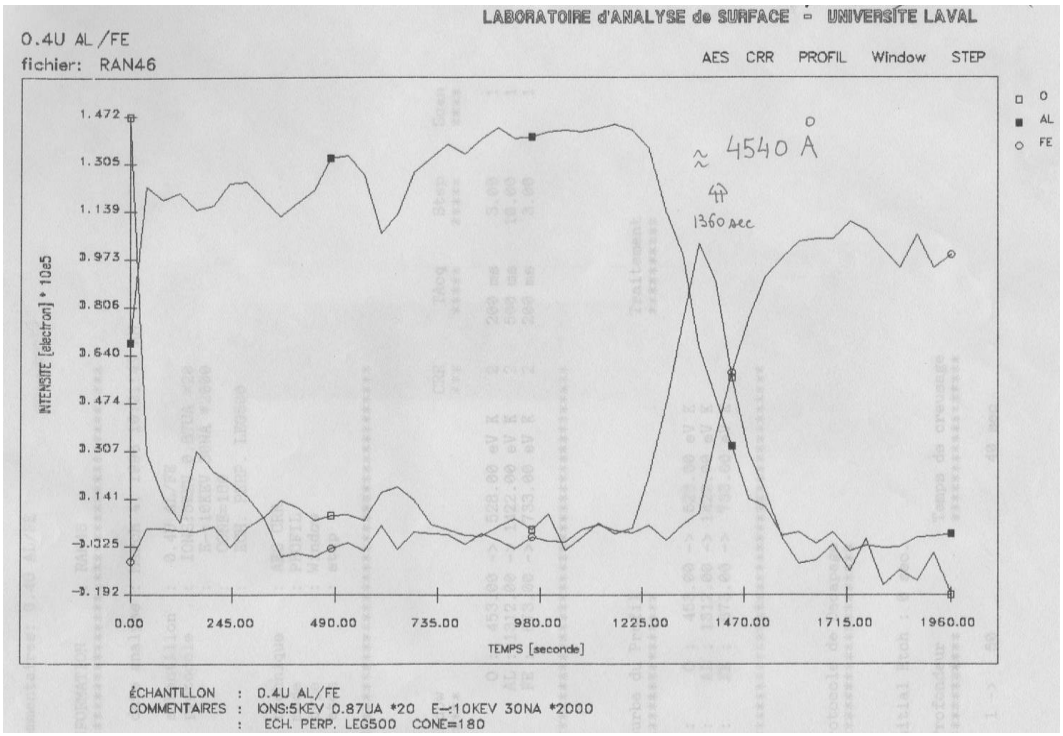

Figure 22: SIMS analysis result of a 0.4 µm thick aluminium layer deposited on a FeNi ribbon.

Adhesion tests were done for each experiment using three methods. The first one consisted of applying a standard tape for such adhesion tests (Masking Tape 3M #250) on the coating and to then peel it off to observe if there was any peeling off of the coating. The second method is to fold the ribbon and verify at which angle it starts to peel off. For the adhesion to be sufficient to resist to the cutting process of the ribbon into small lamellae particles, it should not peel off until the ribbon is totally folded on itself. The third method was to observe the edges of the particles after their cutting operation. Indeed, the shearing stress applied to the cutting zone is very aggressive to the continued adhesion of the surrounding coating. It

appeared from all the tests that the maximum thickness that can be applied to avoid any important peeling of the coating, under ribbon folding conditions or by cutting, is 0.7 µm.

For the first magnetron sputtering experiments, the alumina layers were produced by simple deposition of 0.7 µm of an aluminium layer, on the ribbons. After cutting the ribbons into particles, the lamellar powders was then oxidized in boiling water for half an hour, so as to partially hydrolyse the coating and to help promote oxidation or oxygen penetration. A small amount of an amine (commercial hand soap) was added to the water, in order to increase the depth of hydroxylation [105,106].

A second series of experiments was conducted in a reactive sputtering process, where a low amount of oxygen was added to the vacuum chamber, while sputtering aluminium with a pulsed DC voltage. After an initial ionic etching of the ribbons, a first sub-layer of pure aluminium was deposited to assure good adhesion of the coating to the ribbon. Then, progressively, the partial pressure of oxygen was increased in the system until reaching an unstable region where the aluminium targets tended to oxidize and perturb the plasma around them. The partial pressure must then remain at levels where the rate of etching of the aluminium targets is superior to their oxidation rate. The best deposition thickness tested was as

follows: 0.3 μm of pure aluminium followed by 0.4 μm of reactive sputtering. As can be seen in the process flow chart of the whole process (Figure 16), the resulting layer has been heated many times during the subsequent processes and should have formed a stable stoichiometric oxide of aluminium. The best magnetic results obtained from those experiments on FeNi ribbons are presented in Table 9, Chapter 5.

Some experiments were also conducted with magnesium targets, but it was close to impossible to reach stable deposition parameters with the reactive DC pulsed sputtering technique. Direct deposition of a layer of magnesium by DC sputtering did not either give good results after an oxidation process in water, or at a high temperature in air. The Pilling-Bedworth ratio of magnesia on magnesium is less than one, producing a porous oxide layer that is not suitable for either electrical insulation or as a diffusion barrier.

The following steps were involved in the PVD deposition process applied:

1- Ribbons disposed on a cylinder support, 30 cm high, 80 cm diameter, both sides exposed. The cylinder support turns between a wall and a central magnetron. The active magnetrons zones are 35 cm high and 15 cm wide.

2- Vacuum pumping for a period of three hours using a Turbo Molecular pump, in series with a two stage mechanical pump. Vacuum reached: 1.8 X 10^{-6} mbar, with the cold trap activated (Nitrogen circulation).

3- Ionic etching of approximately 100 atomic layers of the ribbons under an acceleration voltage of 1000 V and under a partial pressure of 2.2 X 10^{-2} mbar, with a mixture 10 % H_2 and 90 % Ar., Nitrogen cold trap active, 5 minutes at 1 kilowatt.

4- Deposition of the under-layer of aluminium in DC sputtering. Hydrogen partial pressure only at the beginning. Pressure maintained at 3 X 10^{-3} mbar. Wall magnetron at a power of 3 kW for a period of 1070 seconds, at a distance of 10.7 cm from the ribbons. Internal/Central magnetron at a power of 3 kW for 356 seconds at a distance of 13 cm. Ribbon polarisation at -75 volts. Ribbon speed set to 8 meters per minute (rotating cylinder).

5- Deposition of the alumina layer in a reactive mode under a DC pulsed polarization current. "Duty Cycle" 5 µs positive, 20 µs negative (f=40 kHz). The coating process duration was a function of the desired thickness. The total magnetron power was maintained at 4 kW under a pressure of 4 X 10^{-3} mbar with an oxygen flowrate of

32 cm^3/min. The sputtering was done in the metallic mode rather than in the “poisoned” mode, where the sputtering rates greatly drop. The magnetrons are thus kept under unstable equilibrium between their surface oxidation and the etching rate by the surrounding plasma of accelerated argon ions. The sputtering rate is kept to values close to those used for the pure aluminium, DC sputtering, operation.

4.5.2. Sol-Gel

The first Sol Gel experiments were developed based on data from the literature [107]. As said, the precursor selected is obtained from aluminium dross during its recycling process, following this reaction [104]:

$$\text{Al dross} + 3C_3H_7OH \Rightarrow Al(OC_3H_7)_3 + 3/2\, H_2 \uparrow \qquad (37)$$

It is named Aluminium iso-propoxide and its chemical formula is:

$Al(OC_3H_7)_3$ where C_3H_7 is the alkyl group reacted with oxygen that can be hydrolyzed in water to form a colloidal suspension, that will, later polymerize or transform into a gel. Indeed, some of the (OR) substituent of the aluminium isopropoxide molecule which was bought as a solid salt or as granules from Chattem Chemical Inc., USA, are transformed by hydrolysis to (OH) substitutes in water, following this reaction:

$$Al(OC_3H_7)_3 + H_2O \rightarrow HO\text{-}Al(OC_3H_7)_2 + C_3H_7\text{-}OH \qquad (38)$$

Then, a polycondensation or peptization phenomenon occurs to regroup those molecules slowly into chains and a three dimensionally cross-linked polymer. A catalyst (an acid or a base) is required for the hydrolysis to occur. We used HNO_3 at one mol per mol of aluminum isopropoxide. The reaction occurred when adding the acid to the thoroughly stirred solution of aluminum isopropoxide salt and water held for 30 minutes at 80°C. A Hybrid Boehmite Sol was formed. After a few hours of aging, the thixotropic behavior of the Sol was evident by shaking the bottle. Its viscosity was dropping abruptly. The viscosity adjustment of such solution was done by diluting with water or alcohol.

On drying, it forms a thin, solid layer of an organic ceramic on a substrate. This can be done very slowly at room temperature, or quickly at ~ 200°C. It simply consists of the removal of excess water and alcohol. The burning of this layer at a higher temperature, above 600°C, will lead to the removal of all OR and OH substitutes and will complete the transition from the organic ceramic state to an oxide state.

If all the subsequent thermal treatments and decomposition of this layer are done in atmospheres with no oxygen present (argon or hydrogen), and where carbon is abundant, the layer can transform into an aluminum carbide (Al_3C_4), rather than an oxide. Aluminium carbide, like all other

metallic carbides, is not a good electrical insulator, as is its corresponding oxide, Al_2O_3. Special attention to inducing high dew points during thermal treatments under hydrogen was paid, for parts produced with lamellar powders, so as to transform the insulator layers correctly.

We began the coating trials with a molar ratio of 1:68 aluminum isopropoxide to water. The equivalent alumina concentration after normal process evaporation was 40g/litre of Sol Gel. The viscosity of the Sol Gel solution increased during the first 24 hours, so as to become completely jellified. Vigorous stirring brought it back to its liquid state. However, the viscosity of the solution remained high, even after stirring, and after a few days of aging. A dip coating operation at a speed of 3 mm per second with such a sol gel solution, aged for 10 days and stirred vigorously for 15 minutes prior to the coating operation, lead to a layer 25 µm thick. The dip coating set up is illustrated in Figure 23.

Coating thicknesses were measured with an optical microscope after cutting the ribbon. Adhesion of this thick coating proved to be very bad, with cracks forming as soon as the ribbon was bent. Major dilution of the sol to create a non-cracking coating was tested, but the thickness of the coating so obtained was so low that it required a minimum of four coating cycles, each separated by a heat treatment step at 220 °C, in order to obtain

electrical insulation and losses close to that obtained with a PVD coating (see Table 9, Chapter 5 , section 5.3.1.3 for results).

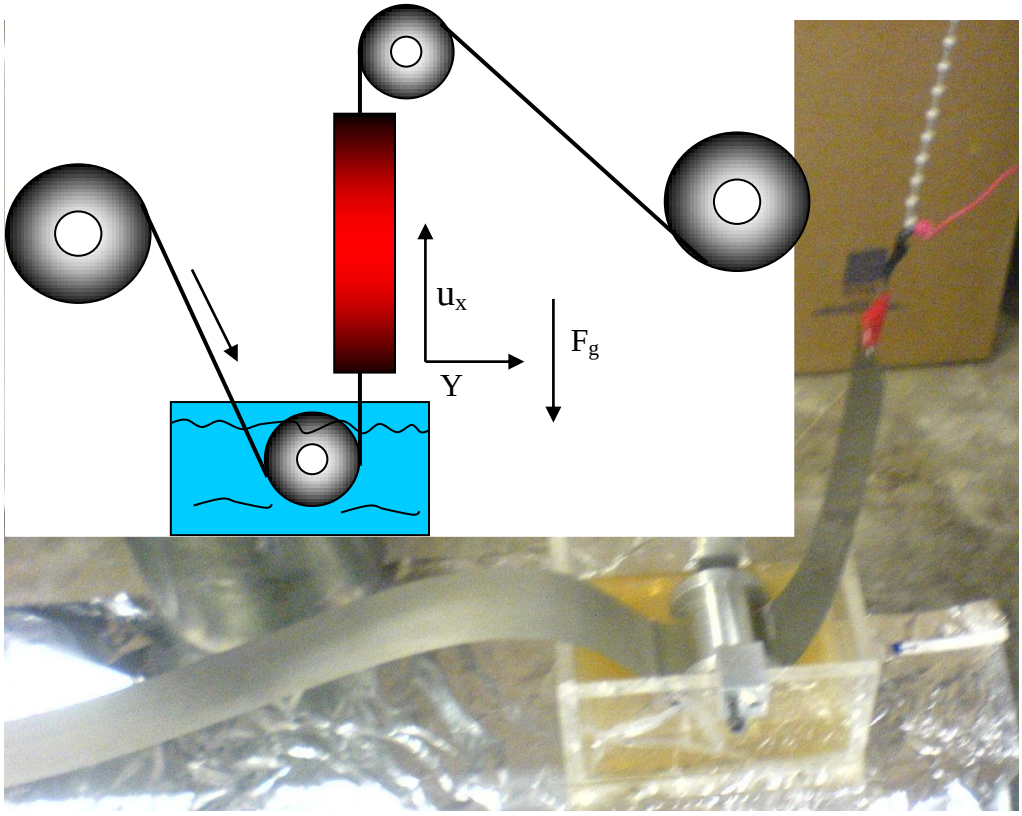

Figure 23: Schematic of the Sol-Gel dip coating process developed for calibrating the layer deposited above a picture of the real set up developed.

Recent work in the literature mentions the use of polyvinylpyrrolidone (PVP) as an additive/plasticiser to the Sol Gel solution, for improving its elasticity, decreasing its surface tension, and improving its adhesion as a coating on metallic substrates [108]. This strategy was adopted for the present tests, so as to decrease the Sol Gel's viscosity, when using higher

concentrations of alumina precursor, thereby obtaining a thicker coating in just one coating cycle. Experimentation with PVP began with a 10 days aged sol of 1:80 molar ratio. By adding 100 grams of PVP-K-30 (ISP Canada) per litre of sol, a coating of 17 μm thick was obtained. This coating cracked partially, after ribbon bending, or during its drying at 220°C. A series of dilutions were applied to obtain a coating less prone to cracking. After a first dilution at a molar ratio of 1:85, the coating no longer cracked during the furnace drying cycle at 220 °C. Unfortunately, ribbon bending or cutting, generated excessive peeling. Table 4 shows thicknesses measured at different molar ratios. The Table also provides an evaluation of the peeled width on either side of a scissor cut. Figure 24 shows the cracking tendency of ribbon coatings with decreasing thickness, together with a typical metallographic picture, used to measure the thickness of the coating, and their peeling/cracking widths at the edge of a cut.

Knowing that the wet coating has an approximate thickness three times greater than that measured after drying at 220°C [108], then, from the Navier Stokes equation for fluid flow on a vertical dragging ribbon, we can estimate the Sol Gel's viscosity. This can be deduced using the following equation:

$$\frac{\partial^2 u_x}{\partial y^2} = \frac{\rho g}{\mu} \tag{39}$$

where;

ρ is the Sol Gel density (assumed 1000 kg/m^3);

g is the gravitational constant of acceleration (9.8 m/s^2);

μ is the viscosity of the Sol Gel (Pa.s, equivalent to 1000 cP)

u_x is the Sol Gel speed in the x direction (m/s)

y is the distance from the ribbon surface (m);

The boundary conditions are:

a) $u_x = u_0$ at y = 0, where u_0 is the retrieval speed .

b) $$\tau_{xy} = \mu\left[\frac{\partial u_x}{\partial y} + \frac{\partial u_y}{\partial x}\right] = 0 \text{ at } y = \delta \tag{40}$$

where

τ_{xy} is the y directed variation of the x directed tensor of the shearing stress in the Sol Gel;

δ is the wet coating thickness.

As u_y= 0, according to equation 24, $\partial u_x/\partial y = 0$ at y = δ.

Applying these two conditions to the differential equation, we obtain;

$$u_x = \frac{\rho g \delta^2}{2\mu}\left[\frac{y^2}{\delta^2} - \frac{2y}{\delta}\right] + u_0 \tag{41}$$

Calculating the average speed of the Sol Gel;

$$\tilde{u}_x = \frac{1}{\delta}\int_0^{\delta}\left[\frac{\rho g\delta^2}{2\mu}\left[\frac{y^2}{\delta^2}-\frac{2y}{\delta}\right]+u_0\right]dy = \left(u_0 - \frac{\rho g\delta^2}{3\mu}\right) \tag{42}$$

immediately prior to entering into the drying furnace. If we estimate that the average sol gel speed is 99% of the ribbon speed, we can estimate the viscosity from the wet thickness measurement by:

$$\mu = \frac{\rho g\delta^2}{0.01u_0} \tag{43}$$

As the Sol contains 1 mol of aluminum isopropoxide and 1 mole of PVP per 100 mol of water, the volume of the wet layer should be approximately 50 times the volume of the dried layer (3.68 times its thickness). The equation becomes;

$$\mu = \frac{1354\rho g\delta^2}{u_0} \tag{44}$$

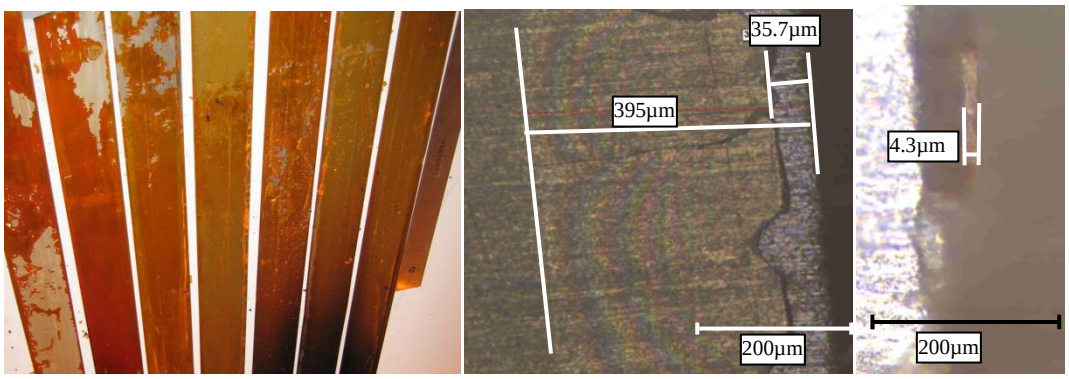

Figure 24: (Left) Ribbon coatings peeling tendency as a function of its thickness, which decreases from left to right. (Center); a typical metallographic picture used to measure the cracking/peeling width on the edge during the cutting operation and (Right); a typical metallographic picture to measure the thickness of the coatings (from a cracked, partially peeled, part of the coating).

The following table shows the calculated viscosities. Viscometer measurements on the last column of the table (Brookfield rotational DV-I+) were conducted on few samples of the sol gels. The following graph also shows the correlation between the calculated and measured viscosities and the corresponding measured coating thickness.

Table 4: Coating properties obtained at different Sol Gel concentrations.

Molar ratio of Sol	Alumina concentration (g/l)	Coating thickness dried at 250°C (µm)	Peeled width at the cut (mm)	Calculated µ (cP)	Measured µ (cP)
1:80	29.4	17±2	>2	1278	1660±10
1:85	27.8	15±2	1.0± 0.5	995	
1:89	26.3	9±2	0.3± 0.2	358	
1:94	25.0	5±1	0.2± 0.1	111	182.4±2
1:99	23.8	4±1	0.15± 0.05	71	79±2
1:103.5	22.7	2.9±0.3	0.13± 0.05	37	38±2

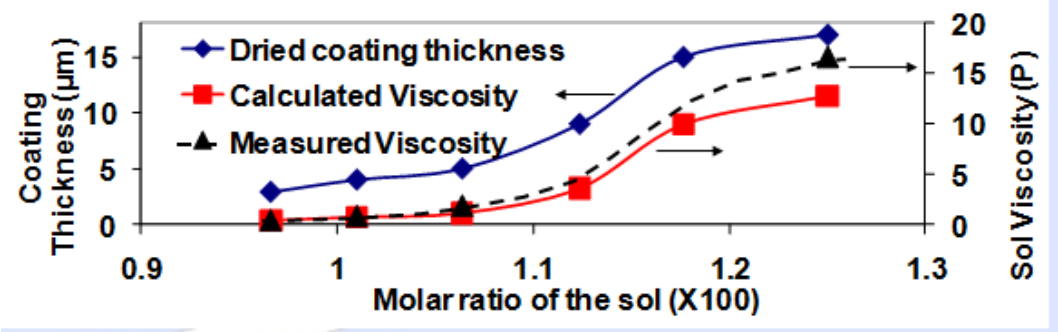

Figure 25: Calculated and measured viscosities of the prepared sol gel and its corresponding coating thickness as measured with an optical microscope using the cracked technique shown in Figure 24.

Measurements are in general agreement with estimates. According to the work of Chenbing [108], the viscosity obtained for a 2.9 µm thick coating is around 30 cP, consistent with theoretical estimates.

Taking into account that the effective thickness after burning the coating at elevated temperature is approximately four times less than the thickness after curing it at 220 °C, the weakest concentration tested gives the correct thickness (~ 0.7 µm) for a dipping operation at a retrieval speed of 3 mm per second for a stable aged Sol Gel.

The next process development step was to accelerate the coating process. In order to accomplish this, a set-up was developed, where the ribbons are circulated horizontally between two nozzles, producing a stream of sol that can flow freely on each side of the ribbon. The extra sol drops formed on the lower edge of the ribbon are collected by small rotating wheels, located just above funnels returning the extra solution to the pump feeding tank. Ribbons travel for a few seconds, at a speed of 10 cm/s, before entering into a series of tubular furnaces. Figure 26 illustrates the process.

A set up to clean the ribbons from their rolling oil prior to the coating operation was also developed, based on the use of an ultrasonic bath and a caustic soap (Detersol™) in water heated at 70°C. It is shown in Figure 27.

After a few trials, and following discussions with Sol-Gel specialists, we decided to change the plasticiser in the Sol-Gel solution developed, so as to make the fumes less toxic during the drying operation of the coated

ribbons. In fact, in addition to water and alcohol during evaporation, the fumes contain decomposition products of PVP (NOx). Changing it to Polyvinyl Alcohol made the fumes non-toxic, except for the alcohol, which is only present at trace levels. Many aluminum isopropoxide and PVA concentration adjustments were needed to obtain the same coating thickness at the end of the drying operation. The PVA comes from “Les adhesives ADHPRO”, and is a liquid grade, named P3441.

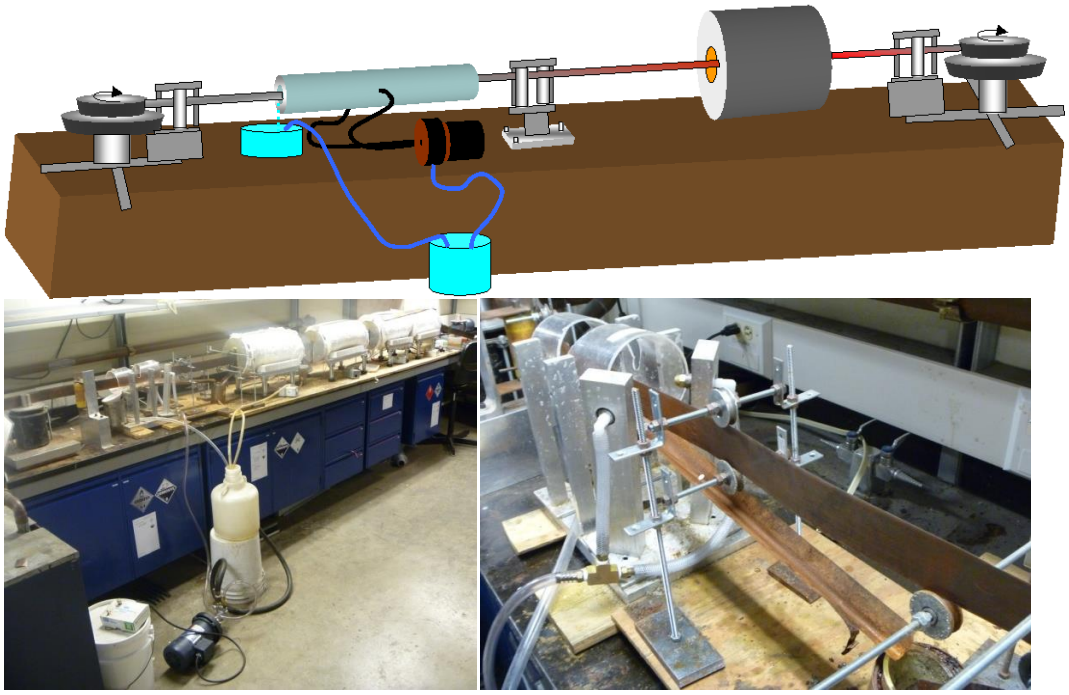

Figure 26: Top; schematic view of the sol gel spray principle developed. Bottom; Sol Gel spray line developed, high speed production line, including four drying furnaces for coating ribbons at 10 cm/s (left), and (right), the nozzle and pulley assembly for guiding the ribbon and collecting extra drops and returning them to the pump intake tank.

Figure 27: Cleaning line developed to prepare the surface of the ribbons (remove traces of oil) prior to the annealing/grain coarsening thermal treatment and the coating operation. From left to right, up line: un-coiler with its brake to keep a certain tension in the ribbon during the cleaning cycle, ultrasonic bath intake roll, bath immersed roll, exit of the bath and the set up for the rinsing bath. Down line, the two rinsing nozzle at the exit of the rinsing bath, the intake of the drying furnace, the exit with its air knife, and the re-coiler.

The following figure shows an example of the measurements of the coating thickness, as measured with an optical (LASER) profilometer, the SENSOFAR PLμ 2300 – Optical Imaging Profiler. This apparatus is located at the National Industrial Material Research Institute of the National Research Council, in Boucherville, Quebec. The apparatus was used in its confocal and its 2D profilometry mode. In its confocal mode, it was used with a 150X objective lens and a 0.95 numerical aperture. The LASER wavelength used is 460 nm. The refractive index of the coating was set to an average between the alumina refractive index and the Poly(vinyl-

alcohol) (PVA) refractive index in its dried state. For alumina, it corresponded to alumina after its sintering treatments at high temperature, with all the organic components of the coating removed. PVA has a refractive index in the range 1.49–1.55. Alumina is known to have a refractive index between 1.76 and 1.83, at a wavelength between 200 nm and 1 μm. The average index of the PVA and alumina was then set to 1.67.

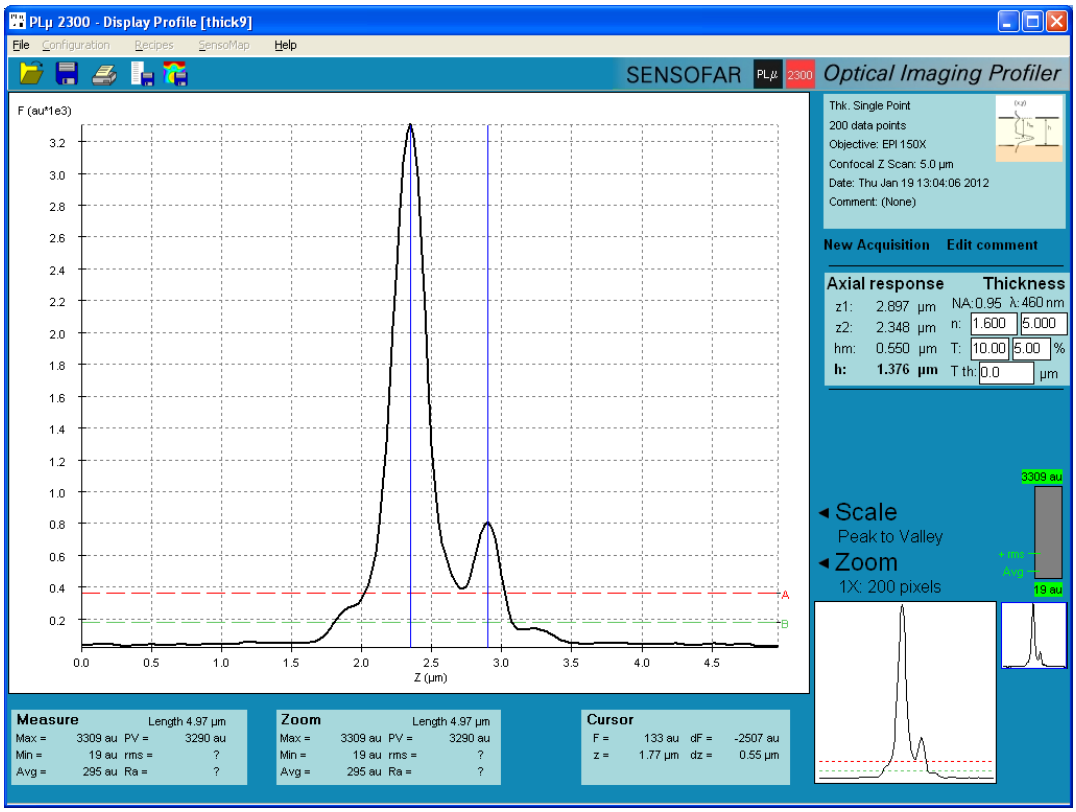

Figure 28: Coating thickness measurement with the SENSOFAR PLμ 2300, using the Confocal mode on a pure iron ribbon coated with two layers of a Sol-Gel solution containing 125 g/ltre of aluminium isopropoxide and 6%vol of polyvinyl alcohol (PVA).

Chapter 5 reports all the magnetic results of the parts produced with the Sol-Gel Technology developed.

4.6. THE THERMAL TREATMENTS

During this study, thermal treatments were applied to the base ribbons, and to the green compacts. For the base ribbons, the treatments under pure hydrogen or a mixture of 80% Argon and 20 % Hydrogen were done before their coating operation. This step was needed in order to recover their compressibility after the cold rolling operation, so as to optimize the compactability, or density, of the pressed compacts using the lamellae particles obtained from those cut ribbons. For that purpose, two methods were used. The first one was to subcontract the operation at VacAero Interrnational, Ville St-Laurent, Qc. Those treatments were done under pure hydrogen with a very low dew point, at 850°C for 3 hours. They were applied on rolls of ribbons weighing ~ 4 Kg, having 20 cm O.D, and 5 cm ID. The second method to anneal the ribbons was applied to the same geometry of rolls of ribbons, but the treatments were done at the MMPC in a tilting electric heater casting furnace (Pyradia). For this operation, a special stainless steel retort was built to be able to run the treatment under a reducing atmosphere of hydrogen without any risk of explosion (90% Ar, 10% H2). A special procedure and set up was developed to be able to purge with argon from the bottom of the retort to its top, and then, to inject hydrogen from the top to the bottom all along the thermal treatment. The

next figure shows the retort in the furnace, with the furnace top just removed for the time to take the picture. The results with that method were not as good as the treatment at VacAero, due to gas leaks. Oxidation of the ribbons occurred. The covers of the retort were distorting quickly, after only one treatment. Even with the system of bolts developed, it appeared impossible to be oxygen leak proof.

Figure 29: Left: Stainless steel retort developed to carry out thermal treatments under a reducing atmosphere on rolls of ribbon at the MMPC, using a tilting electric element heated casting furnace (Pyradia model B7D363625SV). Right: The retort is in the furnace at high temperature and the top cover of the furnace was removed quickly to take the picture.

The thermal treatments applied to the green compacts were done in two types of furnace. In the case of the final sintering treatment, it was done in a horizontal tubular furnace, bought and adapted for the project. Special flanges, tubing, water bubbler to increase the dew point of the atmosphere, and a safety monitoring hydrogen burner, were developed to

be able to run the sintering treatments under pure hydrogen with different dew points. The pre-heating treatments for the forging operation were, however, done in a vertical tubular furnace under pure argon. The following figure illustrate the sintering set up.

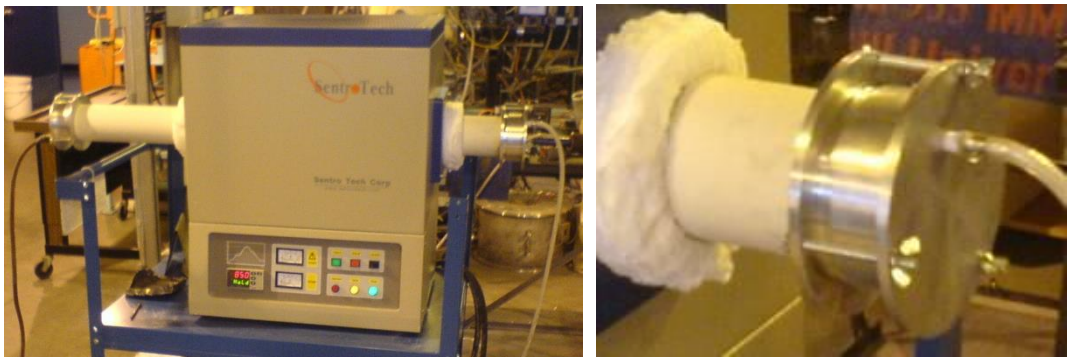

Figure 30: Sintering furnace bought and equipped to do the sintering thermal treatments under hydrogen.

4.7. CUTTING THE RIBBONS INTO PARTICLES

A complete slitter and cutter line was built to be able to cut the ribbons into particles. None of that equipment was commercially available, as “off the shelf” items, because the cutting operation required has never been accomplished for any other industry up to now, to our knowledge. Laser cutting was originally considered but after some verification, the energy required, the cost of the equipment, and the effect on the coating adhesion was not appropriate for the process under development. It was determined that the best approach was to first slit the starting ribbon and to then cut it into square particles. Due to the extremely low thickness of the ribbons,

regular slitting lines for the steel industry were not appropriate, and were also too expensive, particularly for the purpose of this process validation. The use of slitters from the paper industry was also not appropriate because, first of all, the cost and size of equipment available, and also because there are no machines designed for the strength of our metallic ribbons aimed at passing directly from a ribbon 5 cm wide, to many very narrow ribbons, that will be subsequently cut in the transverse direction to produce small square particles. A technology was therefore developed to cut the 5 cm wide, thin, alumina-coated steel strips, into a multitude of thin, small, rectangular, or square-shaped, particles. As explained earlier, the particles must be as thin as possible to limit eddy currents. However, any mass production cutting technology requires a proper clearance between the blades of the knives, in order to avoid exaggerated burrs on the parts. This precise clearance requirement combined with the minimum possible tolerances (±2 μm) on the machining process for the production of the circular knives needed for the slitter, limited the maximum width of the starting ribbon that could be cut in only one step to 5 cm (using a maximum grouping array of 20 circular knives and 20 spacers of each ~2 mm). In order to maintain extremely good alignment between each of the circular knives, a laboratory scale cold roller (Stanat Model TA215, 4 x 6 Reversing,

borrowed from NRC, Industrial Material Institute, Boucherville) was modified to install the array of circular knives. This is commonly termed a “quill set up” by the slitting industry, when used for thicker material. A way to eject the individual thin and delicate coated ribbon strips from the knives immediately after being sheared, without scratching the coating, had to be developed. A special feeder to straighten and bring all the just ejected slit ribbons, (resembling spaghetti), from the slitter to a specially designed cutter, also had to be built. The cutter was bought from the plastic industry, where it is normally used to cut plastic or glass fibers to feed plastic injection molding machines. It is sometimes called a pelletizer, to produce plastic pellets. It was a model specifically designed for our needs, having the capability to be adjusted to a “zero” gap between the rotary cutter and the fixed bed blade, for our very thin ribbons (Scheer Bay, Model AX04G). The following figure shows all the machines built, modified and bought for the cutting operation. The cutting process developed, limits not only the maximum width that can be cut, but also the minimum thickness of the ribbons.

The optimum dimensions (length and width) of the particles for the cutting operation were determined by taking into account the feed-ability of the particles in a standard powder metallurgy pressing process and

associated tooling, and the magnetic performance of the composite, longer particles having the potential to give a better performance. As such, the dimensions of the particles were set to approximately 1.5 by 1.5 mm. Those dimensions represented the best compromise for parts having a minimum section of ~5 mm wide.

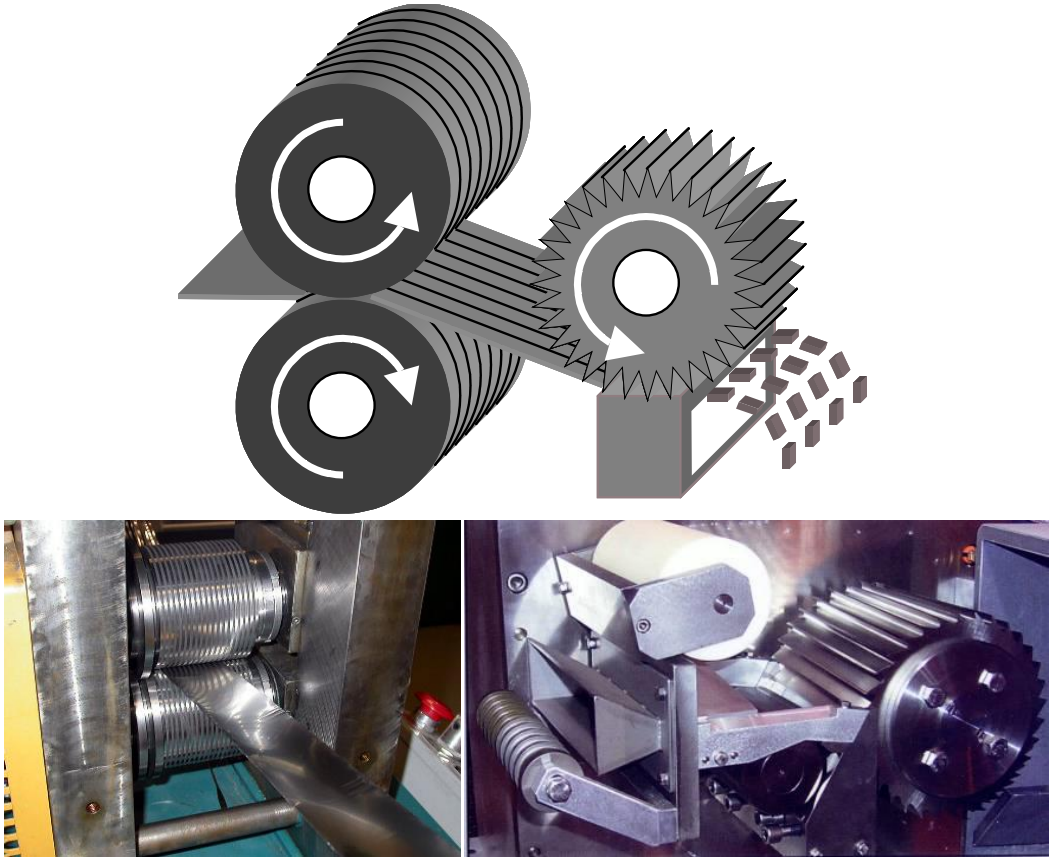

Figure 31: Top: Sketch of the cutting principle adopted to cut the ribbons into lamellar particles, Bottom, pictures of the real slitter and cutter assembly.

The simplicity of the process avoids the need for any screening operation to eliminate under- or over-size particles, as is the case for the regular powder metallurgy process. Nor are any sophisticated coating

operations involving fluidized beds or vacuum drying mixers with injectors to encapsulate the particles, required. Mixing operations are also avoided, provided that one has developed a suitable die wall lubrication technique.

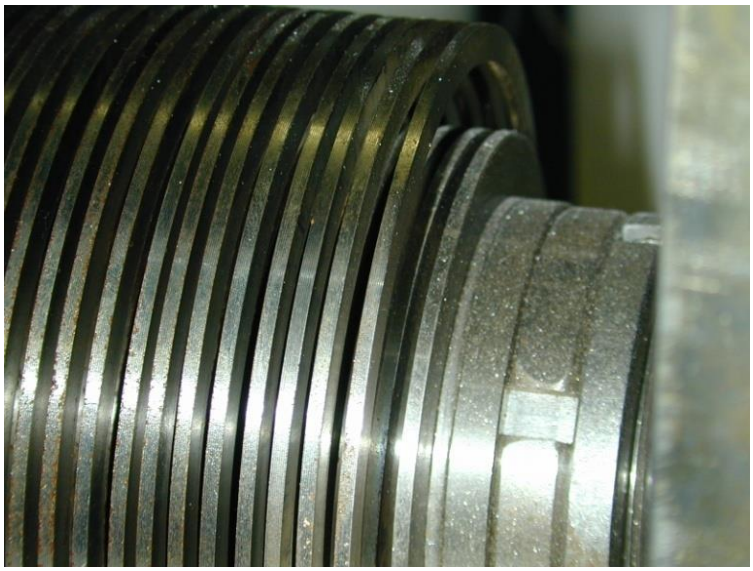

Figure 32:A zoom in, on the top assembly of circular knives and ejector rings floating around them which eject the cut ribbons

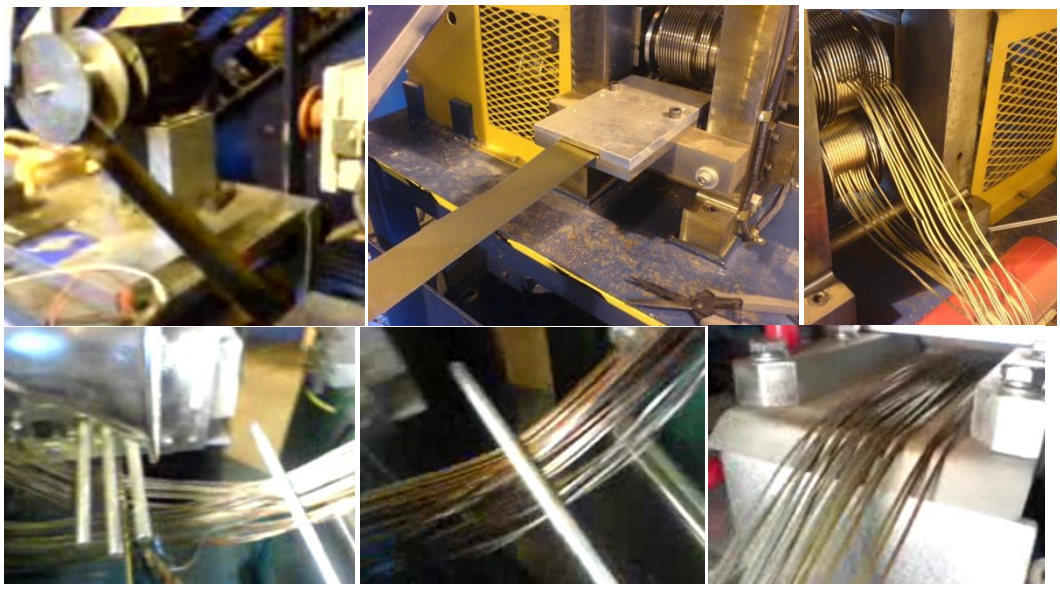

Figure 33: Pictures of the complete cutting line, from top left to bottom right: uncoiler, alignment plate at the intake of the slitter, slit ribbons exiting the slitter, guides and straighteners (first generation), and finally, entry into the cutter.

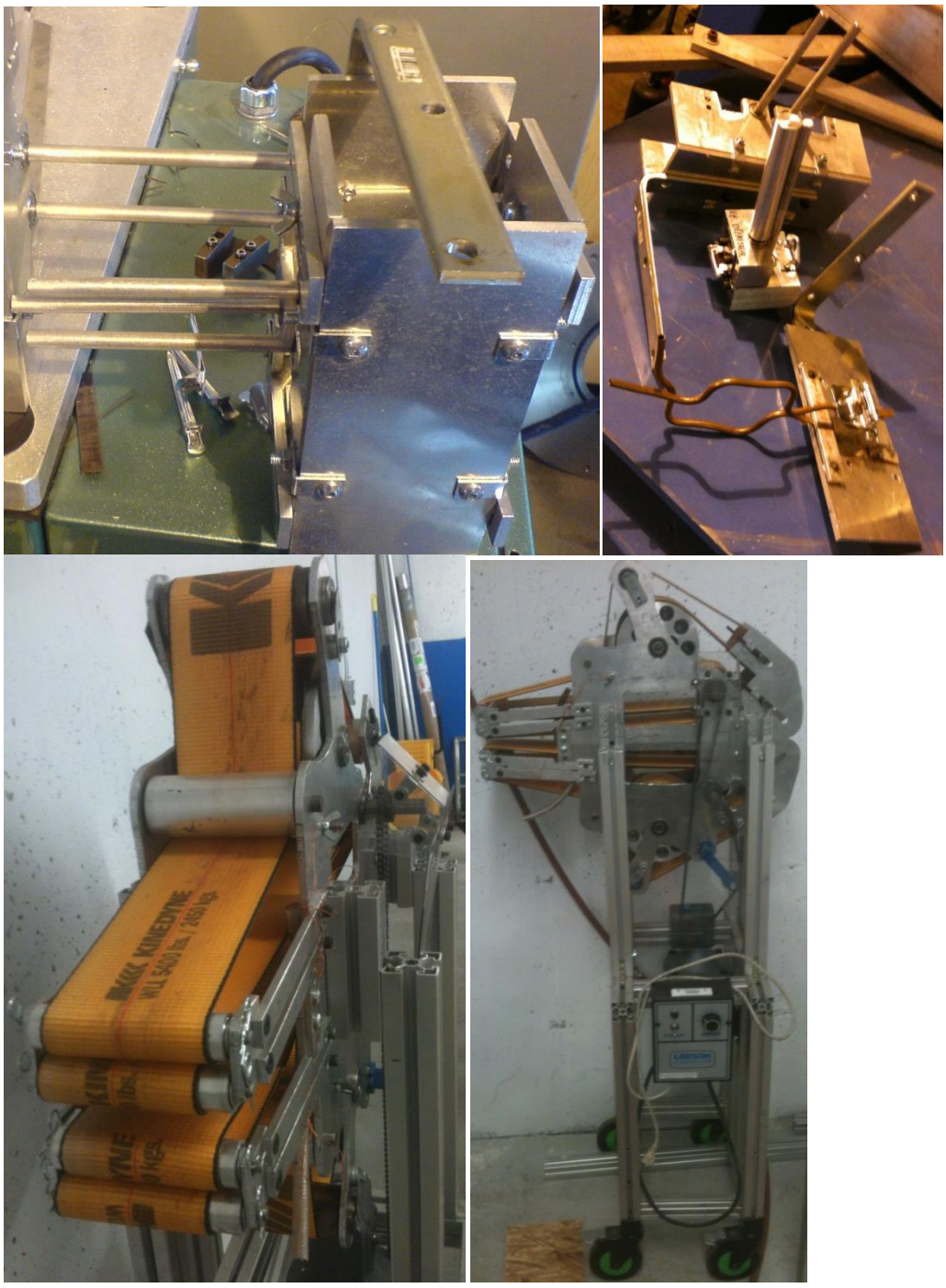

Figure 34: Top: firsts generations (3) of straighteners required to guide and straighten the slit ribbons between the slitter and the cutter, Bottom: Last and final machine built

4.8. SHAPING PROCESS

4.8.1. Laboratory shaping tests: Procedures for magnetic and mechanical characterization.

To reduce the quantity of experimentation, the study in this part of the process concentrated on the Fe-3%Si alloy. The flow behaviour of the lamellae was evaluated using the MPIF standards [109]. However, no flow was measured, either in a Hall funnel or in a Carney funnel. Apparent density was determined using the MPIF standard 48, “Method for Determination of Apparent Density of Metal Powders Using the Arnold Meter”[110]. This test method was more appropriate for the lamellar particles, and consists of slowly sliding, horizontally, a cylinder partially filled with powder, over a 20 cm^3 hole in a hardened steel block, and collecting and weighting the powder entrapped. The tap density was evaluated with the MPIF standard 46, “Method for Determination of Tap Density of Metal Powders” [111]. Lamellae were poured into a graduated cylinder, and then tapped, until completely set. The volume was then measured and used to determine the apparent density.

For mechanical and magnetic characterization, standard rings and bars, shown in Figure 37 and Figure 38, must be produced. The laboratory

compactability and shaping feasibility tests were then done with those geometries. A manual 100 ton hydraulic press, located in the McGill Metals Processing Center, was used. Special spring equipped floating toolings were developed to reproduce a real double action operation, which would be performed on production presses, where both the lower and the upper punches move, relative to the die. This feature gives a symmetrical gradient of density, relative to the mid height of the part. The following set of figures provide a schematic view of the method to feed the powders into the cavity of the tooling and to press and eject a ring, using the floating tooling developed. From (A) to (H), the operations are as follow:

(A) the pre-feeding transparent plastic die inserted above the cavity;

(B) a first punch extension, pushes the powders into the cavity;

(C) the plastic pre-feeding die is withdrawn;

(D) the pressing punch is brought into place;

(E) the punch is pushed into the cavity by the ram of the press, and starts to compact the powders;

(F) the ram now pushes on the die to level it down with an external ejector ring brought in place (not visible here);

(G) and (H) same movement as (F), until complete ejection of the upper punch and the pressed ring.

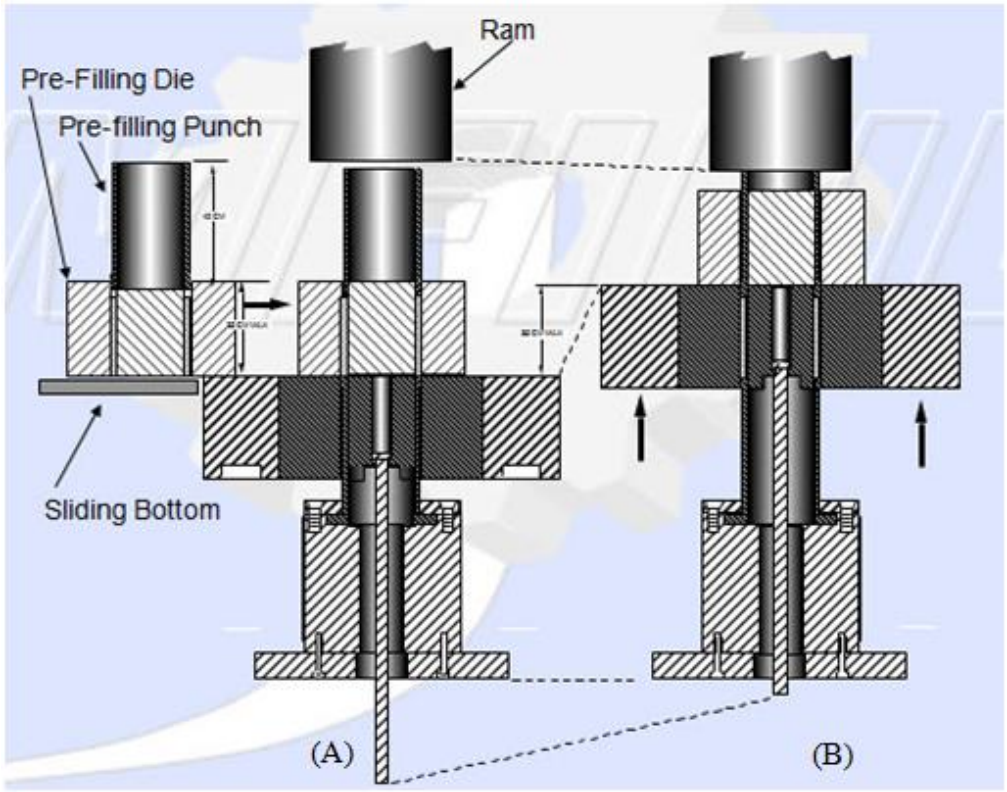

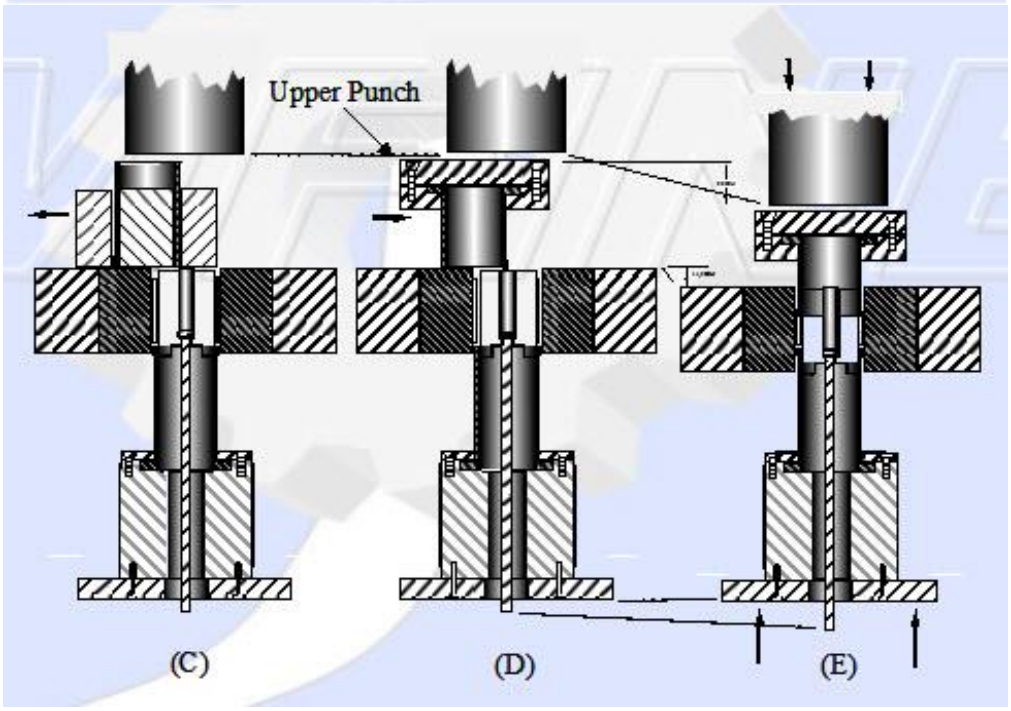

Continued next page

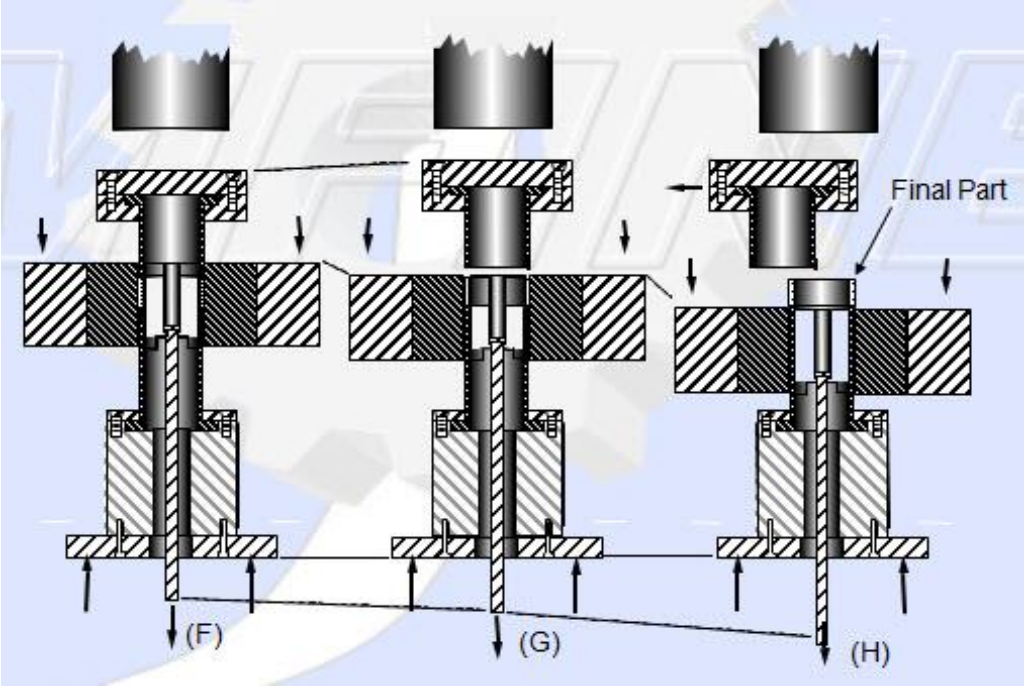

Figure 35: Top, Middle (previous page) and bottom: Feeding and pressing process of a ring, developed to overcome feeding problems encountered with poor flowing lamellar powders.

The best way to obtain the highest density and strength for a given compacting pressure, is by using a low level of dry, powdered, lubricants, added to the powders, combined with the use of die wall lubrication (DWL) [112]. With the use of a higher temperature during compaction (~120°C), using so called “warm compaction”, it is also possible to obtain a slightly higher mechanical strength and density on pressed and ejected parts [113]. It is thought that the positive effect of temperature is mainly due to its action on the binder-lubricant behaviour, in that it can better smear, lubricate and be ejected from the porosities to the die wall during compaction. Its

interactions and cohesion with particle surfaces is better, and can give higher green strength values than a cold compaction at room temperature.

Compaction tests were conducted to evaluate the compactability of these Fe-3%Si lamellar particles, based on the amount of specific binder-lubricant added, and the pressure used. The density of these green parts was determined using MPIF standard 54, “Method for the Determination of the Density of Impermeable Powder Metallurgy (PM) Materials”. The samples are weighed in air and water, and the density is calculated based on these results. For mechanical properties, the Transverse Rupture Strength (TRS) of ¼ inch thick green parts were evaluated using MPIF standard 15, or ASTM standard B312 [114], and compared with the TRS’s of green parts produced from lamellar particle mixes containing either no internal lubricant or 0.75%wt of standard ethylene bis-stearamide lubricant (Acrawax C Atomised from Lonza) . The bars are 31.8 × 12.7 × 6.4 mm.

The binder/lubricant mixed into the powder was a polyethylene powders that proved to give higher green strength on parts, particularly when warm compaction was used [113]. It has an average particle diameter around 12 μm (D50).

Fully sintered, or forged, mechanical properties of the parts produced were determined using a three-point bending test, similar to that used for

the green parts (parts just pressed and ejected for the die cavity), as described by MPIF standard 41 [115]. For forging, or double pressing, of the parts after an annealing treatment, so as to recover their compressibility, special tooling containing a cavity slightly larger and longer than the cold pressed parts, was built. For the forging operation, the hot parts were preheated to 1050°C, over a 4 minute period, under a protective argon atmosphere, in a vertically mounted tubular furnace, blocked at both ends to prevent air from entering the tube. Special grips and positioning tools were made to manipulate the parts as quickly as possible, and to insert them rapidly into the die cavity, so as to be re-pressed to close to full density. Typically, it took less than 4 seconds to insert the hot parts in the die cavity. The press stroke speed was 25 mm/s at low pressure, and half that speed when the pressure was increased to above 500 psi. It typically took another 4 seconds for the press ram to completely close the die cavity and for the pressure to reach its peak. The pressure was adjusted according to the surface of the parts, so as to apply 550 MPa (40 tsi).

The following figure shows a ring pre-heated to 1000°C, being inserted in the forging tooling cavity.

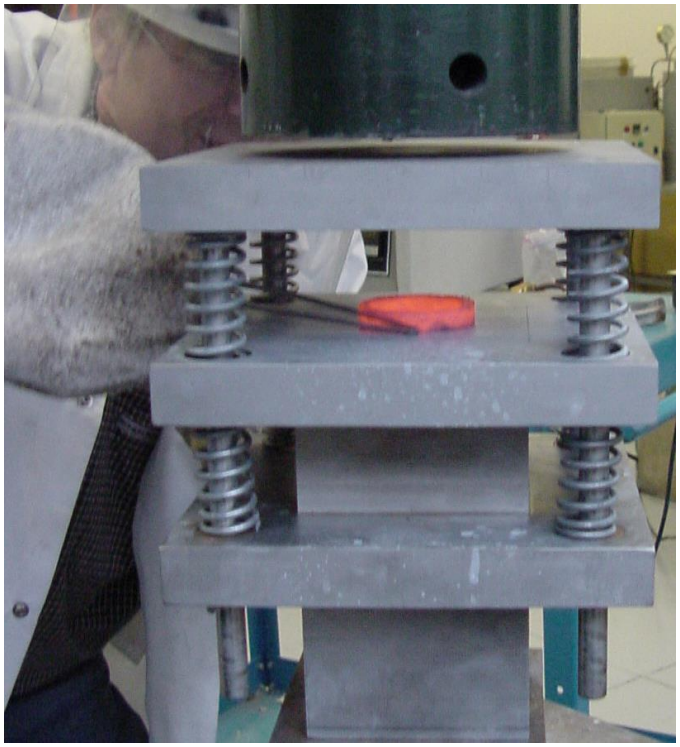

Figure 36: Forging operation of a ring when it is inserted in the forging tooling that was developed.

Figure 37: Powder produced with the new SL-SMC process and an example of a part pressed for characterization (small rectangle and the ring) or motor teeth pre-from ready for forging.

Rings produced for magnetic characterization of the SL-SMC material had an outside diameter of 53.6 mm, an inside diameter of 40.6 mm, and a height of 6.25 mm. A cold pressing floating die and a forging die with slightly larger dimensions was also built, in order to produce single pressed, double pressed and forged rings.

Figure 38: Example of SL-SMC parts, cold pressed, using the optimum conditions developed to date (0.75 wt% Lub), and exhibiting a good surface finish.

4.8.2. Mass Production shaping test procedure

All the mass production shaping tests were conducted at, and in collaboration with, the National Research Institute of Canada, the Industrial Material Institute of Boucherville. They possess a 150Ton Gasbarre industrial production press with an automatic feeding system and all the conveyors to be able to conduct short production runs. Part to part mass stability, part to part density at a given compacting pressure, part to part ejection force stability are the kind of measurements that can be acquired with their equipment.

If required, special feeding systems can be designed, developed and adapted to the production press. Die wall lubrication technology is also accessible. For the present research, a specific feeding system was developed, as described in the results chapter, section 5.3.2.1.

4.9. MAGNETIC CHARACTERISATION

DC and AC magnetic characterization was done on a KJS Associates Hysteresis Graph (model ACT-500, SMT-500, 7385K Fluxmeter), according to ASTM standard A 773 [116]. For AC characterization, 250 turns of 24 AWG wire and 250 turns of 30 AWG wire were respectively used for the

primary and the secondary windings, while 450 turns and 150 turns were used, respectively, for DC characterization.

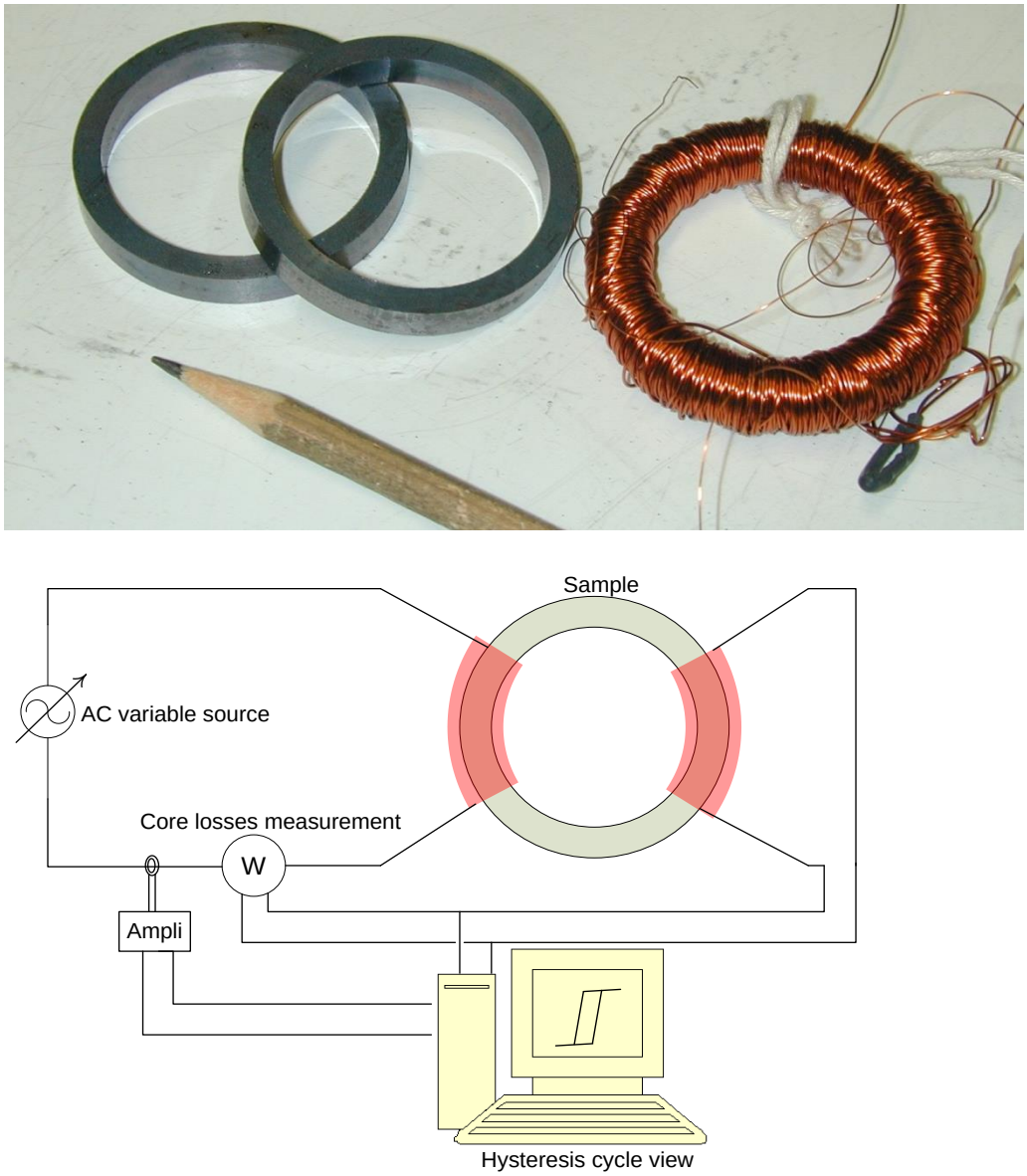

Figure 39: Top: Example of rings pressed and sintered, before and after the winding operation, Bottom: Set up used to measure the magnetic properties of the fabricated rings with lamellar powders.

In order to evaluate the influence of different process parameters on the magnetic properties of the composites, the following parameters were varied:

a) Composition/ribbon thickness: Pure Iron/75μm, Fe-3%Si/125μm, Fe-48%Ni/50μm, and Fe-48%Co-2%V/50μm.

b) Shaping process:

   i. Cold pressing at 700 MPa (50 tsi)

   ii. Double Pressing-Double Sintering (DPDS), with a first step of cold compaction at 700 MPa, followed by a delub / stress relief thermal treatment with two plateaux, one at 700°C for 30 min and another at 900°C for 30 minutes, while under hydrogen. The second cold compaction step was at a pressure of 700 MPa.

   iii. Hot Forging (HF), with a first cold pressing operation at 700 MPa, followed by, optionally a de-lubing/curing treatment in air at 525°C for 15 minutes and/or two plateaux, one at 700°C for 30 min and another at 900°C for 30 minutes, again, under hydrogen. After cooling down, the parts were preheated at 1000°C in an argon atmosphere for 4 minutes, followed by hot compaction at a speed of 25 mm/sec and a compacting pressure of 550 MPa.

c) Final sintering treatment: Under pure hydrogen (less than 4 ppm of oxygen), a first de-lubing plateau at 700°C for 15 minutes, was followed by the main plateau at high temperature, ranging between 850 and 1250°C. All the heating and cooling rates were 5°C/min.

d) Additives:

i. BN: Fine Hexagonal structure Boron Nitride Powders, commercial grade PHPP325B, from Saint Gobain Ceramics, D50: 3 µm

ii. Al: Air Atomized pure aluminium powders, grade AM650 -PM, supplied courtesy of AMPAL Inc., a subsidiary of United States Metal Powders Inc, D_{50}= 100 µm

iii. Fe_3P: Ferro-phosphorus Powders, Arc Metals Inc. D50: 12 µm

Chapter 5 RESULTS FOR EACH PART OF THE PROCESS STUDIED

5.1. RIBBON CASTING PROCESS MODELLING AND EXPERIMENTS

This section presents all modelling results first, at steady state and in a transient mode, and after, all the model validation experiments conducted. A discussion of the model's validity is conducted, by comparing the mathematical results obtained, against similar melt dragging experiments done by other researchers, who cast ribbons in the targeted range of thickness, using slightly different set-ups.

5.1.1. Steady State Modelling results

The following Figures show predicted contours of solidification, density, pressure, temperature, turbulent kinetic energy and velocity fields, within the metal delivery vessel, or tundish, for different materials and operating conditions. The figures show only the tip of the tundish in its real position and angle, at the outlet, in contact with the copper wheel. Refer to Figure 19 for a better understanding of the positioning.

Figure 40 compares a high casting speed, where the Fe-3%Si system still has sufficient time to form a solid before exiting the outlet, to the lowest casting speed possible for convergence of the model.

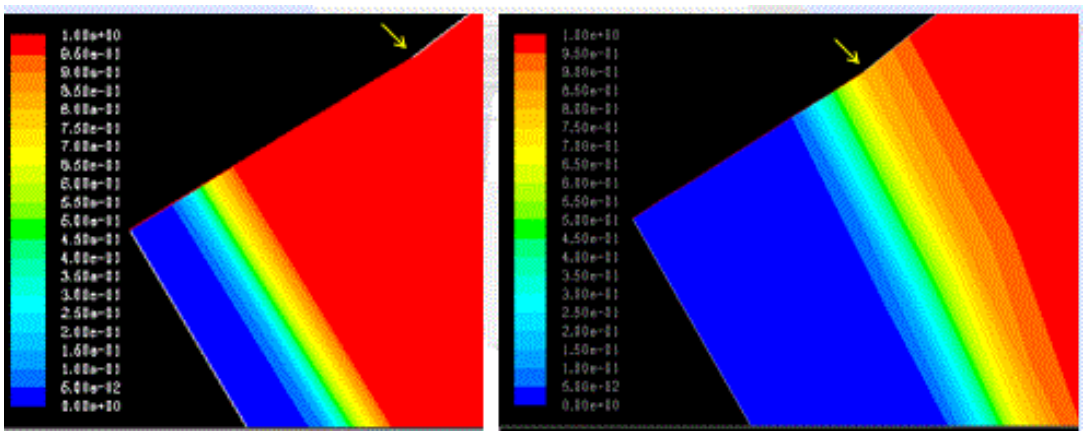

Figure 40: Predicted contours of liquid fraction for Fe-3%Si alloy cast, on the left, at 1.23 m/s, and on the right, at 52.8 cm/sec. The superheat value was set at 50 K. The small arrows point to the gate's top position for a 200μm opening.

At a wheel speed of 1.23 m/s, we can see that the mushy zone is predicted to be very thin, with a liquid fraction of zero on the copper wheel, and for an appreciable portion of the outlet opening. However, it is then 100% (i.e. fully liquid), far before the top, or tip, of the gate. However, at the lowest speed possible (52.8 cm/s), the end of the fully solid zone is very close to the gate's tip, and the mushy zone extends above the gate's tip. This leads to an elevation in pressure at the tip and the consequent recirculation of liquid metal within the tundish.

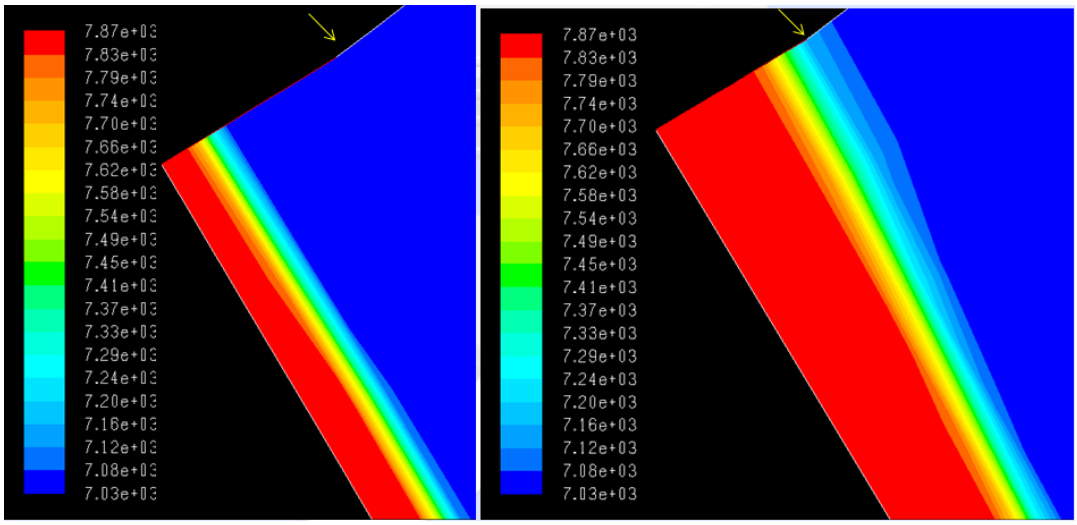

Figure 41: Contours of density for Fe-3%Si alloy cast, on left, at 1.23 m/s, and on right, at 52.8 cm/sec. The superheat value was set to 50 K. The very small arrows show the gate's tip position at 200μm opening.

The contours of density results reported in Figure 41 show essentially the same picture as the liquid fraction results. The limited mushy zone with this alloy should help in easily controlling the system, giving a wide span of permitted speeds and superheat temperatures, and avoiding significant recirculatory flows. It eliminates the risks that recirculation causes a clogging problem, due to the cooling of liquid metal within the tundish. However, it could be difficult to avoid a certain amount of liquid exiting at the outlet on the non- solidified side of the ribbon that could accumulate above the gate, for the same reasons. At 52.8 cm/s, since the model converged at steady state, it proves that recirculation is still not too important and that the quantity of liquid metal exiting at the outlet that could

stay stagnant above the gate could be minimized. The beneficial rubbing effect that was observed with the aluminum AA6061 alloy (see ref 27) could also perhaps be used advantageously with this alloy to produce a uniform, free surface of the ribbon. This would be true, provided the casting speed and superheat temperature can be maintained within very tight values.

Figure 42 shows the velocity field in the outlet region for this alloy of Fe-Si at 1.23 m/s and 52.8 cm/s respectively. This figure is helpful in demonstrating the appearance of the flow recirculation phenomenon, when the mushy zone begins to rub against the gate tip, and limit the convergence of the mathematical model. This phenomenon is at the basis of the clogging problems at the gate, when the casting speed or the superheat values are too low. The model reveals that the minimum operable speed for this casting temperature should be around 50 cm/s in order to avoid too much pressure on the gate tip and internal metal freezing within the tundish.

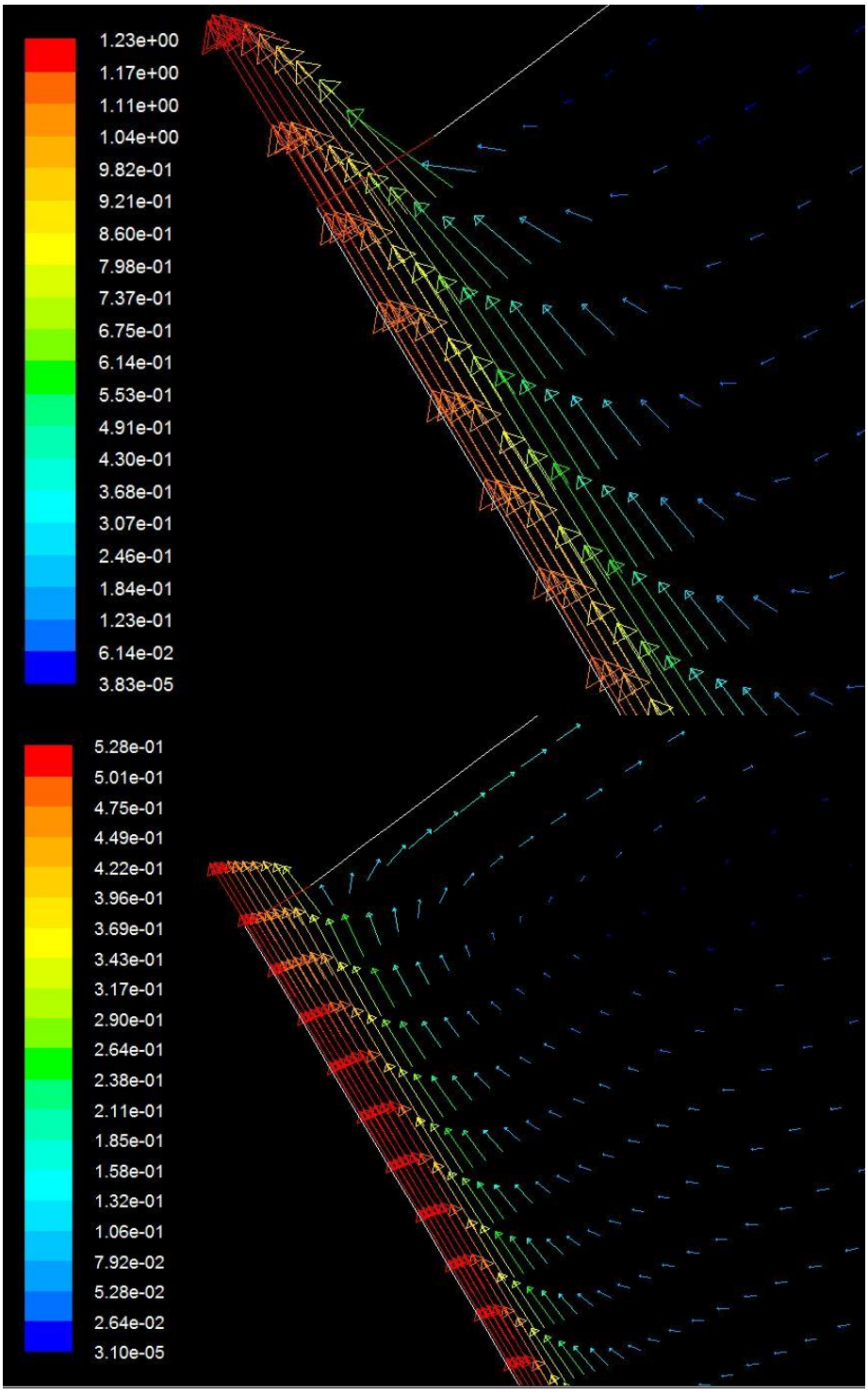

Figure 42: Velocity field for Fe-3%Si alloy cast, top, at 1.23 m/s and, bottom, at 52.8 cm/sec as modeled for a superheat of 50 K.

Figure 43 shows the temperature distribution within the tundish at the two casting speeds studied. We see that the important recirculation observed at 52.8 cm/s causes the temperature of the melt within the tundish to decrease dangerously. Evidently, the temperature must be kept over a certain value to avoid clogging problems. The 80% solidified thickness in this critical condition can be evaluated as 150 μm, according to Figure 40 or Figure 41 (right). This is the optimal condition to maintain good control on the free surface finish, which begins to be rubbed in its mushy state.

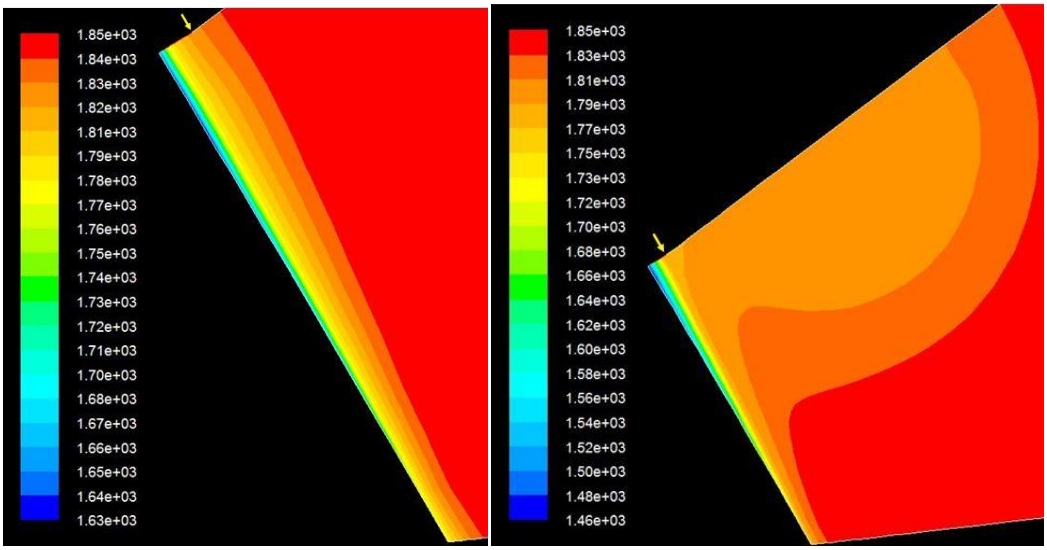

Figure 43: Contours of temperature for the Fe-3%Si alloy, close to the contact zone in the tundish for a casting speed of 1.23 m/s on the left and 52.8 cm/s on right, for a superheat of 50 K.

This condition minimises the amount of liquid metal that can leave the outlet, but it will accumulate above the gate owing to the gravitational forces. It also limits the cooling of the interior of the tundish due to

recirculation, which would eventually cause clogging problems at lower speeds. This condition is reputedly a stable condition, according to the model developed, since the calculation was operated under steady state conditions (not a transient modelling exercise). Convergence reveals that it is a stable condition.

Figure 44 shows the turbulent kinetic energy dissipated at different locations for the two different casting speeds. It can be seen that the maximum kinetic energy of turbulence occurs at the beginning of the contact zone, where the dragging effect starts in a very low speed liquid zone (at the bottom of the figure).

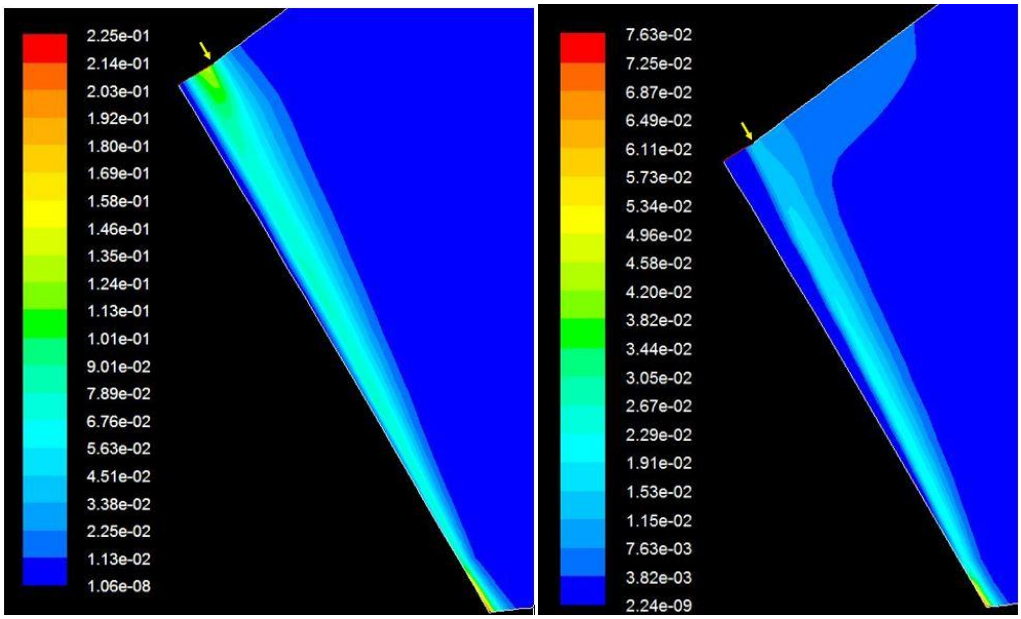

Figure 44: Predicted contours of Turbulent Kinetic Energy for the Fe-3%Si alloy in the tundish close to the contact zone for 1.23 m/s (left) and 52.8 cm/s (right) at 50 K of superheat.

This results in the highest gradient of velocity within the liquid in the tundish. A moderate amount of turbulence is also formed at the outlet, when the ejected liquid volume is squeezed between the solidified layer in contact with the wheel and the fixed tip of the gate. Again, a high gradient of velocity should be present there. At the lower speed, due to the thicker solidified ribbon, the turbulent kinetic energy distribution at the outlet is different. The recirculation zone also shows a small amount of turbulent kinetic energy dissipation.

For comparison, the following figures report on the conditions using the AA6111 alloy, which has an important mushy zone. It can be seen that even at a high casting speed (84 cm/s), when the metal in direct contact with the wheel at the outlet is still more than 25% liquid, over 20% of the metal in the mushy zone in contact with the gate tip is already solidified. The presence of solid nuclei already goes far behind the gate tip. This picture worsens at the lowest possible speed, for which convergence of the model could be obtained (46.5 cm/s). In fact, the fully solidified thickness is predicted to be only about 40 μm and the gate tip rubs against a mushy zone containing more than 70% solid. This would create a lot of recirculation and a very high pressure on the gate tip. The phenomenon predicted would prevent casting at any lower speeds, owing to the risk of

clogging. The gate tip at that speed will certainly help to produce an improved free surface finish of the ribbon, as a result of the rubbing /scraping effect.

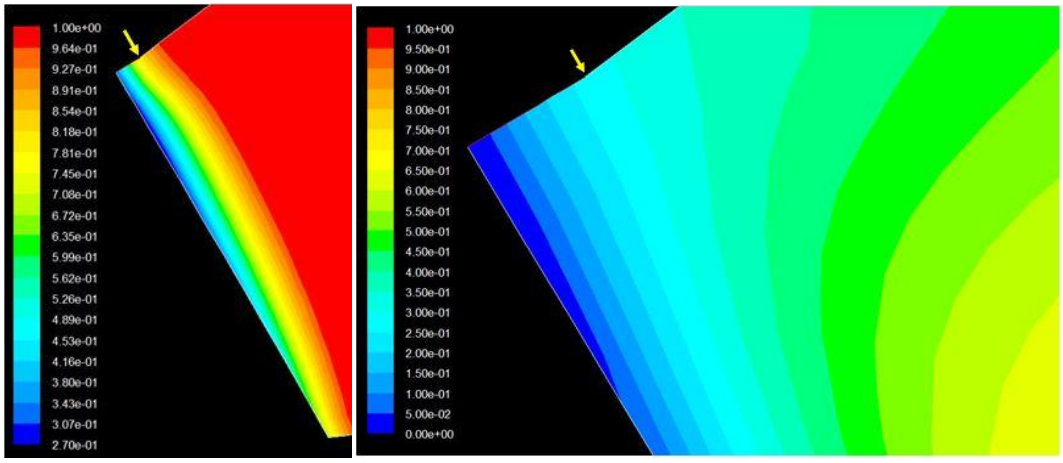

Figure 45: Contours of liquid fraction for the modeling of AA6111 casting at 85.1 cm/s (left) and 46.5 cm/s (right), with 50 K of superheat.

Figure 46 shows the important amount of recirculation of aluminum in the tundish at that low speed. The window of casting speeds and superheat temperatures for the aluminum alloy is thus very small, and the ribbons produced are close to being entirely in their mushy state at the outlet, for all the cases studied. It is then very difficult to obtain stable casting conditions while producing planar surface finishes with this alloy on both surface. Similarly, final solidification and shrinkage pipes defects may develop at both surfaces, since the alloy solidifies in free space after exiting the tundish. Of course, the pressure exerted at the gate tip is high with this high amount of solidified material flowing toward the outlet, hitting the tip and

having to recycle. Figure 47 shows this high pressure point appearing at the tip of the gate and the low pressure zone at the beginning of the contact zone, due to the dragging effect and metal entrainment. The low pressure zone (~ -127 Pa) will have to be addressed eventually, in order to avoid entrapped air between the wheel and the metal decreasing the thermal transfer and causing a poor surface finish. One approach might be to move the tundish away from the wheel, so as to produce a meniscus at the beginning of the contact zone. The other way could be to play with a gas jet under the tundish, so as to decrease the external pressure by a venturi effect (Bernouilli). The relative vacuum in the tundish is in fact very poor and can easily be counterbalanced, with a slight depressurisation of approximately 127 Pa, 0.019 psi, 0.0013 BAR or 0.13% atm.

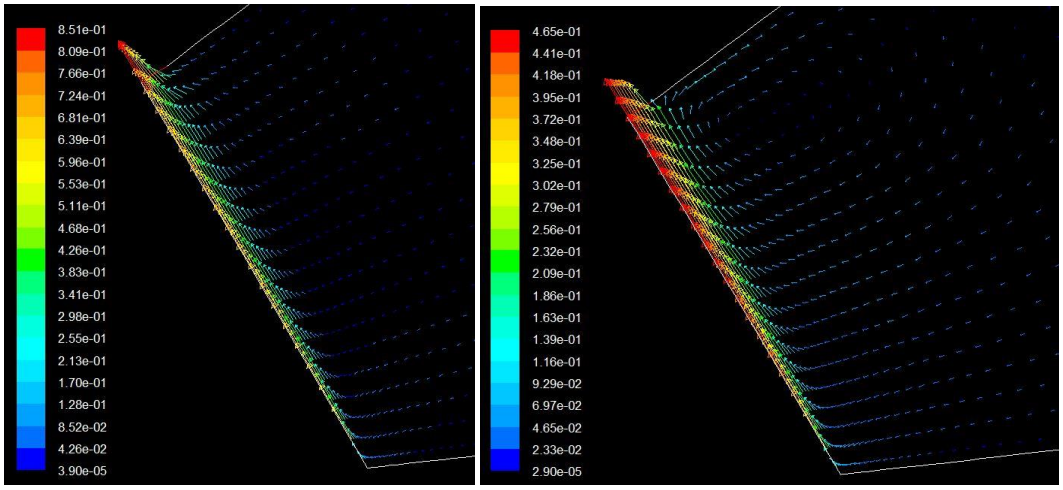

Figure 46: Vectors of velocity field in the modeled domain at the outlet region for the Al6111 at 85.1 cm/s (left) and 46.5 cm/s (right), with 50 K of superheat.

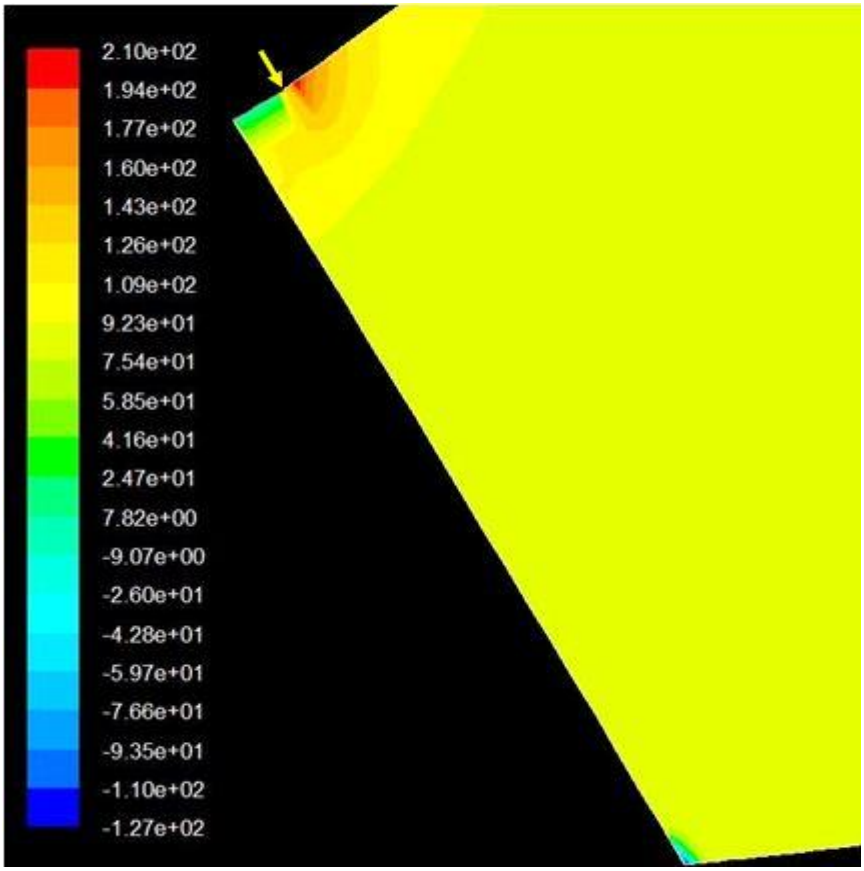

Figure 47: Contours of static pressure at the contact zone for the modeling of the AA6111 alloy, cast at the lowest possible speed for convergence (46.5 cm/s), with 50 K of superheat.

The last material modeled for ease of model validation with experimentation was tin, which has a very low melting point, a low tendency to oxidize, and a very small mushy zone (pure metal).

Figure 48, Figure 49 and Figure 50, show the contours of solidification, temperature and the velocity vectors for the most extreme conditions modeled with Tin, i.e. when close to no solid is present at the outlet and when there is a thick solidified layer that is close to hitting the gate tip, generating important flow recirculations within the tundish. It can be seen

from the Figure 49, as was visible with the other alloys, that when no recirculation occurs, at the higher wheel speed, all the cooled material exits the outlet, while the temperature contours reveal the coolest place in the tundish, is close to the middle of the contact zone. However, when recirculation takes place, the coolest places in the tundish are at its top, against the gate. In Figure 48, we see that the slowest speed producing a converged solution of the model, i.e. 29.7 cm/s, is obtained when the tip of the gate is in contact with metal already solidified at approximately 50% at the outlet. It is difficult to cast at a lower speed without clogging the outlet. Full solid moving at the speed of the wheel is only approximately at a distance of 20% of the gate opening from the gate, or ~43 μm from the gate.

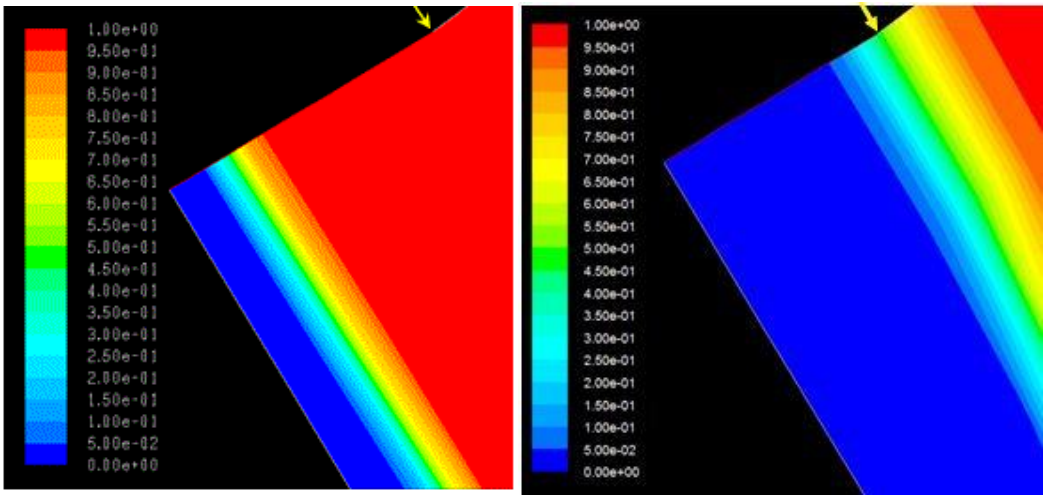

Figure 48: Contours of liquid fraction for the modeling of pure tin cast at 1 m/s (left) and 29.7 cm/s (right), with 45 K of superheat.

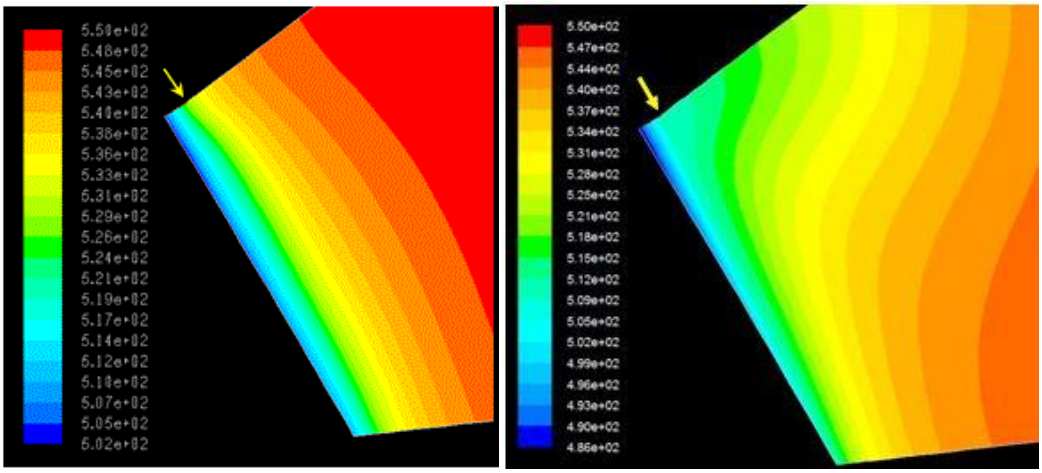

Figure 49: Contours of temperature for pure tin, cast at 1 m/s (left) and 29.7 cm/s (right), with 45 K of superheat.

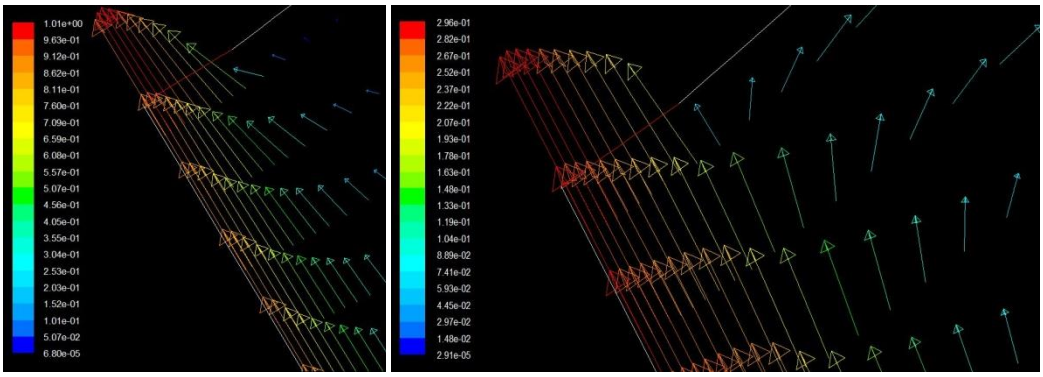

Figure 50: Vectors of the velocity field in the domain modeled for pure tin, cast at 1 m/s (left), and 29.7 cm/s (right), with 45 K superheat.

Overall, it can be seen that the behavior predicted for pure tin is, as expected, very similar to that obtained for iron-3%Si. By contrast, there is an important mushy zone with the aluminium alloy, making the control of the casting conditions to obtain a stable ribbon very difficult, for such a low thickness range.

Figure 51 shows the relation between the thicknesses of the solidified layers formed at the outlet (80% solidified), the casting speed, and the superheat, for the different metals modeled.

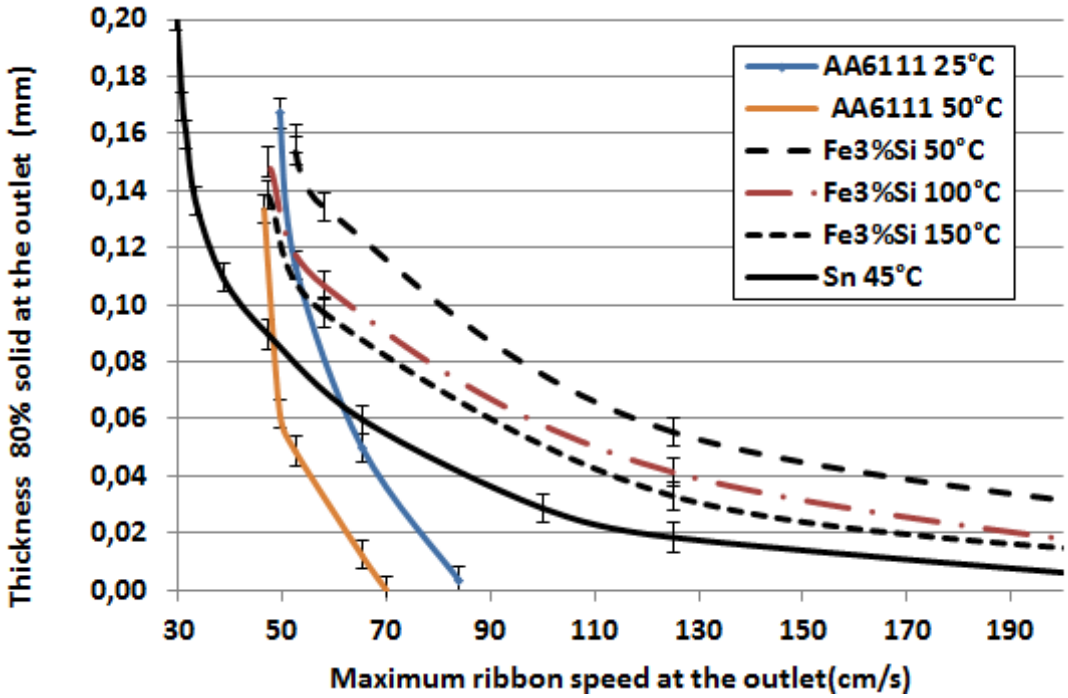

Figure 51: Solidified thicknesses predicted at the outlet of the domain, modeled as a function of the casting speed, for the different metals studied, and for different values of superheat.

These thickness values were measured manually, graphically on the image processed by the software and the error bars are thus related to the uncertainty of the graphical measure. The color scale dictates the locations where 80% of the ribbon is solidified at the outlet. It can be seen that an increase in the superheat value can be used to decrease the casting speed, while obtaining the same solidified thickness or the same amount of solid fraction at the outlet. Lower casting wheel speeds with higher superheat values give higher temperature gradients within the tundish, higher heat fluxes, and thus slimmer mushy zones.

All these mathematical predictions in the graph of the Figure 51 concern the thickness where 80% of the ejected ribbon is solid and thus it ignores melt “drag out” and wetting effects. These are limited, anyways, by the gate opening. The final thickness is in fact determined by the gate opening, but the free surface finish is tributary of the “drag out” and wetting effects through the rubbing effect of the gate tip. This surface finish will be used, in fact, to determine if the model gives good correlation with reality, since the thickness cannot be used to do any correlation with the speed of the wheel and the superheat value. The temperature of the surface of the ribbon, just at the outlet, is also an indication of the model’s validity. Indeed, from Figure 49, we can see that the model predicts a temperature, at the outlet in contact with the gate tip, of 529 K at a speed of 1 m/s, rather than only 506 K at 29.7 cm/s, with a superheat value of 45 K with pure tin, and a solidification temperature of 505 K.

It must be mentioned that the model predict Reynolds number under 100 in all the cases, so this casting configuration and set up is close to fully laminar. In fact, tests were done with different viscous models, including laminar, K Epsilon Realizable and RNG, K-Omega regular or SSt. In all the cases, the results were the same. The Prandtl number which represents the ratio of viscous diffusion rate on thermal diffusion rate, was also calculated

and is found to be in all the cases under the unit value, telling that the most important equation to be solved in this model is the thermal transfer equation and not the turbulent viscous flow equations.

A few assumptions were also made with the present model, regarding the temperature of the water and the quality of the thermal contact with the copper wheel. The following figure reports the effect of the variation of those parameters around the default selected values. It must be said that regarding the thermal contact resistance, as the figure shows, if the value set in the model is under or equal to $1x10^{-6}$ m^2.K/w, it is like leaving a value of the resistance to zero. In all the literature, the recommended or measured values for planar flow casting or melt dragging experiments are $1x10^{-6}$ m^2.K/w. For mould casting with slow solidification speed under a slow bulk stirring effect or no stirring effect at all, the value varies between 1-5 $x10^{-5}$ m^2.K/w. If we consider a layer of air that could be entrapped between the liquid and the copper wheel, with the air conductivity, a layer of 1 µm will give an equivalent contact resistance of 2.5 $x10^{-5}$ m^2.K/w. A 10 µm layer would give a contact resistance of 2.5 $x10^{-4}$ m^2.K/w. However, typical roughness of the copper wheel around 0.5 µm after the polishing step, thus layer of air superior to 1 µm are very improbable. The analysis of the curves tells that a value of 1 $x10^{-5}$ m^2.K/w represent a decrease of the

speed of the wheel by 30% while a value of 1 x10^{-4} m^2.K/w represent a decrease of the speed by a factor 3. Such an important variation can be compensated by an increase of the contact length (opening of the gate) to obtain the same solidified thickness at the same wheel speed. Regarding water temperature, we see that the variation of the water temperature of the wheel from 25 to 95°C (if we consider using the vapour formed at the exit of the wheel to recycle the heat of solidification and cooling) will induce a variation of speed of the wheel by 20%.

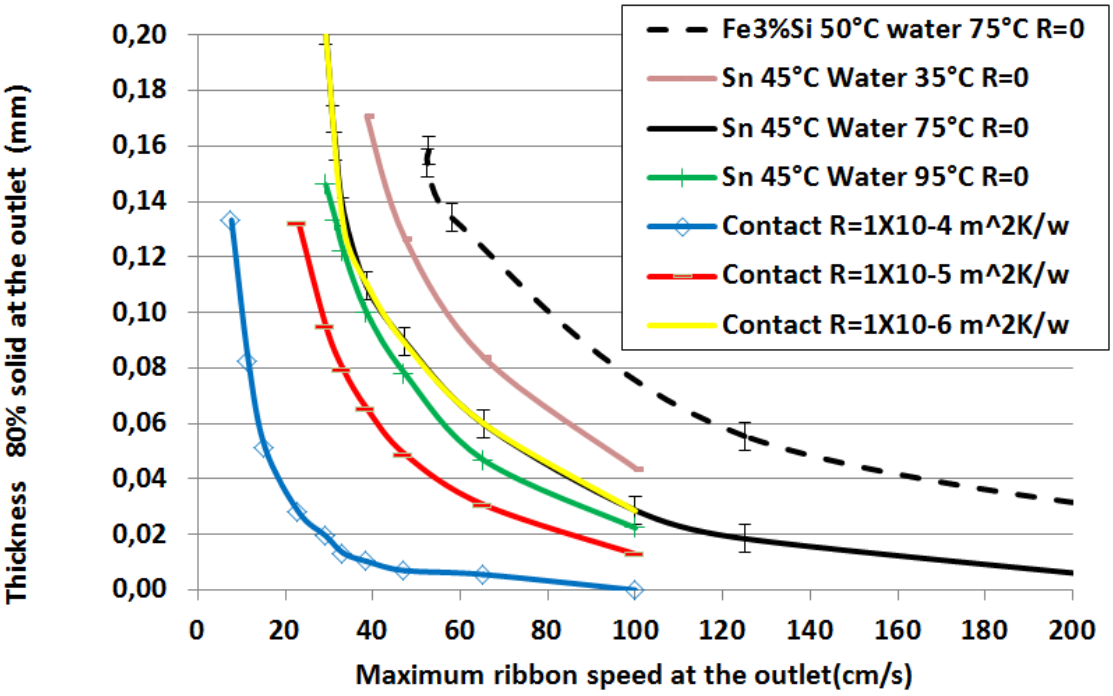

Figure 52: Solidified thicknesses predicted at the outlet of the domain, modeled as a function of the casting speed, for Fe-3%Si and Tin for different values of thermal contact resistance and cooling water temperature in the copper wheel.

5.1.2. Transient modelling results

The following set of figures, given in Figure 53 and Figure 54, show the development of the solidified ribbon thickness and the flow vectors at different time intervals varying between 0.001 s and 0.1 s. Time zero is taken to be when the energy equation is introduced into the model calculation, following the initial isothermal, steady liquid flow, condition.

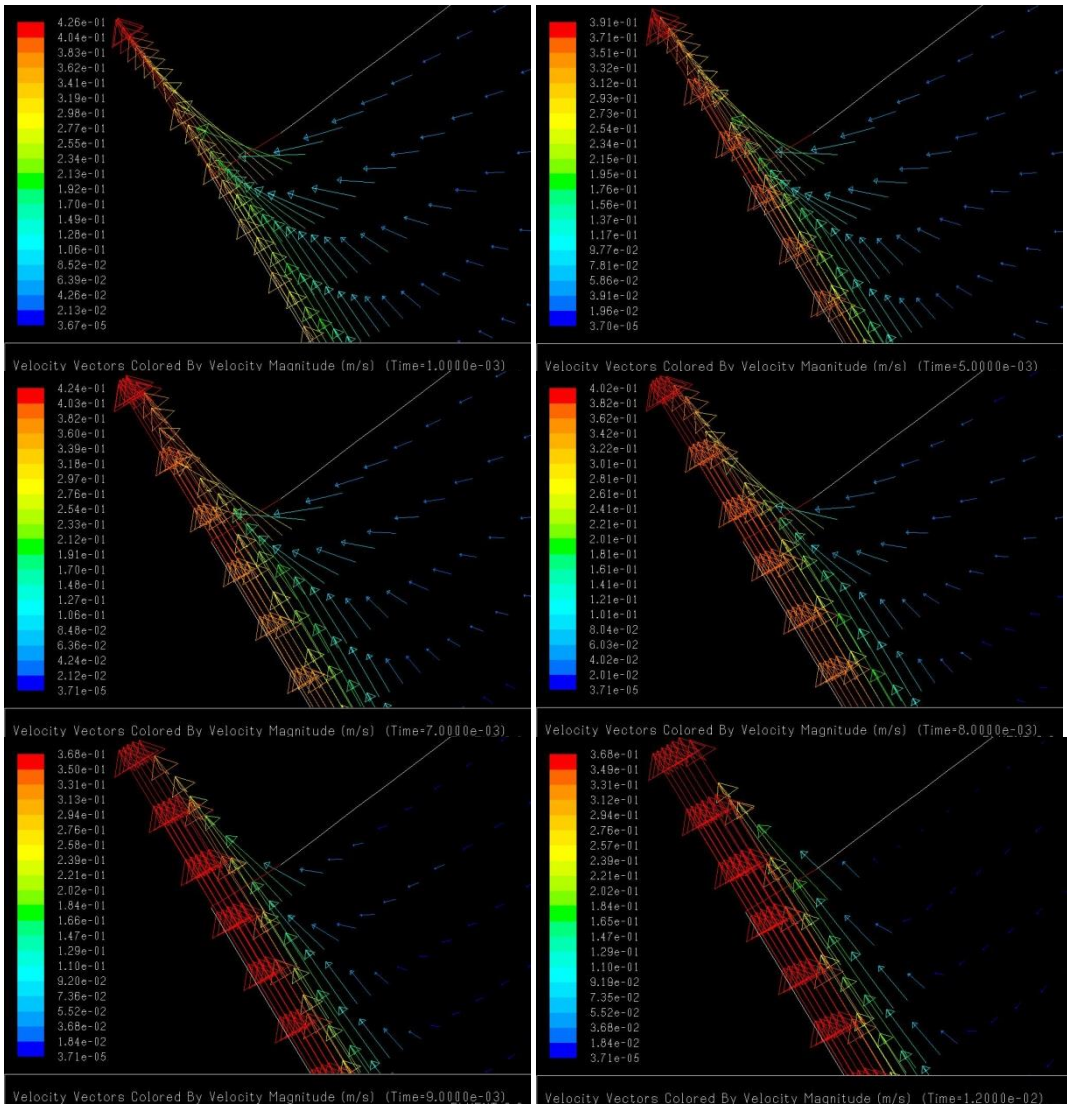

(Continued next page)

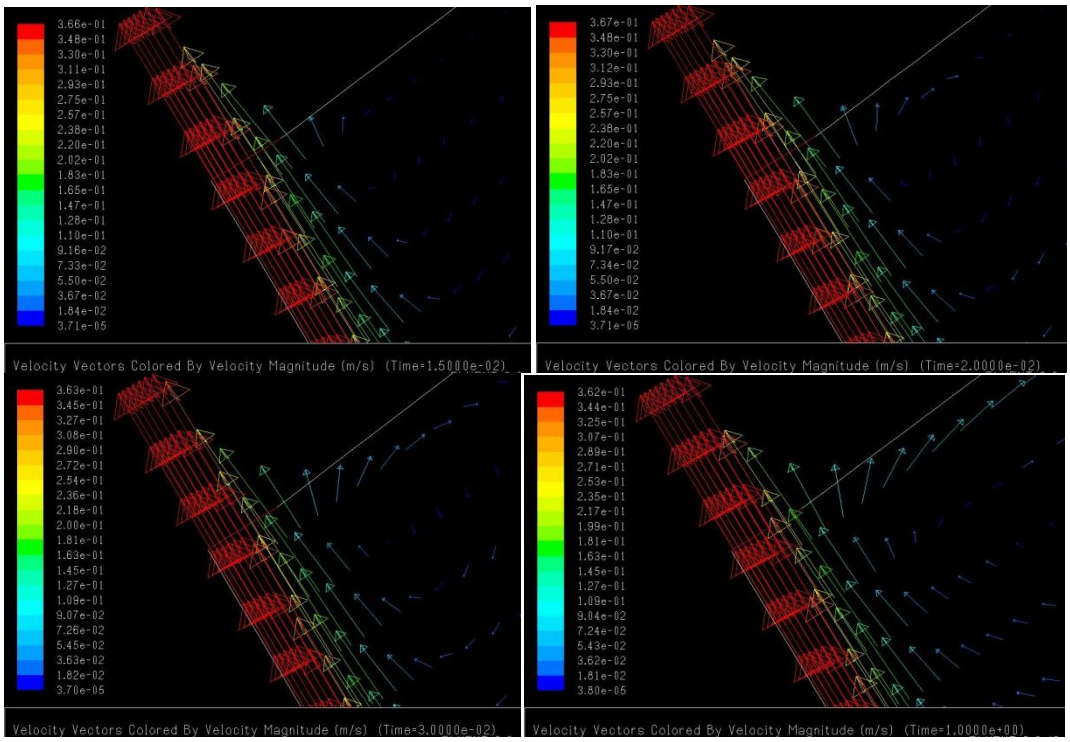

Figure 53: Modelling of velocity vectors for Sn, following the introduction of the energy equation into the solution. Time zero is thus an isotherm, in the fully liquid condition.

From this first set of figures, from left to right and top to bottom, the first six figures shows the flow of metal from zero to twelve milliseconds. We only observe the effect of the development of a solidified layer, which produces an increase of the thickness where the vectors are of the same length (uniform speed thickness, the same as the cold copper wheel surface). However, from the seventh figure on to the last one, as the solidifying thickness is approaching the size of the gate opening, we see the appearance of a recirculation pattern beginning to form slowly, just

above the gate tip. Indeed, vectors start to point in the opposite direction of the gate opening.

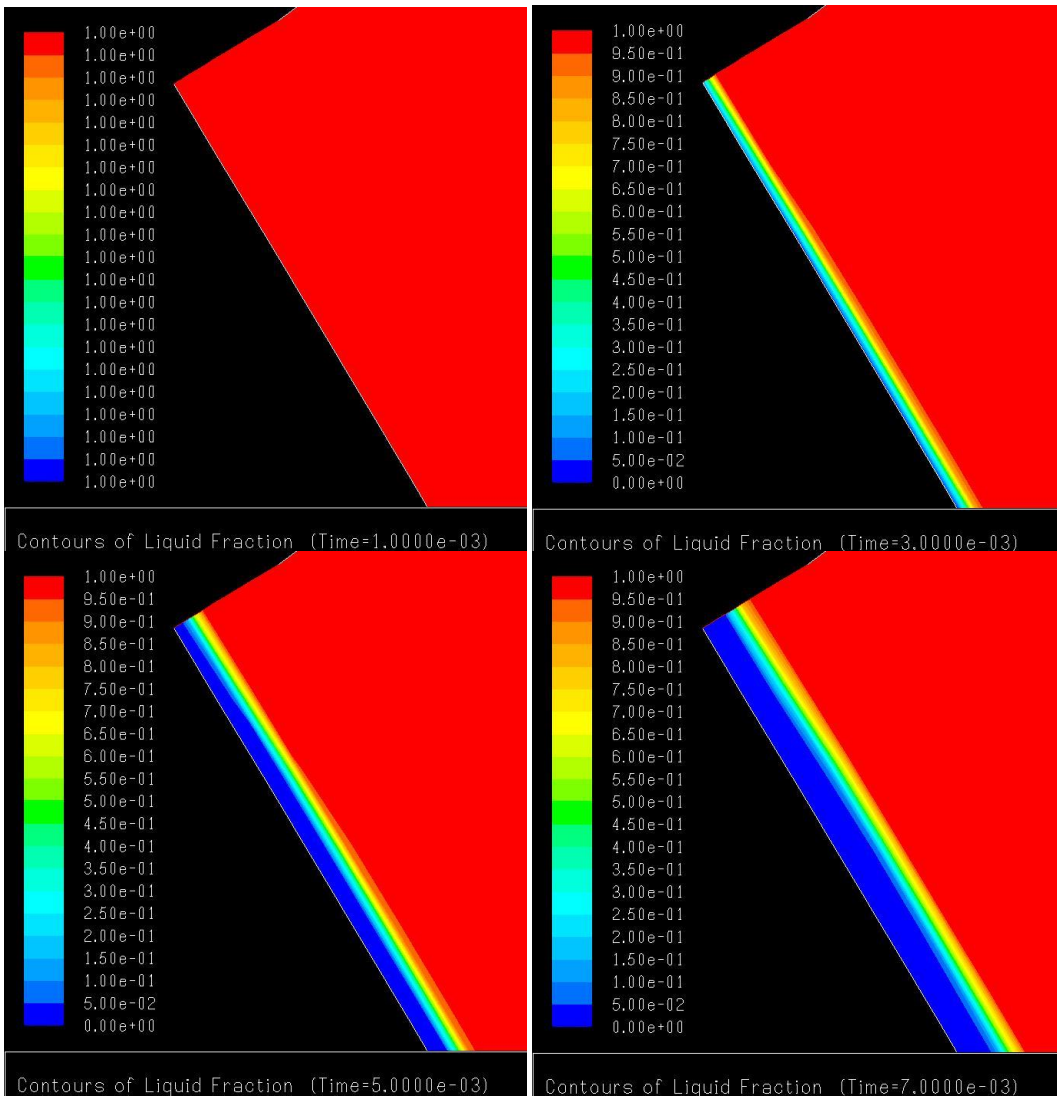

(continued next page)

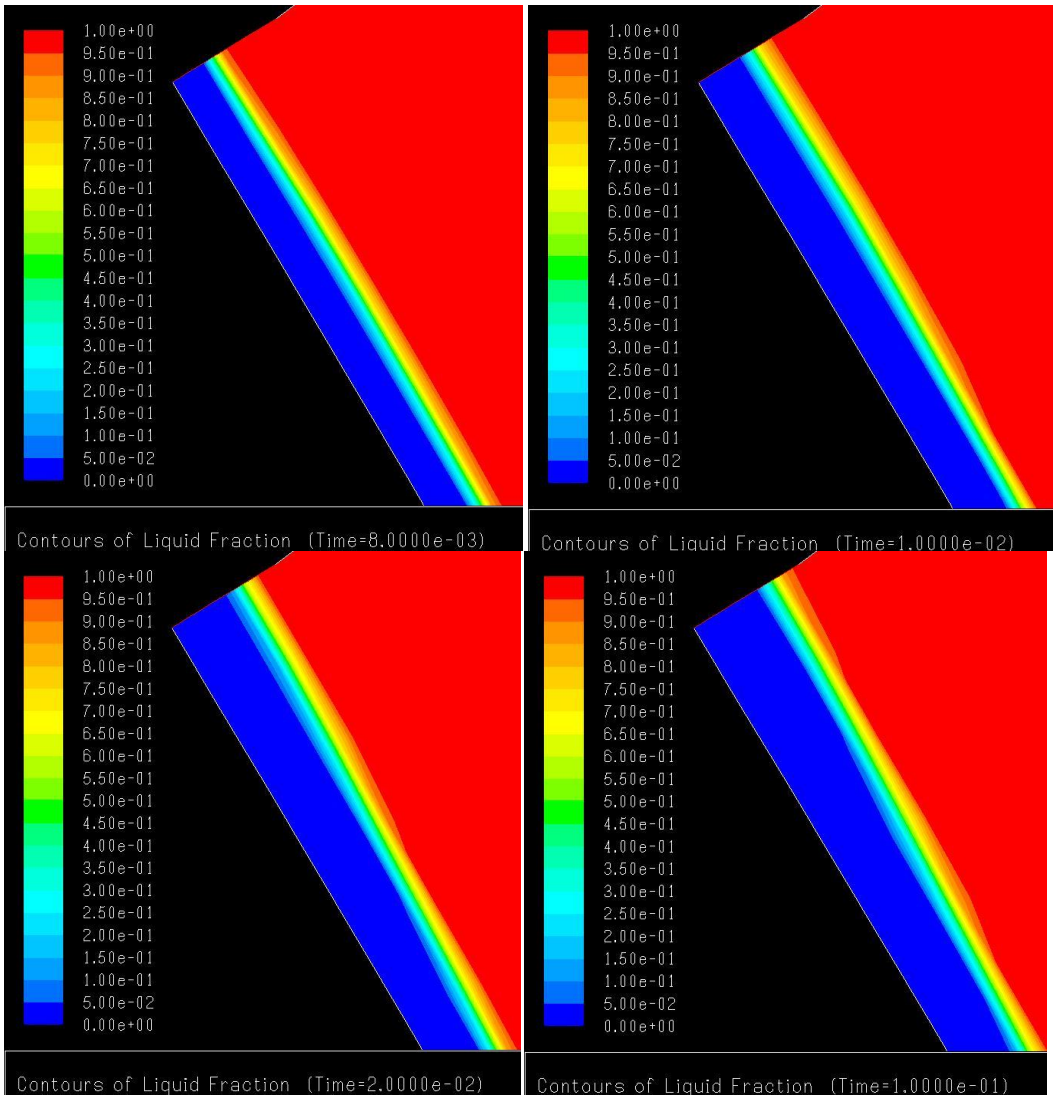

Figure 54: Development of the solidified ribbon thickness for Sn, illustrated by the contours of the liquid fraction at different time intervals, varying between 0.001 s and 0.1 s. following the incorporation of the energy equation into the model. Time zero is taken as an isotherm in the fully liquid condition with 45 K of superheat (45 K above the liquidus temperature).

We see that for pure tin, steady state casting (i.e. a cast ribbon, 80% solidified, to a thickness of 0.13 mm) is reached after only 0.02 s, following

the extraction of heat into the copper wheel, at a speed of 36 cm/s. Approximately 10% of the equilibrium solidified thickness (10% of 0.13 mm, i.e. 0.01 mm) is reached after only 0.001 s, or 1 millisecond. The thickness of the solidified layer increases at a decreasing rate, starting out in the order of 0.01 mm for every micro-second (0.001 seconds).

5.1.3. Casting experiments conducted at the MMPC, and data from the literature for similar experiments.

Three compositions were tried. Unfortunately, heat losses, with the set up developed originally, were too high for casting Fe-3%Si properly. In fact, the melt had time to freeze in the tundish owing to preheating it to an insufficient temperature. This preheating was originally produced by only one electric element introduced in the tundish cavity before every casting experiment. This element had to be retracted before the casting could start, and its temperature was limited to only 1700°C. Significant heat losses from the top and the sides of the tundish caused the walls temperature to decrease too rapidly during the first few seconds needed to retract the element and place the tundish for the casting operation. Future developments will include the incorporation of more preheating elements into the tundish walls . These will stay in place and provide heat throughout

a casting experiment. Similarly, thicker and more highly insulating refractory walls will also be developed all around the tundish. These modifications will not be done during this PhD study, which was limited in time, due to the closure of the MMPC foundry, February 13th, 2012. Nonetheless, for iron based alloys, a Korean team [23,24] has done ground-breaking work with Fe-Ni and Fe-Ni-Si alloys and have proved the feasibility of casting 200 μm thick ribbons at speeds ranging between 1.3 and 2 m/s. The contact length was however significantly longer (3 cm), and used no top confinement or gate to limit the exiting strip. This was limited only by the depth of the liquid bath. The longer contact length required higher casting speeds to produce a similar thickness to the present work. Those results are reported in Table 5, for the purpose of comparison.

Experiments with aluminum alloy AA6111 were carried out with limited success, as Figure 55 illustrates. With this alloy, in fact, many clogging problems occurred at the gate. Many hypotheses were put forward to try to explain the clogging problems. First of all, it must be said that with aluminum alloys, and without any inert gas supply around the inlet, outlet, and above the tundish, a strong and coherent oxide skin tends to form at the contact zone and at the outlet. This could easily clog the very narrow gate opening (200μm, either partially, or totally. Additionally, these

experiments with aluminum occurred early in the PhD, before any mathematical modeling experiments had been carried out. The speed of the wheel was fixed at 2.5 m/s, which appeared to be too rapid, according to subsequent mathematical modeling, as shown in section 5.1.1., Figure 51. Under those circumstances, the model showed that an important portion of aluminum in the outlet was still liquid. That important quantity of liquid aluminum had the tendency to accumulate above the gate. During the experimentation, this accumulation above the gate soon began to freeze on the top of the gate. Some pieces of the oxide scale would occasionally stick to the cast ribbon exiting the gate. All the accumulated metal above the gate eventually froze, clogging the gate, and stopping the cast. To obtain better results, experiments should have been conducted at a lower wheel speed, producing a larger thickness of solidified metal at the outlet. This could improve the results by limiting the possibility for liquid metal to accumulate above the gate. Again, at that time, the preheating was done by only one inserted element in the tundish cavity. This element had to be retracted before the casting experiment could begin, as quickly as possible, without losing too much temperature in the tundish cavity.

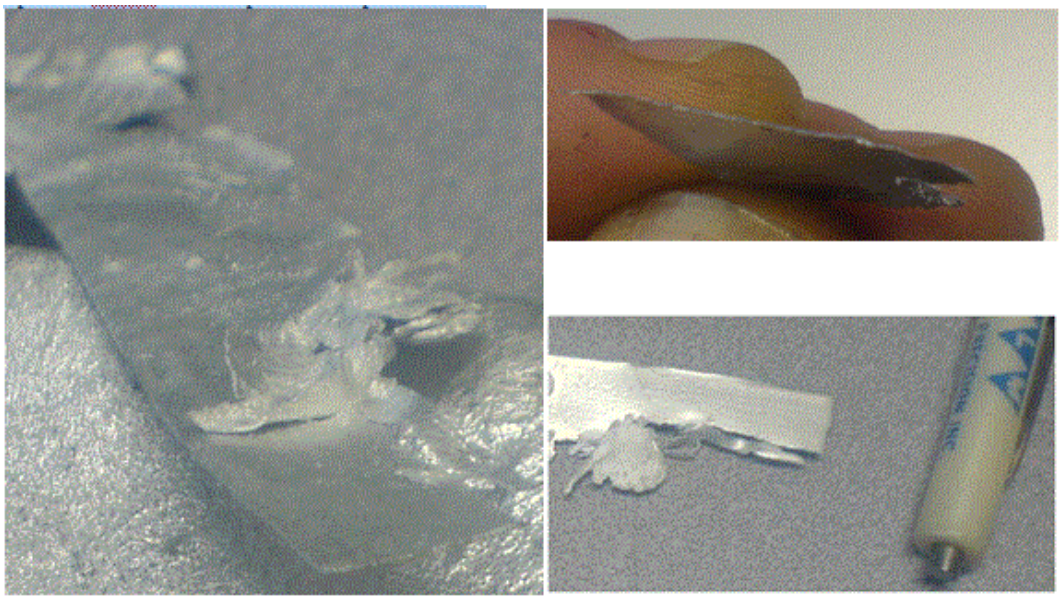

Figure 55: AA6111 alloy casting results showing partial clogging of the gate, 5 mm contact length, 200 µm gate opening, 50 K superheat, 2.5 m/s wheel or casting speed.

In the face of all these difficulties, no additional efforts were put at that time on this alloy, because it appeared preferable to experiment with liquid tin, a metal similar to iron, with respect to thermal properties, surface tension, tendency to form an oxide skin, viscosity and the importance of the mushy zone. It also allows one to run experiments at lower temperatures, providing a good level of security in the laboratory.

In addition, with tin casting with a set point operation of only ~285°C (231°C or 504 K plus the superheat plus the extra 10°C for the time to set the tundish in place after stopping the induction heating), the existing electrical preheating system and the wall insulation were largely sufficient to

run experiments without any risk of metal freezing in the tundish. This was true, despite top opening heat losses, and the fact that the heating element must be retracted from the cavity prior to casting experiments.

Figure 56 and Figure 57 shows ribbons obtained with tin at a speed of 2.5 m/s. The results obviously show that the solidified thickness at the gate position was lower than the outlet opening at this casting speed and superheat value, since no clogging occurred. The ribbon thickness was measured as 350 μm± 100μm (0.015±0.003”). The free surface looks slightly irregular, solidifying only in contact with a gas, with no rubbing or scraping effects. In addition, as for the aluminium alloy, a quantity of liquid tin slowly accumulated above the gate during a casting experiment.

Other experiments were made at lower speed and with a better defined tip, or slot, to try to reach the limits of the model and correlate with it. The original tundish cast ceramic refractory tip was porous and was cracked on its edges, giving longer than 3mm contact length at some points. It was replaced by an iron machined tip that was replaceable.

However, this iron tip appeared to stay at a temperature of only around 150°C with the developed incorporated pre-heaters. Its thermal conductivity was a lot higher than the previous ceramic tip. The following casting experiments were then affected by a clogged tip. Surprisingly, metal still

accumulated above the gate even with a clogged tip. We installed a camera just above the exit of the tundish, in order to see where this metal came from. We realised that leaks come from all around the gate, on its left and right edges, in contact with the porous walls of the tundish. It confirmed that, at least in that case, accumulation above the gate was not due to liquid metal flowing by the tip. The problem came mainly from the refractory walls, which contained many large pores formed during the casting of the refractory (bubbles). A thicker gate could potentially correct this problem by decreasing the probability of having communicating porosities under and above the gate wall.

We decided nevertheless to continue experiments with that tundish and gate, so as not to delay too much the finalization of the PhD.

Figure 56: Tin casting results, (top left; wheel side, top right; free surface side, bottom, side view to appreciate the thickness and planarity). 4 mm contact length, 500 μm gate opening, 45 K superheat, 2.5 m/s wheel speed.

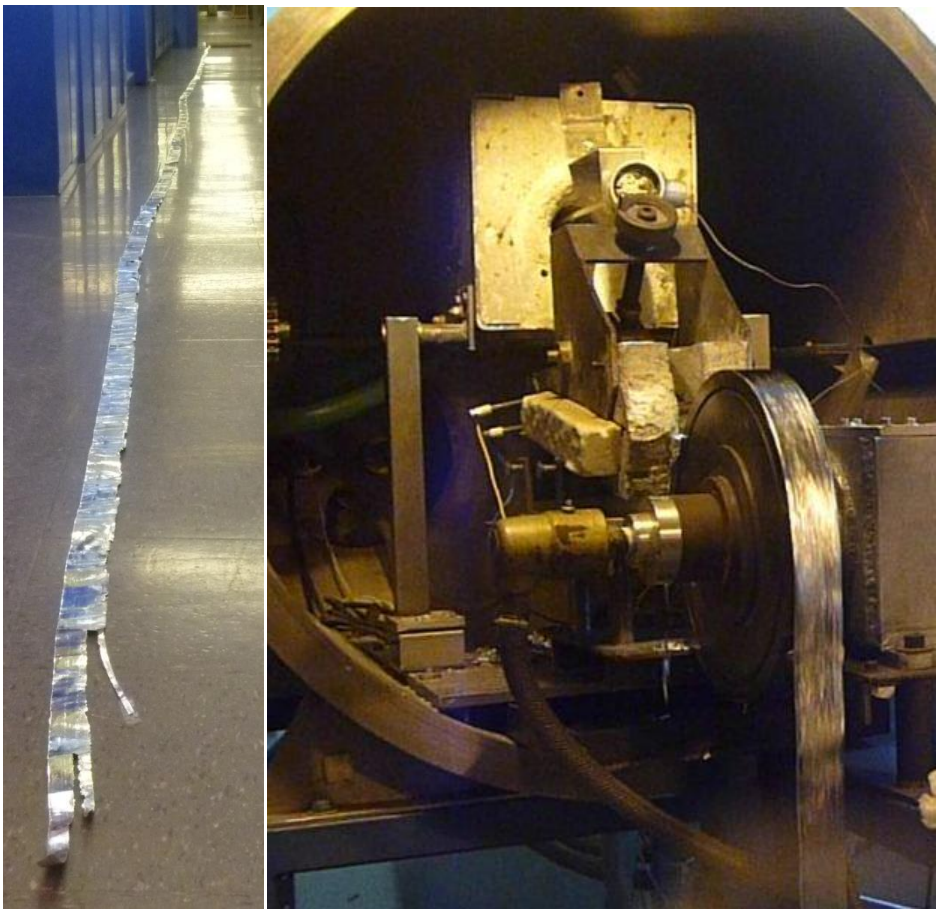

Figure 57: Picture of the 20 meter long steady state ribbon cast, with Sn, 350µm thickness (left), and its casting operation, extracted from the casting movie (right).

The next improvement was then to preheat the iron tip with a torch just before the casting operation, so as to prevent tip clogging, and to see if we could produce a ribbon during the first seconds of the experiment, at the right thickness, without metal accumulation forming above the gate, by passing by the tip slot, before the uncontrolled leaks on each side of the gate started to fill the space above the gate. Indeed, according to the model, the metal should not leak by the tip and accumulate above the gate,

at least if we run at speeds close to the lower limit of convergence of the model.

A casting experiment at 36 cm/s was done and proved that the metal can effectively exit the gate opened at only 240 μm (the value that was set at that particular time) without freezing, and that no accumulation above the gate comes from the tip. The top surface finish of the formed ribbon also started to change, and improve, under the rubbing effect of the gate tip at this low speed. This is thought to be good validatory proof for the model developed since, as we approach the lower limit predicted by the model (29.7 cm/s is the convergence limit according to Figure 48), the upper surface is improved.

However, as forecast, after a few seconds, the camera revealed that the metal started to accumulate on the top, from the edges of the gate, by leaks, and the tip once more clogged up, even with torch preheating. According to a thermocouple reading inserted in the removable metal tip, the tip was only at 160°C when it clogged at the end of the experiment. For the next experiment, in order to decrease the thermal loss between the tip and the closely adjacent cold (running) copper wheel, we covered the tip with a boron nitride paint coating to lower its thermal conductivity (ZYP coating) and we still preheated with a torch just before the casting

operation. We also blocked all the porosities on each side of the gate with a ceramic paste (CERAMABOND 650 from AREMCO). With those improvements, we were able to cast continuously for a much longer time and to slowly decrease the casting speed until we clogged the tip again, according to the model's prediction. The speed was varied from 36 cm/s to 30 cm/s. It produced a good ribbon at 200μm ± 50 μm thickness, without accumulation above the gate. The temperature of the surface of the ribbon at its exit from the tundish was impossible to measure with an optical pyrometer owing to the high reflectivity of the solidifying tin surface. This last experiment proved that the model is right, within an acceptable precision.

The laboratory closure by McGill's EHS prevented us from continuing our experiments and to measure the temperature of the ribbon at the exit. We can reasonably conclude that the minimum speed was determined (~ 30 cm/s), and that this matches the prediction of the mathematical model (29.7 cm/s). As explained earlier, the modelling calculation was done with the assumption of perfect thermal contact, which is the same behaviour as a contact resistance equal or above $1X\ 10^{-6}\ m^2K/w$ and with a water temperature inside the wheel at 75°C and we rather measured a water temperature around 25 °C after the end of the casting experiment. It is

thought that the cooler water giving a thicker solidified thickness in reality or a higher minimum speed by about 10 cm/s could have been somewhat compensated by a slightly higher contact resistance than 1 $X10^{-6}$ m^2/w.

Table 5 finally summarizes the measured parameters of the experiments conducted, and of similar experiments reported in the literature. From this Table, we see that there are different ways to achieve the targeted thickness of ribbons. However, by using a gate to limit the contact length, it is possible to achieve the same ribbon thickness at a lower casting, or melt drag speed, than in any other experiments presented in the literature. The new concept presented here offers many advantages over other set ups reported in the literature. It allows for a complete emptying of the tundish at the end of a campaign, short metal residence times under a “First In-First Out” configuration, inclusion floatout and a surface protective slag. Similarly, the concept allows for an argon protective layer stability like any tundish bottom pouring configuration, unlike usual melt drag processes. Finally, it allows a precise thickness adjustment through the use of a variable gate nozzle. The drawback appears to be that the gate’s tightness to the surrounding walls must be very good in order to

prevent metal leaking on either side of it. It would appear that a very good tundish wall must be fabricated, in conjunction with a well-designed gate.

Table 5: Quantified results of the different experiments conducted in this work, and from the literature with a similar casting set-up (tilted melt drag).

Ribbon nature	**Super-heat (K)**	**Contact length (mm)**	**Gate width (µm)**	**Wheel speed (m/s)**	**Contact time (ms)**	**Thickness (µm)**
Fe 79 Ni 2Si [24]	75	30	---	1.3	23	200-450
Fe 79 Ni [23]	140	30	---	2	15	200-250
AA6022 [29]	25-100	600	Rubbing effect*	0.33	1818	~ 1500
Tin exp #1	45	4/metal above	500	2.5	3	200-500
Tin exp #2	45	4/metal above	350	2.5	3	350±100
Tin exp #3	45	3	240	0.36	11.1	240±60
Tin exp #4	45	3	200	0.36	11.1	200±50
Tin exp #4	45	3	200	0.33	12.1	200±50
Tin exp #4	45	3	200	0.30	13.3	clog
AA6111	50	5	200	2.5	2	200

* A mass of 0.5 kg was applied on a mobile gate to rub the mushy material 5 cm wide (see ref [29])

5.1.4. Comparison of experiments and modeling results, model validation

The goal of this part of the thesis was to prove, mathematically, and to validate, experimentally, within an acceptable level of precision, that the equipment developed should make it possible to cast a ribbon as thin as 200μm, at industrial casting speeds, typical of ferrous based twin roll casters, or of horizontal single belt casting machines, i.e. under 2.5 m/sec. As explained in the introduction, these targeted low thicknesses are commonly produced with high cooling rate machines like Melt Spinners, running at around 25 m/s.

The model developed is a tilted melt dragger and the mathematical model tells us that it should be possible to achieve the targeted thicknesses, running at under 1 m/s, and even under 50 cm/s. This is a convenient casting speed to be able to manipulate, and wind the ribbons being cast. The model also tells us that with a large difference between liquidus and solidus temperatures, as is the case for the aluminum alloy, an extensive mushy zone forms, making it very difficult to find steady state conditions to cast such thin ribbons, using a rubbing gate to control final strip thickness. In fact, the model diverges as soon as the conditions are a

little away from optimum casting conditions in terms of wheel speed and superheat. For these cases, the zone in direct contact with the cooling wheel is never fully solidified, while there is already a lot of liquid recirculation within the tundish, far from the outlet, causing the melt to cool down uniformly, and increasing the risk of a clogging operation problem.

In such conditions, it seems preferable to use a set up like the one developed by K. Akistsu and al [29], where the gate is not rigidly positioned, but rather controlled by a constant applied force. This rubbing effect is said to improve the surface finish of the ribbon. In this case, depending on the configuration and size of the tundish, and the production rate targeted, the force on the gate can be adjusted to prevent too much recirculation and consequent freezing within the tundish. This set up has no fixed thickness and the final thickness is determined only by the contact length, the wheel or casting speed and the superheat.

In our case, we should adjust our gate to be as close as possible to the solidified thickness at the end of the contact length, so as to avoid liquid flowing with the ribbon at the outlet and accumulating above the gate. This adjustment is difficult and critical, since too tight an adjustment will cause clogging problems, whilst too large a one, could allow metal to accumulate above the gate. This is indeed what was observed with the aluminum alloy

and the two first tin experiments operating at too high a speed. However, a camera installed during the lasts experiments revealed that metal could come exclusively from leaks on each side of the gate due to wall porosities and cracks.

From the fourth experiment with tin, where the speed of the wheel was decreased slowly while trying to measure the temperature on the top surface of the ribbon and the tundish tip, with the last improvement implemented to the set up, it is possible to see that a good correlation is obtained with the mathematical model, given the limited control and precision of the superheat temperature, the wheel speed, and the uncertainty regarding the thermal exchange efficiency.

5.2. SOL-GEL COATING TRANSFORMATION STUDY RESULTS AND ANALYSIS

The transformation of the organic-ceramic coating containing a plasticiser and the alcoholic-hydroxyl radical adjacent to the aluminium atom must be done in a proper manner, so as to finish with a pure alumina coating. When the thermal treatments are done in air, this is not a problem.

However, our composite comprises, in large part, iron, which must be protected from oxidation during the thermal treatment. Powder metallurgy sintering and de-lubing treatments are done in a dry hydrogen atmosphere. Exceptionally, for large amount of internal lubricants, to avoid what is called blisters or sooting phenomena, sometimes present in industrial sintering furnaces, the industry will intentionally increase the dew point of the furnace atmosphere by introducing humidity (temperature controlled gas to water bubblers).

This section reports on measurements with a Differential Scanning Calorimetry (DSC)-Thermo-Gravimetry-Analyser (TGA) conducted on the coating under air and under argon. It was not possible to do the DSC-TGA analysis under hydrogen, due to the system's limitations. However, it is possible to appreciate the differences caused by the absence of oxygen in the decomposition atmosphere. It must be noted that in addition to the hydrogen, oxygen and carbon atoms in the plasticiser and the Sol-Gel precursor, there is also the admixed lubricant used in the part to facilitate the shaping of the composite that must be removed.

The Figure 59 shows an equilibrium phase diagram obtained from Fact-Sage thermodynamic calculation software, containing Iron, Aluminium, oxygen, hydrogen and carbon. It is useful to see what will form under

different conditions, and preferably during the transformation of the insulating layer during the different thermal treatments. The goal is to form alumina, to avoid forming aluminium carbide (Al_4C_3) and to avoid oxidising the iron flakes of the composite. Such conditions must be maintained for sufficient time to ensure that the Sol-Gel layer has transformed irreversibly into alumina, during any subsequent thermal treatments.

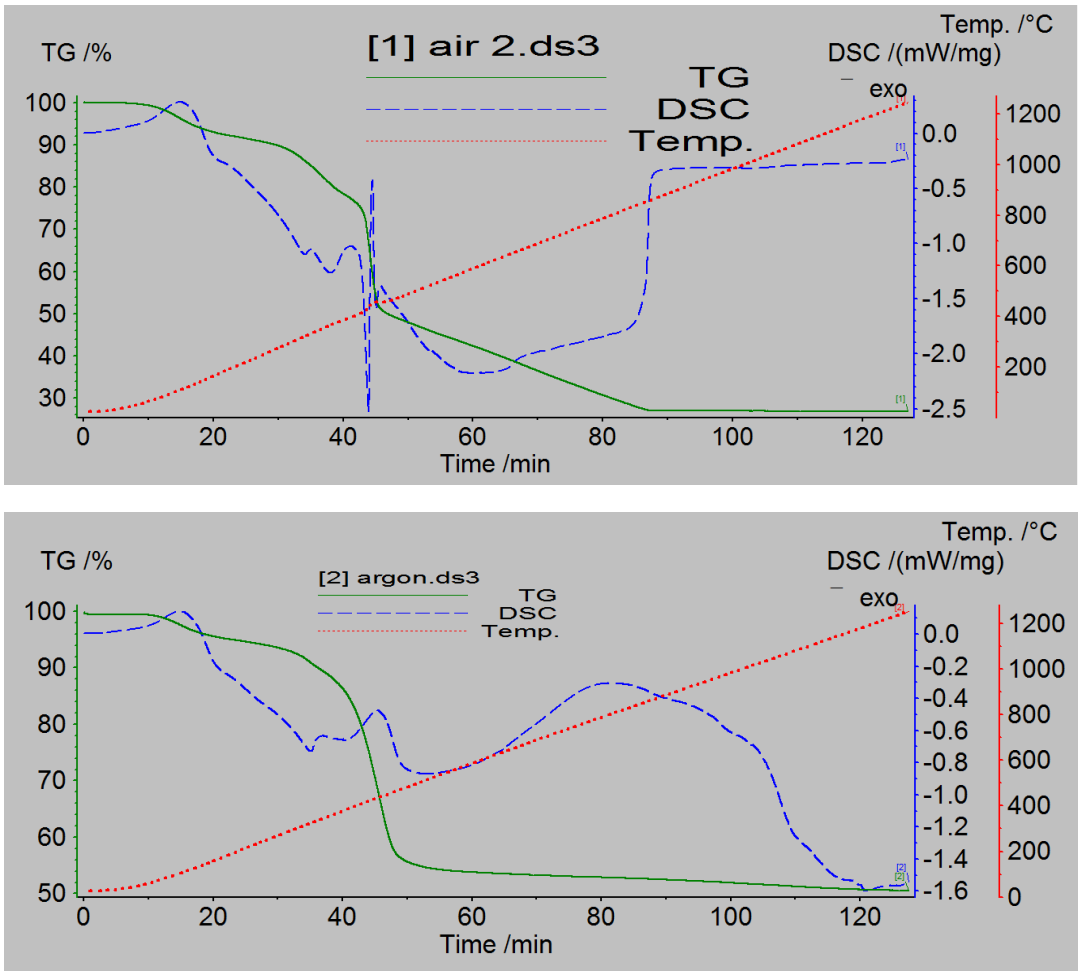

Figure 58: DSC-TGA decomposition curve of the Sol-Gel coating at an heating rate of 10°C/min. Top curve: in Air, Bottom curve: in Argon

It can be seen from the Figure 58 that in air, all the transformation occurs between 400°C where it starts abruptly and 900°C where all reactions have finished and everything has become very stable. Above 400°C, the transformation is so exothermic and rapid that we can even see an explosion with its associated instabilities in all the curves, even the thermocouple measurement curve, occurring at around 450°C. This experiment was repeated three times in the air to understand the peaks and instabilities, and it occurred the three times right at the same time and the same way. The only explanation is an explosion of the coating in air slightly above 400°C.

The curve traced in Argon does not show any explosion. It rather shows a decomposition starting slowly and gradually at a lower temperature, ~350°C, and never really ending before 1200°C. It clearly suggests that under an atmosphere not providing an external source of oxygen, such as dry hydrogen, that the transformation of the Sol-Gel layer is very slow, and may never completely transform into Alumina under 1200°C. That can be really problematic. We can also observe that the total weight loss is significantly lower, 50% of the initial weight rather than 70%. For this higher weight, it is thought that a certain amount of carbon remains in the layer, not being able to catch sufficient oxygen atoms to transform into CO or

CO_2. In those conditions, it is important to determine if the Sol-Gel layer aluminium containing molecules can transform into Al_2O_3, if carbon has not been able to find sufficient oxygen to transform itself into CO and CO_2. It is known and proved thermodynamically, that liquid Al can be produced from alumina, by a combination of high temperatures and high excess of carbon [117]. At temperatures lower than 2100 °C, however, the direct carbothermic reduction of alumina into aluminium is hindered by the formation of the aluminium carbides (Al_4C_3) and aluminium oxy-carbides (Al_2OC and Al_4O_4C).

Thus, it is impossible to completely transform Al into Al_2O_3 as long as free carbon remains in the system. The complex Aluminium hydroxides formed in the Sol-Gel layer will rather transform into aluminium carbide (Al_4C_3) as shown in the Figure 59, unless the level of oxygen in the hydrogen atmosphere is more than 50% and the temperature is above 650°C. At those levels of oxygen, first of all very difficult to obtain, iron will also oxidize. Thus, the only way to correctly form alumina is to first completely eliminate the carbon from the equation by maintaining a good level of oxygen during the de-lubing cycle at the beginning of the sintering thermal treatment. Aluminium carbide will nevertheless be formed partially during this period. The level of oxygen must not be too high to prevent the

oxidation of iron. It was determined, with the help of the Ellingham diagram, that de-lubing, with a dew point of 25°C from room temperature to 750°C at 5°C/min, will prevent the oxidation of Iron. At low temperature (<300°C), oxidation is possible but the kinetics are too slow to cause a problem. At temperatures higher than 300°C, iron oxide is reduced under this gas composition, even in the absence of carbon, so it is safe for the composite.

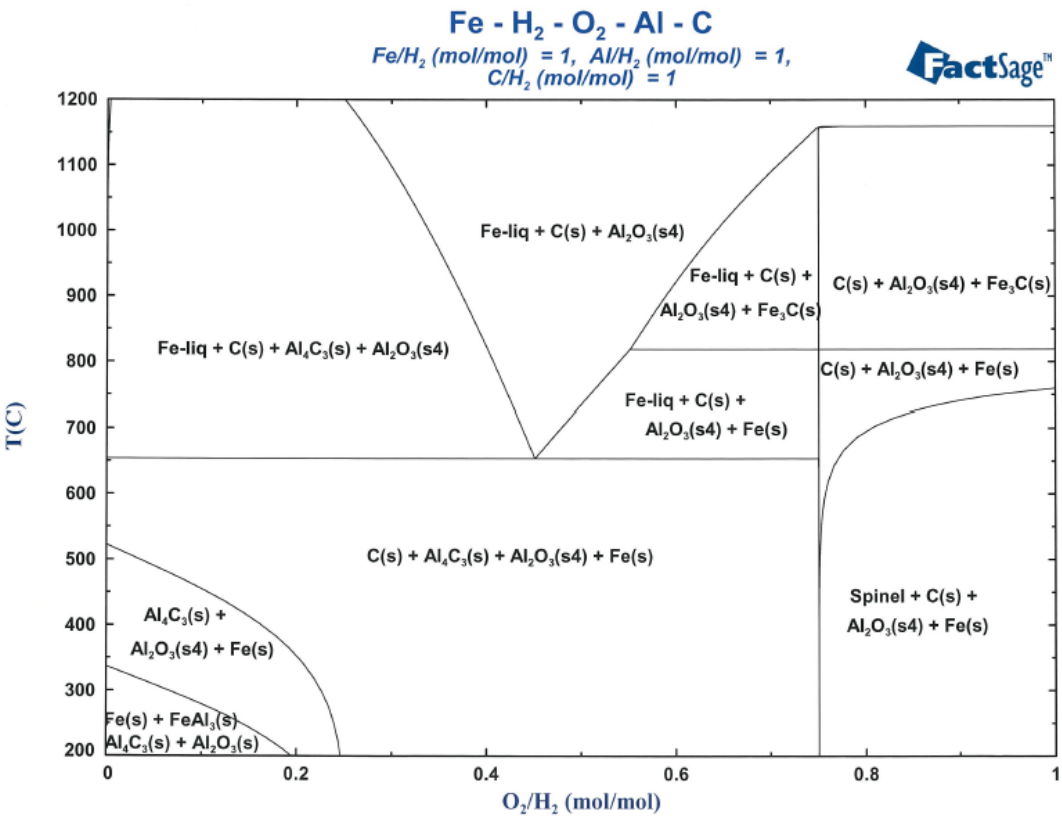

Figure 59: Fact-Sage equilibrium phase diagram containing Iron, Aluminium, Oxygen, Hydrogen and Carbon at normal pressure.

The following figures shows a few Scanning Electron Microscope (SEM) micrographs and associated Energy Dispersive Spectrometer (EDS)

micro-analysis of the coating on a foil or in a composite, transversely cut and polished, showing the interface of two particles with its separating alumina layer.

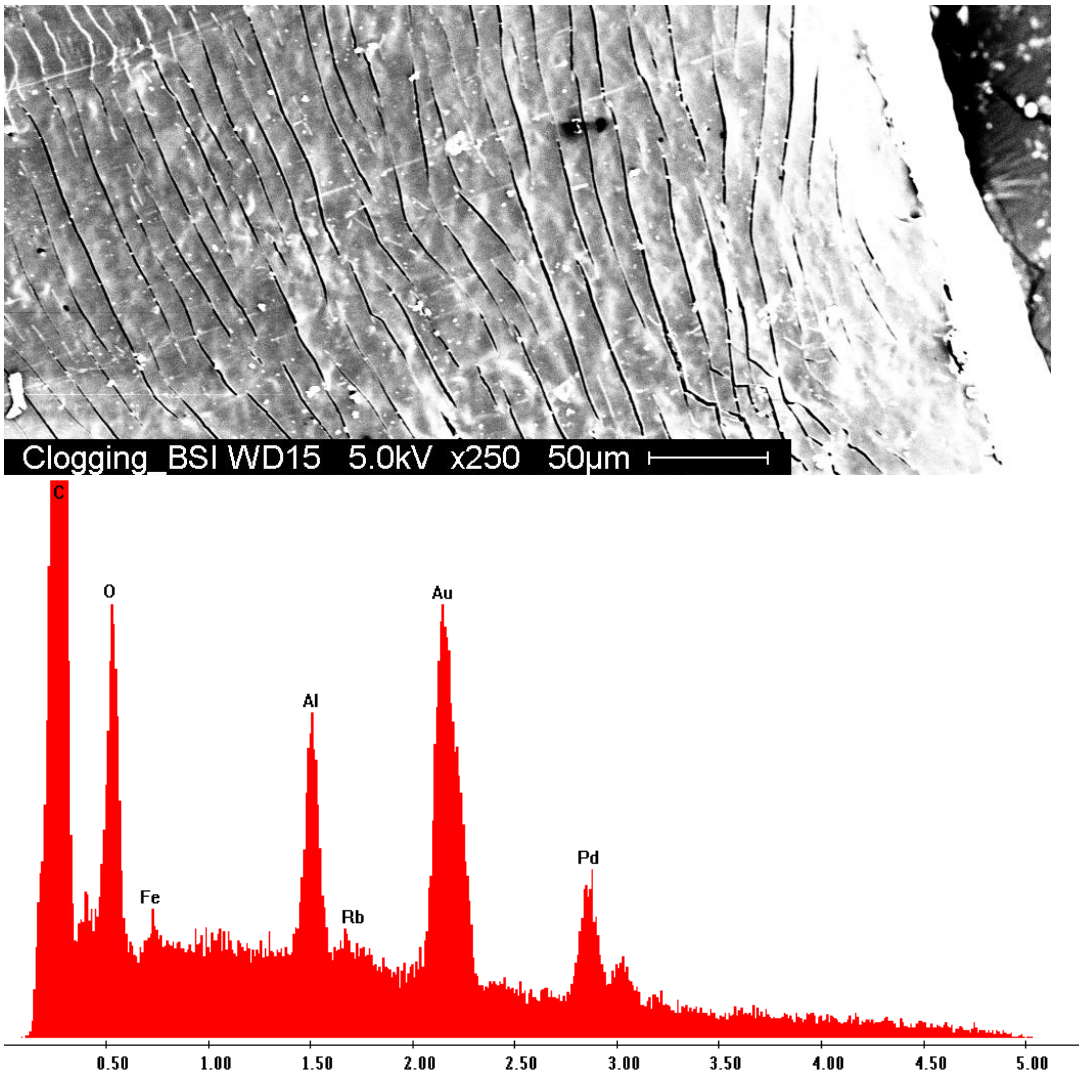

Figure 60: TOP: SEM micrograph of the coating on a foil after its cutting operation, close to its edge, showing cracks formed in the coating, Bottom: EDS analysis of the coating with its layer of Au-Pd PVD deposited to make the insulator more electrically conducting on its surface, for SEM observation (avoid the electron beam charging effect).

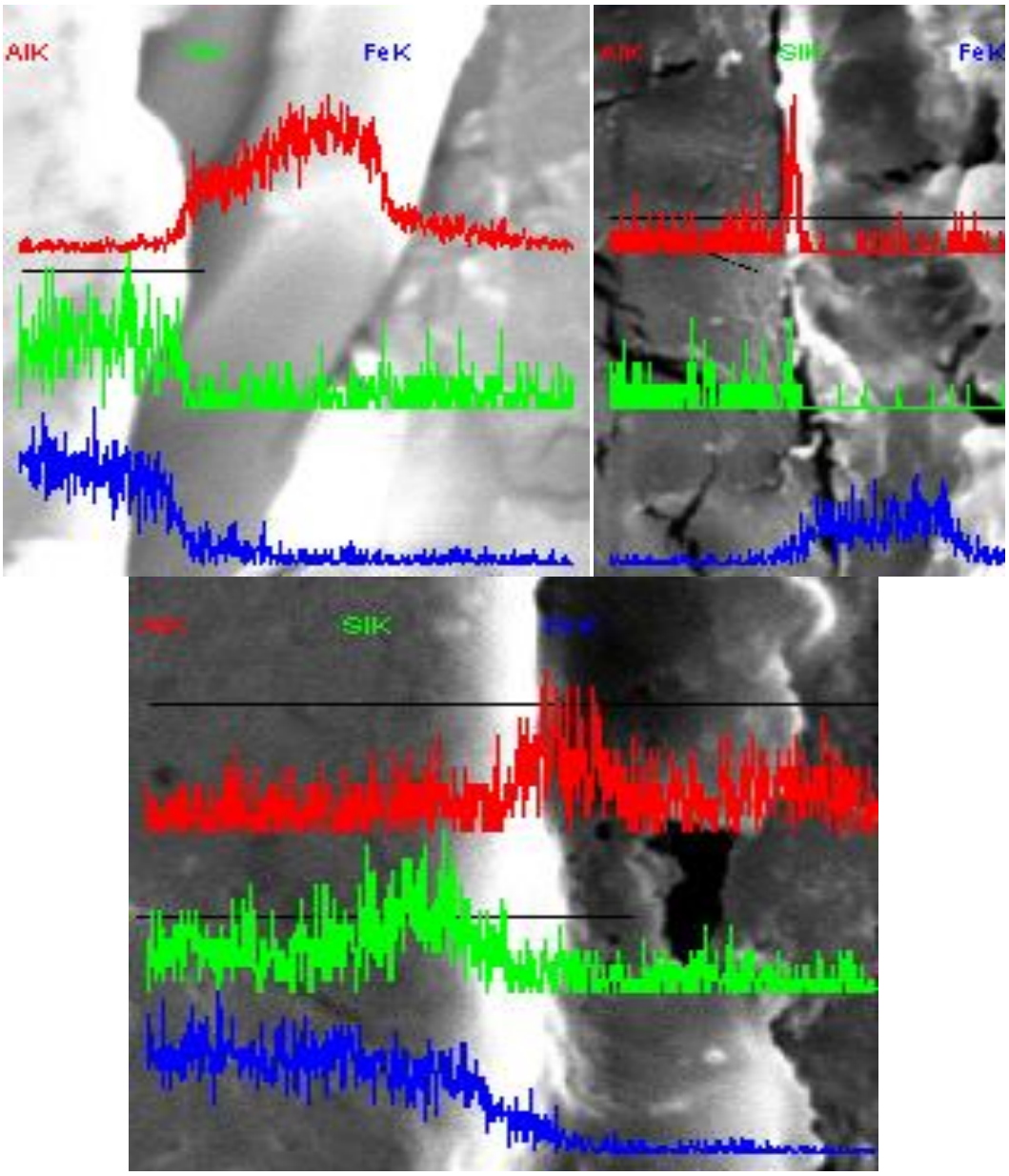

Figure 61: EDS elemental profile analysis on different particles interfaces in a composite part, cut and polished, at different magnifications.

Figure 60 clearly shows the aluminium, oxygen and carbon peaks present in the coating. The iron peak is close to invisible, well covered by the Sol-Gel layer. The cracks in the coating due to the cutting operation must be controlled and kept at an acceptable level (see the experimental

procedure section 4.6.2 and Figure 24 for more information on the Sol-Gel coating crack and peel off measurement). This micrograph shows that only ~ 0.2 mm is affected and the coating stays in place even if it is cracked, making this phenomenon acceptable. The way to keep it at an acceptable level is to introduce a sufficient quantity of plasticiser in the coating recipe, and to keep the coating under a certain thickness (under 3 µm as deposited and dried at maximum 200°C), and cut the ribbons into particles prior to burning the plasticizer and transforming the organic-ceramic coating into a fragile ceramic coating.

Figure 61 shows different EDS elemental profiles at particle interfaces within the composite. The aluminium peak is increasing at the interfaces, revealing the presence of the alumina or aluminium carbide insulator. It can be seen that the Silicon level also tends to increase when the sintering treatment is done at an elevated temperature for a sufficient period of time. It is possible that the silicon of the Fe-3%Si alloy can contribute slightly to the quality of the electrical insulation. There is a slight enrichment of silicon close to the surface of the particles. It can be explained by the transformation of the silicon to its oxide or to a complex oxide with the aluminium oxides on the surface of the particles. The interstitial diffusion rate of silicon in the iron matrix is high.

5.3. SHAPING TESTS

5.3.1. Laboratory shaping tests

5.3.1.1. Properties of Lamellar Powders

The lamellar particles, or lamellae, that were used to produce the sintered lamellar soft magnetic materials (SL-SMC) are shown in Figure 37. They are typically square in shape, measuring 1.5 mm by 1.5 mm, and are either 50 µm thick (pure iron, Fe-47.5wt%Ni and Fe- 49wt%Co- 2wt%V) or 125µm thick (Fe-3wt%Si). Observation of a specific lamellar particle, as in Figure 60, indicates that the organo-ceramic coating applied by the sol-gel method is quite uniform, and that the cutting step did not damage this coating. This coating, as shown in Figure 62b is about 2.0-3.5 µm thick. Following the thermal treatment of the compacted parts, that will lead to a final alumina dielectric thickness less than1 µm (see the best results inTable 4). The edges of these lamellae are not coated, since the cutting operation follows on from the coating step. These allow for the consolidation of final parts using solid state diffusion of metallic atoms during the sintering step.

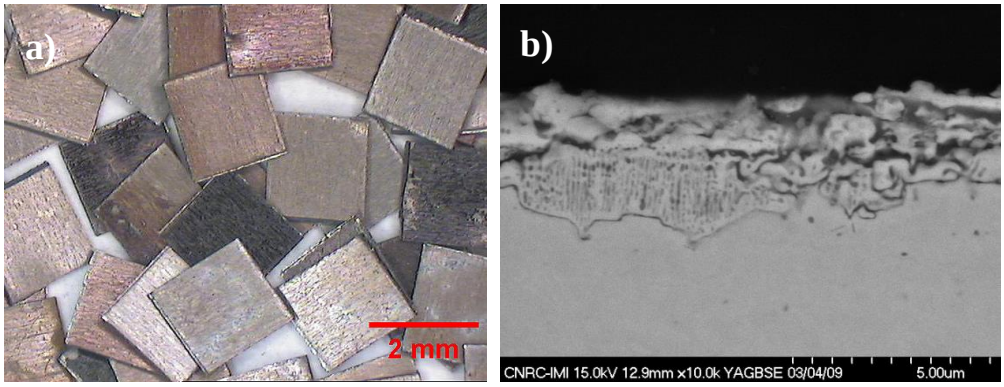

Figure 62: Starting material; insulated flakes: a) Overview, b) focus on one specific lamellar particle, with a Focused Electron Gun SEM (FEGSEM) courtesy of NRC IMI Boucherville.

5.3.1.2. Flow Behavior

The flow characteristics of the flaky material containing 0.75 wt% of polymeric binder-Lubricant (named ‘Lub’ in the following Figures) are given in Table 6. As expected, no flow was observed, either in the Hall flowmeter or in the Carney flowmeter. The lamellar shape and relatively coarse particle size as compared to the size of the funnel orifice, explains this lack of flowability.

Using the Arnold Meter, it was possible to determine the apparent density of the lamellae. The increase from the apparent density to the tap density shown in the Table 6 is about 31%, indicating that the random loose packing of the studied lamellar particles is relatively high, leading to a high bulk density. For comparison purposes, described in reference [118], three different types of copper powders having an identical particle size distribution but different particle shape (spherical, irregular and flake), lead to Increases, from an apparent to a tap density of respectively 18%, 36% and 75%. 31% is thus good, compared to the 75% increases given by the flaky copper powders. The mono-mode particle size distribution and the

regular square shape of the lamellae explain their good packing propensity and ‘stacking’ behaviour when filling a cavity.

Table 6: Flow behavior, apparent density, and tap density of starting flaky material.

	Flow		Apparent Density *	Tap Density
	Hall Flowmeter	Carney Flowmeter	Arnold Meter g/cm^3	g/cm^3
Flakes with 0.75%wt lubricant	No Flow	No Flow	2.28 +/- 0.02	2.98 +/- 0.03

5.3.1.3. Compactability and Green Strength

The compactability of the flaky Fe-Si material, as well as green strength of standard specimens, was determined using a manual (laboratory) pressing operation with a TRS die. Figure 63 and Figure 64 show the compactability curves at room temperature of the insulated Fe-Si lamellae, admixed with 0.75wt% and 1.25wt% binder-lubricant, as compared to the uncoated Fe-Si lamellae admixed with 1.25%wt binder-lubricant. It can be seen that at higher pressures, slightly higher green densities were obtained with the coated flakes containing 0.75%wt binder-lubricant, as compared to 1.25 wt%. Respective densities of 6.61 g/cm^3 and 6.46 g/cm^3 at 60 tsi were obtained. This could be explained by an inhibition of compaction due to the volume of lubricant contained within the porosities. Figure 63 also indicates that for the same amount of admixed lubricant (1.25 wt%), parts with higher

green densities were obtained with the uncoated lamellae as compared to the coated lamellae. For instance, for a compacting pressure of 60 tsi (800 MPa), green densities of 6.46 g/cm^3 vs 6.77 g/cm^3 were respectively obtained. This could be mainly explained by the decrease in the theoretical density of the mix due to the organo-ceramic coating applied on the Fe-Si lamellae, which causes a decrease from 7.74 g/cm^3 for the uncoated Fe-3%Si, to 7.53 g/cm^3 for the coated Fe-3%Si, as determined by gas pycnometry. Indeed, as shown in Figure 64, taking into account this difference in the theoretical density of the particles, similar densification was obtained at compacting pressures below 45 tsi. Similarly, only slightly higher densification of respectively 87% and 85% for the uncoated Fe-3%Si and the coated Fe-3%Si were obtained at higher pressures. On the other hand, a similar increase in densification was observed by decreasing the amount of lubricant from 1.25 wt% to 0.75 wt%, reaching respectively a densification of 85% and 87% at 60 tsi. As compared to unalloyed iron, these relatively limited compressibilities are due to the effect of the silicon as an alloying element in the Fe-3%Si material tested. Because best magnetic properties require reaching the highest density possible, this explains why forging was used in the final processing steps of the SL-SMC, in order to reach densifications higher than 95% in the final parts. It must be

noted that the hardness of Fe-3%Si is, surprisingly, not higher than pure iron in its fully annealed state. In fact, the hardness of both pure iron and Fe-3%Si were measured to be only 95±5 HV, after the annealing treatment at 850°C for one hour in pure hydrogen. However, as received, after the rolling operations, the hardness of Fe-3%Si was twice that of pure iron, at up to 450 HV, compared to only 205±5 HV for pure iron. We can thus say that ribbons are greatly affected by the annealing thermal treatment given after their rolling or eventually direct casting production process, and that Fe-3%Si shows a higher stress hardening rate than pure iron, thereby limiting its compactability.

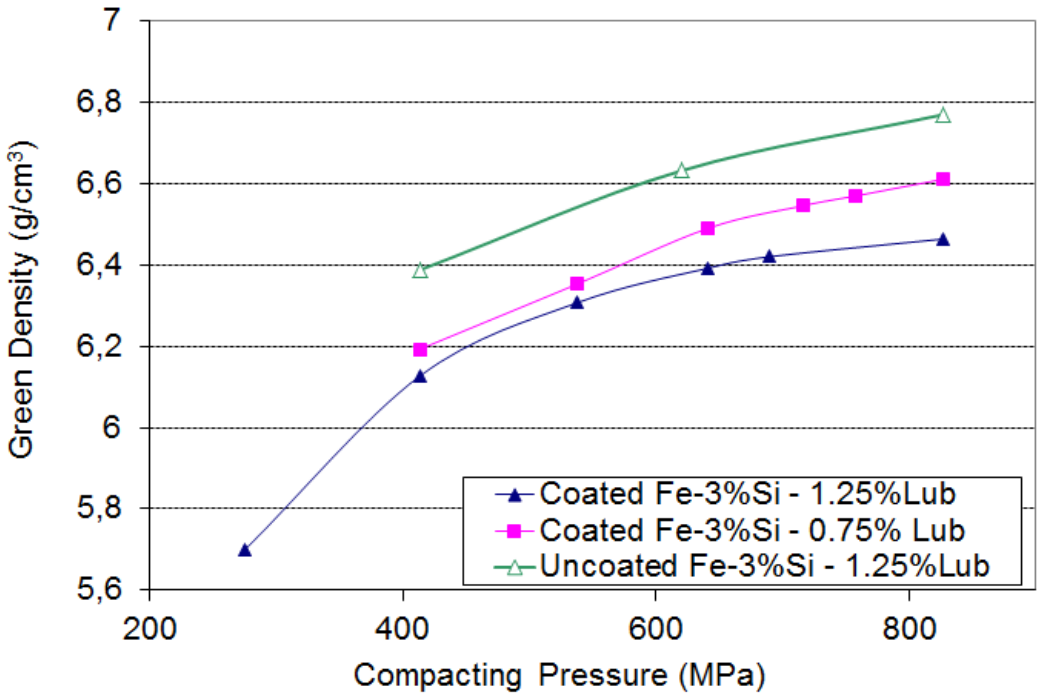

Figure 63: Compactability curves of the flaky material admixed with 0.75%wt Lub and 1.25%wt Lub.

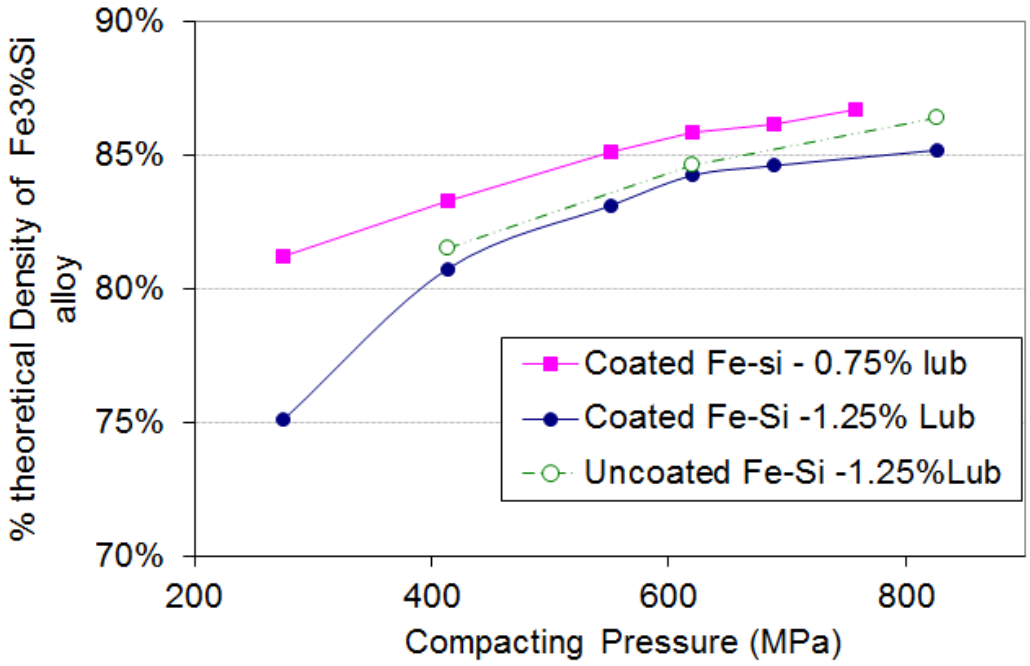

Figure 64: Compactability curves of the flaky material admixed with 0.75%wt Lub and 1.25%wt Lub in terms of the reached ratio of the percentage theoretical density of the particles.

For comparison purposes, Figure 65 gives a densification curve with lamellae particles of pure iron and for a typical commercial, highly compressible, grade of water atomised powders (ATOMET 1001 from Quebec Metal Powders).

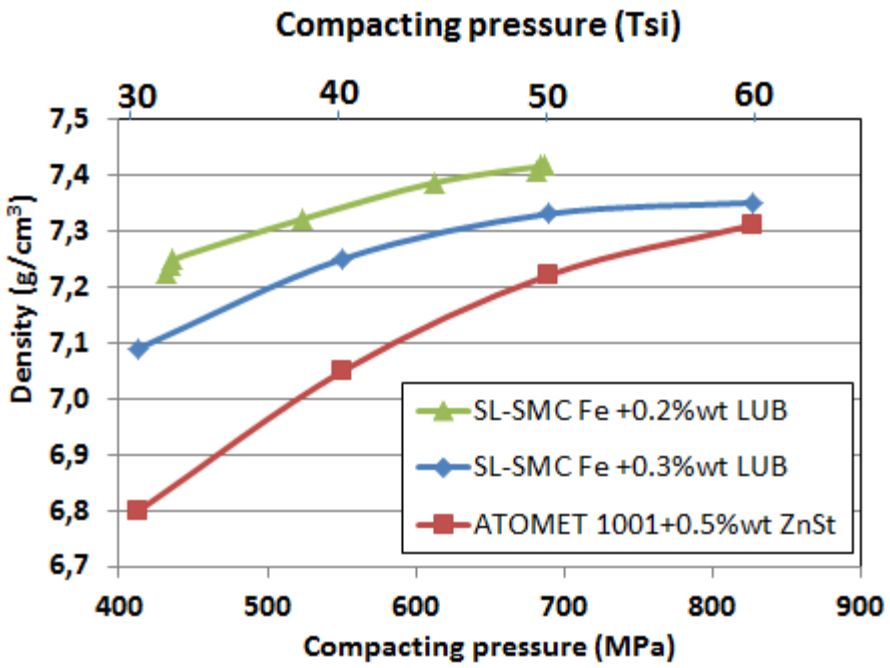

Figure 65: Compactability curves of the pure iron flaky material admixed with 0.2 and 0.3%wt Lub and using use of die wall lubrication compared to ATOMET 1001, mixed with 0.5%wt of zinc stearate.

The green strengths of parts made from conventional ferrous powder mixes are often sufficiently high to allow handling of the parts, and in some cases, even green machining, thanks to the prior deformation and mechanical anchoring of the irregular particles, and the specific binder-lubricants used. However, this is not always the case when using the SL-SMC's lamellar particles used in this study. This is largely due to the sol coating that prevents the possibility of almost all "cold welding" contact between the exposed metal parts of adjacent particles, and also because of their lamellar shape and coarse particle size, that prevent any anchoring, but especially due to their low compressibility, as for the Fe-3%Si alloy.

Delamination of parts on ejection of green parts from the press could be observed, when the compressibility of the base powder was low, such as in Figure 66, where oxidized and strain hardened Fe-Co particles were used. Without a proper lubricant-binder, it is also common that some particles in the corners, or at the surface of the parts, break out, leaving holes or irregularities. Some attempts to characterize such behaviour were done.

Figure 66: De-lamination observed on parts compacted using strain hardened lamellae particles (Fe-Co) and conventional lubricant (left) and (right) the good surface finish obtained with a polymeric binder and soft particles.

Figure 67 and Figure 68 show the green strength measured on TRS bars compacted at room temperature, or at 120°C, with the coated lamellae containing either no internal lubricant or admixed with conventional EBS lubricant or with a specific polymeric binder-lubricant.

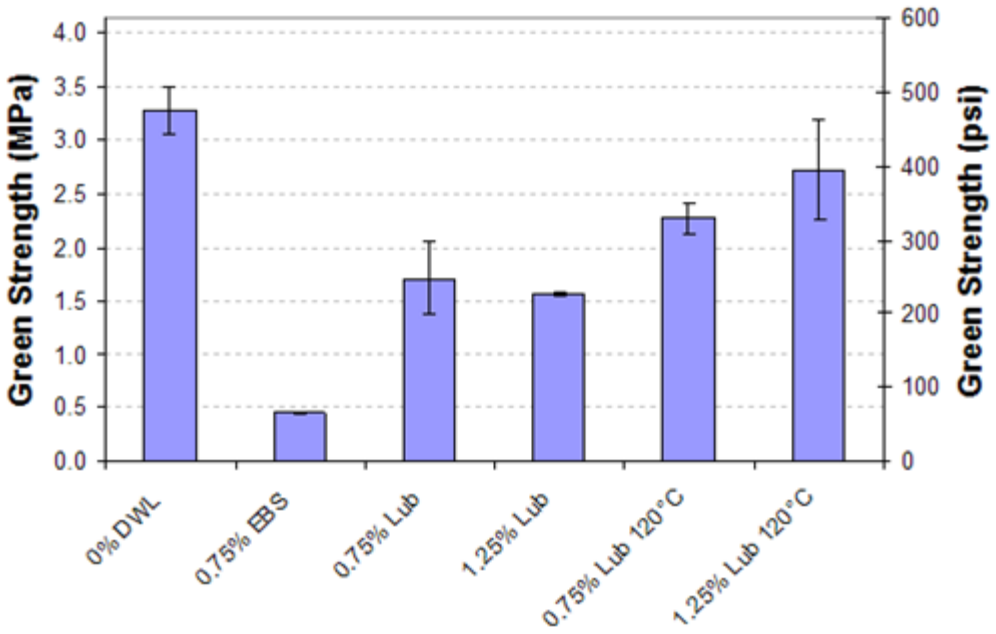

Figure 67: Green strengths of parts compacted at room temperature, or at 120°C, with coated Fe-Si lamellae admixed, or not, with different types or contents of lubricant.

The low compressibility of Fe-3%Si and the presence of a SiO_2 layer naturally forming on the surface of the alloy, prevent the parts from reaching high green strength values. Using a binder lubricant, or a die wall lubrication system, are the two best ways to obtain parts with sufficient strength to be manipulated. In fact, a higher green strength was obtained for parts compacted without internal lubricant using die wall lubrication (DWL), with values approaching 500 psi. Conversely, very low green strength was obtained with parts compacted with EBS internal lubricant. Parts were so fragile that they were very difficult to manipulate, but just enough to evaluate the mechanical testing. Even though the green strength of parts compacted with DWL with no internal lubricant, was the highest

achieved in this study, in agreement with results obtained in conventional ferrous powder mixes, it is important to mention that some lamellar particles in the corners, or at the surfaces of the parts, did break out, leaving holes or irregularities. When the polymeric binder-lubricant was used, a five times higher green strength was measured as compared to EBS lubricant. While this value of green strength is half the value of those obtained for parts compacted with DWL and no internal lubricant, parts with a very nice surface and strong corners were obtained, the polymeric binder being able to hold the lamellar particles in place. Still higher green strengths were obtained when parts were produced by warm pressing at 120°C. At this temperature, the polymeric binder is able to flow between the particles and create a polymeric network that holds the lamellae together. Figure 38 shows a few parts cold pressed at room temperature under the best conditions developed (0.75wt% Lubricant-Binder).

The results are very different with pure iron lamellar composites. This time, the values obtained are superior to what is commonly obtained with regular water atomized powders. As seen in Figure 68, even with a standard commercial lubricant, the values are very high, while those using the high performance lubricant-binder used with Fe-3%Si (polyethylene powders), are well above anything that can be obtained with conventional

water atomized powders. The heating of the die to 120°C does not improve the already extremely high results. This phenomenon could be explained partially by the fact that green strength is measured using a three point bending technique, for which a lamellar structure is stronger if the particles are oriented perpendicularly to the applied pressure. In such a case, as soon as the lubricant binder sticks to the faces of the particles, they are held together and sliding movements are prevented.

However, another hypothesis to explain the superiority of SL-SMC regarding green strength values and that could also explain why the use of heat with warm compaction does not further improve the results, is that it is a lot easier to form a binder network with a lamellar structure. In fact, porosities seem to be a lot more interconnected, even at very high density. This statement comes from the observation of the way the parts absorb water when we try to measure their density by water displacement. Even at 98% density, water enters into the porosities and fills the part very quickly, while producing a strange sound, like a whistle. It is truly possible to measure the theoretical density of lamellae parts leaving a sintering treatment by weighting the parts in air, and then after having been immersed in water. Water totally penetrates the part and the measured density by water displacement is the theoretical one of the alloy with its

coating. Coating thickness can even be evaluated with good precision using the water immersion method. By re-weighing the wet part and subtracting the volume of the cavities filled with water, we return exactly the real density of the parts as measured geometrically. On the other hand, it is well know that porosities begin to stop being interconnected at around 92% of the theoretical density of a part with irregular particles. It is thus probably a lot easier for the binder-lubricant to form an efficient network, with a well ordered porosity network.

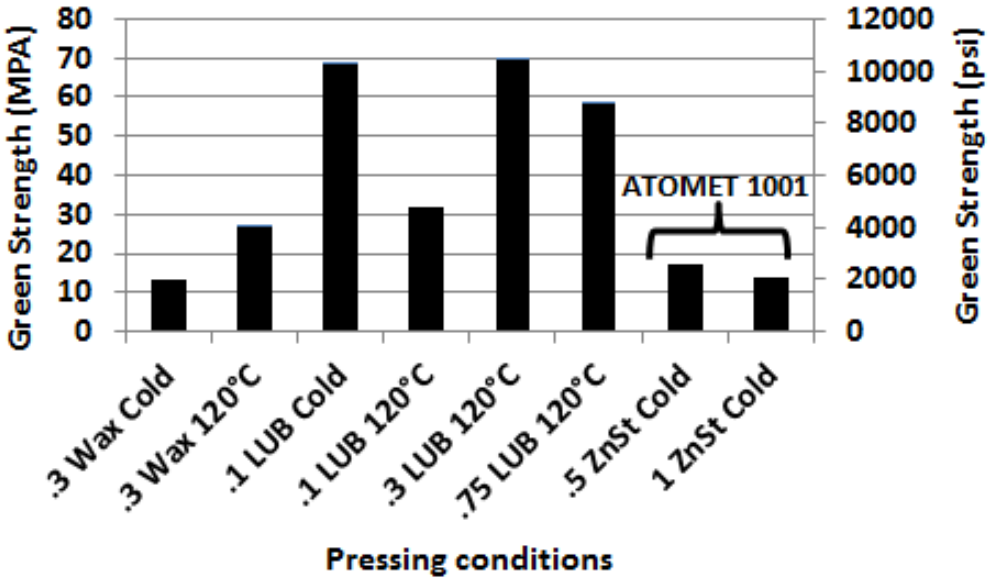

Figure 68: Green strength of parts compacted at room temperature or 120°C at 690 MPa (50 tsi) with coated pure Fe lamellae admixed with different types or contents of lubricants (compared to ATOMET 1001 water atomised powders compact, the two last results on the right of diagram) .

Another interesting behaviour of the SL-SMC's under deformation is that the parts do not break suddenly, like common powder metallurgy parts, but they tend to rather slowly delaminate under an applied shearing stress. We will then only conclude this section by affirming that with a compressible alloy like pure iron or Fe-Ni, the lamellar form of particles is no longer a limitation regarding the green strength. Parts can be obtained easily, and green parts can be manipulated after the cold pressing operation.

5.3.2. Mass Production shaping process

5.3.2.1. Development of a Feeding System for the Industrial Compaction Press

5.3.2.1.1. Concept and Design

Even though it was possible to produce SL-SMC parts on a laboratory scale, having excellent green strength, the future of these new materials depends on the ability to produce parts continuously in an industrial press. However, as discussed before, the flow of these flaky materials is problematic, and in fact no flow was observed at all, using the standard test procedures commonly used for standard metallic particles in powder metallurgy.

The first approach was to look at the different specific production press feeding systems, commonly named “feed shoes” described in the literature and designed to improve the flow and filling of powder metallurgy mixes. Those feed shoes were often developed to improve the filling of thin, or complex, die cavities, as well as to improve the filling rate to increase productivity while maintaining good consistency of parts. The concept of these feeders is mainly to enable a better evacuation of air entrapment in the die cavity and to keep the powder loose. For instance, a fluidized powder feeding shoe [119], as well as feed shoes with agitator/or vibratory pins, have been developed [120,121,122,123]. All these improved feeders, as well as standard feed shoes, are however based on the same principle: filling the die cavity having a specific volume up to the top of this cavity and scraping the excess of powder when the feed shoe retracts, so as to enable the compaction step. Using the flaky material tested in this study, some preliminary tests have shown that filling the die cavity using this principle was inadequate, because some flakes are extracted from the die when the feed shoe of a 150 Tons Gasbarre mechanical production press retracts. This can be seen in Figure 69. It leads to uneven filling of the die with the particles.

Figure 69: Top of the die cavity when the feed shoe retracts, showing lamellae expelled from the die.

New ways of die filling that could be compatible with an industrial continuous process had therefore to be identified. Even though the flow behaviour of the flaky material using standard procedures in a small Hall or Carney funnel was problematic, preliminary tests showed that a given rectangular preform (8.9 cm x 1.7 cm x X cm), similar to the die shape, could be filled uniformly, and lead to a consistent bulk density using a standard volumetric feeder with a vibratory belt. During filling, the flaky material particles drop down so as to arrange themselves mainly on their flat surfaces. When positioning this preform on top of the die aperture, and further opening a ‘slit’ on the bottom of this preform, the loose flaky material in this preform was seen to drop into the die cavity in a ‘plug flow’ mode.

This test shows us that it should be possible to fill a specific amount of flaky material into the die cavity, while the top of this filled material remains below the aperture of the die cavity, and to prevent the extraction of lamellae when the shoe retracts.

Based on these observations, the following feeding device was designed and adapted to an industrial press. The goal of this device was to quickly and reliably fill the die with a constant volume of lamellae. The different feeding steps are described below, as well as in Figure 70.

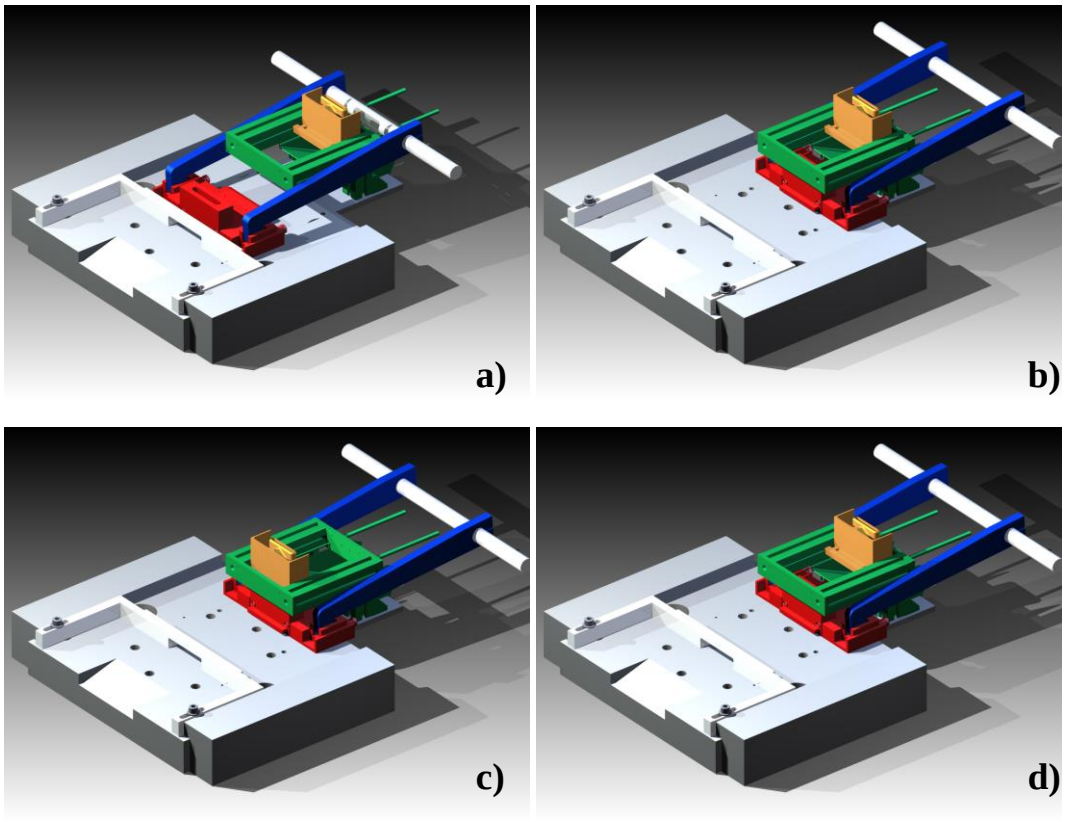

Figure 70: Schematic description of the feeding device, designed to continuously feed the press with the flaky material.

A first preform (in orange) is completely filled with a volumetric feeder having a vibratory belt, while the excess drops into a reservoir. This first preform is filled while located at the back of the press (Figure 70-a)

The second preform (in red) then moves back, allowing the upper punch to go down and press the part (Figure 70-b). This first preform moves forward,

stops above the second preform (in red) and the lamellae drop in this second preform (Figure 70-c). The first preform moves back, and begins to be filled again (Figure 70-c). The second preform moves forward on the die plate, pushes out the part just compacted and stops on the top of the die cavity, opening at the same time a gate located on the bottom. It enables the loose lamellar material in this preform to drop into the die cavity in a 'plug flow' mode.

At the same time, the first preform continues to be filled again (Figure 70-a). The first preform again moves forward, stops above the second preform and the lamellae drop into this second preform (Figure 70-c), and so on. All these movements are done continuously using an automatic control that enables production of up to 5 parts per minute.

5.3.2.1.2. Evaluation of the feeding system

Using the new feeding device described before, the reliability and repeatability of the process to distribute a constant amount of particles to the die cavity was evaluated by collecting one hundred samples on top of the die cavity in a continuous way, and by weighting each sample. Results are given in Figure 71. An average weight sample of 120g with a standard deviation of 0.5% was obtained. This value is similar to conventional ferrous powder compositions used in powder metallurgy. This result is quite

remarkable, given the poor flow-ability of the lamellae material. It is noteworthy also that these excellent results of repeatability were obtained at a very high filling density, significantly higher than the previous manual experiments with the Harnold meter, which gave 2.28 g/cm^3. Indeed, by enabling a low filling rate of the first preform during 10 s., it was possible to drop and stack,little by little, the lamella in the cavity, leading to a filled density of ~2.74 g/cc. This corresponds to ~92% of the tap density of the lamellae (Hausner ratio of ~1.08).

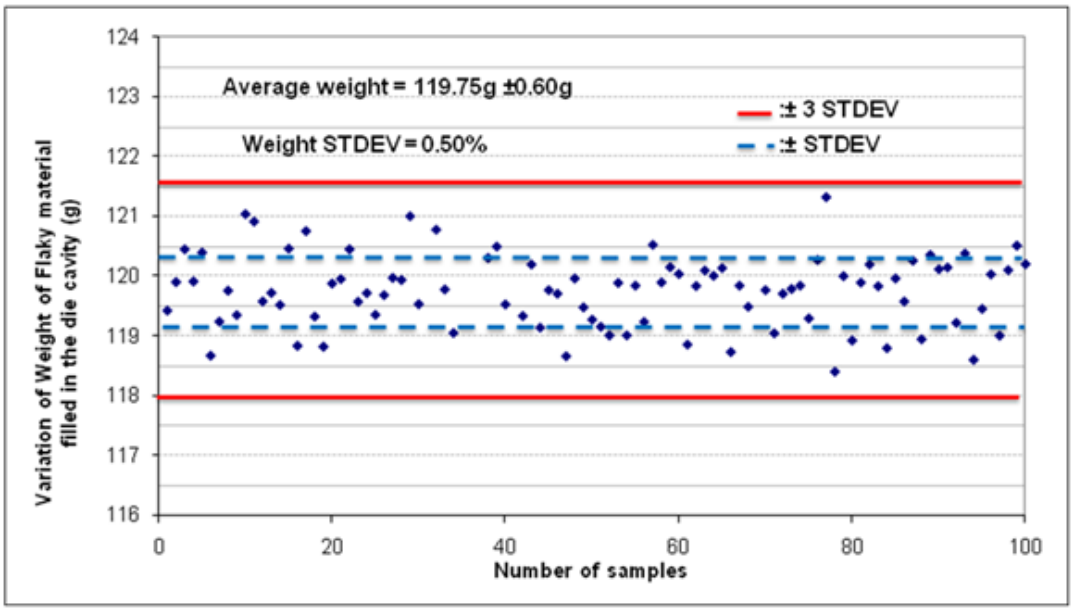

Figure 71: Part weight repeatability of the new feeding system at a press speed of 5 strokes per minute.

5.4. COMPOSITE PROPERTIES

First of all, it is interesting to see a micrograph of this new ceramic/metal matrix composite material, as pressed, and as forged to full density. Fe-47.5%wt Ni ribbons at 50 μm thickness was used for those micrographs. Keeping this image in mind greatly helps one to understand the following properties and their behaviours as a function of the different processing parameters.

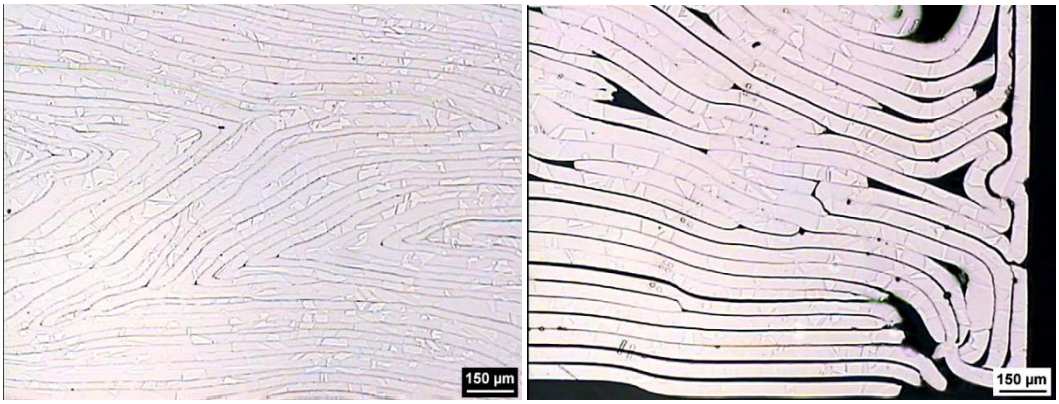

Figure 72: Left: Texture of a forged part; Right: Texture of a sintered part.

5.4.1. Magnetic Properties

5.4.1.1. Pure Iron

The supplier of this material is “Induction Iron Inc. 13909 N Dale Mabry Highway # 203 Tampa, FL 33618-2413”. He claims to be the successor of the well-known high purity ARMCO Iron producer. The company possesses a vacuum induction furnace, where they re-melt only scrap from electrical steel re-cuts, and purify it until the lowest possible carbon, nitrogen and

oxygen levels (max 0.003% for each) are reached. Traces of manganese can also be present. In this case, the certificate of analysis showed 0.33% Mn which could have an influence on magnetic properties.

A first full annealing thermal treatment under pure hydrogen was applied to the foil, so as to allow it to recover its ductility from the rolling operation. This was done at 850°C for three hours. Vickers Hardness measurements on the ribbon, prior to, and after, its thermal treatment, were 205±5 Hv and 95±5 Hv using a 10 gram charge (10gm force). Afterwards, the sol-gel coating operation was performed as described in Chapter 4, section 4.5. Then, the ribbons were cut with a specially developed “quill set” slitter and cutter. A solid lubricant was added to the cut particles and rings were shaped as described in the Chapter 4, section 4.8.

5.4.1.1.1. Effect of different additives

The following table reports on the magnetic properties of SL-SMC based on pure iron ribbons, cold pressed or double pressed and sintered at different temperature, containing Boron Nitride fine powders and pure aluminium powders.

It can be seen that in reality, by varying the coating thickness and sintering conditions, one can create any composite with properties ranging from the best fully dense and sintered DC magnetic material based on pure

Iron, to the best composite for AC applications. Indeed, the sample A0123, which has a very thin coating of alumina and was sintered at 1150°C, gives a maximum relative permeability (μ_r) or simply a “permeability” value, to simplify the text, above 5000. Unfortunately, hysteresis energy losses approach values typical of un-insulated powders. On the other side, sample A0042, with four layers of coating, and sintered at very high temperatures, still registers losses, at 60 Hz, that are under 3.5 W/kg, while having a permeability greater than 1000, and a coercive field under 90 a/m. This coercive field is exceptionally low for an iron part. Part A0132, which includes 0.2% of admixed aluminium powders (that should have completely diffused into the iron particles), exhibits a coercive field of 75 A/m. One speculates that the aluminium could have helped to improve the coercive field of pure iron by decreasing the magneto-crystalline anisotropy of the lattice. Coercive field also benefits from a transient liquid phase, which helps to create better bridges, or magnetic coupling, between particles [30]. It is interesting to see that the presence of a good conductor additive, such as aluminium, does little to harm the insulation of the composite with iron particles. With the other alloys, as it will be seen in the next section, in addition to not diminishing insulation at all, it also allows one to reach the best coercive field values, even with very low temperature sintering

treatments. It would be interesting to try other low melting temperature additives, to see if one obtains the same results, or if the effect is specific to aluminium. In the first experiments with PVD coatings, we found that an under-layer of aluminium, under the alumina coating, was beneficial.

However, this coating needed to be done by a PVD process, which increases the cost of the process. If the same result can be obtained with a simple mixture using a standard Powder Metallurgy part making aluminium grade (average particle size diameter (D_{50}) of 50-100 μm), it opens the door to interesting improvements. It is thought that aluminium helps to correct any defects, or cracks, formed in the alumina coating, and could even increase the ductility of the coating during compaction of the part, by creating an extremely low partial pressure of oxygen in the alumina coating in contact with it. This might create voids in the structure of the alumina coating that might significantly increase the diffusion of oxygen in the alumina and thus gives an improved ductility to the alumina layer. Any remaining free aluminium after the pressing operations can diffuse into the iron matrix and improve the magnetic properties slightly. Higher concentrations of aluminium are therefore under investigation.

Finally, regarding additive additions, the addition of fine Boron Nitride powders to the mix (A0043) does not seem to improve a particle's

insulation. However, it does not harm the DC properties, reporting coercive fields still at 100 A/m and a maximum relative permeability above 1000. As this additive is expensive, there are no plans to increase its quantity above those levels, particularly as it also decreases the density, or the concentration of available ferromagnetic material, within the composite.

Table 7: Magnetic properties of SL-SMC based on pure iron ribbons sintered at different temperatures and containing different additives.

Ident.	Coating type	Additive	Pressing process	Thermal treatment T(°C)-t(min)	Density (g/cm3)	Bmax at 12000 a/m (T)	Hc (a/m)	µmax	Losses at 60 Hz, 1 T (W/kg)	Losses at 400 Hz 1 T (W/kg)
A0010	4 thin	---	DPDS	1175-10+Osc	7.17	1.59	100	1118	4.4	67.0
A0014	1 thick	---	DPDS	1150-10+Osc	7.40	1.69	81	2460	10.6	339.5
A0042	4 thin	---	DPDS	1200-15	7.32	1.65	93	1020	3.3	28.5
A0043	4 thin	0.5% BN	DPDS	1120-10+Osc	7.34	1.56	100	1021	4.2	56.7
A0123	1 thin	---	DPDS	1150-20	7.80	1.85	103	5307	15.7	465.2
A0132	2 thin	0.2% Al	60 tsi	1150-20+Osc	7.19	1.57	75	1246	5.0	116.7

Overall, it is noteworthy to see the tremendous effect of the coating on the particles, even if it is not a total encapsulation. Indeed, it changes the losses at 400 Hz from 465 W/kg with the A0123 to only 28.5 W/kg with the A0042. This really dissipates any doubts that encapsulation of particles must be total.

For comparison purposes, the best grades on the market have losses at 1 Tesla of induction, at 100 Hz of 10 W/kg and 46 W/kg at 400Hz.

Hoganas recently claimed to have developed a grade giving losses at 60 Hz of 6 W/kg and 32 W/kg at 400 Hz [124]. Pure Fe SL-SMC has even lower losses than those values, while retaining permeabilities that are easily double. The A0042 followed conditions similar to any regular Powder Metallurgy structural part, being sintered at 1200°C. As can be seen in Figure 76 of the next section, its properties continue to improve, and even losses decrease, as the sintering temperature is increased. Up until now, no treatments were run above 1200°C.

5.4.1.1.2. Effect of the Processing parameters

The following graphs show the trends for the maximum induction (at an applied field of 12 000 a/m and 10 000 a/m), the permeability, the losses, and coercive fields, all as a function of the density of the parts and their sintering temperatures for different coatings and pressing conditions.

From Figure 73 and Figure 74, we see that all parts follow a general trend of improvement in properties with increasing density, with a very high correlation, excepting those with additives or those suffering from cracks during the second densification process.

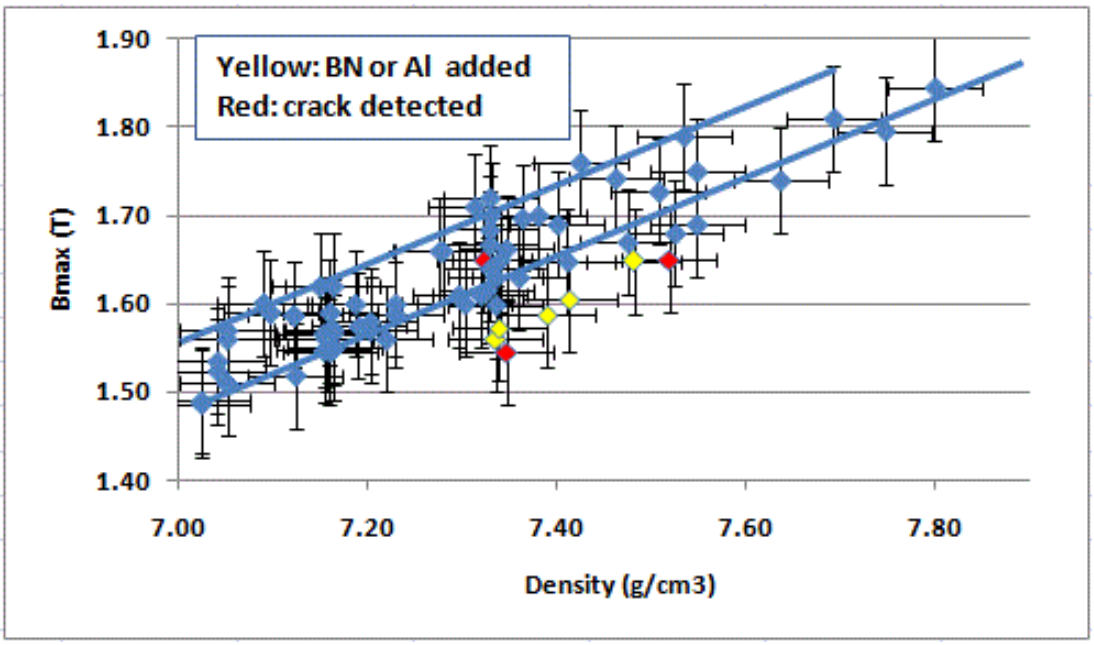

Figure 73: Maximum induction at an applied field of 12 000A/m (upper curve) or 10 000 A/m (lower curve), of parts made with pure iron ribbons processed under different conditions, vs their density.

Indeed, as for any DC magnetic parts, the presence of non magnetic additives will decrease the maximum induction and the permability of the material. As can be seen in the next set of figures, this trend does not hold for the energetic losses. Losses are more related to the sintering treatment agressivity or the amount of diffusion between particles.

In fact, a first improvement is due to the relief of all remaining stresses in parts from room temperature to the common stress relief temperature around 850°C This effect is not shown here where the graph starts at 900°C but it is well illustrated by the recent progress in water atomised powders composite, totally encapsulated, and available in the market [124]. In fact, as they improved the resistance of the refracrtory material

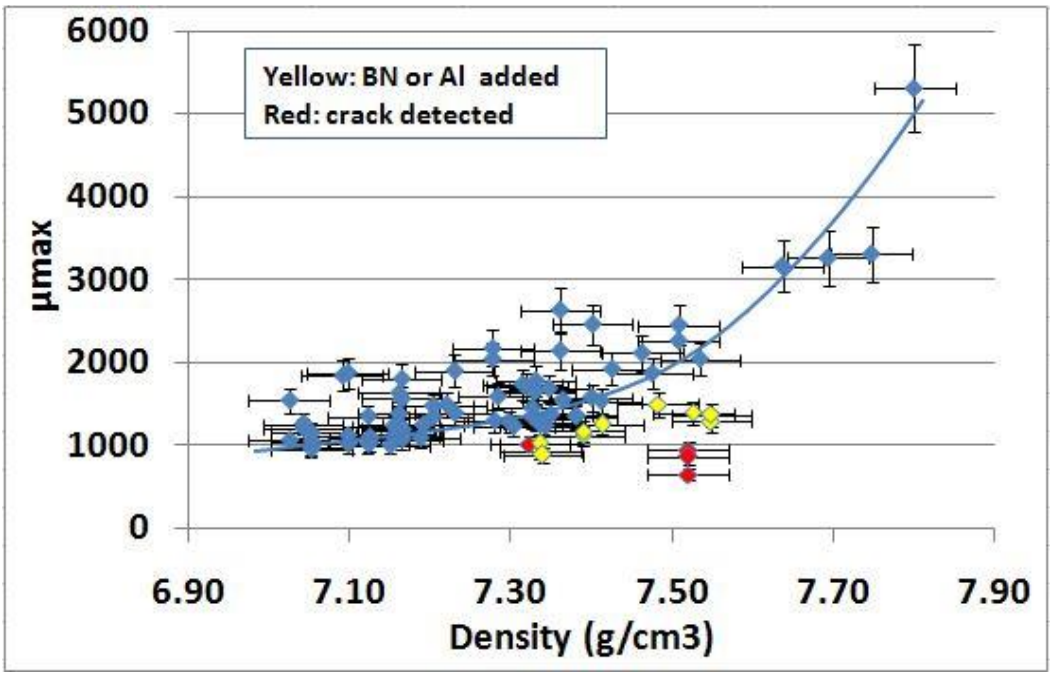

Figure 74: Maximum permeability of a selection of parts made with pure iron ribbons processed under different conditions vs their density.

applied on the particles, the industry succeeded in keeping their insulation up to the stress relief temperature of steel. It allowed for an important decrease in the hysteresis losses, by improving the coercive field, and the permeability. They decreased their coercive field from a few hundred A/m to 120 A/m recently, and increased the permeability from ~ 300-400 to ~800.

In the SL-SMC case, with particles partially insulated with pure alumina, this trend continues as the temperature increases. One sees, in fact, that for the A0010, in Figure 75, that the coercive field is around 140 A/m at a sintering temperature of 920°C and that it drops linearly to only 90 A/m at

1200°C. Permeabilities follow the same trend in passing from ~1020 to 1150°C. These two parameters reveal a constant decrease in hysteresis losses as a certain degree of sintering occurs between particles. It is not related to the relief of internal stresses, because the temperatures are too high to consider residual stresses being present. However, this sintering between particles will also decrease the overall insulation or electrical resistivity in the composite. Thus, the improvement in DC magnetic properties, or hysteresis losses, should eventually become outweighed by the increase in eddy current losses. This is the other important part of the total losses in a magnetic part submitted to an alternative electrical field. In fact, we see that for the A0010, this crossing point seems to occur at 1200°C, where the effect of the improvement in hysteresis losses is exceeded by the increase in eddy current losses. The upward trend in the curve at 1200°C is within the range of error of the measurement, but a sintering treatment at higher temperature should confirm the increase in total losses. This crossover trend could be at a different temperature depending on the efficiency of the coating and the density of the part, as can be seen with the following figures reporting the same properties for other parts. In fact, the A0010 is at a low density, only 7.17 g/cm^3 but the A0042 and A0043 are at around 7.33 g/cm^3, the most common density

obtained for the pure iron DPDS parts. Those parts have globally lower losses and in the case of the A0042, the crossover point is not yet reached, even at 1200°C, and losses are still decreasing. This might be explained by the higher potential for an improvement in hysteresis losses with a part of higher density. This assumption is indeed confirmed by the more important improvement in the permeability and coercive field, both starting from worst values at 920°C than with the A0010, reaching the same values at 1200°C. In term of hysteresis losses, it is as if the increase in sintering temperature brings those two parts to similar performances as the temperature increases.

Regarding the effect of the oscillating thermal treatment around the phase change temperature of pure iron to induce grain growth, both the A0042 and A0043 show an important decrease in the hysteresis losses and accordingly, in the total losses (see the circled points in both graphs). This treatment was applied at the end of the sintering treatment for the repeated sintering treatment at 1120°C. Indeed, a first treatment was applied at 1120°C without the oscillating treatment. After testing the parts, they were unwound and re-treated, this time with the oscillation treatment at the end.

We see that all the DC magnetic properties (or hysterisis properties, HC and μmax) significantly increase with this grain growth treatment. Finally, a

negative effect on μmax, and even Hc, is seen as the sintering temperature increases with the A0043 data. This is probably due to the presence of 0.5% BN. It could be explained by the product reacting with the oxygen or humidity released from the iron particles during the reduction of iron oxides. Indeed, BN above 900°C, in the presence of oxygen, transforms into boric acid, and the released boron can then diffuse into the iron matrix, harming the permeability and coercive field.

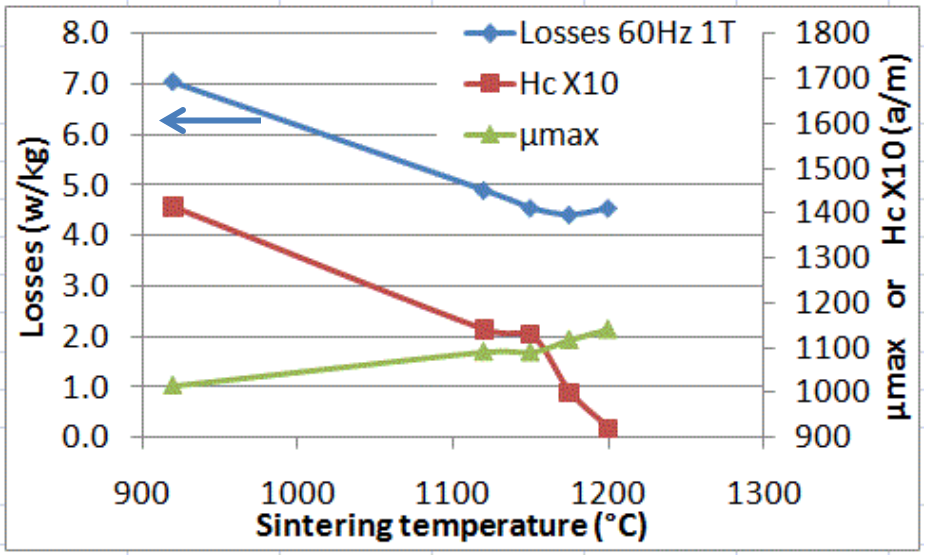

Figure 75: Losses, permeability and coercive field (X10) as a function of the sintering temperature for the sample A0010 (4 thin layers, DPDS, 7.17 g/cm^3).

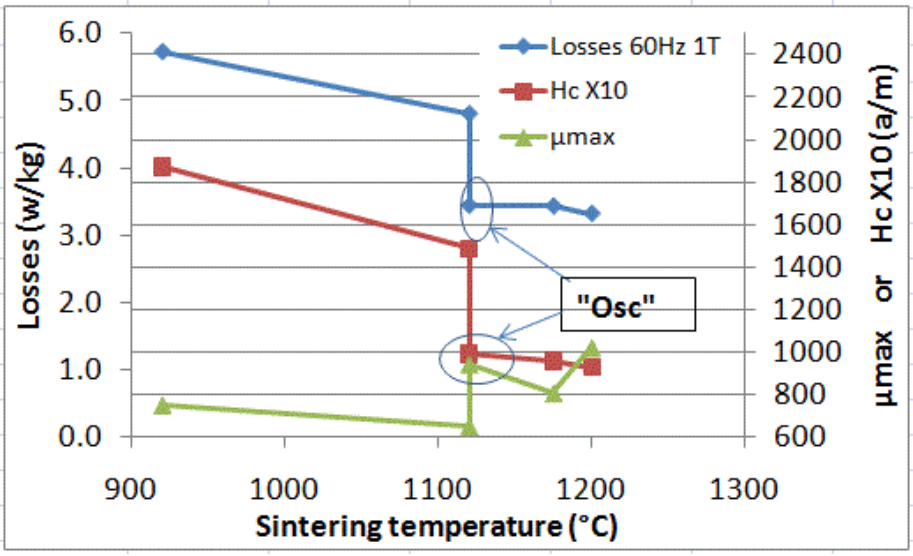

Figure 76: Losses, permeability and coercive field (X10) as a function of the sintering temperature and conditions for the sample A0042 (4 thin layers, DPDS, 7.32 g/cm^3).

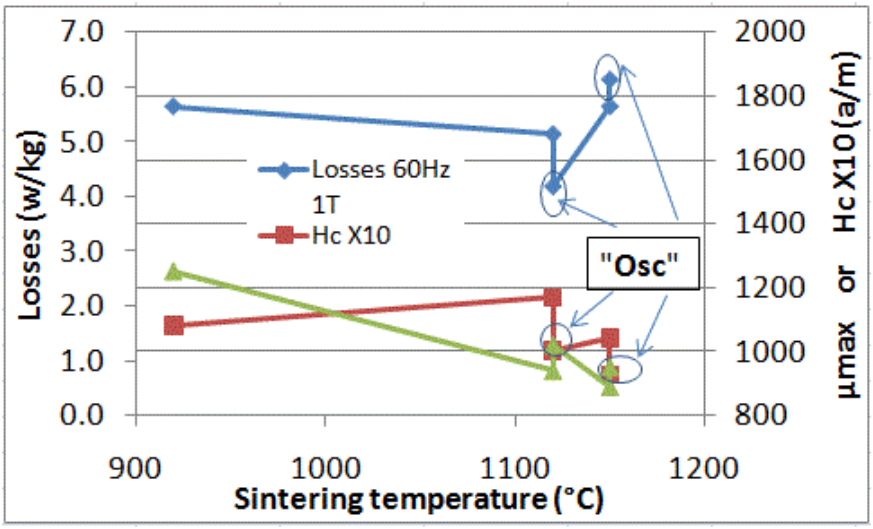

Figure 77: Losses, permeability and coercive field (X10) as a function of the sintering temperature and conditions for the sample A0043 (with 0.5% BN, 4 thin layers, DPDS, 7.34 g/cm^3)

5.4.1.2. Fe-3%Si

The supplier of this alloy is Arnold Engineering Co., from Illinois, (Group Arnold, 300 N. West Street, Marengo, Ill, 60152). The commercial grade of this foil is named Arnon 5, for 0.005 inch thickness. It is the thinnest bare (uncoated) silicon iron available on the market. It contains 3.25% Si and 0.03% carbon in its received state, as cold rolled. Its hardness varies from 28 to 44 HRC, from batch to batch, depending if it has received a stress relief treatment at the steel supplier plant (~280 to 450 HV with 50gm). Its density is 7.65 g/cm^3. Other impurities are negligible. A first full annealing thermal treatment under pure hydrogen is applied on the foil to allow it to recover its ductility from the rolling operation. This is done at 850°C for three hours. The hardness decreases to 90-100 HV (50gm), or ~ 55 HRb (95 Brinell). It is noteworthy that a hardness value as low as the one with pure iron is obtained after the annealing treatment and the green density is a lot lower than with pure iron, as seen in section 5.3.1.3 on pages 184 to187. The stress hardening rate with compaction/deformation should be higher, given the presence of silicon in the atomic lattice. Afterwards, the coating operation was done as described in Chapter 4. Then, the ribbons were cut with the specially developed “quill set” slitter and cutter. A solid

lubricant was added to the cut particles, and rings were shaped as described in Chapter 4.

5.4.1.2.1. Effect of different additives

First of all, one must mention that this grade, due to its very low compressibility/compactability, must be forged in order to reach interesting densities. Indeed, its green density, when pressed at 830 MPa, is only around 6.5 g/cm^3. This is clearly insufficient for magnetic applications.

One must also mention that typical properties for wrought Fe-3%Si at full density, like the best laminations for electric motors, have permeabilities around 5000, coercive fields around 40 a/m, and a maximum induction at an applied field of 12 000 A/m, in the range of 1.7 T. As can be seen in Table 8, it is noteworthy that the SL-SMC process does not involve any compromise in those DC magnetic properties when processed under the best conditions.

The three first conditions presented include 0.75% BN, which shows the lowest losses, well under 2 W/kg, i.e. close to 50% lower than pure Iron. BN is thus beneficial to the losses for this alloy. It is thought that contrary to pure iron, BN cannot be transformed, even at high temperature, because any released oxygen from iron oxide reduction reacts with the dissolved silicon content of the alloy and transforms into silica before BN can

decompose. Thermodynamically, SiO_2 formation is favored over BN decomposition.

The four following conditions of the table do not have any additives, but nevertheless show losses close to half those obtained with the pure iron SL-SMC, particularly at 60 Hz. They also have very high maximum induction, up to above 1.7 T, similar to the pure iron SL-SMC. It shows that a silicon addition up to 3%, even if not a ferromagnetic, is not really detrimental to the induction. Silicon generally helps in the permeability, and greatly decreases the coercive field. Indeed, values close to 5000 are reached, and coercive fields under 40 A/m are commonly obtained. We can see that the permeabilities are generally better for samples having only two layers of coating, for only minor increases in the losses (less than 10%).

The improvements of the DC magnetic properties (hysteresis curve), explains, overall, why the total losses are lower with this alloy. It is also roughly five times more electrically resistive [125], giving it a better chance to obtain lower eddy current losses. This statement is however mitigated, since some parts can exhibit losses reaching above 15 W/kg at 60 Hz and 400 W/kg at 400 Hz, when improperly insulated (results not presented here).

Table 8: Magnetic properties of SL-SMC's based on Fe-3%Si ribbons sintered at different temperature and containing different additives.

Ident.	Coating type	Additive	Pressing process	Thermal treatment T(°C)-t(min)	Density (g/cm3)	Bmax at 12000 a/m (T)	Hc (a/m)	µmax	Losses at 60 Hz, 1 T (W/kg)	Losses at 400 Hz, 1 T (W/kg)
A0044	4 thin	0.75%BN	Forged	1150-10	7.40	1.65	36	1000	1.65	22.0
A0098	2 med	0.75%BN	Forged	1150-20	7.10	1.47	37	3790	1.89	21.1
A0048	2 thick	0.75%BN	Forged	1200-15	7.25	1.56	40	4722	1.83	24.4
M809	4 thin	---	Forged	1120-10	7.50	1.71	36	1020	2.07	26.1
A0108	2 med	---	Forged	1150-20	7.42	1.66	42	1827	2.16	34.6
A0105	2 thin	---	Forged	1175-10	7.39	1.65	42	1894	2.18	35.2
A0087	2 med	---	Forged	1200-15	7.30	1.58	38	1071	2.38	45.3
A0118	2 med	0.2%Al	Forged	1120-10	7.08	1.42	63	1299	2.62	28.7
A0156	2 med	0.2%Al	Forged	920-30	7.36	1.63	43	1616	2.45	48.5

Similarly bad insulation with pure iron SL-SMC can generate losses above 30 W/kg at 60 Hz, and above 900 W/kg at 400 Hz. These bad parts were processed by using ribbons that had either been poorly cleaned of adherent rolling oil prior to applying the Sol-Gel coating, or had received too thick a Sol-Gel coating that peels off when the ribbon is cut into particles. A few bad parts also contained BN and were not kept under a good protective atmosphere during the preheating cycle, prior to the forging operation. To preheat the parts for forging requires about four minutes for small parts in a regular furnace, or just a few seconds when applying induction heating. Induction heating could therefore be a nice alternative for mass production

rather than heating in a conventional furnace such as a rotary hearth furnace.

Finally, in Table 8, it is noteworthy that sample A0156, containing 0.2%Al, gives properties close to the best conditions reached, using a thermal treatment at only 920°C. It is also surprising that a conductor additive does not harm insulating conditions, particularly for low temperature sintering conditions and times, where it had no time to totally diffuse into the matrix of the particles. Adding aluminum definitely helps in the insulating process. In the past, a PVD process was used to coat the ribbons with aluminum prior to oxidizing the aluminum's exterior. That was very effective, but the cost of the present aluminum powder addition is much lower by comparison. A smaller particle size will be tried in future work, to see if a more uniform or finer distribution could be more efficient, being closer to the effect of a uniform aluminum PVD coating.

5.4.1.2.2. Effect of the Processing parameters

The first point discussed with Fe-3%Si is the effect of any residual carbon in the parts. Since a forging operation is used to densify the parts, it was important to know if a de-lubing treatment prior to the forging operation was needed, so as to decrease the carbon content, before closing the porosities with further densification. It is clear that parts at low densities like

Fe-3%Si green parts, should be minimally manipulated, owing to their very low green strength [126] and attendant fragility. As such, it could be interesting to avoid a de-lubing process.

Figure 78 was used as a base graph and carbon level measurements were plotted against corresponding coercive fields. We can see, first of all, that we are generally in a good agreement with the literature data [127], except for obtaining slightly better values of the coercive fields. This is probably due to the advantages conferred by the lamellae shaped particles. It should be underscored that the comparison is done with non-insulated, water atomized, standard particles, fully sintered under the best industrial conditions for DC magnetic applications. It is then noteworthy to be able to achieve equivalent high performance results with a composite dedicated to AC applications. In the order from the least contaminated condition reported, to the most pure, the dots correspond to:

1. A curing of the cold pressed parts in air at 525°C for 15 minutes as is commonly done for the Fe-3%Si SL-SMC parts in this research. After the forging operation, a sintering treatment follows at 1120°C under pure hydrogen, for 10 minutes. This condition corresponds, for example, to the sample A0118 reported in the Table 8. All other parts reported in the Table 8 thus have better, or equal, carbon

contents, since they were cured in air, in addition to receiving a higher temperature sintering treatment after forging.

2. No curing in air before forging, sintering at 1350°C for 10 minutes. No parts reported in this research were processed with this condition. It was tested only to see what was needed to decarburize the part as completely as when a curing in air is applied. One sees that even above 1350°C under pure hydrogen, decarburization is not as good as doing a regular sintering treatment on a part that has previously been burnt in air at 525°C.
3. No curing in air. After forging, a sintering treatment at 850°C for 30 minutes in a pure hydrogen atmosphere.
4. No curing in air. After forging, a sintering treatment at 850°C of 30 minutes in a 10% H2-90% Ar atmosphere.

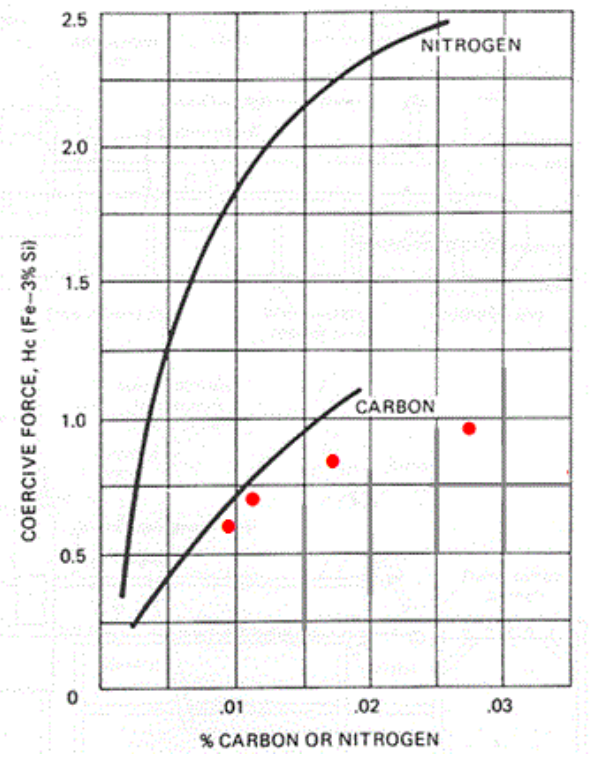

Figure 78: Coercive field (Hc) as a function of the carbon and nitrogen content in a Fe-3%Si regular powder metallurgy sintered part [127]. Dots added to the original graph are from this work with SL-SMC using Fe-3%Si base alloy.

Figure 79 and Figure 80 report the effect of part density on the maximum induction and permeability. Behaviors are similar to those with pure iron SL-SMC's. It is, however, interesting to note here that aluminum or BN additions can sometimes give good permeabilities that are above the general trend. Magnetic permeability is a very sensitive property. The spreading of all permeability results is due to the large number of parameters varied, and some difficulties during the forging step that produces cracks in the rings. In general, the most important parameters that could provide higher permeabilites than the trend line, are the final

thermal treatment time and temperature. In fact, when a grain grows and sintering causes metallic necks to form between particles, magnetic permeabilites increase. This can be seen from Table 8, where the highest permeability was achieved at 1200°C. We conclude that the addition of aluminum definitely has good potential for improving mechanical properties, without harming other properties. Further tests are ongoing to validate the beneficial effects of an aluminum addition. A BN addition is also not detrimental to permeability, since the best results come from parts with 0.75%BN, as seen in Table 8.

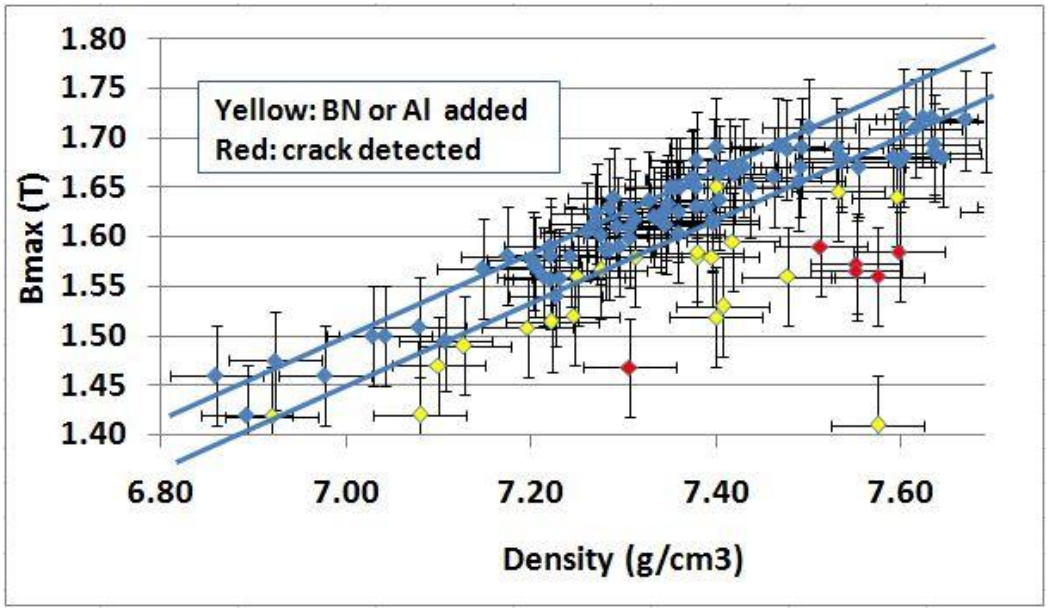

Figure 79: Maximum induction at an applied field of 12 000A/m (upper curve) or 10, 000 A/m (lower curve) of a selection of parts made with Fe-3%Si ribbons, processed in different conditions, as a function of their density.

Many problems occurred when forging the rings and when ejecting them following the forging operation. First of all, the manual entering and centering operation of the rings, at high speed, in the forging die cavity, was difficult to develop. Also, a large part of the experimentation was conducted using a damaged core pin, making part ejection much more difficult and causing de-laminations and cracks. One can see from Table 8, the bad effect on some of these parts on permeability. These effects do not affect their maximum induction and coercive fields (A0044 and M809), which are far less sensitive to defects.

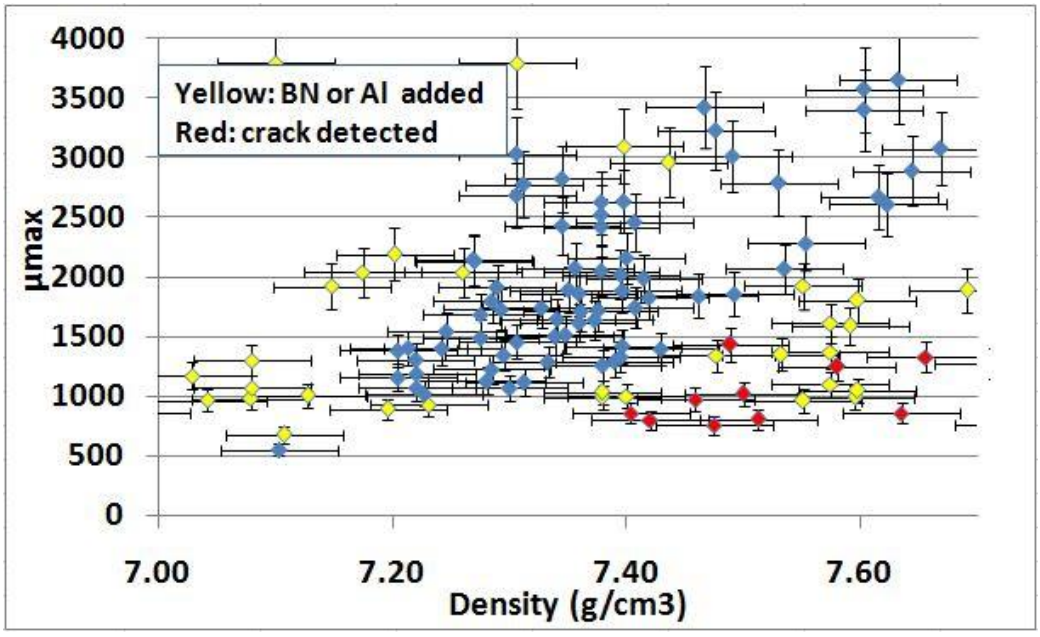

Figure 80: Maximum permeability of a selection of parts made with Fe-3%Si ribbons, processed for various conditions, vs the part's densities.

The next three figures (Figure 81, Figure 82 and Figure 83) report, respectively, on the effects of the sintering temperature on energetic losses, coercive fields and permeabilities of three Fe-3%Si SL-SMC parts

presented in Table 8. From the first graph, it can be seen that sintering above a temperature of 1150°C, when the part contains BN, can be slightly detrimental to the energetic losses. This was observed with the pure iron SL-SMC (A0043, Figure 77). However, despite a minor increase in losses when sintering at 1200°C, the permeability definitely jumps to values that are worthy of the best silicon steel laminations. This indicates that the optimum sintering treatment could definitely be above 1200°C, where good welding between particles occurs, despite slight decreases in insulation.

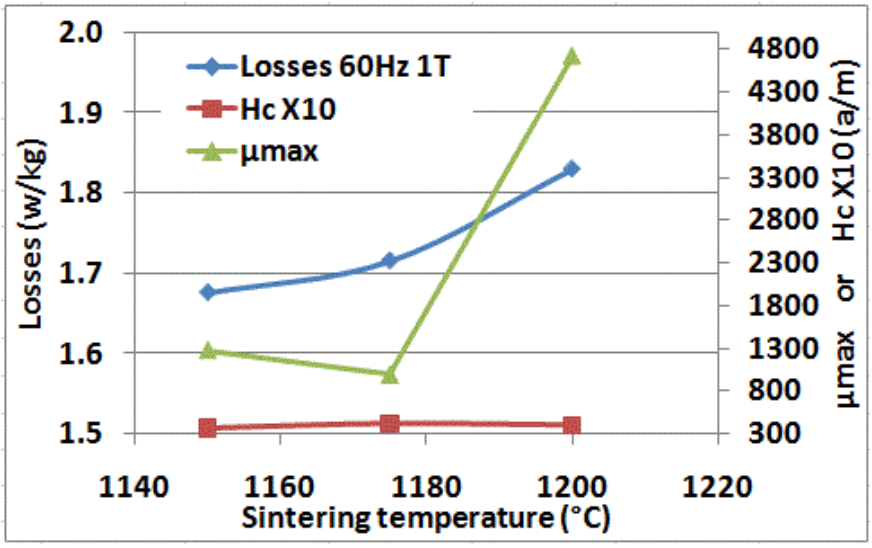

Figure 81: Losses, permeability and coercive field (X10) as a function of the sintering temperature for sample A0048 (with 0.75% BN, 2 thick layers, forged, 7.25 g/cm^3)

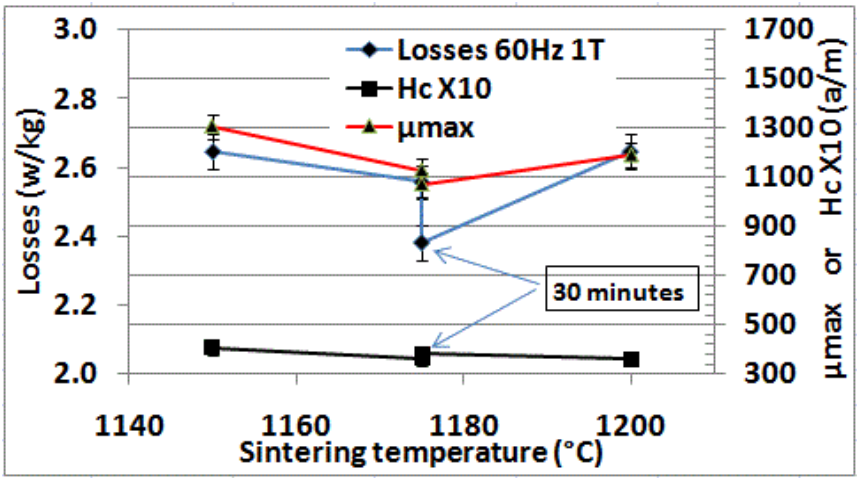

Figure 82: Losses, permeability and coercive field (X10) as a function of the sintering temperature and conditions for sample A0087 (2 medium layers, forged, density 7.30 g/cm^3)

All the illustrated trends in that Figure are negligible, and tests at higher temperature are needed to reveal if one has yet reached the point at which there is a deterioration in losses. Overall, for the two last conditions presented, without additives or with aluminium, the properties are still stable or improving, up to 1175°C, and even 1200°C. These are similar to the results realized for the pure iron samples.

It is remarkable that the alumina coating is highly resistant to the aggressive sintering treatments, even after the high level of deformation produced in the hot forging step.

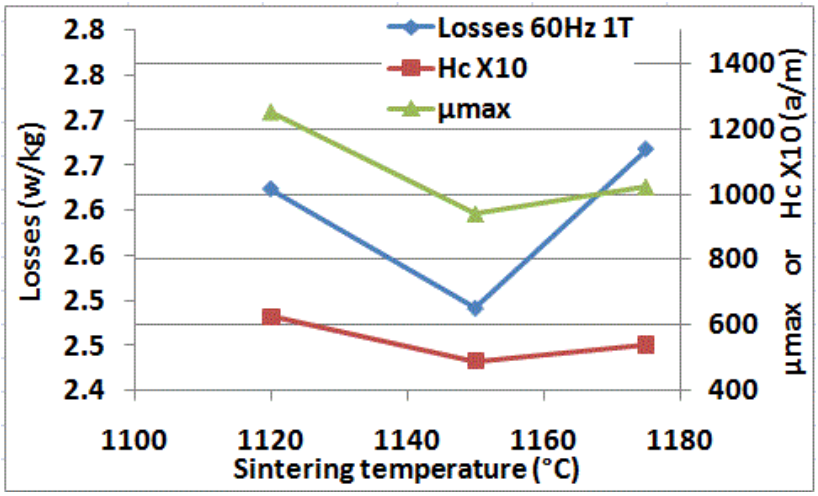

Figure 83: Losses, permeability and coercive field (X10) as a function of the sintering temperature for sample A0118 (with 0.2% Al, 2 medium layers, forged, density 7.08 g/cm^3).

Figure 84 gives the temperatures needed, at different dew points of different hydrogen containing atmospheres, to reduce silicon dioxide from the pure ceramic, or from silicon steel. We can see that the reduction of any silica formed on the surface of the particles through the oxidation of the dissolved silicon in the alloy that diffuse to the surface, should start around 1175°C, given the very low dew point for the laboratory tubular furnace. It would not be surprising to see a decrease in insulation occurring above 1175°C related to that phenomenon. For that reason, the consolidation should continue, or accelerate, between particles' edges above that temperature. The optimum sintering parameters would definitely be above, but may be close to, 1175°C. Results above 1200°C should confirm that

assumption and allow us to appreciate to what extent the quality of insulation under 1175°C is related to the presence of silica (silicon dioxide).

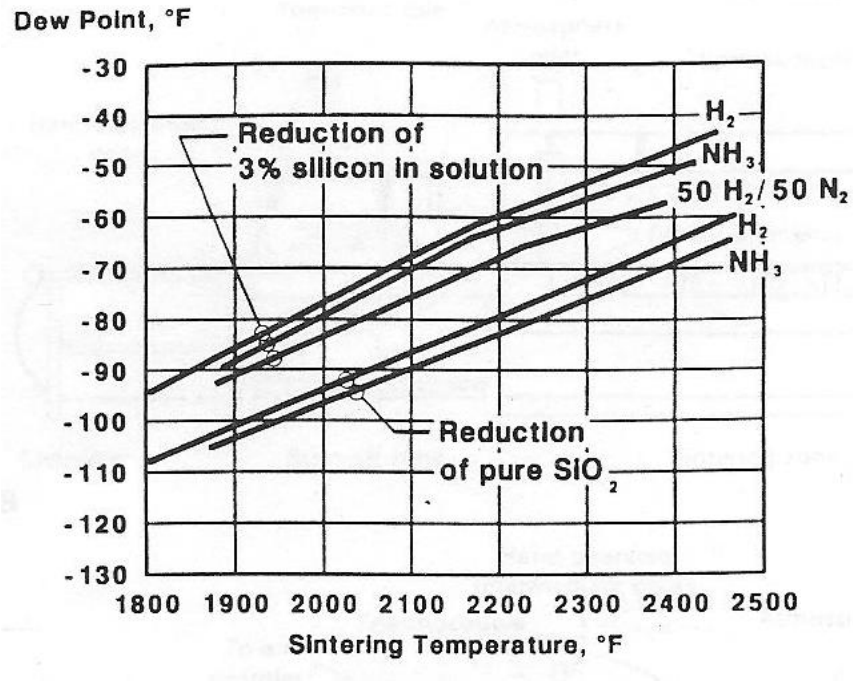

Figure 84: Dew point required to reduce pure SiO_2, or silicon dissolved in iron, as a function of the sintering temperature, for various reducing atmospheres [127].

5.4.1.3. Fe-47.5 Ni

The supplier of this alloy is named Aperam, formerly Imphy (ArcellorMittal), from IMPHY, France, (BP 1 - 58160 - Imphy). The commercial grade of this foil is named Supra 50, and its thickness is 50 μm. It is the thinnest, bare (uncoated), Fe-47.5%Ni, available in the market. It is a high purity Fe-Ni alloy, containing 47.5% Ni. This composition was selected, because it gives the highest maximum induction (1.55 Tesla) of

the Fe-Ni alloy family, with a very high relative permeability. This is lower than the permeability of permalloys, containing around 80% Ni. Nonetheless, its permeability values are well above 20 000. The alloy, as received, cold rolled, has a density of 8.2 g/cm^3.

A first full annealing thermal treatment under pure hydrogen is applied on the foil, so as to allow it to recover its ductility from the rolling operation. This is done at 850°C for three hours. Afterwards, the coating operation is performed, as described in Chapter 4. Then, the ribbons were cut with a specially developed “quill set” slitter and cutter. A solid lubricant was added to the cut particles, and rings were shaped as described in Chapter 4 for characterisation of magnetic properties.

5.4.1.3.1. Effect of different additives

Fe-Ni alloys are required for applications demanding very high permeabilities. However, the selected alloy, containing close to 50% nickel, was selected because it still retains a very high maximum induction, while simultaneously giving improved permeabilites. Fe-78%Ni could have given a higher permeability, but would have delivered much lower values for the maximum induction, that were already affected by the presence of the insulator and the porosities of a composite produced by powder metallurgy techniques. This alloy can give, under optimum conditions, permeabilites

greater than 20 000, with a maximum induction at 1.55 T, and coercive fields at 5 A/m. Table 9 shows the limit of the SL-SMC process for this highly sensitive alloy. Permeabilites above 16 000 can be reached with a maximum induction up to 1.5 T and coercive fields under 20 A/m. At those values of coercive fields and permeabilities, the measuring apparatus and precision of the method can be questioned. In fact, the manufacturer of the hysteresisgraph guaranties a precision of ± 10 A/m with the scale and method used. Other winding procedures and testing parameters could be more appropriate to evaluate the performance of such sensitive materials.

We will only say that, again with this alloy, we can process materials for AC applications with DC properties very close to the best ones reached with conventional wrought materials intended for DC applications. It should also be mentioned that there is absolutely no need to apply a thermal treatment at high temperature to the base ribbon used after its production, to optimize grain growth in order to reach the optimum performance of the alloy with the SL-SMC process. The final thermal treatment on parts is sufficient.

Regarding the losses in an AC field, the losses are lower with this alloy, as predicted, than with the other ones. The best performances are obtained with the less dense parts (A0041, A0136, A0162 and A0163). However, for

those lower density parts, the permeabilities achieved are lower than the levels, hoped for that alloy. They were only cold pressed once, and the A0136, A0162 and A0163 contained a small amount of aluminium. This explains their low density and permeability.

Regarding the influence of additions to Fe-Ni alloys, BN does not seem to make an interesting contribution, particularly for the losses and maximum induction, if we take into account its high cost, but aluminium coated Fe-Ni particles or aluminium added as an additive should still be considered, so as to get low losses. More data are needed at various sintering temperatures to better discriminate the potential improvement of the parts with an aluminium addition. We can again already say that this additive does not seem to harm insulation and could be useful for composite strength, or even magnetic properties. Even maximum induction does not seem to be negatively affected by aluminum additions, as can be seen from Figure 85 of this section. In fact, the lower values of induction are solely due to the low density of a single pressing operation, and not to any dilution, since the yellow dots (parts with aluminium) are on, or over, the trend curve.

From the first line in Table 9, corresponding to the best result obtained with the PVD coating at the start of this project, as compared to all the other

results obtained with the sol-gel coatings, it is believed the sub-layer of pure aluminum was helpful, during the cold pressing process and the forging process.

Table 9: Magnetic properties of SL-SMC based on Fe-47.5%Ni ribbons sintered at different temperature and containing different additives.

Ident.	Coating type	Additive	Pressing process	Thermal treatment T(°C)-t(min)	Density (g/cm3)	Bmax at 12000 a/m (T)	Hc (a/m)	µmax	Losses at 60 Hz, 1 T (W/kg)	Losses at 400 Hz, 1 T (W/kg)
[7]	*PVD*	---	*Forged*	*850°C*	*8.00*	*1.5*	*7*	*17000*	*0.84*	*16.1*
A0041	4 thin	---	DPDS	1120-10	7.60	1.30	20	5912	0.90	12.1
A0004	2 thin	---	DPDS	1150-10	7.92	1.50	15	10628	1.64	55.6
A0005	1 thick	---	DPDS	1175-10	7.79	1.45	20	5989	2.82	104.3
A0030	4 thin	---	DPDS	1175-10	7.69	1.43	16	6205	2.18	75.8
A0070	4 thin	---	DPDS	1175-10	7.90	1.46	17	16586	3.06	113.8
A0071	4 thin	.25% BN	DPDS	1175-10	7.80	1.44	23	6910	2.71	92.8
A0114	3 thin	---	Forged	1150-20	7.85	1.46	26	8366	5.73	188.4
A0161	3 thin	---	60 tsi	920-30	7.19	1.34	19	3099	1.49	40.9
A0136	3 thin	0.2% Al	60 tsi	1175-30	7.34	1.35	17	2110	1.57	46.2
A0162	3 thin	0.2% Al	60 tsi	920-30	7.24	1.34	17	2050	1.36	32.3
A0163	3 thin	0.5% Al	60 tsi	920-30	7.21	1.26	20	1464	1.39	32.5

First of all, it should be mentioned that the Fe-Ni samples coming from the PVD coating experiments, were all forged. This forging was responsible for higher densities and higher maximum inductions (1.5 Tesla). These higher densities also allowed for higher maximum relative permeabilities (17,000) and lower coercive fields (7 A/m). These better DC magnetic properties allowed for very low losses at low frequencies. Similar losses, at 60 Hz, were obtained with Sol-Gel coatings, but only for the lowest density

parts, where less deformation occurs and less contact is established between particles. With the exception of sample A0041, which also gave low losses at higher frequency, parts insulated with the Sol-Gel coating, even at very low density, were unable to supply the extremely low losses recorded for the insulated Fe-Ni alloys, using the PVD coating process, containing a sublayer of aluminum. Regarding the potential contribution of a sublayer of pure aluminum, the following observations can be made. During the cold pressing operation, two phenomena can occur to help keep a good level of insulation with the presence of aluminium. First, any cracks occurring during deformation in the alumina layer exposes the aluminium under-layer to the atmosphere. The newly exposed aluminum in the crack then transforms to alumina, and can prevent any electric conduction between adjacent particles. Secondly, it is possible that the thin alumina layer formed above the pure aluminium layer could have a higher ductility due to the high diffusion rate of oxygen atoms occurring at the interface of the alumina and the aluminium sub-layer, causing void diffusion in the ceramic layer. During the forging operation, the remaining free aluminum on the surface can form a transient liquid phase, which can help in the formation of the part, by providing liquid lubrication, and in sintering between particle edges by producing liquid phase sintering. It is also

possible that the free aluminum migrates to any cracks in the insulating layer, replaces any oxidised iron or nickel atoms (e.g. FeO) in the film back to Fe, while simultaneously transforming itself to alumina to help repair any cracks in the insulating layer. The exact and most efficient phenomenon occurring cannot be demonstrated easily, but the potentially beneficial effect of the presence of a sub-layer of aluminium on the properties of the parts seem to be proven by those comparisons. Results of parts with, and without, this underlayer of aluminum will have to be compared in the future, the main layer of alumina being produced by the Sol-Gel method rather than by a expensive DC pulsed magnetron sputtering technique, like the one that produced the sample in Table 9. It will allow one to determine if a PVD process has to be conserved for a sublayer of aluminum, or if the Sol-Gel technique alone can give the same results.

5.4.1.3.2. Effect of Processing Parameters

Figure 85 shows again a very good correlation between the density and the maximum induction. Figure 86 shows more precisely the influence of the density on the permeability reached. It is evident, again, like for the Fe-3%Si with the large spreading of the results, that the density is not the only important contributing factor but it limits the maximum values that could be reached. For that reason, a very high compacting pressure combined with a

very low internal lubricant content, in combination or not with a die wall lubricant technology, or DPDS, or forging process, must be considered if this alloy is selected to obtain high permeabilities above ten thousand, as expected.

There are two points above the trend group, one is a forged part with a very high density (black dot) and the other one comes from the part A041 with a low density due to a single pressing operation. Its permeability is above the trend of the other low density parts due to the contribution of the sintering treatment at a higher temperature.

Finally the other green dot in the Figure 86 shows the permeability of the single pressed part A0161. Again, it is on the low side of the trend, not due to its pressing process or density, but because its final thermal treatment was only at 920°C, limiting the strength of the metallic contacts formed at edges of particles, and thus the permeability. Permeability with such alloy can sometimes appears to be not related at all to density, since it is so sensitive to purity (sulphur, carbon, oxygen and nitrogen content), residual stress, particles joints or magnetic coupling between particles and, grain size.

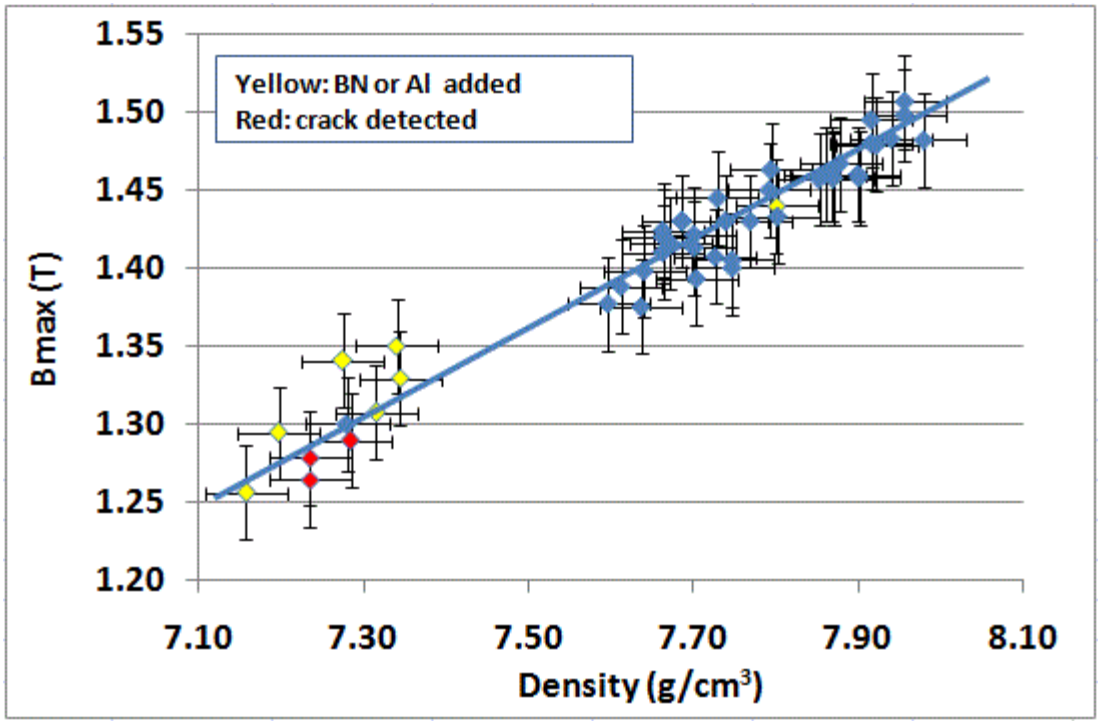

Figure 85: Maximum induction at an applied field of 12 000a/m of a selection of parts made with Fe-47.5%Ni ribbons processed in different conditions as a function of their density.

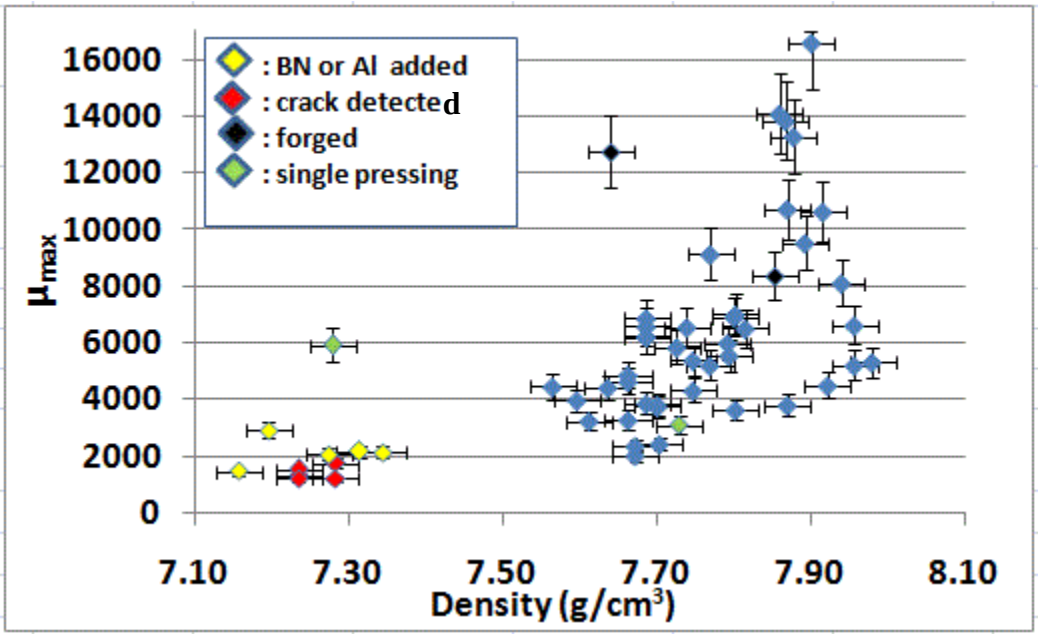

Figure 86: Maximum permeability of a selection of parts made with Fe-47.5%Ni ribbons, processed under different conditions, as a function of their density.

Figure 87, Figure 88 and Figure 89, illustrate the effects of the processing parameters on different single parts. Figure 87 shows a constant improvement in the DC magnetic properties as the temperature increases, with a minimum of losses at 1150°C, and a slight increase at higher temperatures. This is a very high density part having only two layers of coating without any additives. Figure 88 shows however that, for the A0030 with four layers of alumina rather than only two, a minimum for the losses is not yet reached even at 1175°C. The thinner coating of A0004 could have limited its ability to sustain a very high sintering temperature.

The A0041 reported in Figure 89 seems to confirm the minimum in losses at 1150 °C, even with its four layers of coating, but it is followed by a very weak, (close to insignificant), increase in losses above this temperature. Results with the A0041 must however be validated, since there is an abnormal variation of the permeability with temperature. It is thought to be related to the formation of a crack in the part during manipulations to remove the copper winding or any other manipulations after the treatment at 1120°C. It is interesting to see that even with a crack, the part can exhibit a good level of maximum induction, combined with a permeability above 1000 and with very low losses. It can give an

overview of what could be eventually reached by sinter-joining many parts together to obtain a very complex part not feasible with a single pressing operation.

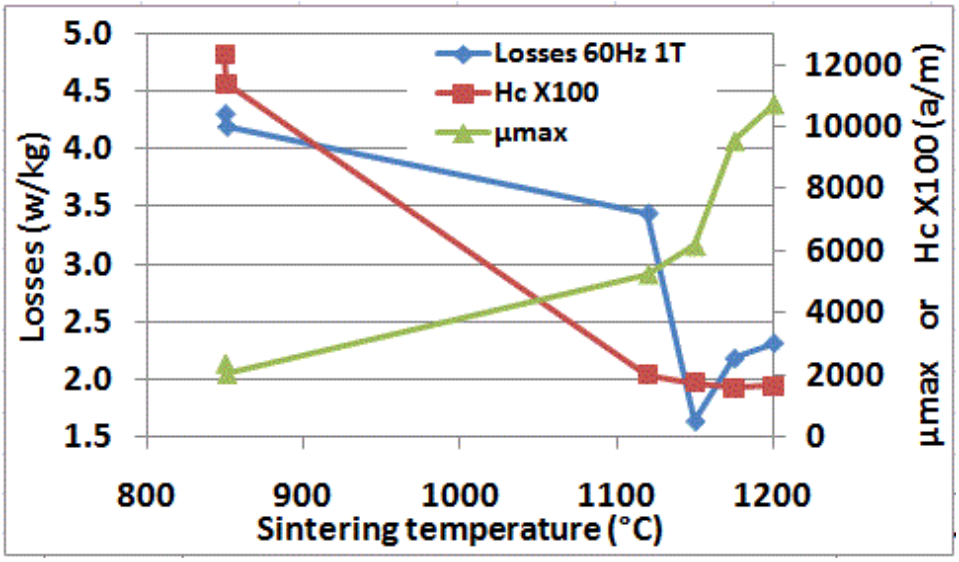

Figure 87: Losses, permeability and coercive field (X100),versus sintering temperature for sample A0004 (Fe-Ni, 2 thin layers, DPDS, 7.92 g/cm^3)

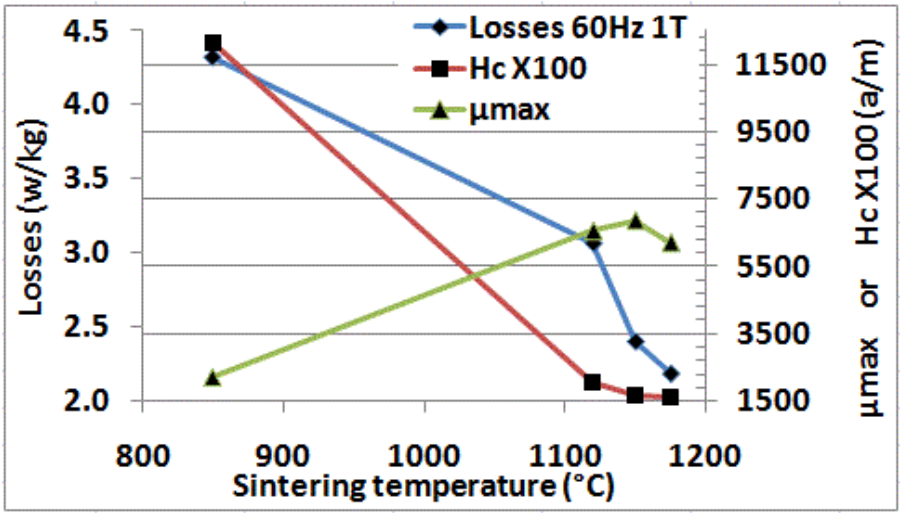

Figure 88: Losses, permeability and coercive field (X100) versus sintering temperature for sample A0030 (FeNi, 4 thin layers, DPDS, 7.69 g/cm^3)

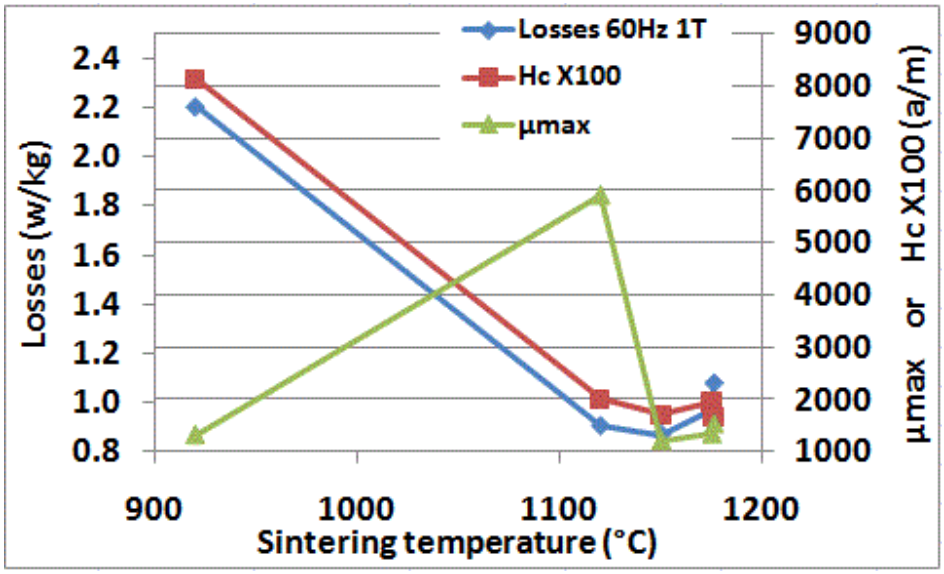

Figure 89: Losses, permeability and coercive field (X100) versus sintering temperature for sample A041 (FeNi, 4 thin layers, DPDS, 7.38 g/cm^3).

For this alloy, therefore, the optimum sintering temperature seems to be definitely around 1150°C-1175°C. However, additional experiments at 1200°C and higher will better illustrate the optimum conditions. It must be mentioned that the optimum temperature recommended by the ribbon producer for a grain growth thermal treatment is between 1150 to 1175°C. It must also be said that the nickel addition in iron significantly decreases its fusion point, thus requiring a lower temperature to achieve efficient solid state diffusion between particles during sintering. It is therefore not surprising to see a certain loss of insulation when temperatures above 1150°C are applied to these parts.

Finally, the effect of the sintering temperature and time on parts containing aluminium does not seem to be very different. Part A0136 reported in Table 9 containing 0.2% Al, did not show any increase or decrease in the losses, when its sintering temperature was increased from 1150°C to 1175°C for 30 minutes. Similarly, other DC magnetic properties remained unchanged. Further tests are ongoing with parts containing up to 1% Al, to see the best sintering parameters and optimum properties reachable.

5.4.1.4. Fe-49%Co-2%V

The supplier of this alloy is named Aperam, formerly Metal IMPHY (ArcellorMittal), from the city of Imphy, France, (BP 1 - 58160 - Imphy). The commercial grade of this foil is named AFK502, named by other companies or by the literature as Permendur 50, or Hyperco. Its thickness is 50 µm. This is the thinnest bare (uncoated) Fe-49%Co available on the market. It is a high purity Fe-Co alloy containing 49% Co. A 2% vanadium content is added to increase the ductility of the alloy and to decrease its re-ordering tendency, when the temperature is increased close to 900°C for annealing. Re-ordering leads to an important deterioration in DC magnetic properties, increasing the coercive field and decreasing the relative permeability of the alloy. Its relative permeability is similar to

silicon steel, when processed under the best conditions. The best conditions, when no re-ordering of the lattice occurs, can be achieved with a rapid cooling rate from sintering or casting, followed by a stress annealing thermal treatment at a maximum of 900°C. The lattice structure in the “disordered” state is body centered cubic (BCC). This composition was selected because it gives the highest saturation induction for a ferromagnetic alloy, 2.4 Tesla. It is received as cold rolled. Its density is 8.1 g/cm^3. Other impurities are negligible in this alloy.

A first full annealing thermal treatment under pure hydrogen is applied on the foil to allow it to recover its ductility from the rolling operation. This is done at 850°C for three hours. After this, the coating operation was carried out as described in Chapter 4. Then, the ribbons were cut with a specially developed “quill set” slitter and cutter. A solid lubricant was added to the cut particles, and rings were shaped as described in the Chapter 4, section 4.8.1 for characterising electrical properties.

5.4.1.4.1. Effect of different additives

Table 10 reports the best results obtained up to now with the Fe-Co alloy. The compressibility at room temperature of this alloy is very low, like for the Fe-3%Si. For this reason, all samples were hot forged. However, at high temperature, it appears a lot more compressible than Fe-3%Si, and

even a forging pressure half that for Fe-3%Si is still sufficient to exceed 95% of full density. It thus appears that all the results presented here, suffer from important deformation, after a forging operation at 40 tsi.

Studies are still ongoing to limit the pressure and the deformation, so as to reach approximately 95% of theoretical density without seriously deforming the insulation between lamella particles. This work involves many adjustments. First, we will try to decrease the deformation with a higher final inside diameter of the rings. A sliding movement between particles is however needed to eliminate porosities while ejecting entrapped gas [128]. In order to be able to reach a higher density with less sliding movement, we need to work or deform the part at a higher temperature. In order to do so, one can replace the slow hydraulic pressing operation by a drop hammer action at higher speeds and/or change the forging die material from H13 to stainless steel 420. The latter grade of steel is a martensitic, quenchable steel that is a lot less thermally conductive than H13. Preheating the die set to 300°C would also help a lot. All these strategies should be of help, not only for Fe-Co, but also for Fe-3%Si alloy.

Fe-Co is mainly used where a very high power density or induction is required. From Table 10, it can be seen that induction values close to 2 T

are obtained, even at densities under 7.60 g/cm^3 (see the A0149). The theoretical density of this alloy is 8.1 g/cm^3, but if we take into account the presence of the alumina coating (~4% of the volume, or ~1.1% of the weight), it decreases to 7.78 g/cm^3. This means that 97.5% densification was achieved at 7.57 g/cm^3.

Figure 90 shows the effect of the density and the amount of non magnetic additives, on the induction, for all the population of parts produced, and not only those reported in the Table 10. We can see that additives limit not only the density reached, but also it brings the induction values under the average curve of induction as a function of density. It is however, not too dramatic, depending on the benefits that can be obtained on the losses or mechanical properties.

The same observation can be made with the trend in permeability as a function of the density and additive content in Figure 91. Regarding the losses, in general, results have been disappointing up until now. Except for sample A0093, containing 0.75%BN, all the losses are too high compared to the good results obtained with all the other alloys for the SL-SMC process. Efforts aimed towards less deformation, but with a similar densification, should help on that side. However, insulation must be better adapted to this alloy in the future, considering that the only good results

come from a part with four layers of alumina coating the particles, plus a high amount of BN, combined with the lowest densification possible, it is clear that the amount of insulation must be increased.

Samples A0152, A0153 and A0154 received a curing treatment in air at a lower temperature than any of the other ones before forging (325°C rather than 525°C). We can see that for those three parts, and also for the A0149 which contains a small amount of aluminium, the coercive fields are appreciably lower than for the other samples, including the best one containing BN. Those lower coercive fields not associated with an improvement in the losses, tells us again that the problem of high losses does not come from hysteresis losses, but rather from eddy currents due to defective insulation.

We will nevertheless consider trying an alloy with a lower amount of cobalt, giving a lower tendency to re-order when crossing the 900°C region during cooling down after sintering. 27% cobalt seems to be well suited for that, with a maximum induction very close to the 49% Co composition. It is also more ductile. Finally, a good trend for a decrease in losses could appear in the future with an increase in the amount of aluminium, since the A0154 gave the second best losses, even if it is only sintered at 920°C. 920°C could be the best thermal treatment after forging

if it limits the re-ordering of the lattice, detrimental to DC magnetic properties.

Table 10: Magnetic properties of SL-SMC based on Fe-49%Co-2%V ribbons sintered at different temperature and containing different additives.

Ident.	Coating type	Additive	Pressing process	Thermal treatment T(°C)-t(min)	Density (g/cm3)	Bmax at 12000 a/m (T)	Hc (a/m)	µmax	Losses at 60 Hz, 1 T (W/kg)	Losses at 400 Hz, 1 T (W/kg)
A0092	4 thin	---	Forged	1150-10	7.60	1.97	140	2709	9.72	218.5
A0152	2 thin	---	Forged	920-30	7.58	1.99	92	2160	10.00	263.4
A0093	4 thin	.75% BN	Forged	1175-10	7.29	1.84	131	1352	4.53	71.0
A0149	2 thin	0.2% Al	Forged	1150-20	7.57	1.96	88	1899	9.02	206.3
A0153	2 thin	0.2% Al	Forged	920-30	7.48	1.93	110	1410	10.13	259.7
A0154	2 thin	0.5% Al	Forged	920-30	7.46	1.91	98	1591	8.27	213.8

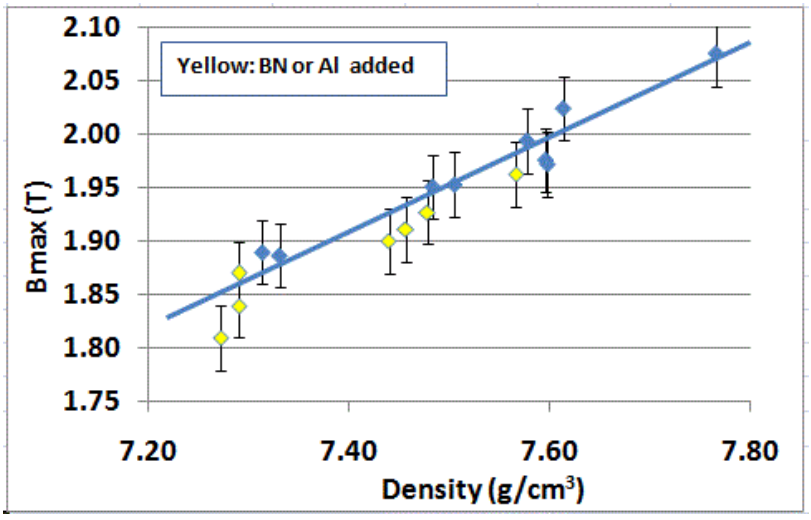

Figure 90: Maximum induction of a selection of parts made with Fe-Co ribbons, processed under different conditions, versus their density.

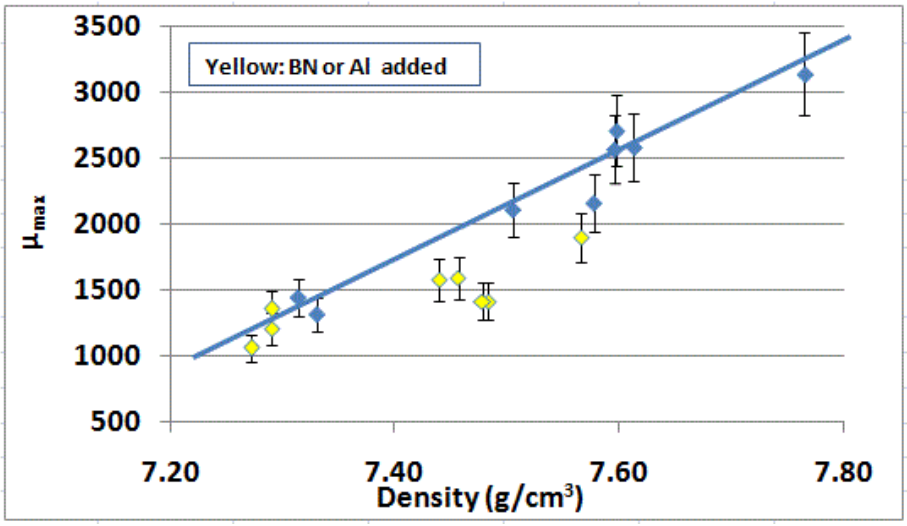

Figure 91: Maximum permeability of a selection of parts made with Fe-Co ribbons, processed under different conditions, versus their density.

5.4.1.4.2. Effects of the Processing Parameters

Due to the poor results obtained with that alloy, we will limit our analysis of the processing parameters to only the best sample containing BN. Figure 92 shows that an optimum is crossed at 1175°C, owing to a clear deterioration in the DC magnetic properties. This behaviour with the DC properties (H_c and μmax) should not occur when the sintering temperature is increased, unless some contamination is occurring. We then suspected, like for other alloys except for Fe-3%Si as explained in the Fe-3%Si section, that BN starts to decompose above 1175°C and that Boron can diffuse into the Fe-Co matrix. Samples not containing BN did not show degradation in their losses up to 1200°C. Future work should

help us better understand this limitation of samples with BN. We will also test an alloy containing a slightly lower amount of Cobalt, i.e. 27 or 42%, which eliminates the tendency of re-ordering.

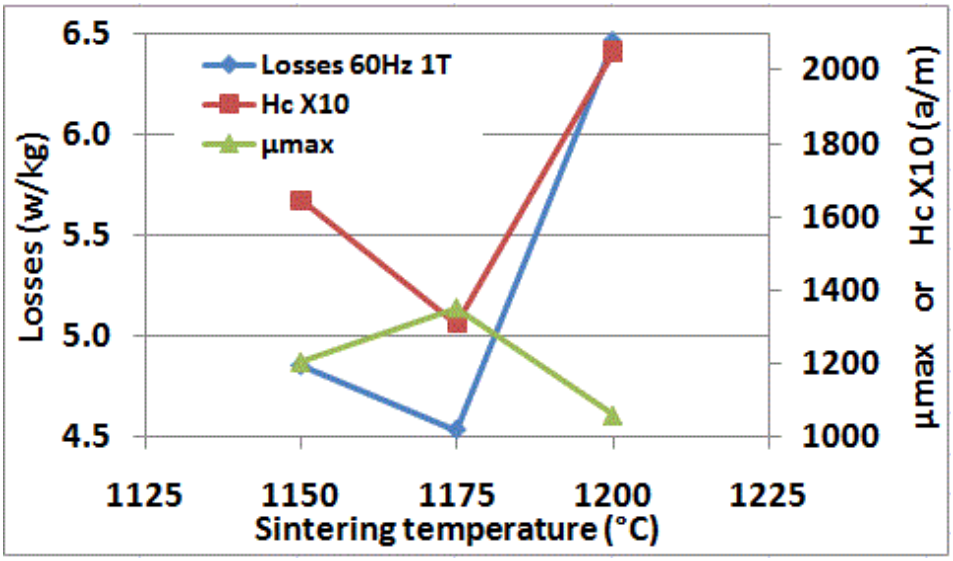

Figure 92: Losses, permeability and coercive field (X10), versus sintering temperature, and conditions for the sample A093 (Fe-Co, 0.75%BN, four thin layers, forged, 7.29 g/cm^3).

5.4.2. Mechanical Properties of the composite

Table 11 reports on the densities and transverse rupture strengths of the composite parts formed, using the different alloys studied, depending on their processing conditions.

The results show that all these composites have sufficient strength to withstand the majority magnetic applications since 100 MPa seems to be the required value to be on the market (see the Somalloy specification

values, from Hoganas Corp on the web) and all our results are above that value.

Table 11: Mechanical properties and density of composite parts produced.

Alloy	After Forging T (°C)-t (min.)	Density (g/cm^3)	TRS MPa (psi)	
			mean	STDEV
Fe	1175-15	7.62	392 (57 700)	35 (5166)
Fe-3Si	1175-15	7.39	126 (18 600)	5 (725)
Fe-47.5Ni	850-30	7.90	266 (39 100)	41 (5940)
Fe-47.5Ni	1175-15	7.88	674 (99 150)	50 (8660)
Fe-49Co-2V	920-30	7.46	223 (32 800)	5 (725)
After DPDS				
Fe	1175-15	7.62	120 (17 660)	5 (725)
Fe-47.5Ni	1175-15	7.90	136 (20 000)	5 (725)

We can see that for the forged Fe-47.5Ni alloy, when the temperature is increased from 850°C to 1175°C, the Transverse Rupture Strength, or TRS, value nearly triples, indicating a strong sintering bond between the metal components of the SL-SMC. This combination of treatment and deformation is therefore probably too aggressive for the insulating layer of Fe-Ni parts. Optimum magnetic properties for AC application are thought to be obtained with only a slight metallic bonding between particles to keep the highest resistivity possible.

Present SMC's on the market, formed from irregular "water atomised" powders completely encapsulated and joined by an organic or an oxide matrix, have TRS values in the order of 40 to 100 MPa. Forged, or DPDS SL-SMC's, sintered at optimum temperature for their magnetic properties

(~1175°C), exhibit superior TRS values, from 120 MPa for DPDS to close to 400MPa for forged parts, for the same composition, i.e. pure iron composite. Aluminium additions seem to give slightly improved mechanical properties at low sintering temperatures, but tests are still ongoing regarding additive additions.

Similarly, Fe_3P gave a tremendous improvement in strength (above 500 MPa) but with a dramatic deterioration in losses. Lower amounts should be tested before concluding on any benefit of this additive.

Tin and copper infiltration, or addition, will also be investigated in the future, as will impregnation with resins for increasing the strength, and facilitating prototyping by machining in large pucks.

In general, regarding density values presented in this, or in the other tables, if we take into account the presence of the less dense insulating coating, close to no porosity remains in the forged or DPDS parts. Those values are also significantly higher than common SMC's in the marketplace. Future efforts should be oriented toward keeping those values, while limiting the deformation of parts, rather than increasing them.

Chapter 6 MODELLING THE MAGNETIC PERFORMANCE IN SOME APPLICATIONS

6.1. INTRODUCTION

This chapter includes two modelling studies to evaluate the potential improvements possible by introducing SL-SMC technology for rotating electrical machines. The first part was carried out in collaboration with the "Laboratoire d'Électrotechnique, d'Électronique de Puissance et de Commande Industrielle (LEEPCI), Electrical Engineering department of Laval University, with Professor Maxime Dubois and his Master's student, Jude Delma. It uses a complex machine configuration, requiring the composite to be used in its three dimensions to carry the magnetic field. It is important to model some applications with those 3D configurations because even if the SL-SMC presented in this thesis are not fully isotropic, they might well answer the needs of the new emerging 3D design market. This can be close to being exclusively and most economically served by composite materials. This work uses complex computer modelling methods and software.

The second part of the chapter is a presentation of theoretical calculations, or mathematical modelling using simple 2 D designs of machines, including, or not, permanent magnets.

6.2. MODELLING IN A TRANSVERSE FLUX PERMANENT MAGNET MACHINE

In the first part of this chapter, a comparison is made between two Clawpole Transverse-Flux Machines (TFM) with a hybrid stator [129], using concentrators fabricated with regular water atomised particles, or Soft Magnetic Composites (SMC) for one of them, plus another concentrator fabricated from a SL-SMC, made with Fe-3%Si. The purpose is to determine the improvements that this new material can bring to this type of machine.

6.2.1. Evaluation of the magnetic performances of SL-SMC in the easy and hard directions for a 3D application.

In order to evaluate the magnetic performance of soft magnetic composites using lamellar particles, samples with annular and parallelepiped shapes were fabricated. As explained earlier (see the Experimental procedure for magnetic characterisation), the standard ring test identified the material's magnetic properties in the easy directions.

However, the

Figure 93 shows rather the technique used to measure the properties in the hard directions. The parallelepiped samples allowed the measurement of the material's magnetic properties in the hard direction. A

magnetic circuit of amorphous material was used to channel the magnetic flux to the parallelepiped samples. Amorphous material losses are negligible, and its permeability is very high compared to that of the lamellar material.

The results for SL-SMC are for parts made with the iron-3% silicon alloy. These parts were forged, annealed and sintered at 1212°C under hydrogen. Preliminary results in 2008 seemed to show that it was an optimum sintering temperature for Fe-3%Si. It offers both low iron losses and high flux density.

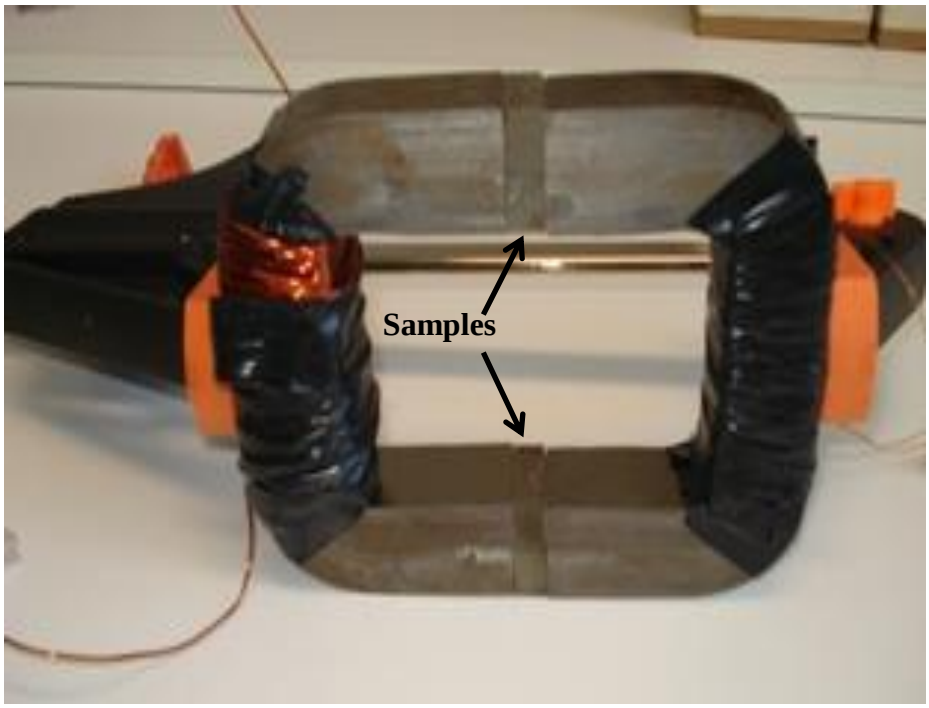

Figure 93: Methods for the evaluation of magnetic properties of the parallelepiped samples for the properties parallel to the pressing direction (hard direction of magnetisation).

The following table reports on all the magnetic results.

Table 12: Comparison of magnetic properties for SL-SMC (Lamellar), SMC (water atomised particles), and M19 laminations at 0.35mm thickness

Materials	DC magnetic properties			AC losses 1T (W/kg)	
	Bmax [1] (T)	HC (A/m)	μmax	60Hz	400Hz
SL-SMC / easy direction	1.59	60	2300	1.95	26.4
SL-SMC / hard direction	-	390	900	40	1118
Magnetic steel M19[2] 0.35mm	1.7	77	10000	1.36	18.9
SMC[3]	1.4	150	290	11	77

[1]:@ H = 8000A/m

[2]: M19 is the old nomenclature for standard electrical steel. It was based on the total energetic losses at 1 Tesla 60 Hz, in watt per pounds divided per 10 (19 w/lb max). It is the best most common grade of non-oriented electrical steel (M15 being the best available).

[3]:Atomet EM-1 Registered mark of Quebec Metal Powders Ltd (Rio Tinto Metal Powders)

We observe that the SL-SMC has a high permeability, and a saturation flux density close to that of laminated electrical steel. As explained previously, this high permeability is due to the metallic links

existing between particles in the direction of favorable magnetization, due to the sintering/forging process. Such is not the case with SMC's.

Furthermore, the lamellar structure allows for more compact layouts which substantially increase the part density and its saturation flux density as compared to SMC materials. It also minimizes the air gap between the layers of magnetic materials, still providing rather good permeability in the direction of unfavorable magnetization as compared to SMC's (that is, in the direction parallel to pressing direction).

In the direction of favorable magnetization, core losses are also much lower than SMC's. Figure 94 shows the iron losses measured on a ring sample. A mathematical model (multi-variable regression exercise, curve fitting) of the iron losses was derived from the experimental data and is also shown in Figure 94. This model was determined by adjusting the constants and power values of the empirical classical losses equations (see equation 33 to 36, chapter 3, section 3.10 and 3.11). The curve fitting exercise was based on losses measurement at various frequencies of sinusoidal excitement field and for various levels of induction in the sample.

This modelling has been done firstly in the direction of favourable magnetization. The model obtained is given by equation 45

$$\frac{P_{Core\_SL-SMC}(f,B)}{m} = 0.026B^{2.07}f + 9.9\cdot10^{-5}B^2f^2 \qquad (45)$$

where P_{Core}/m represents the specific core losses. We can see that the curve generated by equation 45 represents the measured core losses for 1T induction very well. The two terms in equation 45 represent hysteresis and eddy current losses, respectively.

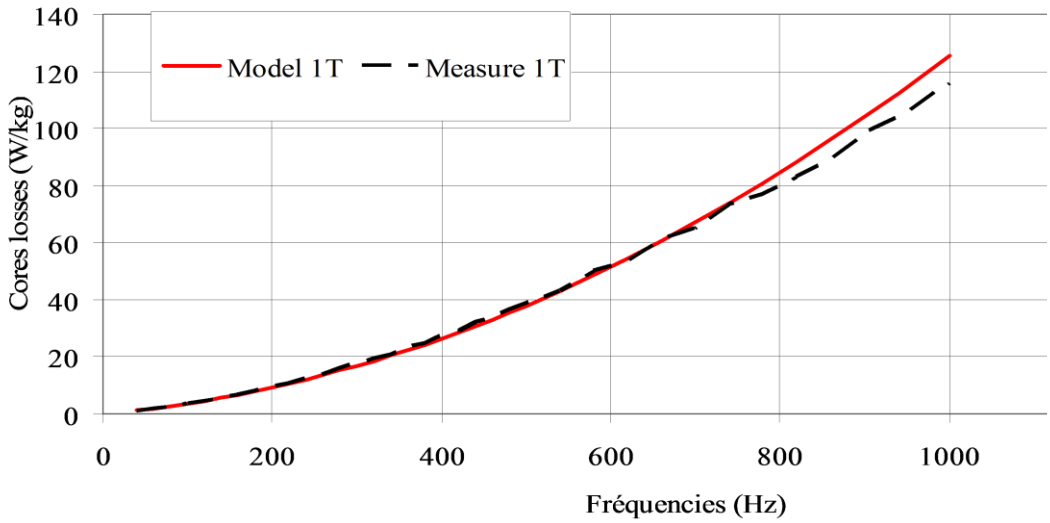

Figure 94: Real and modeled core losses as function of frequency of an applied field for SL-SMC (easy direction).

Figure 95 shows the contribution of each of these losses according to the frequency of the magnetic field. At frequencies lower than 100 Hz, core losses are mainly due to hysteresis losses.

As expected, we see that the hysteresis losses in the SL-SMC are much less important than in SMC's. Sintering or forging of parts allow for the removal of air gaps, plus complete stress relief in the particles, plus

metal grain growth. The small quantity of eddy current losses confirms the excellent thermal resistance of the coating and the layered structure of the part so consolidated.

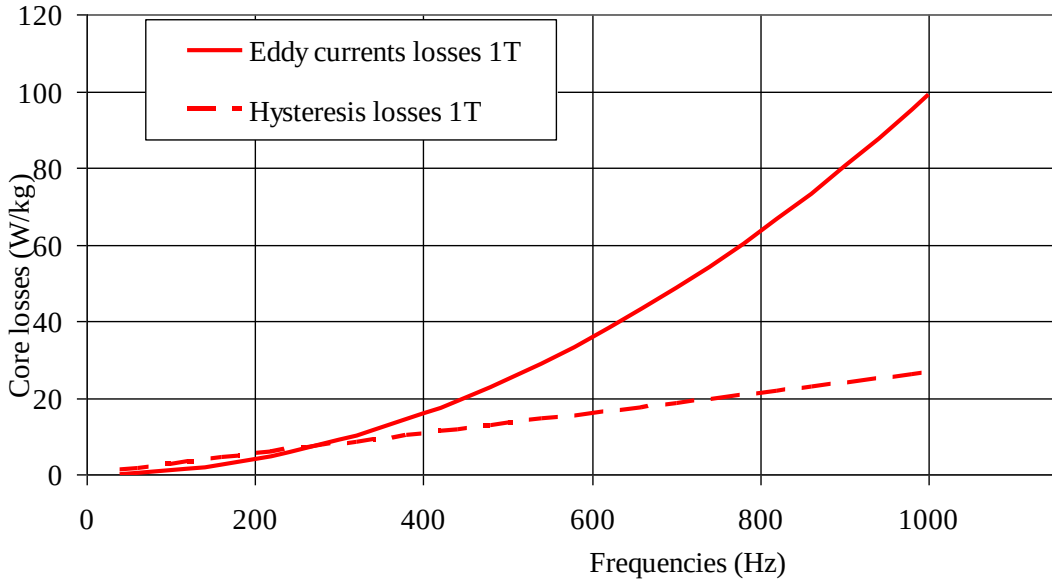

Figure 95: Hysteresis and Eddy current losses in SL-SMC. (in the direction of easy magnetisation)

The graphs in Figure 96 were drawn from eq. 45, 46 and 47, which model, respectively, core losses in magnetic circuits made with SL-SMC, SMC [129] and M19 rolled sheet steel [129]

$$\frac{P_{Core\_SMC}(f,B)}{m} = 0.18B^{1.7} f + 5\cdot 10^{-5} B^2 f^2 \quad (46)$$

$$\frac{P_{Core\_M19}(f,B)}{m} = 0.024B^{1,7} f + 6\cdot 10^{-5} B^2 f^2 \quad (47)$$

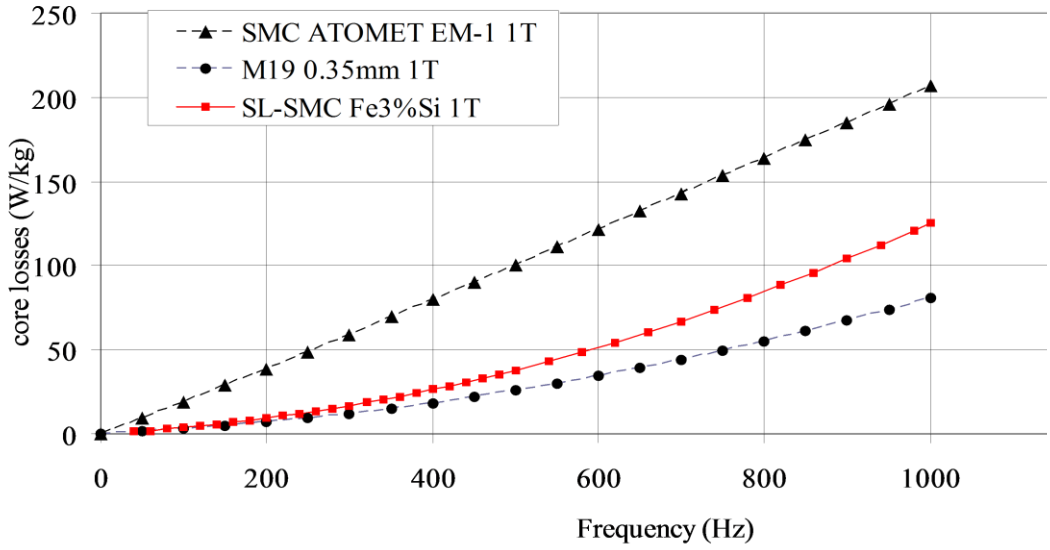

Figure 96: Losses as function of frequency of an applied field for SMC, rolled steel sheet and SL-SMC (easy direction).

One can see that the SL-SMC part has a magnetic behavior comparable to that of rolled sheet steels. The scale of Eddy Current will be influenced by the thickness of lamellar particles and the electrical resistivity of the alloy, as in rolled sheet steels. The thickness of the coating also influences Eddy Currents between particles, which affect losses. Due to its molding properties, SL-SMC's could constitute an advantageous option as compared to SMC's and to rolled sheet steels, for certain machine topologies.

Similar measurements were carried out on a parallelepiped sample of the lamellar material for the hard direction to magnetise. The results are

reported in Figure 97. The core losses this time were mathematically modelled for the unfavourable direction (see eq. 48).

$$\frac{P(f,B)}{m} = 0.30B^{2.87}f + 6.23\cdot10^{-3}B^2f^2 \tag{48}$$

Figure 98 shows the contribution of each type of loss. In the hard direction, the eddy currents are more important because they circulate on the particle's plane. Effective electrical insulation thickness is thus limited to something above 2 mm taking into account inter-particle contacts. Regarding hysteresis losses, in this direction, the thickness of metallic grain is limited by the thickness of particles (125 µm). As with regular SMC's, each particle interface can be considered as an air gap, limiting permeability by harming the movement of Bloch walls and producing demagnetizing fields.

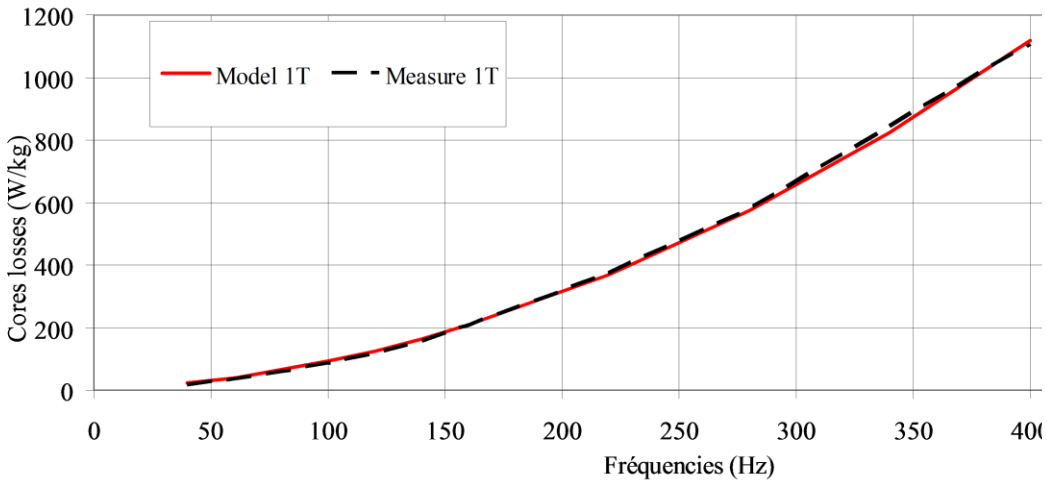

Figure 97: Real and modeled core losses as a function of frequency of an applied field for SL-SMC (hard direction).

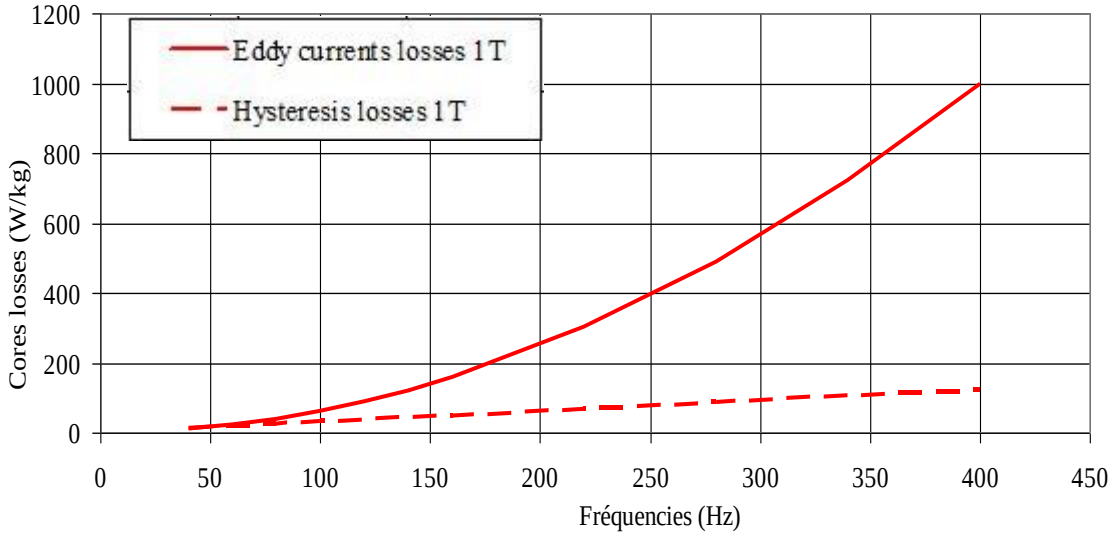

Figure 98: Hysteresis and Eddy current losses in SL-SMC. (hard direction)

Table 13 presents the mechanical properties of hot forged, iron-silicon based, SL-SMC's, as compared to a SMC which uses a 1% resin as an insulating and binding coating.

Table 13: Mechanical properties of SL-SMC and SMC parts studied

Identification	Density (g/cm^3)	TRS (MPa)	UTS (MPa)
SL-SMC	7.40	210	95
SMC[1]	7.1	124	-

[1]: Atomet EM-1 Registered mark of Quebec Metal Powders Ltd (Rio Tinto Metal Powders)

6.2.2. Interest of SMC in the design of Clawpole Transverse-flux Machine with Hybrid Stator

Studies of Transverse-Flux Permanent Magnet Machines (TFPM) have shown a good potential for very high force densities leading to very compact electrical machines. In [130], a theoretical study based on double-rotor, double sided TFPM geometry with flux-concentration, as shown in Figure 99 left, indicates that force densities up to 200 kN/m^2 are possible.

Among the various geometries proposed for TFPM machines [131], one finds the Clawpole TFM proposed by [132]. In Figure 99 Top, the Clawpole TFM has the advantage of single-side stator and a single row of permanent magnets. These characteristics greatly facilitate the machine's construction and manufacture. With the Clawpole TFM, the flux density vector has high components in 3 dimensions, mainly in the stator core. It thus requires the use of SMC's for the stator core. The force density of TFPM machines is strongly dependent on pole pitch and air gap thickness [133,134]. The TFM's generally have a high number of poles and thus, short pole pitches. The combination of short pole pitches and SMC material, leads to high core losses in the stator. In M. Dubois, N. Dehlinger, H. Polinder and D. Massicotte [129], a solution is proposed for

the reduction of iron losses in the Clawpole TFM by using a combination of Fe-Si rolled steel sheet and SMC's in the stator; see Figure 100.

Laminations are used to carry the flux around the coil, while SMC are used near the air gap to deviate the flux coming from the air gap towards the laminated C-core. The use of SMC material contiguous to an air gap on the rotors and stators provide easy machining of rotors and stators, thus leading to very thin air gaps. These can be as little as 0.55 mm. In the rotor, flux-concentrators are also made of SMC for this reason.

The available flux in the air-gap is limited by the permeability (reluctance) of the concentrators, as well as by their maximal flux density. In certain TFPM machines, concentrators are made by rolled sheet steel [131]. But in this case, the air gap cannot be kept low and regular. In fact, a stack of steel sheets cannot be machined easily, and it would be intricate to use sheets with different widths, so as to assemble concentrators. Thus the global reluctance in such kind of machine is high due to thicker air gaps, which, in turn, limits the flux in the stator. Parts made with SL-SMC's were molded. Bow forms can be obtained.

Moreover, as parts are highly dense and sintered, they can eventually be machined. Thus, SL-SMC is an interesting material for making flux-

concentrators with low reluctance, high flux density and low losses, without increasing the machine air gap.

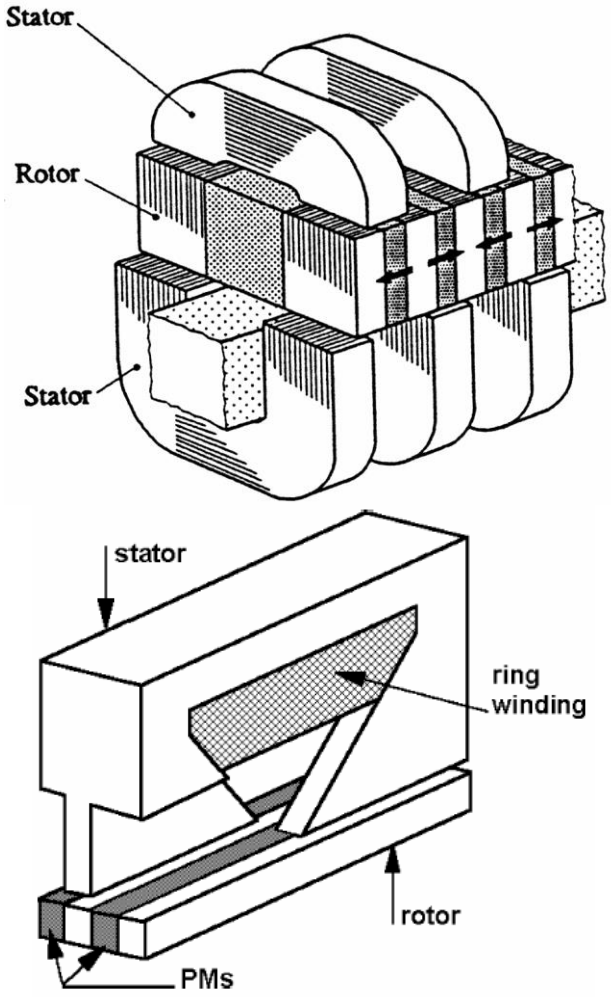

Figure 99: Top: Double-rotor, double sided TFPM geometry with flux-concentration. Lower: Clawpole TFM concept, with full SMC stator[132].

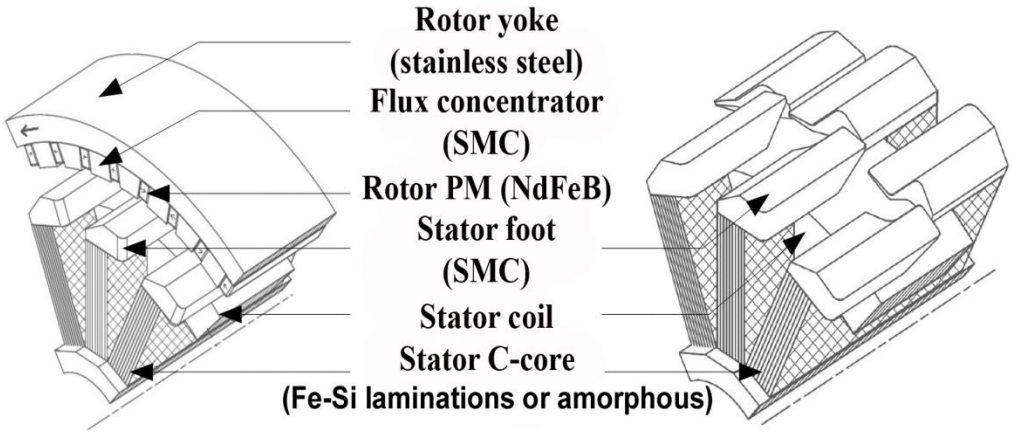

Figure 100: Clawpole TFM with Hybrid Stator [129]

6.2.3. Evaluation of the performances of Clawpole TFM with concentrator made with SL-SMC

Using the 3D Finite Element Analysis (FEA) magnetostatic package, MagnetVI® from Infolytica, we (P. Lemieux, J. Delma, M. Dubois) [135], evaluated the impact of a SL-SMC, by incorporating it into the design of the Clawpole TFM with a hybrid stator of Figure 100. We compared two machines, one with concentrators made with SMC's and the other with SL-SMC's.

Figure 101 presents the B-H curve of the materials used in simulation. The magnetization curve of the SL-SMC for its easy direction is determined from the setting described in

Figure 93. It was not possible to determine exactly this curve in the hard direction, because the amorphous material used to channel the

magnetic flux through parallelepiped samples saturates before the parallelepipeds themselves. In fact the parallelepipeds have a maximum induction above 1.5 T while the amorphous materials saturate just above 1T. In Table 12, we can see that SL-SMC part also has a good permeability in its hard direction. We then assumed that the B-H curve is isotropic for the simulation. Core losses are modelled using eq. 45 and 48 for SL-SMC's and equation 46 for SMC's. Knowing the variation in magnetic induction in each direction of the parts and knowing the parts density (see Table 13), core losses can be determined.

The geometry used for the comparison is shown in Figure 102. In this application, the concentrator's easy directions are directed according to machine radius and its rotation axis. Symmetrical boundary conditions are imposed in the calculations; accordingly, a single pole pair of the machine needs to be considered. Flux and torque are computed for 24 different positions in one cycle; that is for every 15 electrical degrees. In calculation A, the concentrator's material chosen is SMC, while in calculation B, the concentrator's material is the SL-SMC.

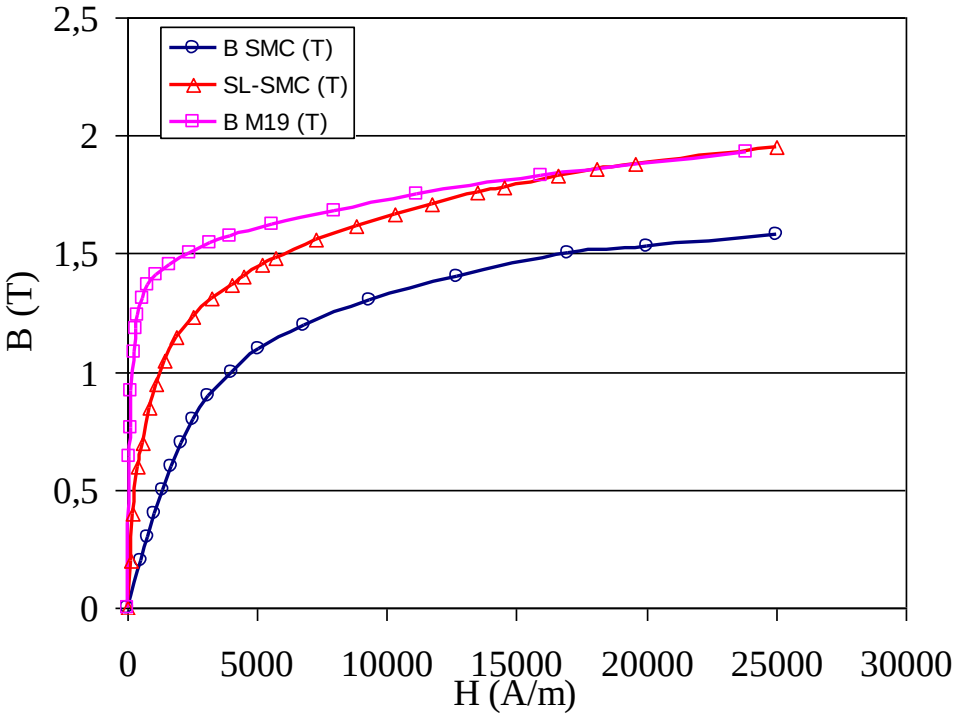

Figure 101: B-H curves of SL-SMC, SMC and laminated steel used in the FEA calculations.

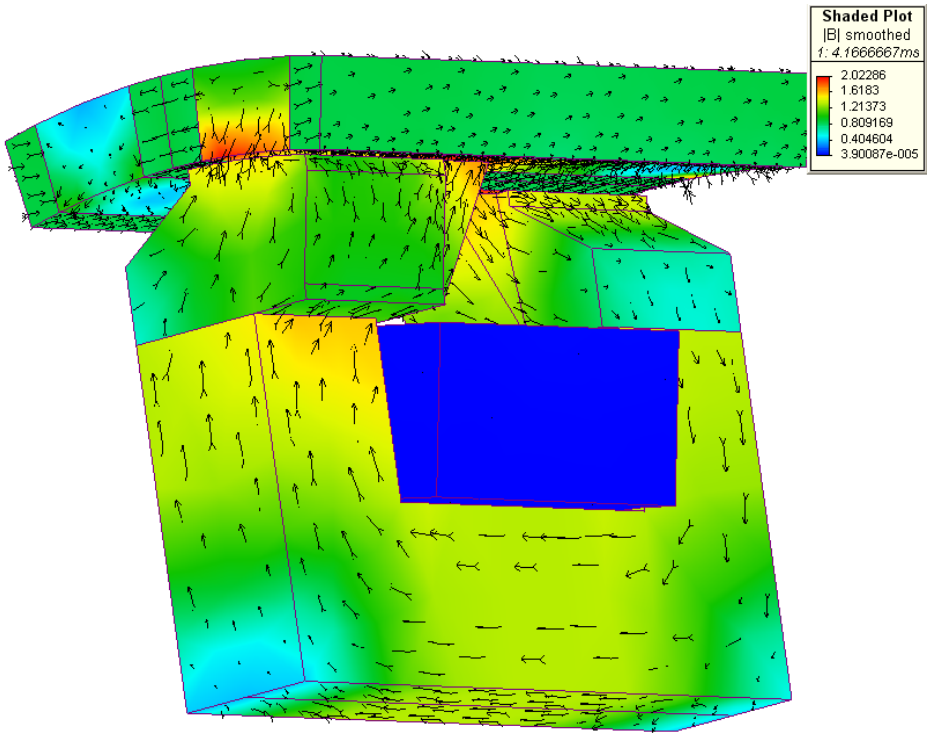

Figure 102: One pole pair of the clawpole TFM used in the FEA computation.

Considering the machine in Figure 102, with 30 poles (p = 15) used as a generator at 240 RPM, the No-load induction in the C-core is plotted, for each type of concentrator, in

Figure 103, as a function of time for one electric period. We can see a substantial increase in the maximum induction when the concentrators are made with Fe-3%Si, SL-SMC, compared to an SMC concentrator. The 13.6% increase is due to the higher permeability and the higher magnetization of the SL-SMC. It reduces the reluctance of the machine and increases the magnetic induction available in the machine air gap. This increase of the induction will be directly reflected in the apparent power of the machine. A slight modification in the design of the concentrators, the permanent magnets and/or the stator foot in order to optimise it for the use of the SL-SMC material, could have given slightly better results. For quantitative comparison, however, the designs were kept identical, in order to validate all the results with a real bench test.

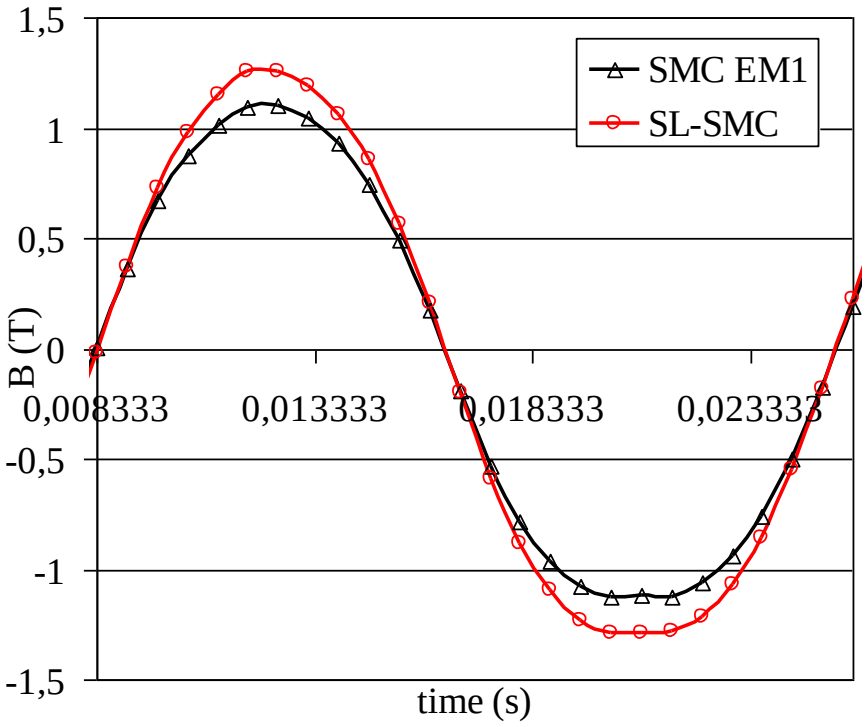

Figure 103: Induction in the C-core when no charge is input to the machine

Table 14: Influence of SL-SMC on the performance of a Transverse-Flux Machine with Hybrid Stator (simulation)

Concentrator material	No-load RMS induction in C-core	No-load core losses in Concentrators due to fundamental frequency	Total no-load core losses in the machine
	(T)	W	(W)
SL-SMC	0.90	33.9	96.13
Powder SMC	0.78	38.5	94.14

As shown in Table 14, the no-load core losses in SL-SMC concentrators are 12% less important than those in the SMC

concentrators. The simulation shows that the alternative component of the magnetic field in the concentrators has three dimensions. The decreasing of the core losses indicates that this alternative component varies mainly in the concentrator's "easy" directions. The increase in the magnetic flux in the air gap and accordingly in the stator, naturally leads to an increase in the stator core losses, particularly in the stator foot. However, the stator foot is still produced using SMC material in the mathematical model. Because of the important increase in the stator core's losses, the machine's global core losses are increased by 2% as shown in Table 14. However, this increase in losses is much lower than the increase in the apparent power of the machine (13.6%), giving a more efficient machine, *in toto.*

If the scenario is to run the machine at the same power output, it is important to note that the simulation of the total losses of the machine with SL-SMC does not also take into account the resistive losses (Joules losses) in the electrical copper winding of the machine. Less copper winding would be needed for the machine, for the same power output, since it runs at a higher total induction with the SL-SMC.

For future work, in addition of doing a bench testing validation of the simulated values, the replacement of the stator feet by SL-SMC could give

different results. We know that this intricate geometry component, still fabricated as an SMC, contains important three dimensional components of its magnetic field, and that the path of the magnetic field lines are complex. The simulation is difficult to do at this stage because we have, first of all, to determine the best way to press it, in one or many sub-parts, so as to maximize the orientations of the lamellae in the main direction of the field path.

Overall, simulations obtained by using the properties of the new composite in its different directions in a clawpole transverse-flux machine with an hybrid stator demonstrates that the lamellar composite is highly advantageous, even if the material is not always exposed to a field only oriented in its easy direction.

6.3. COMPOSITES IN INDUCTION MACHINES VS PERMANENT MAGNET MACHINES

The total performance of an electro-mechanical device like a motor or an alternator is dependent upon its total magnetic permeability. According to the following equation [136],

$$f = \mathrm{N.I} = \mathrm{H.L} = \frac{B.L}{\mu_{tot}} = \phi \Re_{tot} \tag{49}$$

and to

$$\Re_{tot} = \Re 1 + \Re_2 = \frac{1}{A}\left(\frac{L_1}{\mu_1} + \frac{L_2}{\mu_2}\right) = \frac{L_{tot}}{A\mu_{equ}} \quad (50)$$

where

f is the magnetomotive force (ampere-turn, A);

N is the number of copper winding turns;

I is the electric current (A);

H is the magnetic field strength (A/m);

L_1, L_2, or L is a partial or the total magnetic circuit path length (m);

B is the magnetic flux density (Tesla or Wb/m^2, or $kg/A.s^2$);

μ_1, μ_2, or μ_{equ} is the magnetic permeability of a part of the circuit or its total equivalent permeability ($=\mu_o\mu_r$, H/m or $m.kg/s^2.A^2$);

ϕ is the magnetic flux (Wb or $kg.m^2A^{-1}s^{-2}$), and

$\Re_1$, $\Re_2$, $\Re_{tot}$ is the partial or total reluctance of the circuit (H^{-1} or $A^2s^2/kg.m^2$).

A is the section of a magnetic flux path (m^2)

For a fixed magneto-motive force, a higher permeability will give a higher magnetic flux density, and then a higher torque or power. We then see that reluctance and not permeability is summed in a magnetic circuit.

We can calculate an equivalent relative permeability, μ_{equ} , for a multi-component circuit from the equation:

$$\mu_{equ} = \frac{\mu_1 \mu_2 (L_1 + L_2)}{(\mu_1 L_2 + \mu_2 L_1)} \tag{51}$$

For an air gap, the relative magnetic permeability μ is 1. A permanent magnet behaves as an air gap regarding its magnetic permeability, since its polarization is fixed. For the soft magnetic materials of a stator or rotor, μ depends on the material (Table 15). If one computes values for the different magnetic materials in a typical 1 HP permanent magnet motor with a large equivalent gap including the magnets (6.25 mm) or an alternative current motor with a very narrow gap (100μm), both motors having a total magnetic path length of 15 cm, we will obtain the following equivalent permeabilities (Table 15) for the different motors (equation 51).

Table 15: Equivalent magnetic permeabilities of permanent magnet motors (PM) and a AC motors (AC) with a 15 cm flux path.

Soft magnetic materials	Relative permeability (μ_r)	PM equivalent relative permeability (μ_r)	AC equivalent relative permeability (μ_r)
SMC (water atomized)	500	23.5	375
SL-SMC Forged (Fe-Si)	3 000	24.5	1155
Lamination M-19	5 000	24.6	1305

From these results, one sees that for permanent magnet motors, a decrease in the soft magnetic material's permeability is not too critical for overall motor performance. The water atomized SMCs lead to a 4% decrease in the equivalent permeability. However, for a smaller gap machine such as an AC motor, the handicap is tremendous, decreasing permeability by a factor 3 compared to lamellar composites. The lamellar composite suffers only 11% equivalent permeability decrease compared to the standard M19 lamination steel. These results well illustrate why Lamellar SMC could potentially be used in any motor configuration compared to water atomized SMC, which are limited to permanent magnet motors.

6.4. ESTIMATION OF THE ELECTRICAL RESISTIVITY OF THE COMPOSITE

Since this composite is not isotropic, a standard 4 point measure of electrical resistivity does not give a representative value of the behaviour of the composite in an alternative field. In fact, Eddy currents will develop in a direction which depend of the applied field, and thus will be limited by the insulation present on lamellae particles as witness the good results of losses with the developed composite when the field is applied to its best orientation. A direct measurement will give the resistivity in surface and

parallel to the lamellae particles, which are well electrically bounded to each other. It is however possible to deduct the value of the effective electrical resistivity of the composite relative to its different directions by using the classical loss equations derived from Maxwell's equations [137] , and by comparing the new composite with common isotropic material with well-known and measured electrical resistivity. Losses equation can be expressed as :

$$P = P_h + P_e = k_h f B^n + k_e f^2 B^2 \quad (52)$$

Where P_h stands for hysteresis losses, and P_e for Eddy current losses or what is commonly named classical losses, K_h, K_e and n are constants, f and B are the frequency of the field and its peak induction.

More precisely, for a plate or a foil, we can state that :

$$P_e = \frac{\pi^2 \sigma d^2}{6} (Bf)^2 \quad (53)$$

or for a ring of rectangular shape [138]

P_e (W/m^3)= $\frac{\sigma \pi f^2 B^2 A_{sq}}{4}$ in term of losses per unit volume or :

P_e (w/kg)= $\frac{\sigma \pi f^2 B^2 A_{sq}}{4\rho}$ in term of losses per unit mass

Where

σ is the electrical conductivity of the material ($1/\rho$, x10^6 ohm^{-1}m^{-1} or 10^6 siemens/m)

d is the thickness of the foil or lamination (m)

A_{sq} is the square section of the ring (m^2)

ρ is the density of the material (kg/m^3)

From the section 7.1.1 of the present thesis, equation 45, 46 and 47 gives the values of all those constants for rectangular section rings made with SL-SMC, Atomet EM-1 made SMC and a stacking of M19 Fe-3%Si non oriented silicon steel. Equation 48 gives the constants for the SL-SMC polarized in its worst direction. Those equations are repeated here for the ease of analysis.

Equation 45, 46, 47, 48 repeated from the section 7.1.1

$$\frac{P_{Core\_SMC}(f,B)}{m} = 0.18B^{1.7}f + 5\cdot10^{-5}B^2f^2$$ Atomet EM-1 SMC,

$$\frac{P_{Core\_SL-SMC}(f,B)}{m} = 0.026B^{2.07}f + 9.9\cdot10^{-5}B^2f^2$$ SL-SMC with 125µm thick Fe-3%Si lamellae

$$\frac{P_{Core\_M19}(f,B)}{m} = 0.024B^{1,7}f + 6\cdot10^{-5}B^2f^2$$ M19 at 350 µm thick lamination (Fe-3%Si).

$$\frac{P(f,B)}{m} = 0.30B^{2.87}f + 6.23\cdot10^{-3}B^2f^2$$ SL-SMC same but in its worst direction

It can be seen that K_e, for the same dimensions and similar density values for the SL-SMC is double , at 9.9×10^{-5} , compared to the ATOMET EM-1 SMC at 5×10^{-5}. The typical electrical resistivity of Atomet EM-1 is 15 000 µ-ohm-cm. The SL-SMC analysed in section 6.2 thus has an electrical resistivity around 7500 µohm-cm, which is 150 times superior to the resistivity of the Fe-3%Si composing it. If the SL-SMC is polarized relative to its worst direction, its electrical resistivity is this time 6.23×10^{-3} which is 110 times more conductive than Atomet EM-1. It gives an electrical resistivity around 136 µohm-cm, which is still about three times more resistive than the base Fe-3%Si strips used to fabricate the lamellae particles. It is interesting to see that even in the worst direction, the coating still has an appreciate contribution to the electrical resistivity of the ferromagnetic material used.

Finally, from the first part of the equations 45, 46, 47 and 48, K_h can be deduced, and in this case, its value is proportional to the inverse of the relative permeability of the material for low frequencies where the skin depth of the field is higher than the foil or particle's thickness or diameter, as expressed by [139]:

$$K_h = 2 f S/\mu$$

Where S is a form factor, and μ is the magnetic permeability of the material.

It tells us that the SL-SMC has a permeability that is 0.18/0.026 or 6.9 times higher than the permeability of Atomet EM-1 SMC, which is typically around 300. It fits with our measured results. We can see also that the permeability of the SL-SMC is very similar to the one of M19 laminations, with a K_h value 0.026, vs 0.024, or only an 8% lower permeability.

For the worst direction of polarisation, we get a K_h value of 0.3, but it must be mentioned that this inserted parallelepiped in the amorphous core was an assembly of many small ones machined in a TRS bar, so it is possible that this value gives a worse picture than what we really have in the transverse direction to the lamellae particles. Air gaps might have remained in this assembly. It would give a permeability close to half of the Atomet EM-1 value, for a thickness of ribbons very close to the average particle size of Atomet EM-1. It would be surprising to get a lower value, particularly since a total anneal and grain coarsening take place with the SL-SMC and not with the Atomet EM-1 epoxy resin insulated and cured at only 200 to 300°C.

Chapter 7 CONCLUSIONS

The concept of direct casting presented allows for a complete emptying of the tundish, a short metal residence time under a “First In-First Out” configuration, inclusion float out, and surface protective slag stability like any tundish bottom pouring. This is unlike the usual melt drag process. It allows also for a precise thickness adjustment through the use of a gate. The mathematical model developed was validated with tin casting experiments. This model predicts a successful casting operation with Fe-3%Si, for a comfortable window of speed under 50 cm/s, a 3 mm slit opening, or contact length, and a casting temperature 50 K above the liquidus temperature of the alloy.

Due to its no flow characteristics in a standard production press feeder, or in a Carney or Hall flowmeter, these lamellae powders require a pre-feeding or pre-compacting station, using vibration, and a specially adapted design to feed a production press. However, with that adaptation, it was possible to reach a part to part weight variation similar to any other standard powder pressing operation (standard deviation of 0.5%) at a speed of 5 parts per minute.

The green strength of Fe-3%Si SL-SMC, which has a very low compactability, i.e. 6.5 g/cm3, is very low at 50 tsi, compared to irregular shaped powders. The latter SMC's can form interlocking regions and/or anchoring sites while deforming under pressure. Consequently, this grade, which needs a hot forging operation in order to reach convenient densities for magnetic applications, can still reach an acceptable level of green strength to be manipulated for subsequent operations, by using the proper binder-lubricant, or by using die wall lubrication without any lubricants (3.5 to 4 MPa).

The green strength of pure Fe and Fe-Ni SL-SMC's are typical of any other powders in powder metallurgy. Furthermore, with the use of a good binder-lubricant, they can reach values above 60 MPa, which is about five times what is typically reached in the PM industry with water atomised powders. It is partially due to their very high compactability, reaching densities above 7.35 g/cc for a compacting pressure of only 50 tsi. The three point bending test is also advantageous to the lamellae composite, provided particles are oriented perpendicular to the applied force, which was the case in the tests conducted.

- SL-SMC exhibits ductile behavior under stress, with slow delamination rather than abrupt failure.

- Mechanical properties of SL-SMC range from values reached with the best SMC's on the market (100 MPa), to close to those reached with the same wrought alloys (700 MPa), depending on the consolidation process and the sintering treatment selected.

The SL-SMC process at the time of writing this thesis gives typically the following properties, respectively, for Fe, Fe-3%Si, Fe-47.5%Ni, FeCo:

- Losses at 1 T 60 Hz of 3-5 W/kg, 1.5-2.5 W/kg, 0.9-1.5 W/kg, 4.5 W/kg;
- Bmax at 12 000 A/m of 1.65-1.75 T, 1.60-1.70 T, 1.3-1.5T and 1.85-2 T;
- μmax of 1000-1500, 1000-5000, 2000-16000 and 1350.

The optimum sintering temperatures for the grades are as follow:

- Pure iron without additives: around, or above, 1200°C, with coarse aluminium powders, not yet determined, with BN, around 1120°C but BN is mostly useless;
- Fe-3%Si, without additives or with Al: around 1175°C to 1200°C, with BN at 1150°C;
- Fe-Ni pure or with any of the additives tested: 1150-1175 °C;
- Fe-Co pure: above 1200°C (not yet known). With BN, 1175°C.
- The grain growth oscillation thermal treatment around 910°C for pure iron SL-SMC is tremendously beneficial to its properties, particularly after a sintering at only 1120°C, as it can cut losses by up to 30%.

- Maximum Induction is a linear function of the density. Higher densities values are obtained with DPDS and Hot Forging.
- SL-SMC's give the same level of maximum induction as standard laminations of the same alloy at a comparable density or stacking factors. These are higher values than standard SMC's on the market.
- SL-SMC gives maximum relative permeabilites more than double those compared to equivalent SMC's, close to values given by wrought alloys in their best conditions. This property is very process sensitive, improving with grain size, density, purity, and particles joint strength, which is helped by longer thermal treatment at higher temperature.
- Hc values typical of the best laminations on the market, and less than half of other SMC.
- Losses are at their lowest values when sintering at 1175°C,for10-30 minutes, for all alloys studied.
- Losses less than half those of SMC's at 60 Hz, which are double the best laminations currently on the market, as tested with an Epstein Frame. The Epstein Frame test for lamination does not reveal consolidation of stacking effects like edge welding or residual stress.
- Losses are similar at 400 Hz for SMC, SL-SMC and lamination stacking.

- Based on mathematical modelling of different motor topologies, thanks to its high permeability values, the SL-SMC process is capable of supplying composites that give only a minor decrease in the performance of conventional 2 D design motors without permanent magnets, with thin air gaps like induction machines. These designs were developed for the lamination stacking technology more than 100 year ago. If designs are reviewed as was done for permanent magnet motors, employing SMC recently launched to the market, to fully take the 3D design advantage given by the composites, SL-SMC could produce motors with never before reached levels of performance and power densities levels, without permanent magnets, It could become very important with the shortage of supply and the strategic issues affecting the rare earth elements extraction and magnet industry these days.
- In recent 3D design comprising permanent magnets like Transverse Flux Permanent Magnet (TFPM) topologies, the use of SL-SMC in some parts of the machine can bring an improvement to the total power by up to 13%, and a decrease in the losses of the machine as compared to other water atomised SMC, as was demonstrated by a complex computer modelling exercise using the measured properties in

the good and bad direction. From that modelling exercise, using the curve fitting equations developed to fit the experimental values obtained, it was possible to determine that the SL-SMC composite typically develops an electrical resistivity in its best direction that is 150 times superior to its used base alloy. This value goes to only three times in its worst direction of polarization. In its best direction, it means that SL-SMC's exhibit resistivities that are only half the resistivities of other composites made with typical water atomised particles, totally encapsulated. From that same curve fitting exercise, it appears that SL-SMC relative permeabilities are typically seven times higher than other SMC's, whose particles are totally encapsulated.

- Improvements are still possible for Fe-Co and Fe-3%Si through a better forging process and also a better choice of alloy. It includes higher temperature pre-heating, higher speed forging with the use of a hammer press, and the replacement of H13 tools by stainless steel 420 for lower heat conduction during deformation. Regarding the alloy, limiting the silicone level to 1 or 2 % would increase the compactability and remove the need for a forging process. Limiting the cobalt content will allow higher temperature for forging or sintering without the problems associated with structure re-ordering.

- For all the alloys studied, improvements are still possible through the development of better performing coatings, the use of additives, or infiltrate, during sintering. This could form a liquid phase (transient or not), such as the aluminium powders used in the present study. Aluminium contents will be pushed up to 2% to further evaluate its potential and will be added also as an infiltrates after pressing, rather than as an additive.
- Copper, tin and nickel based commercial brazing alloys will also be tested for the infiltration process. The goal is to enhance diffusion between particles that can lower sintering temperatures without harming the efficiency of the alumina coating. Aluminium powder additives clearly showed indeed that it does not harm electrical resistivity and could potentially help the DC and mechanical properties. More tests are needed to validate the potential. It is not sure if the effect of the powders could have the same impact as an evaporated under layer of aluminium under the alumina coating, as was done with PVD technology in the past.
- SL-SMC did not show any significant deterioration in properties as the sintering temperature was increased up to 1200°C. Properties need to be studied following even higher sintering temperatures.

FUTURE WORK

The future work for the development of this technology is first of all to modify the tundish developed, so as to incorporate $MoSi_2$ permanent heating elements in the refractory, and to heat the tundish to a temperature very close to the casting temperature, i.e. above 1600°C, in order to avoid slot clogging. With that addition, it should become easy to cast thin ribbons of the desired thickness. We will then have to develop the proper surface treatment to remove oxidation on the ribbon surface, or to install an atmosphere chamber all around the casting zone and the cooling zone of the ribbon, in order to avoid exaggerated oxidation. Tests of Sol-Gel Coating adhesion on different surface finishes, including plus or minus oxidation, will need to be done. The sub layer of aluminium will also have to be tested to see if we can significantly improve the composite's insulation. It is proposed to also test other coatings, like SiO_2, or MgO. The latter is supposed to adhere better to iron surface, due to the better matching between the lattice parameter of iron and MgO. A multilayer of SiO2, Al_2O_3 and MgO, could also be beneficial, giving more deformability at high temperature during the sintering or forging operation. A ceramic eutectic could in fact be produced, which might decrease the fusion point

of the ceramic alloy. As soon as we will able to cast our own ribbons, we will be able to play on their thickness and their composition. Thickness and composition variation on the properties of the composite would be interesting to study. Many other designs of machines can be tested by playing on the direction of pressing or lamellae orientation. It will be interesting to determine the effect of the imperfect orientation of particles that we produced all along this study, in the rings with very narrow sides or cross section. In order to verify that point, we need to press a disc rather than a ring, and cut a ring in the disc to have a better lamellae orientation. Continue to better characterize the effect of Fe_3P or Al and Fe_3O_4 particles added to the SL-SMC material, to better sinter the edges, or better insulate the edges. Infiltrate the remaining porosities to give better strength, impregnate with a epoxy resin. Due to capillarity and the form of particles, this kind of lamellae composites have completely open porosities even well above 95% density and really suck liquids. This was verified using water, during water displacement density measurements.

CONTRIBUTIONS TO ORIGINAL KNOWLEDGE

To date, direct casting technologies for casting very thin ribbons have been used exclusively as a means to reach amorphous or nano-crystalline metal structures, mainly under controlled atmospheres. With the exception of a South Korean team and K. Akitsu et al. [23, 24, 29], all research has been focussed on finding the best parameters, configuration, and set up, to reach specific metallic structures (e.g. amorphous metals and alloys through rapid cooling), with little regard to the cost of the process or ease of operation. Typical melt spinning and planar flow casting devices need external pressurization of the liquid metal so as to pass the metal through a narrow slot set above a rapidly spinning copper wheel. These are therefore, by definition, batch processes. In addition to this, from our knowledge, there has been no previous CFD modelling effort of this kind of rapid solidification technique for very thin ribbon.

One essential novelty of the research presented, therefore, is the development a net shape, sheet casting process, that is capable of producing very thin laminates of acceptable uniformity in thickness, in the easiest way, at the lowest cost, using a continuous process at a moderate speed without the need of an external pressure. An amorphous or micro-

crystalline structure was not the target of the present research, since a grain coarsening treatment is applied to optimize magnetic properties. The ribbons cast will be ductile and of high iron content, maximizing magnetic induction properties at minimum cost. The approach presented is based on the single wheel melt drag process at 45 °. The South Korean team and K. Akitsu et al., mentioned above, have conducted a research project very close to what we have done here, but with different alloys. They did not develop a computer fluid dynamic model involving solidification to simulate their experiments. In our case, we were able to positively validate the model developed with casting experiments using pure tin. The model predicts easy casting operations with the iron based soft magnetic ribbons needed for the SL-SMC process. The model allows us to determine the thickness solidified at the tundish outlet and the temperature distribution everywhere in the tundish and at the outlet, associated with the amount of recirculation occurring in the tundish. With the model developed, we can predict under which conditions, where and when, the risk of clogging is high, and to adjust the design of the tundish and its preheating so as to assure good operating conditions. This work proves that it is possible to directly cast at low speed (less than 1 m/s) and in continuous operation, ribbons 200 μm thick. Those ribbons can be advantageously used after

one pass of rolling, to produce performing SL-SMC's. It was too difficult to produce good casting conditions during the time of this PhD with iron based material, due to insufficient preheating capacity for the tundish developed. The model was thus validated with a low melting temperature material, pure tin.

It appears that this new concept of direct casting of ribbons, consisting of a 45° tilted dragging set up, allows for a complete emptying of the tundish, a short metal residence time, under a "First In-First Out" flow configuration (no dead zone, straight flow), inclusion floating capability and surface protective slag stability like any tundish bottom pouring, and unlike usual melt dragging processes. It allows also for a precise thickness adjustment of the produced ribbon through the use of a gate.

Another contribution to original knowledge is that for the first time, soft magnetic particles have been consolidated with real metallic bonds between particles, so as to form a new kind of soft magnetic composite. This new processing approach represents a clear contribution to original knowledge, as our worldwide obtaining of patents bear witness. The performance of this composite, which exceeds every other composite on the market regarding mechanical properties, maximum induction,

permeability and losses at 60 Hz, testifies to the originality of this new approach.

We proved through this work that it is possible to keep eddy currents to an acceptable level in a consolidated part, even if electrical contacts occur between lamellar particles (at edges). Because of the high form factor of the lamellae particles (2 mm x 2 mm x 70 μm) and the well performing layers of refractory insulation developed, it becomes possible to form metallic joints for giving high mechanical strength composites, but still with low energetic losses. This technology is possible only with a mass process that allows for a coating operation on the flat main faces of the lamellar particles, but not at their edges. We proved that a low electrical resistivity composite when measured with a four point electrical conductivity surface technique, still have low energetic losses due to the use of high form factor lamellae, when used on its best orientation.

Accordingly, additional novelty can be found in the coating type that was developed for the particles. For the first time, an economic mass production coating technology was formed using a Sol-Gel spray technology. Very few investigators have used Sol Gel technology to coat particles for soft magnetic composites [70]. In all those cases, it was done using a very slow dipping process. We have developed a Sol-Gel Spray

process to coat ribbons rather than a dipping process, in order to be able to improve deposition speeds (from 1 mm/s to more than 30 mm/s) for very thin insulating layers (~0.1-0.8 μm). The approach allowed for full annealing and grain coarsening treatments on final parts, because So-Gel decomposition forms refractive ceramic layers such as silica, titania, alumina, or others.

It proved to be an efficient process, with long sintering treatment under a reducing atmosphere at high temperature and with hot forging step to fully densify parts while keeping sufficient insulation to control Eddy current losses. The process of this work was developed with a cheap alumina precursor and it involves only water as a solvent, which make it an environmentally safe process.

Soft magnetic composites have never been hot forged to full density because it has been necessary to keep electrical insulation between their rounded particles. In this thesis work, even if it was not the main objective, optimization of energetic losses as a function of the forging deformation for different field frequency was studied for the first time on a soft magnetic composite.

Finally, it was possible to estimate the electrical resistivity of that kind of anisotropy composite in the different direction compared to its pressing

direction or its main particles orientation in a plane normal to the pressing direction. This was done by comparing its eddy current losses in an AC electromagnetic field to other similar, but isotropic materials. This was accomplished with the help of the Bertotti or Classical equations of the energetic losses in a ferromagnetic part under an alternating field. It was determined that the technology of the composite developed allows for electrical resistivities that are 150 times higher than the base alloy when used in the direction normal to the main particles orientation and 3 times the base alloy, in the direction parallel to the main particles orientation.

LIST OF REFERENCES

1 M. Persson, Developments in soft magnetic components, Metal Powder Report (UK) Vol. 55, Sinter Revolution Supplement, pp.10-11, No. 2000.

2 P. Viarouge, J. Cros, and I. Haouara, "Conception des machines électriques avec des matériaux composites fer-résine," Revue internationale de génie électrique, vol. 5, pp. 299-310, 2002

3 R. M. German, Powder Metallurgy Science, 2nd edition ed. New Jersey: Metal Powder Industry Federation, 1994.

4 A. G. Jack, Exploitation of Soft Magnetic Composites for Electrical Machines", 1998 PM World Congress Special Interest Seminar, Barcelone Spain.

5 J. Cros and P. Viarouge, "New structures of polyphase claw-pole machines," Industry Applications, IEEE Transactions on, vol. 40, pp. 113-120, 2004..

6 A.G. Jack, “Axial Flux Motors Using Compacted Insulated Iron Powder and Laminations - Design and Test Results," Proceeding of the IEEE IEMDC'05 Conference 2005, San Antonio, Texas, USA, pp. 378-385.

7 P. Lemieux, 2004, Patent PCT-CA04-00147, EP 1595267 “High performance magnetic composite for AC applications and a process for manufacturing the same”, 2004

8 Lars Hultman, Zhou Ye, Soft Magnetic composites-Properties and applications, Adv. Powder Metall. Part. Mater., MPIF, Princeton, N.J., USA (2002),14-26.

9 G. Q. Lin, Z.W. Li, Linfeng Chen, Y.P. Wu, C.K. Ong , Influence of demagnetizing field on the permeability of soft magnetic composites. J. of Magn. and Magn. Materials, 305, 2006, pp. 291-295

10 J. P. Papai and C. E. Mobley: Int. Symposium on Casting of near net shape products, TMS, Y. Sahai, J.E. Battles, R.S. Carbonara, and C.E. Mobley, eds., Warrendale, PA, 1988

11 James R. Dale, Wrought Versus Powder Forged Connecting rod, Powder Metallurgy Vol. 48, Number 1 March 2005, pp. 5-5(1)

12 Metals Handbook Desk Edition, Edited by Howard E. Boyer and Timothy L. Gall, ASM, Metals Park Ohio, 44073, Seventh printing 1992, First Edition 1985 p. 26.7

13 Sahai, Y. and Gupta, M., Mathematical modeling of fluid flow, heat transfer, and solidification in two-roll melt drag thin strip casting of steel. ISIJ International (Japan), Vol. 40(2), 2000, pp. 144-152.

14 Sahai, Y. and Gupta, M., Mathematical modeling of thermally induced stresses in two-roll melt drag thin strip casting of steel. ISIJ International (Japan), Vol 40(2), 2000, pp. 137-143.

15 Bao, P. and LI, P., New technologies of high speed twin roll strip casting. Zhuzao (Foundry), 54(9), 2005, pp. 847-851.

16 D. Li, M. Isac, R.I.L. Guthrie, “Study of microstructure and mechanical properties of Continuous cast AA6111 strips following casting, rolling and heat Treatment”, MS&T 2007, Detroit, September 16-20, 2007, Conference Proceedings, pp.321-350.

17 Hazelett Strip-Casting Corporation, 135 West Lakeshore Drive, Colchester, VT 05446, http://www.hazelett.com/contact_us/index.php.

18 CASTRIP LLC, 1915 Rexford Road, Suite 150, Charlotte, North Carolina , 28211, USA, http://www.castrip.com/Contact/contact.html

19 DANIELI, Via Nazionale, 41, 33042 Buttrio (UD) Italy, http://www.danieli.com/

20 F. Zhou , K.Y. He , K. Lu, Kinetics of the Primary Nanocrystallization in an Amorphous Fe-Cu-Si-B Alloy, NanoStructured materials, Vol 9, 1997, pp. 387-390.

21 Liebermann H. and Graham C., Production Of Amorphous Alloy Ribbons And Effects Of Apparatus Parameters On Ribbon Dimensions, IEEE Transactions on Magnetics, Vol Mag-12, No 6, 1976, pp. 921 - 923

22 Arai, K. Tsuya, N. , Ribbon-form silicon-iron alloy containing around 6.5 percent silicon, IEEE Transaction on Magnetics, Vol 16, No 1, 1980, p-126-129.

23 J. Namkung, M.C. Kim, C. G. Park, Magnetic properties of melt quenched Ni–Fe alloy strips, Mater. Sci. Eng. A, 375-377, 2004, p. 1116.

24 Namkung, J., PARK, C.G. and KIM, M.C., Study on the 79Ni-(21-x)Fe-xSi Alloy Strips Fabrication & Magnetic Properties of Their Strips. RIST Journal of R&D, 19(3), 2005, pp. 185-190.

25 J. Namkung, M.C. Kim, C. G. Park, Effect of Si addition on the magnetic properties of melt-quenched Ni–Fe alloy strip Mater. Sci. Eng. A, 449–451, 2007, p. 430.

26 K.M. Lim, S. Y. Park J. Namkung, M.C. Kim, C. G. Park, The relationship between microstructure and magnetic properties of Si-containing permalloy strips fabricated by melt drag casting, Mater. Sci. Eng. A, 449-451, 2007, p. 444.

27 Kim, M.K., Namkung, J., Kim, M.C., Kim, Y.C. and Ahn, Y.S., Thermal Expansion Properties of Fe-42Ni-Si Alloy Strips Fabricated by Melt Drag Casting Process. Journal of the Korean Institute of Metals and Materials, 45(4), 2007, pp. 209-215.

28 Park, S.Y., Lim, K.M., Namkung, J., Kim M.C. and Park, C.G., The effects of Si addition on microstructure and magnetic properties of permalloy strips fabricated by melt drag casting. Scripta Materialia, 54(4), 2006, pp. 621-625.

29 K. Akitsu, T. Haga, S. Kumai and H. Watari: Casting of Aluminium Alloy Strip by Improved Single-Roll Caster, Proc. of 36th Int. MATADOR Conf., Springer, Manchester, U.K., 2010, 2.29.

30 P. Lemieux, R. Angers, "Magnetic Properties of Fe-P-Sn and Fe-Sn Alloys", Advances in Powder Metallurgy and Particulate Materials-MPIF, Princeton, N.J., USA, Vol. 6, 1994, pp.23-35.

31 E. T. Stephenson, A. R. Marder, The effects of Grain size on the core loss and permeability of motor lamination steel, IEEE transactions on Magnetics, Vol. Mag-22, No 2, March 1986, pp. 101-106.

32 De Campos M. F., Teixeira J. C., Landgraf F. J. G., The optimum grain size for minimizing energy losses in iron, Journal of magnetism and magnetic materials, 2006, vol. 301, no. 1, pp. 94-99

33 University of Birmingham, History of Magnetism, http://www.aacg.bham.ac.uk/magnetic_materials/soft_magnets.htm

34 L.P. Lefebvre, S. Pelletier , Y. Thomas, US Patent # 6,548,012, Manufacturing soft magnetic components using a ferrous powder and a lubricant, December 18 2001

35 Bozorth Richard M., Ferromagnetism, New York, Van Nostrand, Chapiter 17, 1951

36 Giorgio Berotti, General Properties of Power Losses in Soft Ferromagnetic Materials, IEEE Transactions on Magnetics, Vol. 24, No. 1, Jan. 1988, p. 621

37 Stanley Charles, Cuthbert Curie, US Patents # 421,067, Art Of Making cores for electro-magnets , February 11 1890.

38 P. N. Roseby, H.M.E. Heinicke, US Patent # 1,859,067, Method of producing Magnetic Materials, Mai 17 1932.

39 K. Kaschke, US Patent # 2,330,590, Dust Iron Core, September 28 1943.

40 G. Katz, US Patent # 2,783,208, Powdered Iron Magnetic core material, January 4 1954

41 Horie Hiromichi, Morita Mikio, Arima Itsuo, US Patent # 4,543,208, Magnetic core and method of producing the same, September 24 1985.

42 Rutz Howard, Hanejko Francis G., US Patent # 5,063,011, Doubly coated iron particles, November 5 1991.

43 Ward Robert W., Gay David E., US Patent # 5,211,896, Composite Iron Material, May 18 1993.

44 G. Roberts, A. Davidson, S. Gair, and J. Hajto, "An overview of the powder processing of soft magnetic composites," Engineering Science and Education Journal, vol. 10, 2001, pp. 237-240.

45 A. Kordecki, B. Weglinski and J. Kaczmar, "Properties and Applications of Soft Magnetic Powder Composites", Powder Metallurgy, Vol. 25, No. 4, 1982, pp 201-208.

46 B. Weglinski, "Soft Magnetic Powder Composites - Dielectromagnetics and Magnetodielectrics", Reviews on P/M and Physical Ceramics, Vol. 4, No. 2, 1990, pp 79-154.

47 L.P. Lefebvre, S. Pelletier and C. Gélinas, "Effect of electrical resistivity on core losses in soft magnetic iron powder materials", Journal of Magnetism and Magnetic Materials, 176, 1997, L93-L96.

48 C. Gélinas, F. Chagnon and S. Pelletier, "Development of an Iron-Resin Composite Material for Soft Magnetic Applications", Advances in Powder Metallurgy & Particulate Materials - 1996, Compiled by Terry M. Caddle and

K.S. Narasimhan, Metal Powder Industries Federation, Princeton, NJ, 1996, pp 20-85 to 20-97.

49 C. Gélinas, Y. Thomas, L. Azzi et P. Lemieux, 2005 “Shaping of Soft Magnetic Powders with improved properties”, in Advances in Powder Metallurgy & Particulate Materials, 2005, Metal Powder Industries & Federation (MPIF), Princeton, N.J., USA, 2005, pp.3.84-3.96

50 A.F. Bandur, US Patent # 2,230,228, Manufacture of Magnetic cores, February 4 1941

51 Soileau Trasimond A., Speaker Lawrence W., US Patent # 4,601,765, Powdered Iron core magnetic devices, July 22 1986

52 Pollock Harriet C., Smith Andrew L., US Patent # 4,602,957, Magnetic Powder Compacts, July 29 1986

53 David E. Gay, US Patent # 5,595,609, Annealed polymer-Bonded soft magnetic body, January 21 1997.

54 Patricia Jasson, US Patent # 5,754,936, Iron powder components containing thermoplastic resin and method of making same, May 19 1998

55 David Lashmore, US Patent # 6,251,514, Ferromagnetic powder for low core loss, well-bonded parts, parts made therefrom and methods for producing same, June 26 2001

56 Edmond Adams, William M. Hubbard, US Patent 2,937,964, Magnetic Flake Core, May 24 1960.

57 Kugimiya Koichi, Sugaya Yasuhiro, Inoue Osamu, Satomi Mitsuo, Hirota Ken, US Patent # 5,352,522, Composite material comprising metallic alloy grains coated with a dielectric substance, October 4 1994.

58 Elgelid Cecilia; Groenlund Anne; Larsson Lars-Aake, Patent WO 02058865, Compressed and heat treated soft magnetic iron-based powder alloys, August 1 2002.

59 Alton R., Opitz Butler, US Patents 3,255,052, Flake Magnetic Core and method of making same, June 6 1966

60 Pavlik Norman M., Cunningham James W, US Patent# 3,848,331, Method of producing molded stators from steel particles, November 19, 1974

61 Reynolds William T., Pavlik Norman M. , Krause; Robert F , US Patent# 4,158,580, and 4,158582, Method of making pressed magnetic core components, June 19, 1979

62 Krause Robert F., Kokal Harold R., Bularzik Joseph H., US Patent # 6,117,205, Soft magnetic metal components manufactured by powder metallurgy and infiltration, September 12, 2000

63 Krause Robert F. , Pavlik Norman M. , Grunert Kurt A., US Patent # 4,265,681, Method of producing low loss pressed magnetic cores from microlaminations, May 5 1981

64 I. P. Gilbert, V. Moorthy, S. J. Bull, J. T. Evans, and A. G. Jack, "Development of soft magnetic composites for low-loss applications," Journal of Magnetism and Magnetic Materials, vol. 242-245, 2002, pp. 232-234,

65 Marc De Wulf, Ljubomir Anestiev, Luc Dupré, Ludo Froyen, and Jan Melkebeek, Magnetic properties and loss separation in iron powder soft magnetic composite materials, J. Appl. Phys. Vol. 91, 2002, p. 7845.

66 O. de la Barrière, C. Appino, F. Fiorillo, C. Ragusa, H. Ben Ahmed, M. Gabsi, F. Mazaleyrat, and M. LoBue, Loss separation in soft magnetic composites, J. Appl. Phys. Vol. 109, 2011, p. 07A317;

67 YouGuang Guo; Jian Guo Zhu; Watterson, P.A.; Wei Wu, “Study of permanent magnet transverse flux motors with soft magnetic composite core,” IEEE transaction on Energy Conversion, Vol. 21, #2, June 2006, p. 426, Sept. 2004.

68 Yunkai Huang; Jianguo Zhu; Youguang Guo; Zhiwei Lin; Qiansheng Hu;, Design and Analysis of a High-Speed Claw Pole Motor With Soft Magnetic Composite Core, IEEE Transaction on Magnetics, Vol 43, No.6, June 2007, p. 2492

69 M. R. Dubois, P. Lemieux, C. Cyr, and D. Massicotte, "Effect of Machining on the Properties of Resin-Based Soft Magnetic Composites," in International Conference on Electrical Machines Greece, 2006

70 Y. X. Pang, S. N. B. Hodgson, J. Koniarek, and B. Weglinski, "The influence of the dielectric on the properties of dielectromagnetic soft magnetic composites. Investigations with silica and silica hybrid sol-gel derived model dielectric," Journal of Magnetism and Magnetic Materials, 2007, vol. 310, no1, pp. 83-91

71 Koch Hans-Peter, Harzer Andreas, Patent US. 6,620,376, “Soft magnetic material and method for manufacturing it”, Sept. 2003

72 Bednarcik Jozef, Kollar Peter, Roth Stefan, Eckert Jürgen, Co-based soft magnetic bulk amorphous ferromagnets prepared by powder consolidation, Physica Status Solidi (a), Volume 199, Issue 2 , Pages 299 – 304, 2003.

73 A. Hsiao, Z. Turgut, M.A. Willard, E. Selinger, D.E. Laughlin, M.E. McHenry, R. Hasegawa, Crystallization and nanocrystallization kinetics of Fe Based amorphous alloys., Proc. MRS Symp. Vol. 577, pp. 551-556; Materials Research Society, Warrendale, PA, 1999

74 Frédéric Mazaleyrat,Valérie Leger, Richard Lebourgeois, “Permeability of soft Magnetic Composites from Flakes of Nanocristalline Ribbon”, IEEE Transactions on Magnetics, Vol. 38, No. 5 September 2002.

75 H. Y. Chang, P. C. Yao, D. R. Huang, and S. E. Hsu, “Magnetic Properties of composite amorphous Powder Cores”, Science and Technology of Rapidly Quenched Alloys Symposium/Boston, Ma, USA, Proceeding Vol. 80, 1987, pp. 423-428, Materials Research Society.

76 Shen B., Kimura H., Inoue A., Omori M., Okubo A., “Preparation of Fe65Co10Ga5P12C4B4 Glassy alloy with good soft magnetic properties by Spark-Plasma Sintering of Glassy Powder”, Materials Transaction, Vol43, No.8, 2002,pp1961-1965

77 Krause Robert F., Pavlik Norman M., US Patent 4,158,581, Method of making magnetic component for direct current apparatus, June 19, 1979

78 R. M. German, Powder Metallurgy Science, 2nd edition ed. New Jersey: Metal Powder Industry Federation, 1994, p. 243.

79 ASTM A976-97, Standard Classification of Insulating Coatings by Composition, Relative Insulating Ability and Application.

80 S. Sakka and K. Kamiya, "The Sol-Gel Transition: Formation of Glass Fibers & Thin Films", J. Non-Crystalline Solids, Vol. 48, 1982, p.31.

81 Kawashima Asahi, Ying Wang, Eiji Akiyama, Hiroki Habazaki, Katsuhiko Asami, Koji Hashimoto, Preparation of protective multiplayer SiO2 and Al2O3 coatings on austenitic stainless steel by sol-Gel Method, Zairyo to Kankyo, Corrosion Engineering, Vol. 43, N. 11, Nov. 1994, pp. 654-659

82 Chengbin Jing, Jinxia Hou, “Sol-Gel Derived Alumina/Polyvinylpyrrolidone Hybrid nanocomposite Film on Metal for Corrosion Resistance”, J. Of app. Polymer Sc., Vol. 105 2007, pp.697-705.

83 S. Schiller, K. Goedicke, J. Reschke, V. Kirchhoff, S. Schneider, F. Milde, Pulsed magnetron sputter technology, Surface and Coatings Technology, Volume 61, Issues 1-3, 1993, pp. 331-337

84 R. S. Nowicki, Properties of RF-sputtered Al2O3 films deposited by planar magnetron, Journal of Vacuum Science and Technology, Vol. 14, 1977, p. 127

85 P. Vuoristo, T. Mantyla, P. Kettunen, Properties of magnetron-sputtered electrically insulating Al203 coatings on copper, Journal of Materials Science, Vol. 27, 1992, pp. 4985-4996

86 R. Cremer, K. Reichert, D. Neuschutz, G. Erkens, T. Leyendecker, Sputter deposition of crystalline alumina coatings, Surface and Coatings Technology Vol. 163–164, 2003, pp. 157–163.

87 I. Safi, Recent aspects concerning DC reactive magnetron sputtering of thin films: a review, Surface and Coatings Technology, Vol 127, 2000, pp.203-219.

88 P. J. Kelly and R. D. Arnell, Control of the structure and properties of aluminum oxide coatings deposited by pulsed magnetron sputtering, Journal of Vacuum Science and Technology A, Vol. 17, No. 3, 1999, p.945

89 C. Pan, P. O'Keefe, and J. J. Kester, MgO Coating by Reactive Magnetron Sputtering for Large-Screen Plasma Display Panels, SID Symposium Digest of Technical Papers -- May 1998 -- Volume 29, Issue 1, 1998, pp. 865-868

90 H. Kupfer, R. Kleinhempel, F. Richter, C. Peters, U. Krause, T. Kopte, and Y. Cheng, High-rate deposition of MgO by reactive ac pulsed magnetron sputtering in the transition mode, Journal of Vacuum Science and Technology A, Vol. 24, 2006, p. 106.

91 R. Cremer, M. Witthaut , D. Neuschu tz, G. Erkens, T. Leyendecker, M. Feldhege, Comparative characterization of alumina coatings deposited by RF, DC and pulsed reactive magnetron sputtering, Surface and Coatings Technology, Vol. 120–12, 1999, pp. 213–218

92 P. Lemieux, Roderick Guthrie, Mihaiela Isac: Alumina coated steels by the sol gel method for a new lamellar soft magnetic composite , TMS 2009, San Francisco, California, 2009, p. 3.3

93 P. Lemieux, Sylvain Pelletier, Yannig Thomas, Mihaiela Isac and Roderick I.L. Guthrie, Development and shaping of lamellar soft magnetic composite, compiled by Thomas J. Jesberger, Stephen J. Mashi, Adv. Powder Metall. Part. Mater., MPIF, Princeton, N.J., USA, 2009, 10.120

94 B.E Launder and D. B. Spalding: The numerical computation of turbulent flows, Comput. Meth. Appl. Mech. Eng., Vol 3, issue 2, 1974, p. 269.

95 Ansys-Fluent 12.0 theory guide, Ansys, Canonsburg, PA, USA, 2009, 17.1

96 Carman, P. C., Fluid flow through a granular bed, Trans. Inst. Chem. Eng. London, 15, 150–156, 1937.

97 V. R. Voller and C. Prakash: A Fixed grid numerical modeling methodology for convection-diffusion mushy region phase-change problems, Int. J. Heat Mass Transfer, Vol. 30, 1987, p. 1709

98 V. R. Voller, A. D. Brent, C. Prakash: The modelling of heat, mass and solute transport in solidification systems, Int. J. Heat Mass Transfer, Vol. 32, No. 9, 1989, p. 1719

99 O. Lenoble, J.F. Bobo, L. Hennet, H. Fischer, PH. Bauer and M. Piecuch, “Structure, magnetism and thermal stability of Fe-Al2O3 multilayers”, Thin solid films, Vol. 275, 1996, p. 64.

100 Ceramic and Glass Materials: Structure, Properties and Processing, edited by James F. Shackelford, Robert H. Doremus, Springer Science, 233 Spring street, New York, NY, 10013, USA, 2008, p18.

101 P. Weiss, L’hypothèse du champs moléculaire et la propriété ferromagnétique J. Phys. 6, 1907, p.661

102 Soshin Chikazumi, Physics of Ferromagnetism, Oxford University Press, New York, 1997, p. 125

103 Yicheng Chen, Pragasen Pillay, An Improved Formula for Lamination Core Loss Calculations in Machines Operating with High Frequency and High Flux Density Excitation, http://users.encs.concordia.ca/~pillay/c28.pdf

104 Seung-Joon Yoo, Ho-Sung Yoon, Hee Dong Jang, Jung-Woon Lee, Seung-Tae Hong, Min-Jae Lee, Se-Il Lee and Ki-Won Jun, “Synthesis of aluminium isopropoxide from aluminum dross”, Korean Journal of Chemical Engineering, Vol. 23 issue 4, 2006, p. 683.

105 Noguchi H., Yoshimura C, Anodizing of aluminum die castings in amine alkaline baths containing fluoride, Hyomen gijutsu (Journal of the surface finishing society of Japan), vol. 40, no12, 1989, pp. 1409-1414.

106 S. Wernick, R. Pinner and P.G. Sheasby, The surface Treatment and Finishing of Aluminium and its alloys, 5th edition, Vol. 1 and 2, ASM International, Finishing Publication LTD., 1987.

107 Kawashima Asahi, Ying Wang, Eiji Akiyama, Hiroki Habazaki, Katsuhiko Asami, Koji Hashimoto, Preparation of protective multiplayer SiO2 and Al2O3 coatings on austenitic stainless steel by sol-Gel Method, Zairyo to Kankyo, Corrosion Engineering, Vol. 43, N. 11, Nov. 1994, pp. 654-659

108 Chengbin Jing, Jinxia Hou, “Sol-Gel Derived Alumina/Polyvinylpyrrolidone Hybrid nanocomposite Film on Metal for Corrosion Resistance”, J. Of app. Polymer Sc., Vol. 105 (2007), 697-705

109 MPIF Standard # 3, Determination of Flow Rate of Free-flowing Metal Powders Using the Hall Apparutus, Metal Powder Industries Federation, Princeton, NJ, 1998.

110 MPIF Standard #48, Determination of Apparent Density of Metal Powders Using the Arnold Meter, Metal Powder Industries Federation, Princeton, NJ, 1998

111 MPIF Standard # 46, Method for Determination of Tap Density of Metal Powders, Metal Powder Industries Federation, Princeton, NJ, 1998

112 P. Lemieux, Y. Thomas, P.E. Mongeon, S. St-Laurent, Benefits of Die wall Lubrication for Powder Compaction , Advances in Powder Metallurgy & Particulate Materials, Metal Powder Industries & Federation (MPIF), Princeton, N.J., USA, 2003, pp. 3.16-3.25.

113 P. Lemieux., S. Pelletier, P.-E Mongeon, Y.Thomas, S. St-Laurent, Combining Electrostatic Die Wall Lubrication and Warm Compaction to Enhance Green Properties of P/M Components, Advances in Powder Metallurgy & Particulate Materials, MPIF, Princeton, N.J., USA, 2002, pp.3-.34 to 3-46.

114 MPIF Standard # 15 Determination of Green Strength by Transverse rupture of rectangular compacts, Metal Powder Industries Federation, Princeton, NJ, 1998

115 MPIF Standard # 41, Determination of Tranverse Rupture Strength of Powder Metallurgy Materials, Metal Powder Industries Federation, Princeton, NJ, 1998

116 ASTM A773-01, Standard Test Method for DC Magnetic Properties of Materials Using Ring and Permeameter Procedures with DC Electronic Hysteresigraph’, ASTM International, West Conshohocken, PA, 2009

117 E. Balomenos, D. Panias, I. Paspaliaris, B. Friedrich, B. Jaroni, A. Steinfeld, E. Guglielmini, M. Halmann, M. Epstein, I. Vishnevsky, Carbothermic Reduction of Alumina, Proeedings of EMC 2011, PP. 729-744.

118 H.H. Hausner, Friction Condition in a Mass of Metal Powder, International Journal of Powder Metallurgy, Vol. 3, Issue 4, 1967, pp.7-13.

119 Gasbare Products, Inc., http://www.gasbarre.com/divisions/gasbarre-fluidized.htm

120 Y. Hashimoto, M. Murakami and Y. Seki, "`Whizz' Solutions Agitate for a Better-Filled Die", Metal Powder Report, Volume 57, Issue 12, December 2002, Pages 26-29

121 Y. Hashimoto, M. Murakami and Y. Seki, "Improvement of Die Filling by "Agitating-Shoe", Advances in Powder Metallurgy & Particulate Materials, compiled by V. Amhold, C.-L. Chu, W.F. Jandeska Jr., H.I. Sanderow, MPIF, Princeton, NJ, 2002, part 4, pp. 252-257.

122 Boies, D., Guillot, M., Carrier, P., Bouassida, S., Tandjaoui, B., « Design improvement of a die filling shoe », Advances in Powder Metallurgy & Particulate Materials, Metal Powder Industries Federation, Princeton, NJ, 2004.

123 Guillot, M., Blanchet, J., Lacasse, J.-F., Bouchard, I., « Study of the effect of an improved die filling shoe on density variations », Advances in Powder Metallurgy & Particulate Materials, MPIF, Princeton, NJ, 2008.

124 http://www.hoganas.com/en/Segments/Somaloy-Technology/Our-Products/For-electric-motors/, 2011

125 Metals Handbook, Desk Edition, Edited by Howard E. Boyer and Timothy L. Gall, ASM Metals Park, Ohio, 44073, 1985, seventh printing 1992, p.20.2

126 P. Lemieux, Sylvain Pelletier, Yannig Thomas, Mihaiela Isac and Roderick I.L. Guthrie "Development and shaping of lamellar soft magnetic composites", Adv. Powder Metall. Part. Mater., MPIF, Princeton, N.J., USA, 2009, 10-120.

127 Chaman Lall, Fundamentals of High Temperature Sintering: Application to Stainless Steels and soft magnetic Alloys, Int. J. of Powder Met., Vol. 27, No.4., APMI, 1991, 315

128 Howard A. Kuhn, B. Lynn Ferguson, Powder Forging, MPIF, Princeton, N.J.,1990.

129 Maxime R. Dubois, Nicolas Dehlinger, Henk Polinder and Daniel Massicotte. “Clawpole Transverse-Flux Machine with Hybrid Stator” ICEM 2006, Chania, Greece, paper 412.

130 Weh H., “Permanentmagneterregte Synchronmaschinen hoher Kraftdichte nach dem Transversalflusskonzept,” etzArchiv, vol.10, no.5, pp. 143 - 149, 1988. [In German].

131 Maxime R. Dubois , Henk Polinder “Study of TFPM machines with toothed rotor applied to direct-drive generators for wind turbines” NORPIE 2004, Trondheim, Norway, June 14-16, 2004

132 Maddison C.P., Mecrow B.C. and Jack A.G., “Claw Pole Geometries For High Performance Transverse Flux Machines”, ICEM 98, Vigo, Spain, p. 340-345.

133 Kang D.H., Chun Y.H., and Weh H., “Analysis and optimal designof transverse flux linear motor with PM excitation for railway traction”, IEE Proc. Electr. Power Appl., vol. 150, no. 4, July 2003.

134 Hasubek B.E., Nowicki E.P., “Design Limitations of Reduced Magnet Material Passive Rotor Transverse Flux Motors Investigated using 3D Finite Element Analysis”, Canadian Conf. on Electr. & Computer Eng. Vol. 1, 7-10 March 2000, pp. 365 – 369.

135 P. Lemieux, O. Jude Delma, Maxime R. Dubois, Roderick Guthrie, “Soft Magnetic Composite with Lamellar Particles - Application to the Clawpole Transverse-Flux Machine with Hybrid Stator”, Proceeding of the 18th International Conference on Electrical Machines ICEM 2008, Vilamoura (Algarve), Portugal, September 6-9, 2008

136 Martin A. Plonus, Applied Electro-Magnetics, McGraw Hill, pp 319-330, 1978.

137 G.Bertotti, F.Fiorllo and G.P.Soardo, “Dependence of power losses on peak magnetization and magnetization frequency in Grain-oriented and non-oriented 3% SiFe,” IEEE Trans. Magn. vol. 23, sept 1987, pp. 3520-3522.

138 Colin J. Dunlop, Modeling Magnetic Core Loss for Sinusoidal Waveforms, Thesis for the grade of Naval Engineer and Master of Science in Electrical Engineering, Massachusetts Institute of Technology, June 2008.

139 John Barranger, “Hysteresis and eddy-current Losses of a transformer lamination viewed as an application of the Poynting theorem”, Lewis Research Center, Cleveland, Ohio, Nasa Technical note NASA TN D-3114, NASA, Washington DC, 1965.